

# **1. EXECUTIVE SUMMARY**

Farrokh Najmabadi  
Kenneth R. Schultz

Robert W. Conn

Robert A. Krakowski  
Don Steiner

## Contents

1.1.	SYNOPSIS . . . . .	1-1
1.1.1.	TITAN Plasma Engineering . . . . .	1-4
1.1.2.	TITAN-I Fusion Power Core . . . . .	1-6
1.1.3.	TITAN-II Fusion Power Core . . . . .	1-8
1.1.4.	Implications For RFP Physics Research . . . . .	1-13
1.1.5.	Conclusions . . . . .	1-13
1.2.	OVERVIEW OF TITAN PLASMA ENGINEERING . . . . .	1-18
1.2.1.	RFP Confinement Concept . . . . .	1-18
1.2.2.	Confinement . . . . .	1-23
1.2.3.	Magnetics . . . . .	1-34
1.2.4.	Impurity Control . . . . .	1-49
1.2.5.	Fueling . . . . .	1-56
1.2.6.	Start-Up and Shutdown . . . . .	1-57
1.2.7.	Current Drive . . . . .	1-73
1.2.8.	Summary and Key Technical Issues . . . . .	1-82
1.3.	OVERVIEW OF TITAN-I FUSION POWER CORE . . . . .	1-86
1.3.1.	Configuration . . . . .	1-86
1.3.2.	Materials . . . . .	1-93
1.3.3.	Neutronics . . . . .	1-97
1.3.4.	Thermal and Structural Design . . . . .	1-98
1.3.5.	Magnet Engineering . . . . .	1-104
1.3.6.	Power Cycle . . . . .	1-109
1.3.7.	Divertor Engineering . . . . .	1-110

1.3.8.	Tritium Systems . . . . .	1-116
1.3.9.	Safety Design . . . . .	1-119
1.3.10.	Waste Disposal . . . . .	1-122
1.3.11.	Maintenance . . . . .	1-124
1.3.12.	Summary and Key Technical Issues . . . . .	1-130
1.4.	OVERVIEW OF TITAN-II FUSION POWER CORE . . . . .	1-133
1.4.1.	Configuration . . . . .	1-133
1.4.2.	Materials . . . . .	1-140
1.4.3.	Neutronics . . . . .	1-147
1.4.4.	Thermal and Structural Design . . . . .	1-149
1.4.5.	Magnet Engineering . . . . .	1-153
1.4.6.	Power Cycle . . . . .	1-153
1.4.7.	Divertor Engineering . . . . .	1-155
1.4.8.	Tritium Systems . . . . .	1-159
1.4.9.	Safety Design . . . . .	1-163
1.4.10.	Waste Disposal . . . . .	1-167
1.4.11.	Maintenance . . . . .	1-170
1.4.12.	Summary and Key Technical Issues . . . . .	1-173
	REFERENCES . . . . .	1-176

# 1. EXECUTIVE SUMMARY

## 1.1. SYNOPSIS

The TITAN research program is a multi-institutional [1] effort to determine the potential of the reversed-field-pinch (RFP) magnetic fusion concept as a compact, high-power-density, and “attractive” fusion energy system from economics (cost of electricity), safety, environmental, and operational viewpoints.

In recent reactor studies, the compact reactor option [2-5] has been identified as one approach toward a more affordable and competitive fusion reactor. The main feature of a compact reactor is a fusion power core (FPC) with a mass power density in excess of 100 to 200 kWe/tonne. Mass power density (MPD) is defined [2] as the ratio of the net electric power to the mass of the FPC, which includes the plasma chamber, first wall, blanket, shield, magnets, and related structure. The increase in MPD is achieved by increasing the plasma power density and neutron wall loading, by reducing the size and mass of the FPC through decreasing the blanket and shield thicknesses and using resistive magnet coils, as well as by increasing the blanket energy multiplication. A compact reactor, therefore, strives toward a system with an FPC comparable in mass and volume to the heat sources of alternative fission power plants, with MPDs ranging from 500 to 1000 kWe/tonne and competitive cost of energy.

Other potential benefits for compact systems can be envisaged in addition to improved economics. The FPC cost in a compact reactor is a small portion of the plant cost and, therefore, the economics of the reactor will be less sensitive to changes in the unit cost of FPC components or the plasma performance. Moreover, since a high-MPD FPC is smaller and cheaper, a rapid development program at lower cost should be possible, changes in the FPC design will not introduce large cost penalties, and the economics of learning curves can be readily exploited throughout the plant life.

The RFP has inherent characteristics that allow it to operate at very high mass power densities. This potential is available because the main confining field in an RFP is the poloidal field, which is generated by the large toroidal current flowing in the plasma. This feature results in a low field at the external magnet coils, a high plasma beta, and a very high engineering beta (defined as the ratio of the plasma pressure to the square of the magnetic field strength at the coils) as compared to other confinement schemes.

Furthermore, sufficiently low magnetic fields at the external coils permit the use of normal coils while joule losses remain a small fraction of the plant output. This option allows a thinner blanket and shield. In addition, the high current density in the plasma allows ohmic heating to ignition, eliminating the need for auxiliary heating equipment. Also, the RFP concept promises the possibility of efficient current-drive systems based on low-frequency oscillations of poloidal and toroidal fluxes and the theory of RFP relaxed states. The RFP confinement concept allows arbitrary aspect ratios, and the circular cross section of plasma eliminates the need for plasma shaping coils. Lastly, the higher plasma densities particularly at the edge, together with operation with a highly radiative RFP plasma, significantly reduce the divertor heat flux and erosion problems.

These inherent characteristics of the RFP [6] allow it to meet, and actually far exceed, the economic threshold MPD value of 100 kWe/tonne. As a result, the TITAN study also seeks to find potentially significant benefits and to illuminate main drawbacks of operating well above the MPD threshold of 100 kWe/tonne. The program, therefore, has chosen a minimum cost, high neutron wall loading of 18 MW/m<sup>2</sup> as the reference case in order to quantify the issue of engineering practicality of operating at high MPDs. Furthermore, two different detailed designs, TITAN-I and TITAN-II, have been produced to demonstrate the possibility of multiple engineering-design approaches to high-MPD reactors. TITAN-I is a self-cooled lithium design with a vanadium-alloy structure. TITAN-II is a self-cooled aqueous loop-in-pool design with 9C ferritic steel as the structural material. Both designs would use RFP plasmas operating with essentially the same parameters. Both conceptual reactors are based on the DT fuel cycle, have a net electric output of about 1000 MWe, are compact and have a high mass power density of 800 kWe per tonne of FPC. The TITAN study has also put strong emphasis on safety and environmental features in order to determine if high-power-density reactors can be designed with a high level of safety assurance and with low-activation material to qualify for Class-C waste disposal.

An important potential benefit of operating at a very high MPD is that the small physical size and mass of a compact reactor permits the design to be made of only a few pieces and a single-piece maintenance approach will be feasible [7,8]. Single-piece maintenance refers to a procedure in which all components that must be changed during the scheduled maintenance are replaced as a single unit, although the actual maintenance procedure may involve the movement, storage, and reinstallation of other reactor components. In TITAN designs, the entire reactor torus is replaced as a single unit during the annual scheduled maintenance. The single-piece maintenance procedure is expected to result in the shortest period of downtime during the scheduled maintenance period

because: (1) the number of connects and disconnects needed to replace components will be minimized; and (2) the installation time is much shorter because the replaced components are pretested and aligned as a single unit before committment to service. Furthermore, recovery from unscheduled events will be more standard and rapid because complete components will be replaced and the reactor brought back on line. The repair work will then be performed outside the reactor vault.

The operating space of a compact RFP reactor has been examined using a comprehensive parametric systems model which includes the evolving state of knowledge of the physics of RFP confinement and embodies the TITAN-I and TITAN-II engineering approaches (Section 3). Two key figures of merit, the cost of electricity (COE) and mass power density (MPD), are monitored by the parametric systems model and are displayed in Figure 1.1-1 as functions of the neutron wall loading. Figure 1.1-1 shows that the

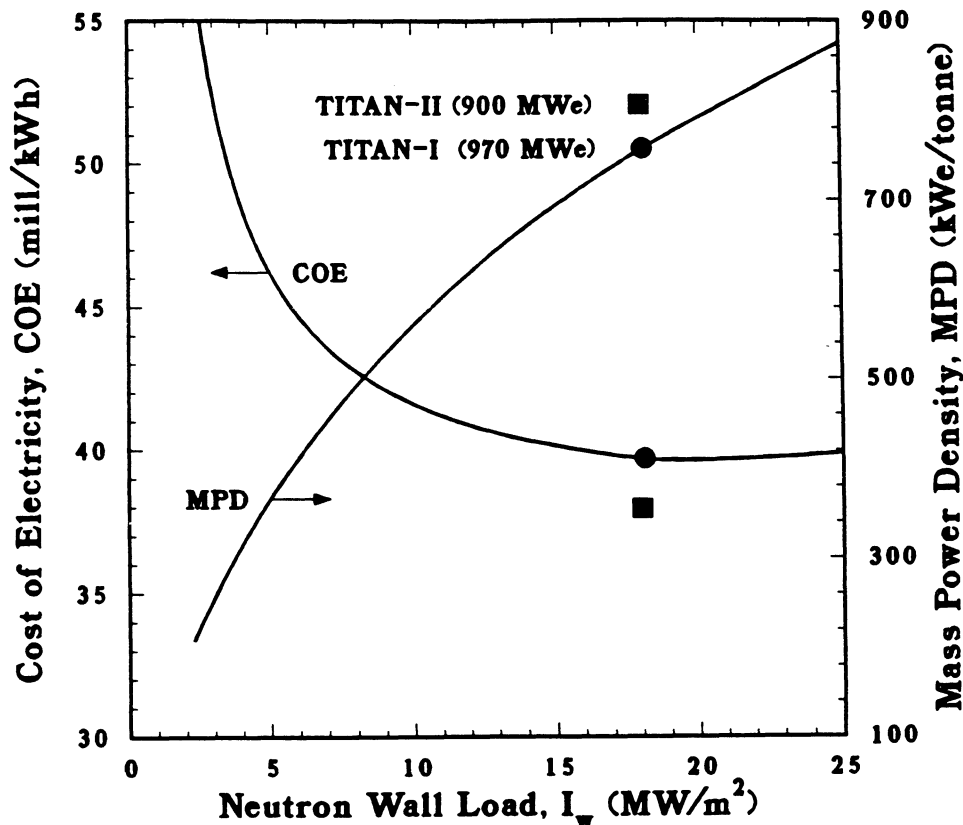


Figure 1.1-1. The COE and MPD as functions of neutron wall loading for the TITAN-class RFP reactors. TITAN-I (filled circle) and TITAN-II (filled squares) reference design points are also shown.

COE is relatively insensitive to wall loadings in the range of 10 to 20 MW/m<sup>2</sup>, with a shallow minimum at about 19 MW/m<sup>2</sup>. The MPD is found to increase monotonically with the wall load. For designs with a neutron wall load larger than about 10 MW/m<sup>2</sup>, the FPC is physically small enough such that single-piece FPC maintenance is feasible. These considerations point to a design window for compact RFP reactors with neutron wall loading in the range of 10 to 20 MW/m<sup>2</sup>. The TITAN-class RFP reactors in this design window have an MPD in excess of 500 kWe/tonne, and an FPC engineering power density in the range of 5 to 15 MWt/m<sup>3</sup>; these values represent improvements by factors of 10 to 30 compared with earlier fusion reactor designs. The FPC cost is a smaller portion of the total plant cost (typically about 12%) compared with 25% to 30% for earlier RFP designs [4,5]. Therefore, the unit direct cost is less sensitive to related physics and technology uncertainties.

Near-minimum-COE TITAN-I and TITAN-II design points, incorporating distinct blanket thermal-hydraulic options, materials choices, and neutronics performances have been identified in Figure 1.1-1. The major parameters of the TITAN reactors are summarized in Table 1.1-I. In order to permit a comparison, the TITAN reference design points have similar plasma parameters and wall loadings allowing for certain plasma engineering analyses to be common between the two designs.

In the following sections, we briefly review the major features of the TITAN designs and examine the physics requirements for achieving this class of reactors. Greater detail can be found in the body of this report.

### 1.1.1. TITAN Plasma Engineering

The TITAN RFP plasma operates at steady state using oscillating-field current drive (OFCD) [9,10] to maintain the 18 MA of plasma current. This scheme utilizes the strong coupling, through the plasma relaxation process which maintains the RFP profiles [11], between the toroidal and poloidal fields and fluxes in the RFP. Detailed plasma-circuit simulations have been performed that include the effects of eddy currents induced in the FPC. The calculated efficiency of the OFCD system is 0.3 A/W delivered to the power supply (0.8 A/W delivered to the plasma).

The impurity control and particle exhaust system consists of three high-recycling, toroidal-field divertors. The TITAN designs take advantage of the beta-limited confinement observed in RFP experiments [6,12,13] to operate with a highly radiative core plasma, deliberately doped with a trace amount of high-*Z* Xe impurities. This distributes

Table 1.1-I.

## OPERATING PARAMETERS OF TITAN FUSION POWER CORES

	TITAN-I	TITAN-II
Major radius (m)	3.9	3.9
Minor plasma radius (m)	0.60	0.60
First-wall radius (m)	0.66	0.66
Plasma current (MA)	17.8	17.8
Toroidal field on plasma surface (T)	0.36	0.36
Poloidal beta	0.23	0.23
Neutron wall load (MW/m <sup>2</sup> )	18	18
Radiation heat flux on first wall (MW/m <sup>2</sup> )	4.6	4.6
Primary coolant	Liquid lithium	Aqueous solution
Structural material	V-3Ti-1Si	Ferritic steel 9-C
Breeder material	Liquid lithium	LiNO <sub>3</sub>
Neutron multiplier	none	Be
Coolant inlet temperature (°C)	320	298
First-wall-coolant exit temperature (°C)	440	330
Blanket-coolant exit temperature (°C)	700	330
Coolant pumping power (MW)	48	49
Fusion power (MW)	2301	2290
Total thermal power (MW)	2935	3027
Net electric power (MW)	970	900
Gross efficiency	44%	35%
Net efficiency	33%	30%
Mass power density, MPD (kWe/tonne)	757	806
Cost of electricity, COE (mill/kWh)	39.7	38.0

the surface heat load uniformly on the first wall ( $4.5 \text{ MW/m}^2$ ). Simultaneously, the heat load on the divertor target plates is reduced to less than  $\sim 9 \text{ MW/m}^2$ . The ratio of impurity density to electron density in the plasma is about  $10^{-4}$ ,  $Z_{eff}$  is about 1.7, and 70% of the core plasma energy is radiated.

The “open” magnetic geometry of the divertors, together with the intensive radiative cooling, leads to a high-recycling divertor with high density and low temperature near the divertor target ( $n_e \simeq 10^{21} \text{ m}^{-3}$ ,  $T_e \simeq 5 \text{ eV}$ ) relative to the upstream separatrix density and temperature ( $n_e \simeq 2 \times 10^{20} \text{ m}^{-3}$ ,  $T_e \simeq 200 \text{ eV}$ ). The radial temperature profile is calculated to decay sharply to 2 eV near the first wall. Negligible neutral-particle leakage from the divertor chamber to the core plasma and adequate particle exhaust are predicted. The first-wall erosion rate is negligibly small because of the low plasma temperature and high density at that location.

The plasma start-up scenario for TITAN reactors can be divided into three phases: a 1-10 ms formation phase (up to 0.2 MA of plasma current), a fast current ramp (2-3 s, up to 10 MA), and a slow ramp to full plasma current. The plasma is ohmically heated to ignition during the current ramp-up phases when the impurity control system and equilibrium-field (EF) control are fully active. The required poloidal and toroidal fluxes for start-up are produced by the normal-conducting ohmic-heating (OH) coils with a bipolar swing. The TITAN start-up power is obtained directly from the grid (500 MW maximum) and no on-site energy storage is required. A pair of superconducting EF coils produce the required vertical field. These coils are energized during the start-up by the OH-coil circuit. A pair of small EF “trim” coils are included to produce the exact vertical field needed during start-up. They are also utilized for equilibrium control during the burn and OFCD operation.

### 1.1.2. TITAN-I Fusion Power Core

The TITAN-I fusion power core (FPC) is a lithium, self-cooled design with a vanadium alloy (V-3Ti-1Si) structural material. Magnetohydrodynamic (MHD) effects had precluded the use of liquid-metal coolants for high-heat-flux components in previous designs (mainly of tokamaks), but the magnetic field topology of the RFP is favorable for liquid-metal cooling. In the TITAN-I design, the first wall and blanket consist of single-pass, poloidal-flow loops aligned with the dominant poloidal magnetic field. Other major features are: separation of the first-wall- and blanket-coolant circuits to allow a lower coolant-exit temperature from the first wall; and utilization of MHD turbulent-flow heat transfer at the first wall, which is made possible by the low magnetic-interaction

parameter. The TITAN-I thermal-hydraulic design (Table 1.1-I) can accommodate up to  $5 \text{ MW/m}^2$  of heat flux on the first wall with a reasonable MHD pressure drop, a high thermal-cycle efficiency and a modest pumping power of about 45 MWe. A molten-salt tritium-extraction technique is used.

A unique feature of the TITAN-I design is the use of the integrated-blanket-coil (IBC) concept [14]. With the IBC concept, the lithium coolant in the blanket circuit flowing in the poloidal direction is also used as the electrical conductor of the toroidal-field and divertor coils. The IBC concept eliminates the need to shield the coils and allows direct access to the blanket and shield assemblies, thereby easing the maintenance procedure.

The general arrangement of the TITAN-I FPC is illustrated in Figures 1.1-2 and 1.1-3. The operational (maintenance and availability), safety, and environmental issues have been taken into account throughout the design. For example, the entire FPC is contained in a vacuum tank to facilitate the remote making and breaking of vacuum welds. All maintenance procedures would be performed by vertical lift of the components (the heaviest component weighs about 250 tonnes), which reduces the size of the expensive confinement building. The number of remote handling procedures is few and the movements are uncomplicated. All the primary-coolant ring headers are located above the torus for easy access during maintenance. This ensures that the coolant will remain in the torus in the event of a break in the primary piping. The most severe safety event will be a loss-of-flow accident (LOFA). The FPC and the primary-coolant loop are located in an inert-gas-filled (Ar) confinement building which, together with the blanket containers and the vacuum vessel, form three barriers to prevent air influx to reduce the hazards of lithium fires and to provide protection for the public from radioactive materials. Lithium drain tanks are provided for both the reactor vault and the vacuum tank to reduce passively the vulnerable blanket lithium inventory.

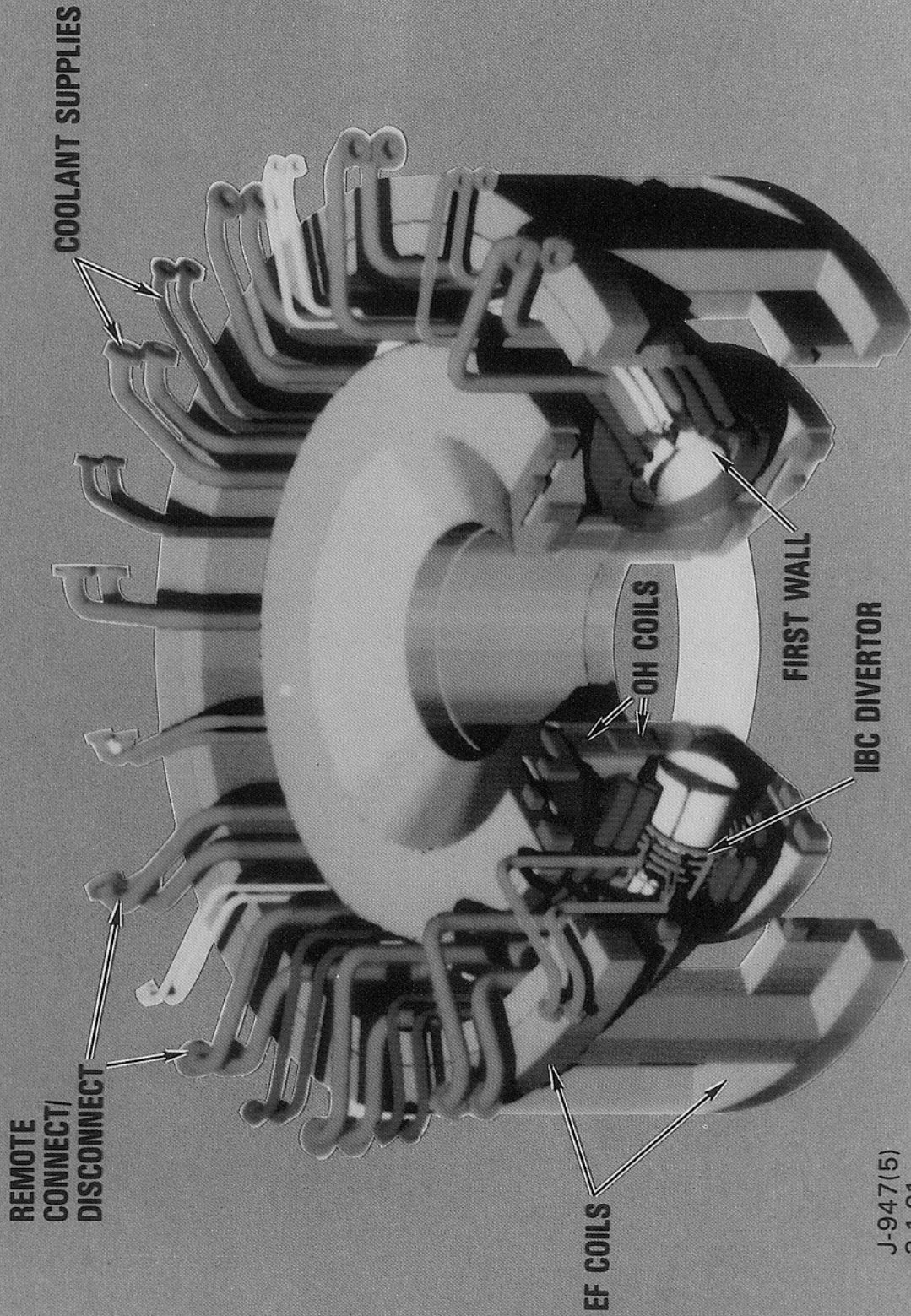
A low-activation, low-after-heat vanadium alloy is used as the structural material throughout the FPC in order to minimize the peak temperature during a LOFA and to permit near-surface disposal of waste. The maximum temperature during a first-wall loss-of-coolant accident (LOCA) and system LOFA (the most severe accident postulated for TITAN-I) is  $990^\circ\text{C}$ . Lithium-fire accident scenarios and site-boundary dose calculations were performed to understand the potential release of radioactivity under major accident and routine release conditions. The safety analysis indicates that the liquid-metal-cooled TITAN-I design can be classified as passively safe, without reliance on any active safety systems. Thus, a high Level of Safety Assurance [15,16] for the compact TITAN-I design is expected.

### 1.1.3. TITAN-II Fusion Power Core

The TITAN-II FPC is a self-cooled aqueous "loop-in-pool" design with a dissolved Li salt ( $\text{LiNO}_3$  with 5 at.% lithium) as the breeder. The structural material is 9C ferritic steel [17], a reduced-activation, high-strength alloy (12Cr-0.3V-1W-6.5Mn-0.08C). The first-wall and blanket lobes are integrated and contain the pressurized coolant at 12 MPa. The structural load from the pressurized lobes is supported by an outer support shell that packs several lobes into a blanket module, as illustrated in Figures 1.1-4 and 1.1-5, and forms 1/12 of the reactor torus. Three toroidal divertor chambers divide the reactor torus into three sectors, each containing four blanket modules. The coolant enters the lobes from the bottom, flows around the torus poloidally, and exits through the top plena. Subcooled-flow-boiling heat transfer is needed to cool the first wall. The blanket zone contains beryllium rods with 9C ferritic-steel cladding as neutron multiplier.

Different lithium compounds were considered as the breeding salt in the aqueous solution, and solubility, corrosion, and radiolysis effects in a fusion environment were evaluated. The  $\text{LiNO}_3$  solution was selected as the reference breeding material because it has a pH value close to neutrality and can be much less corrosive. Furthermore, preliminary estimates of radiolytic yield indicated that the formation of an explosive gas mixture of hydrogen and oxygen may be avoidable for  $\text{LiNO}_3$  because of the presence of nitrate ions. Account is taken of the thermophysical properties of the salt solution, which are significantly different from those of the pure water. The TITAN-II tritium-control and extraction system would be, in principle, an extension of the technology developed by the Canadian CANDU fission-reactor program [18].

A very key feature of TITAN-II is that the fusion power core and the entire primary loop are submerged in a pool of low-temperature, low-pressure water. The basic sources of thermal energy after reactor shutdown are from the hot loop and the induced afterheat from the torus first-wall and blanket structures. The first-wall- and blanket-coolant channel configurations are designed to allow natural circulation to develop in the case of a LOFA. In the case of a major break in the primary-coolant pipes, the cold pool would absorb the thermal and afterheat energy from the hot loop. Calculations show that the pool remains at a temperature low enough to prevent the release of tritium or other radioactivity in the blanket-coolant system. As such, the TITAN-II design appears to achieve complete passive safety (Level 2 of Safety Assurance as defined in References [15,16]).



J-947(5)  
3-1-91

**Figure 1.1-2.** The TITAN-I fusion power core. The coolant supplies to the first wall are in white, to the IBC are in blue, to the shield are in red, and to the divertor-IBC are in yellow.

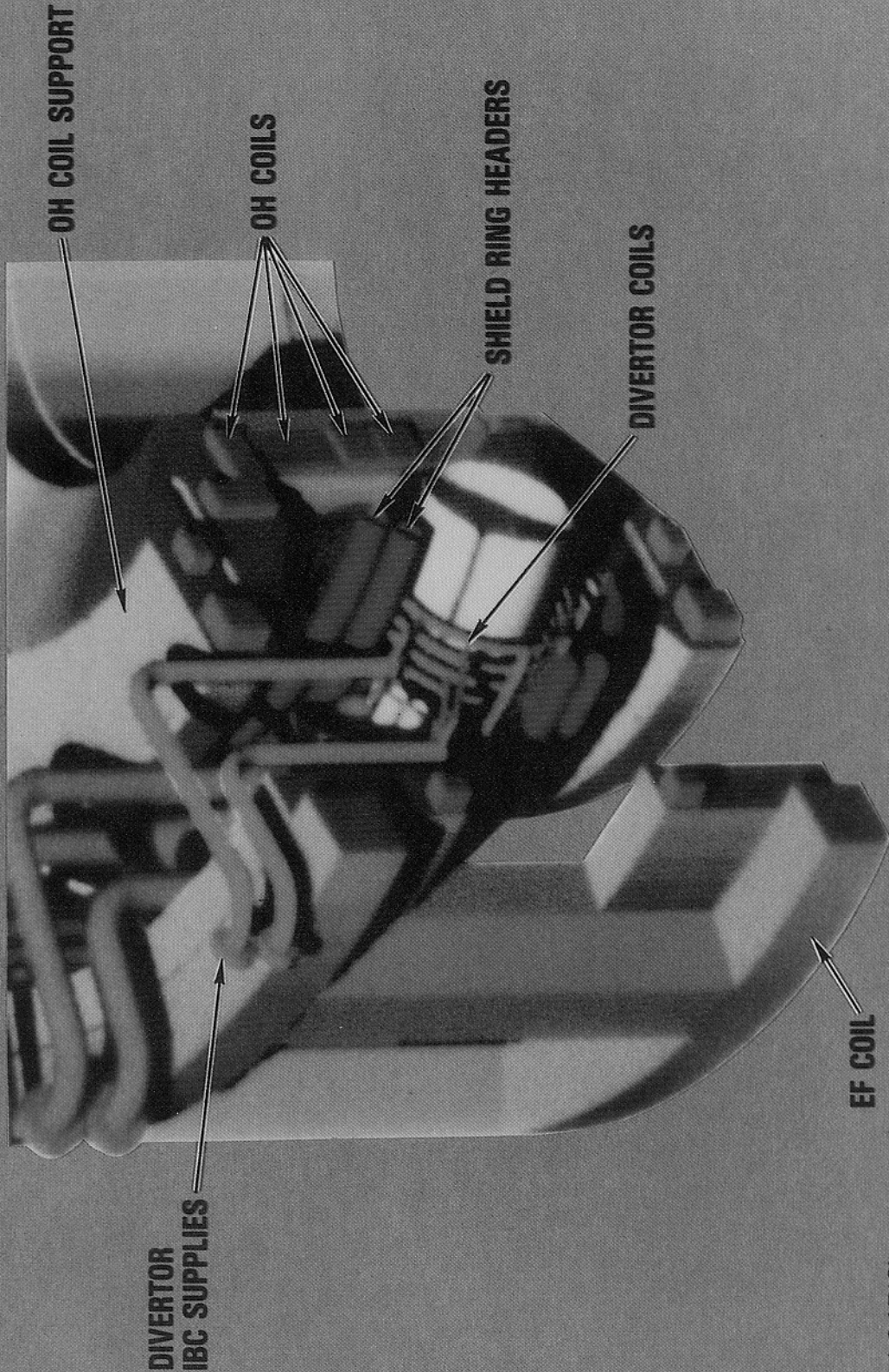
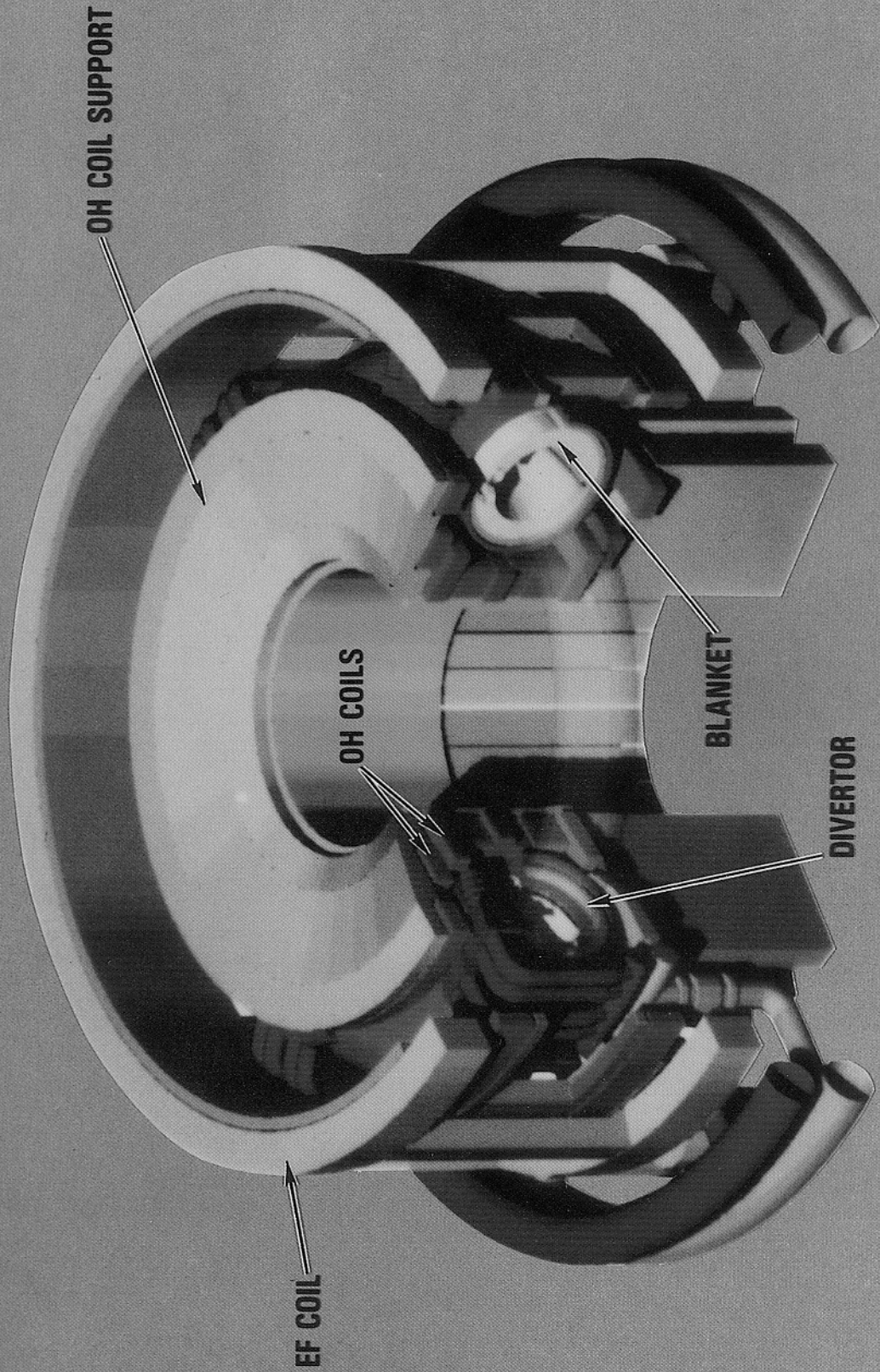


**Figure 1.1-3.** Cut-away view of the TITAN-I fusion power core. The coolant supplies to the first wall are in white, to the IBC are in blue, to the shield are in red, and to the divertor-IBC are in yellow.

J-947(6)  
3-1-91



J-947(3)  
3-1-91

**Figure 1.1-4.** The TITAN-II fusion power core. The coolant inlet headers are in white and the outlet headers are in red.

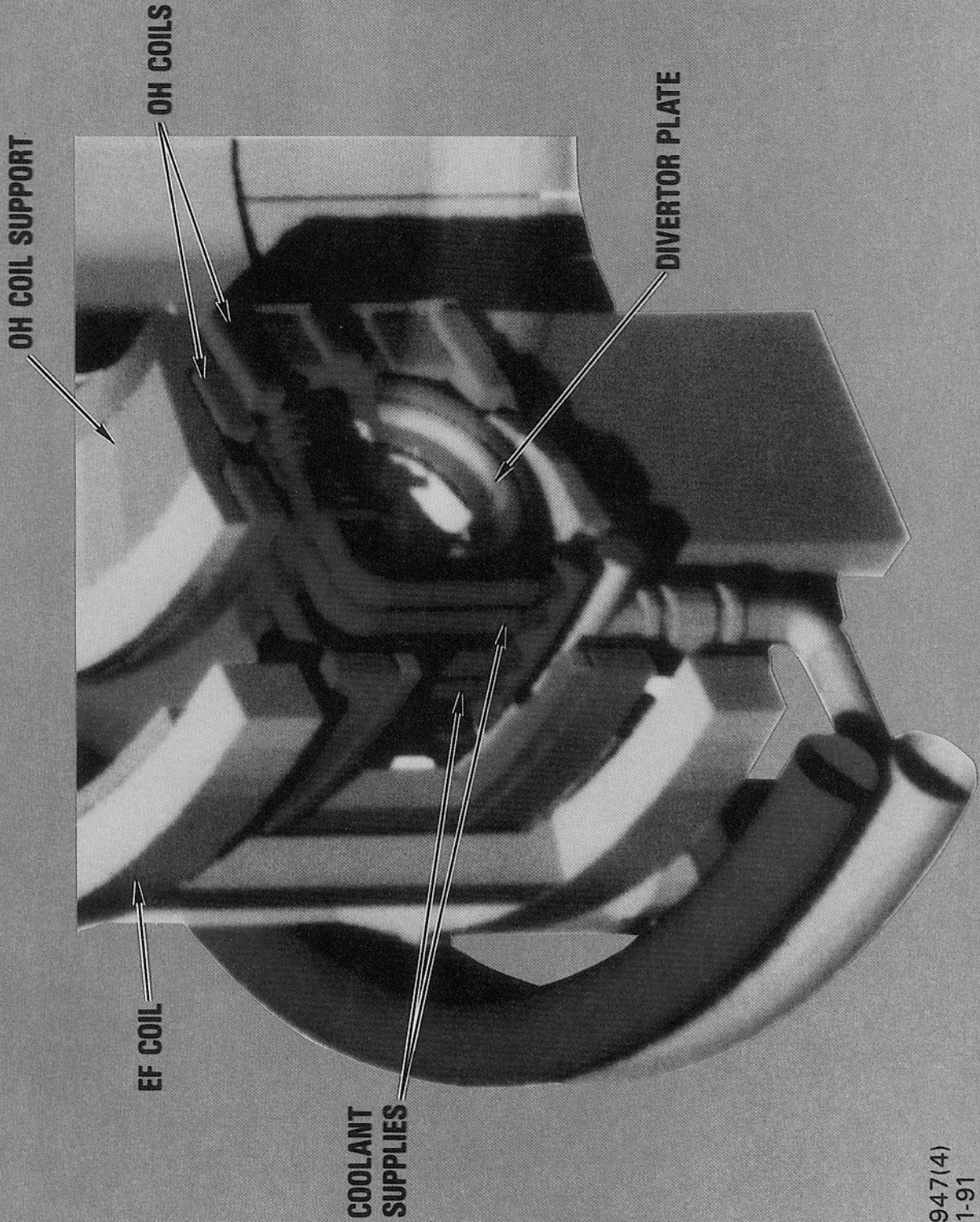


Figure 1.1-5. Cut-away view of the TITAN-II fusion power core. The coolant inlet headers are in white and the outlet headers are in red.

J-947(4)  
3-1-91

#### 1.1.4. Implications For RFP Physics Research

The experimental and theoretical bases for RFPs have grown rapidly during the last few years [6, 13, 19-22], but large degrees of extrapolations to TITAN-class reactors are still required. The degree of extrapolation is one to two orders of magnitude in plasma current and temperature and two to three orders of magnitude in energy confinement time (Table 1.1-II and Figure 1.1-6). However, the TITAN plasma density, poloidal beta, and current density all are close to present-day experimental achievements. The next generation of RFP experiments [13,22] with hotter plasmas will extend the data base toward reactor-relevant regimes of operation (Figure 1.1-6). The TITAN study has brought out and illuminated a number of key physics issues, some of which require greater attention from the RFP physics community.

The physics of confinement scaling, plasma transport, and the role of the conducting shell are already major efforts in RFP research. However, the TITAN study points to three other major issues. First, operating high-power-density fusion reactors with intensely radiating plasmas is crucial. Confirming that the global energy confinement time remains relatively unaffected while core-plasma radiation increases (a possible unique feature of RFPs) is extremely important. Second, the TITAN study has adopted the use of three "open-geometry" toroidal divertors as the impurity control and particle exhaust system. Even with an intensely radiative plasma, an array of poloidal pump-limiters would encounter serious erosion of the limiter blades (and possibly the first wall). The physics of toroidal-field divertors in RFPs must be examined, and the impact of the magnetic separatrix on RFP confinement must be studied. If toroidal divertors are consistent with confinement and stability in RFPs, then high-recycling divertors and the predicted high-density, low-temperature scrape-off layer must be also confirmed. Third, early work in the TITAN study convinced the team that high MPD, compact RFP reactors must operate at steady state. Current drive by magnetic-helicity injection utilizing the natural relaxation process in the RFP plasma is predicted to be efficient [9,10] but experiments on OFCD are inconclusive. Testing OFCD in higher temperature plasmas must await the next generation of RFP experiments, namely ZTH [13] and RFX [22].

#### 1.1.5. Conclusions

The TITAN research supports the technical feasibility of high-MPD RFP fusion reactors. The TITAN designs have an MPD value of about 800 kWe/tonne of FPC, approaching that of a pressurized-water fission reactor (PWR), as shown in Figure 1.1-7. By

**Table 1.1-II.**  
**PARAMETERS OF MAJOR RFP DEVICES**

Device	Major Radius (m)	Minor Radius (m)	Plasma Current (MA)	Current Density (MA/m <sup>2</sup> )	Electron Temperature (keV)	Average Density (10 <sup>20</sup> m <sup>-3</sup> )	Poloidal Beta
TPE-1RM <sup>(a)</sup>	0.50	0.09	0.13	5.1	0.60	0.3	0.1
ETA-BETA-II <sup>(b)</sup>	0.65	0.125	0.15	3.0	0.08	1.0	0.1
HBTX1A <sup>(c)</sup>	0.80	0.26	0.32	1.5	0.10	0.2	0.05
OHTE/RFP <sup>(d)</sup>	1.24	0.20	0.50	4.5	0.4 - 0.6	0.5 - 3.0	0.1 - 0.2
ZT-40M <sup>(e)</sup>	1.14	0.20	0.44	3.5	0.3 - 0.5	0.4 - 0.9	0.1 - 0.2
RFX <sup>(f)</sup>	2.00	0.48	2.0	2.8	0.5 - 2.0	0.3 - 2.0	0.10
CPRF/ZTH <sup>(g)</sup>	2.40	0.40	4.0	8.0	0.5 - 5.0	0.3 - 5.0	0.10
FTF/RFP <sup>(h)</sup>	1.80	0.30	10.4	37.	10. - 20.	6.0 - 9.0	0.1 - 0.2
TITAN <sup>(i)</sup>	3.80	0.60	18.2	16.	10. - 20.	9.0	0.2

(a) Existing experiment at ETL, Japan [23,24].

(b) Existing experiment at Padova, Italy [25 - 27].

(c) Existing experiment at Culham, U. K. [28,29].

(d) Existing experiment at General Atomics, U. S. A. [30,31].

(e) Existing experiment at Los Alamos National Laboratory, U. S. A. [32,33].

(f) Planned experiment at Padova, Italy [34].

(g) Planned experiment at Los Alamos National Laboratory, U. S. A. [34].

(h) Conceptual neutron source, a Los Alamos National Laboratory study, U. S. A. [35].

(i) Conceptual reactor design, a UCLA-led multi-institutional study, U. S. A.

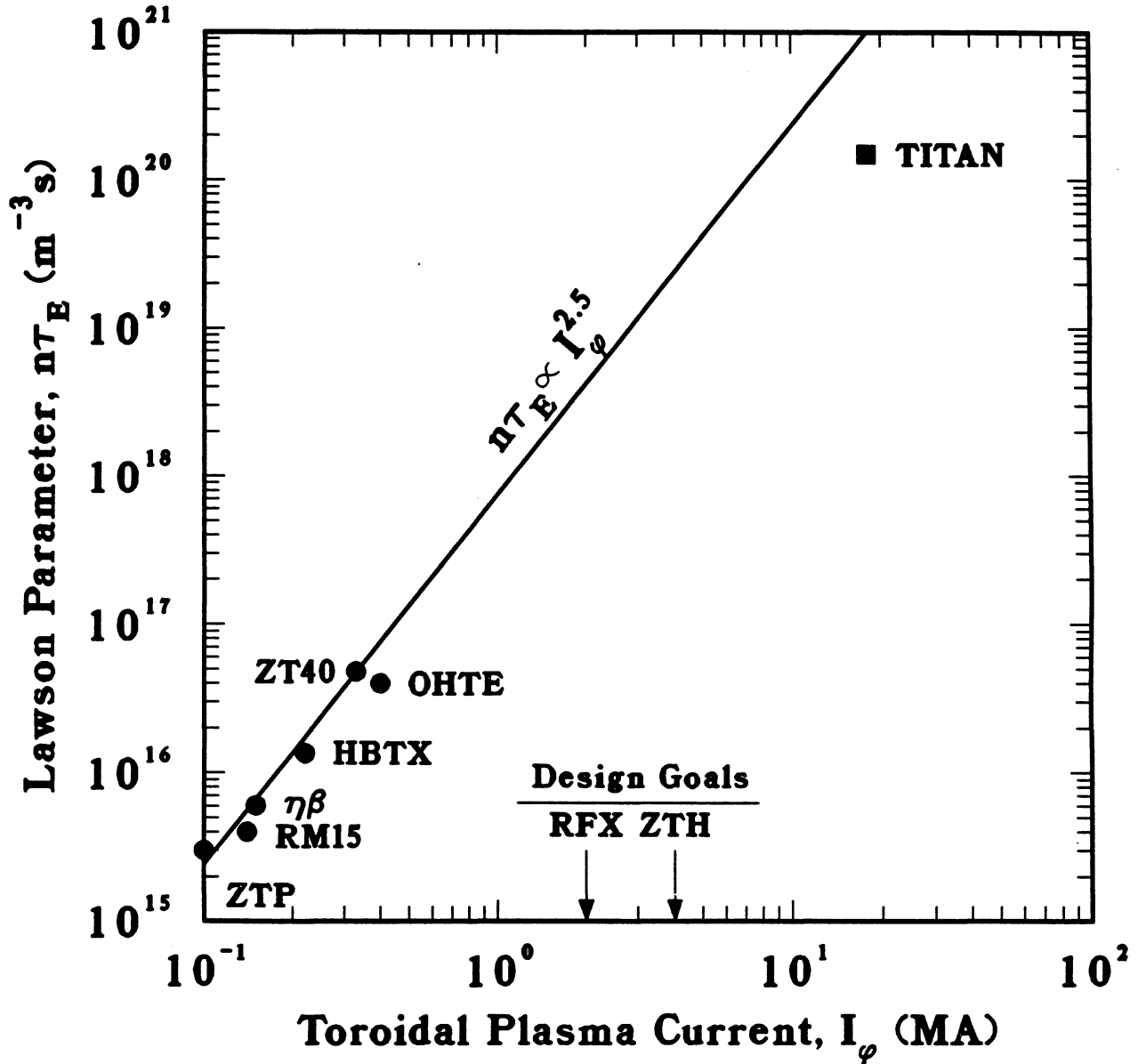


Figure 1.1-6. Variation of the confinement parameter with plasma current with data from several experiments. These early data formed the basis of scaling relationships used in early studies of the RFP reactor [8].

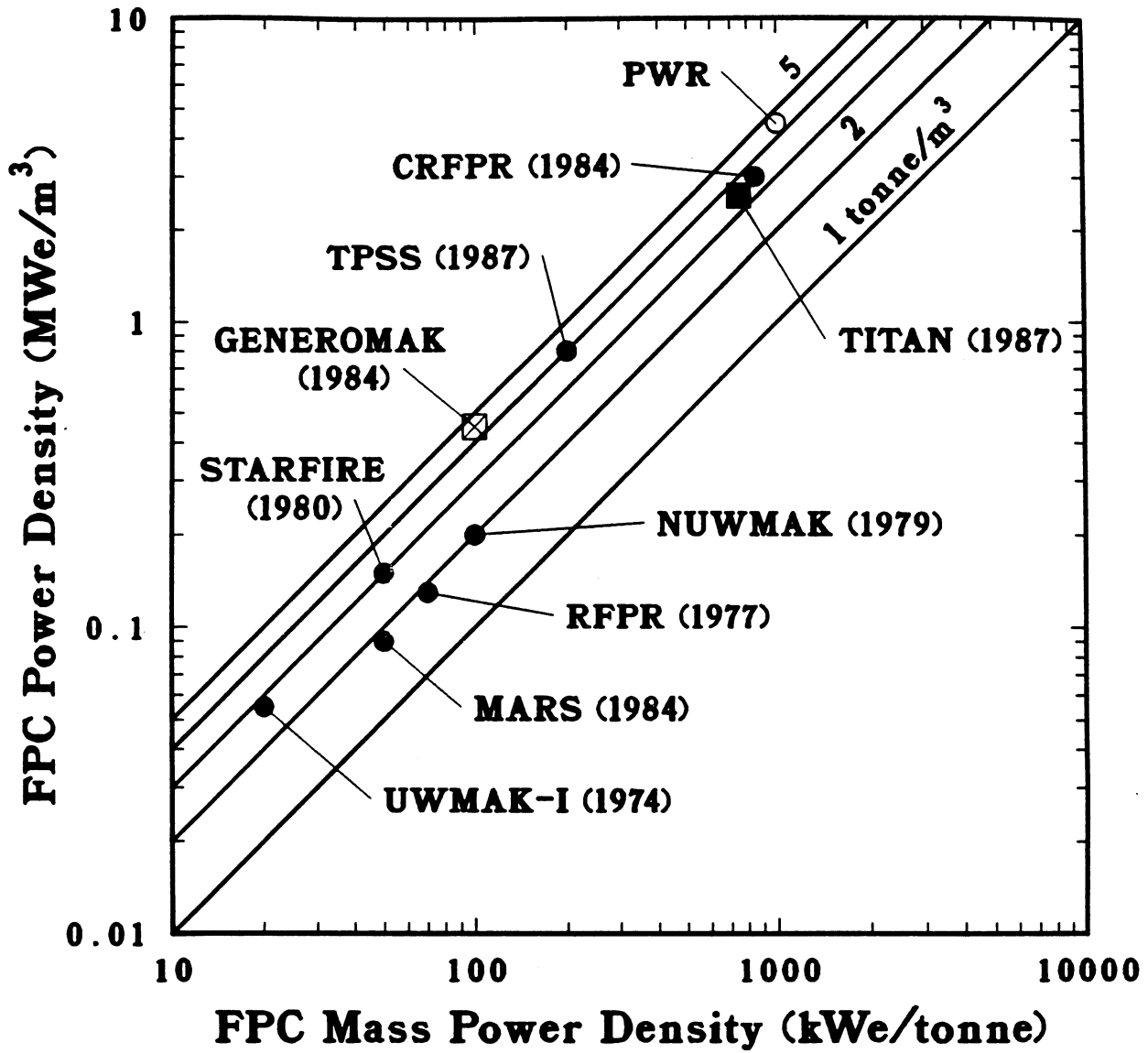


Figure 1.1-7. The MPD and the FPC power density of several fusion reactor designs, including TITAN, and a fission PWR.

contrast, earlier studies of tokamak and tandem mirror reactors such as STARFIRE [36] and MARS [37] had MPD values of around 50 kWe/tonne. Recent work suggests tokamaks may achieve values between 100 to 200 kWe/tonne [3]. The RFP has inherent characteristics that allow it to operate at very high MPDs [6]. Parametric studies show that such compact RFP reactors would include machines with neutron wall loading in the range 10-20 MW/m<sup>2</sup>. Reactors in this “design window” are physically small and a potential benefit of this “compactness” is improved economics. Also, the cost of the FPC for TITAN reactors is a small fraction of the overall estimated plant cost (< 10%), making the economics of the reactor less sensitive to changes in the plasma performance or unit costs for FPC components. Moreover, since the FPC is smaller and cheaper, a development program should cost less. The TITAN study further shows that, with proper choice of materials and FPC configuration, compact reactors can be made passively safe and, thus, the potential attractive safety and environmental features of fusion need not be sacrificed in compact reactors.

The compactness of the TITAN designs would reduce the FPC to a few small and relatively low-mass components, making toroidal segmentation unnecessary. Thus, a “single-piece” FPC maintenance procedure in which the first wall and blanket is removed and replaced as a single unit is possible. This unique approach permits the complete FPC to be made of a few factory-fabricated pieces, assembled on site into a single torus, and tested to full operational conditions before commitment to nuclear service. The low cost of the FPC means that a complete, “ready-for-operation” spare unit can be kept on site for replacement in case of unscheduled events. All of these features are expected to improve the plant availability.

It must be emphasized, nevertheless, that in high-power-density designs such as TITAN, the in-vessel components (*e.g.*, first wall and divertor plates) are subject to very high surface heat flux and that their design remains an engineering challenge. Also, the RFP plasma itself must operate in the manner outlined: with toroidal-field divertors, with a highly radiative core plasma, and at steady state. Future research will determine if, in fact, the physics and technology requirements of TITAN-class RFP reactors are achievable.

The rest of this section provides overviews of the TITAN plasma engineering and TITAN-I and TITAN-II fusion-power-core design efforts. Each subsection also highlights the advantages and key technical issues for achieving high-MPD RFP reactors.

## 1.2. OVERVIEW OF TITAN PLASMA ENGINEERING

Although two separate fusion-power-core designs were studied for the TITAN reactors, lithium cooled for TITAN-I and an aqueous solution of a lithium salt as the coolant and breeder for TITAN-II, both designs had the same plasma parameters. Therefore, most of the plasma simulation effort was not duplicated and, although there are certain references specifically to the TITAN-I design, only minor modifications would be required for TITAN-II. The TITAN plasma simulations incorporate the latest understanding and models developed for RFPs (Section 2); in several cases, new and improved models had to be developed for the TITAN study. More detailed descriptions of the theoretical and experimental aspects of the RFP confinement concept are given in Section 2, and References [6,38,39] and the references contained therein. Because of the relative lack of theoretical and experimental data bases for RFPs, the sensitivity of the design point to various physics assumptions has also been investigated (Section 3.4.2). A detailed description of the plasma engineering for the TITAN reactors is given in Sections 4 through 7. A detailed description of the necessary R&D areas for compact RFP reactors has also been produced and is reported in Section 8.

### 1.2.1. RFP Confinement Concept

The RFP, like the tokamak, belongs to a class of axisymmetric, toroidal-confinement systems that uses both toroidal,  $B_\phi$ , and poloidal,  $B_\theta$ , magnetic fields to confine the plasma. Stability in the tokamak is provided by a strong toroidal field ( $B_\phi \gg B_\theta$  everywhere) such that the safety factor,  $q = r_p B_\phi / (R_T B_\theta)$ , exceeds unity, where  $R_T$  and  $r_p$  are, respectively, the major and minor radii of the plasma. In the RFP, on the other hand, strong magnetic shear produced by the radially varying (and decreasing) toroidal field stabilizes the plasma with  $q < 1$  at relatively modest levels of  $B_\phi$ . Theoretically, an electrically conducting shell surrounding the plasma is required to stabilize the long-wavelength MHD modes. In both the RFP and the tokamak, equilibrium may be provided by either an externally produced vertical field, a conducting toroidal shell, or by a combination. Figure 1.2-1 compares the radial variation of the poloidal and toroidal fields and the safety factors for the tokamak and RFP.

The RFP magnetic topology is dominated by the poloidal field generated by the current flowing in the plasma. This feature has several reactor-relevant advantages. The poloidal field decreases inversely with the plasma radius outside the plasma. The toroidal field is also weak outside the plasma relative to the tokamak. The magnetic field strength

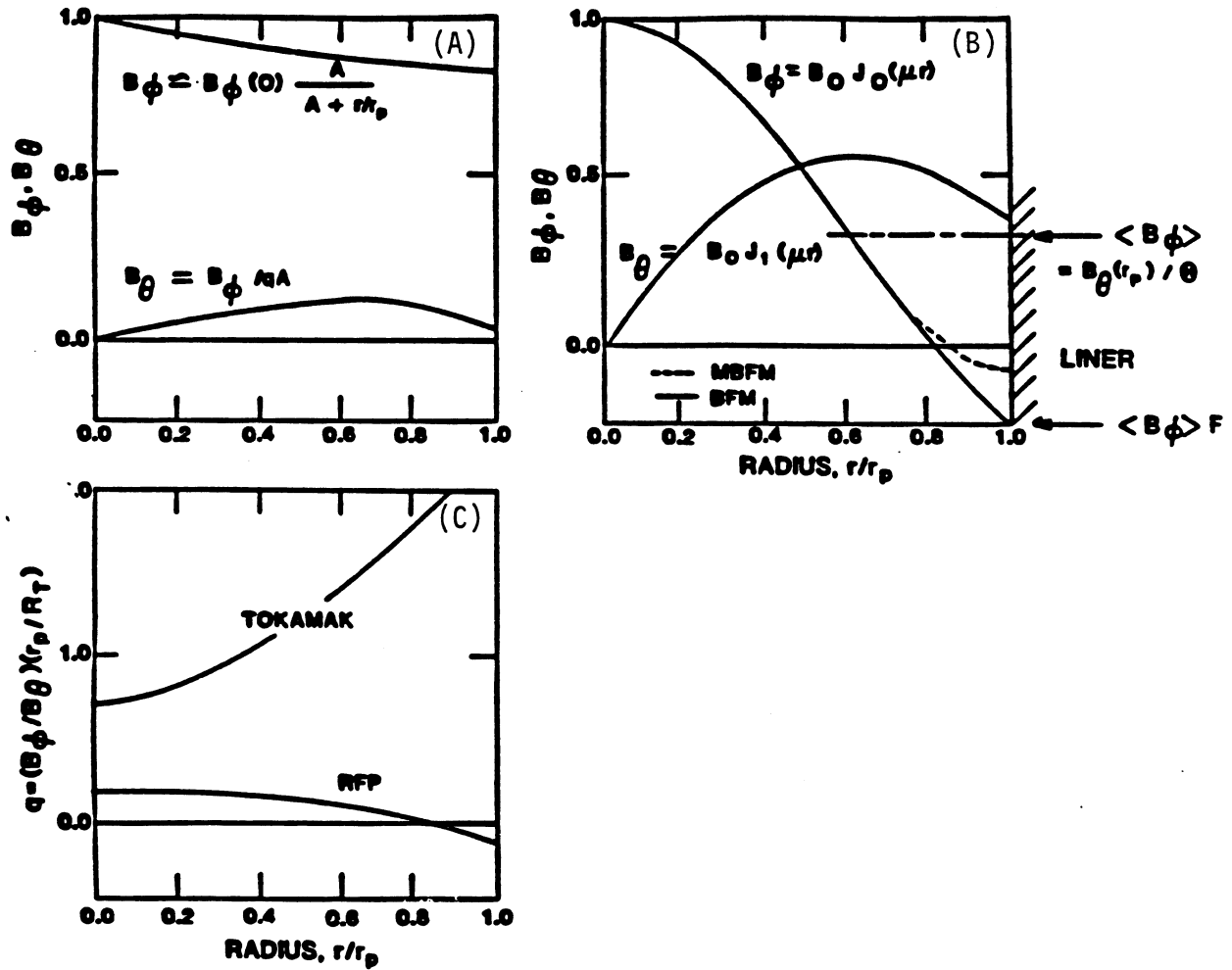


Figure 1.2-1. Magnetic-field distribution for tokamak (A) and RFP (B) and the  $q$  profiles for tokamak and RFP (C).

at the external conductors, therefore, is small, and a high engineering beta (defined as the ratio of the plasma pressure to the magnetic field pressure at the magnets) results; less-massive resistive coils with a low current density are possible. The RFP experiments operate at reactor-relevant values of total beta (5% to 10%). Furthermore, by relying on the magnetic shear to stabilize the plasma, the RFP can support a large ratio of plasma current to toroidal field, and stability constraints on the aspect ratio,  $R_T/r_p$ , are removed; the choice of the aspect ratio, therefore, can be made solely on the basis of engineering constraints. High-current-density operation and strong ohmic heating to ignition are also positive consequences of the shear-stabilized RFP. Lastly, the close coupling of the current and magnetic-field components within the RFP plasma also promises a unique and highly efficient current-drive technique.

The field configuration and toroidal-field reversal in the RFP are the result of the relaxation of the plasma to a near-minimum-energy state. A theory of relaxed states developed by Taylor [11] postulates that a pinch should relax to a magnetic-field configuration determined by minimizing the magnetic energy subject to constraints imposed on allowed motion or magnetic-field variation. Taylor then considered the relaxation of a plasma with small but finite resistivity in a flux-conserving cylinder, subject to the invariance of the magnetic helicity,  $K \equiv \int \mathbf{A} \cdot \mathbf{B} dV_p$ , where  $\mathbf{B} \equiv \nabla \times \mathbf{A}$  and the integration is over the plasma volume. The helicity is a measure of the linkage between the poloidal and toroidal magnetic flux. The relaxed, minimum-energy state was found to be force-free and described by  $\nabla \times \mathbf{B} = \mu \mathbf{B}$ , where  $\mu = \mu_o \mathbf{j} \cdot \mathbf{B}/B^2$  is the ratio of local parallel current and field. For the minimum-energy Taylor state, the  $\mu$  profile is uniform across the plasma. The solution to the equilibrium equation in cylindrical geometry for a spatially constant  $\mu$  gives the Bessel-function model (BFM), with  $B_\phi \propto J_1(\mu r)$  and  $B_\theta \propto J_0(\mu r)$ , where  $J_1$  and  $J_0$  are Bessel functions of the first kind. These relaxed states can be described solely in terms of two dimensionless quantities: the reversal parameter,  $F$ , and the pinch parameter,  $\Theta$ , where

$$F \equiv \frac{B_\phi(r_p)}{\langle B_\phi \rangle}, \quad (1.2-1)$$

$$\Theta \equiv \frac{B_\theta(r_p)}{\langle B_\phi \rangle}. \quad (1.2-2)$$

The average toroidal field within the conducting shell,  $\langle B_\phi \rangle$ , is defined as

$$\langle B_\phi \rangle = \frac{2}{r_p^2} \int_0^{r_p} B_\phi(r) r dr. \quad (1.2-3)$$

The locus of relaxed states then forms a curve in  $F$ - $\theta$  space, as is shown in Figure 1.2-2 (labeled as BFM). The same figure also shows the experimental data that lie to the right of the curve predicted by the BFM model. The experimental equilibria represented in Figure 1.2-2 differ from the Taylor model because plasma has finite pressure,  $\mu$  is not uniform across the plasma, and a perfectly conducting wall is not used. These data represent near-minimum-energy states. The concept of a preferred locus of relaxed states in  $F$ - $\theta$  space, as originally postulated by Taylor, remains applicable, however.

The theory of relaxed states as applied to the RFP concept has several important consequences. Firstly, the theory predicts that the relaxed states depend only on the pinch parameter,  $\Theta$ , and these states are independent of initial conditions provided that the time scale is sufficiently long for the relaxation process to occur. Secondly, if the plasma current and toroidal flux are maintained constant in time (*i.e.*, constant  $\Theta$ ), then the relaxed-state equilibrium will be sustained. Experimentally, the RFP configuration

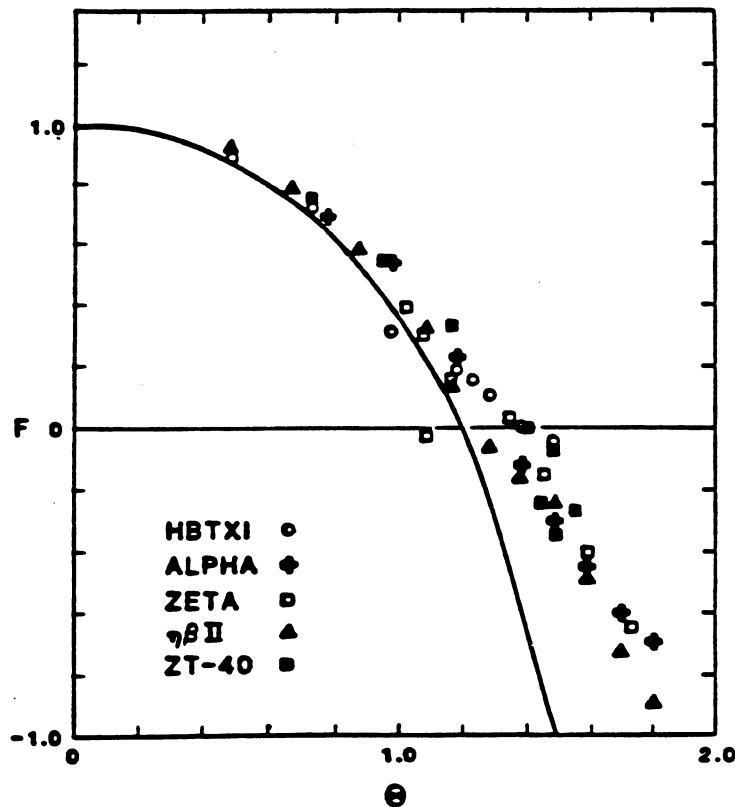


**Figure 1.2-2.** Locus of operating points on the  $F$ - $\Theta$  diagram. The solid line (BFM) is the curve predicted by Taylor's theory [11] and the data points are from several RFP experiments.

shown in Figure 1.2-2 exists for times much larger than the resistive decay time of the field profiles. This sustainment process involves continuous generation of the toroidal field within the plasma to compensate for the resistive decay of the toroidal field and to maintain the field profile; this process is often called the RFP "dynamo." The RFP dynamo converts poloidal flux or toroidal currents to poloidal currents or toroidal flux and is driven by localized plasma fluctuations of fluid velocity,  $\delta u$ , and magnetic field,  $\delta B$ , to give a non-zero time-averaged electric field,  $\langle \delta u \times \delta B \rangle$ .

The  $F$ - $\Theta$  relationship (Figure 1.2-2) reflects a strong coupling between the toroidal and poloidal fields within the plasma: the toroidal field is continuously regenerated by driving toroidal current with an external poloidal-field circuit. Indeed, such a relaxation-assisted plasma current ramp has been demonstrated in RFP experiments and is envisioned for the start-up of RFP reactors. The strong coupling of the poloidal and toroidal fields in RFPs also offers the possibility of a steady-state current-drive mechanism based on "magnetic helicity injection" [9] because the resistive decay of plasma currents can be viewed as a dissipation of magnetic helicity. Current drive through "electrostatic helicity injection" has been experimentally demonstrated in spheromaks [40], which are also relaxed-state systems like RFPs. Another helicity injection technique is the oscillating-field current drive [9,41]. In this scheme, oscillating voltages are applied to the toroidal and poloidal circuits in the appropriate phase to drive a DC toroidal current in the plasma with the plasma, in effect, behaving as a nonlinear rectifier.

An important achievement for RFP was the discovery in 1965 of a period of improved stability and reduced turbulence on the ZETA device [42]. The quiescent period observed in ZETA was preceded by a turbulent phase with large energy losses and strong plasma-wall interactions. Furthermore, self-reversal of the external toroidal field relative to the on-axis field was observed, but the importance of these observations was not fully appreciated at the time. To reduce energy losses and plasma-wall interactions, experimental RFPs during the 1970s used fast magnetic-field programming with typical rise times of a few microseconds to force the reversal externally. These experiments required electrically insulated discharge tubes to accommodate the high voltages needed to generate fast-rising magnetic fields. Many important advances in RFP physics were made in these machines, although the reactor relevance of these high-voltage, pulsed devices was minimal.

With experience from fast-programming machines and a general theory of relaxed states [11], modern RFP experiments in the late 1970s and 1980s have returned to slow-rising plasma current (0.1 to 1.0 ms) and the facility for slow  $B_\phi$  control to assist and optimize the self-reversal process and to minimize RFP formation losses. These machines

use a metallic liner around the plasma, are equipped with improved vacuum systems, and operate with improved magnetic-field geometry. The first of these modern machines was ETA-BETA-II at Padova [25-27], which began operation in 1979. Today, high-temperature plasmas are routinely produced in many intermediate-size machines, such as TPE-1R(M) at ETL, Sakura-Mura [23,24], ZT-40M at Los Alamos National Laboratory [32,33], HBTX1A at Culham [28,29], and OHTE/RFP at General Atomics [30,31]. General parameters of these more recent RFP experiments are listed in Table 1.1-II. The design parameters of the TITAN reactor are also listed for comparison and Figure 1.2-3 gives a size comparison between existing, planned [34], and conceptual [35] RFP designs.

The plasma parameters obtained in these experiments have been improving steadily. Reactor-relevant values of  $\beta_\theta$  in the range 0.1 to 0.2 are routinely achieved (total beta in RFPs is typically 50% of  $\beta_\theta$ ). Electron temperatures in the range 0.4 to 0.6 keV, densities exceeding  $10^{20} \text{ m}^{-3}$ , and energy confinement times approaching 1 ms are typical of these intermediate-size experiments. In addition, ion temperatures approaching 1 keV have been achieved under conditions where anomalous ion heating is observed (*i.e.*, high values of  $I_\phi/N$ ). Data from a number of machines indicate a nearly linear temperature-current scaling under some conditions, which suggests  $\tau_E \propto T_e^{3/2}$ . Furthermore, both experimental and theoretical evidence suggest a strong scaling of  $n\tau_E$  with the plasma current,  $n\tau_E \propto I_\phi^{5/2}$ . The scaling of plasma pressure with current suggests  $p \propto I_\phi^\nu$ , where  $\nu \leq 2.0$ ; the equality indicates a constant- $\beta_\theta$  scaling, although evidence exists for a slow decrease in  $\beta_\theta$  with plasma current.

### 1.2.2. Confinement

Extensive measurements of the dependence of the plasma temperature on current for a range of RFPs indicate that the on-axis electron temperature increases with plasma current raised to a power in the range of 0.5-1.0. Temperature increases on the order of 1 eV/kA have been observed. The ZT-40M data over a range of conditions show  $T_e(0) \propto I_\phi^{1.2}$  and  $n_e T_e(0) \propto I_\phi^2$  (*i.e.*, approximately constant  $\beta_\theta$  if  $T_e(0)/T_e$  is constant and  $T_i \simeq T_e$ ). In other experiments on ZT-40M with current flat-top operation and longer pulses, it was found that  $T_e(0) \propto I_\phi^{0.7}$ , but in these conditions  $n \propto I_\phi^{1.3}$ , again resulting in  $n_e T_e(0) \propto I_\phi^2$  and a constant- $\beta$  scaling.

More recent results from HBTX1A [20] and ZT-40M [19] suggest that the temperature-current scaling might be better described by postulating a constant  $\beta$ , with a slope determined by  $I_\phi/N$ . Evidence from a number of experiments indicates that the maximum value of  $\beta_\theta$  varies relatively little over a range of conditions and from one machine to

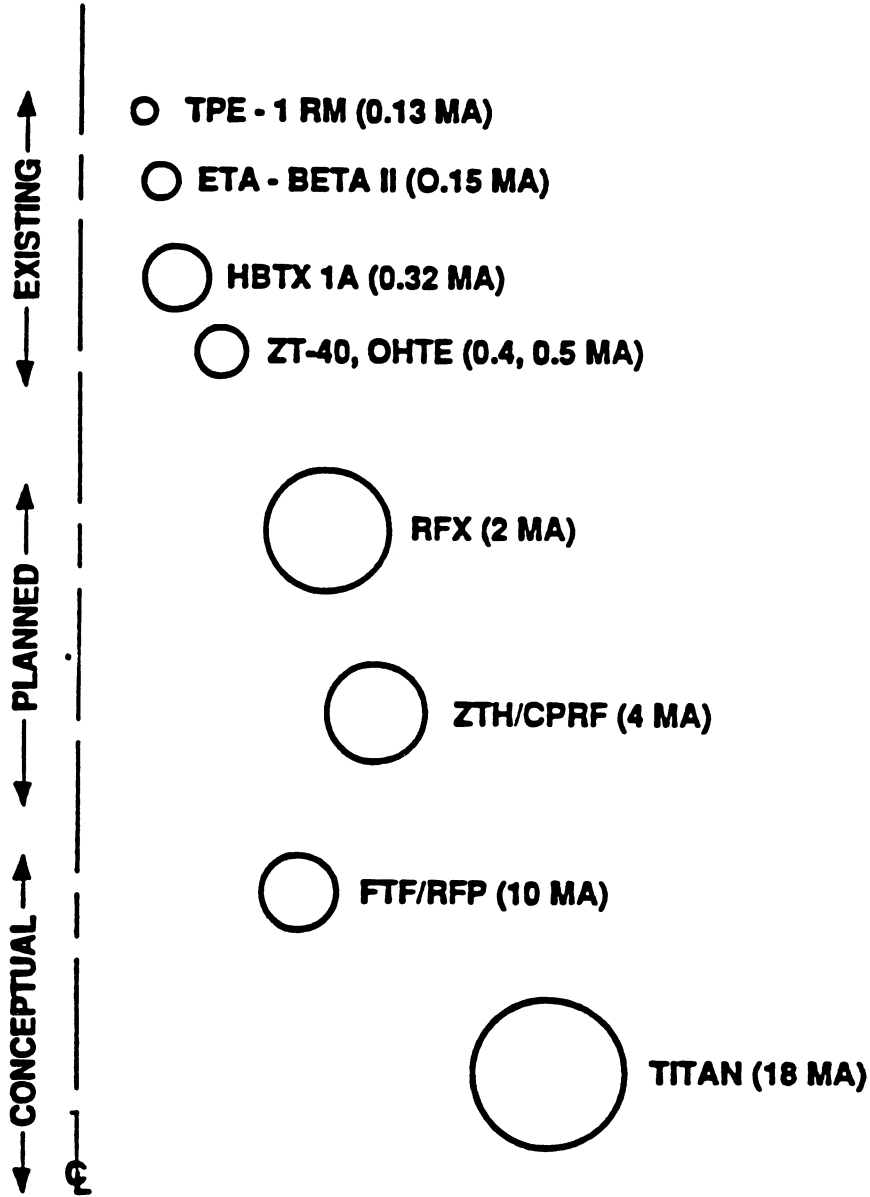


Figure 1.2-3. Comparison of plasma cross sections for present, planned, and conceptual RFP devices of Table 1.1-II.

another. Some variation of  $\beta_\theta$  with  $I_\phi/N$  has been reported, with  $\beta_\theta$  increasing somewhat as  $I_\phi/N$  is reduced. It should also be noted that the range over which favorable scaling is obtained appears to be extended by improved wall-conditioning methods and by reduction in field errors [21].

The first recent estimates of energy confinement in RFPs have been made possible by the relatively stationary conditions achieved in flat-top current discharges. With the global energy confinement time,  $\tau_E$ , defined as plasma energy divided by the ohmic power and defining an effective global diffusivity as  $\chi_E = (3/16)r_p^2/\tau_E$ , it follows that in general  $\chi_E = \eta\beta_\theta/\mu_o$ . Depending on assumptions made with respect to the constancy of  $\beta_\theta$ ,  $j_\phi/n$ ,  $Z_{eff}$ , profiles, *etc.*, and the scaling of  $\eta$  with temperature or current, a range of scaling of  $\chi_E$  with current, beta, and geometry can be derived. Assumption of classical scaling for  $\eta$  results in  $\tau_E \propto I_\phi^\nu r_p^2$  with  $\nu = 1.5$ . Any variations from these assumptions as well as variations in profile factors, impurity concentration, and  $Z_{eff}$ , will alter the dependence of  $\tau_E$  on  $I_\phi$  and  $r_p$ . Until experimental data on the plasma profiles and  $Z_{eff}$  become available, the expression

$$\tau_{Ee} = C_\nu I_\phi^\nu r_p^2 f(\beta_\theta) \quad (1.2-4)$$

is used to parametrically fit the existing experimental data. Typical values of the current scaling exponent,  $\nu$ , ranges from 1. to 1.5 for  $\tau_{Ei} = 4\tau_{Ee}$ . The function  $f(\beta_\theta)$  models the soft  $\beta$  limit and is assumed to have a value of one for  $\beta$  values below the  $\beta$  limit and to go to zero when the  $\beta$  limit value is exceeded.

The observed scaling of plasma pressure with current suggests a beta limit wherein intrinsic transport would adjust through changing MHD activity if other loss channels (*e.g.*, radiation) become available. Under this hypothesis, as the fraction of the total energy loss carried through the radiation channel,  $f_{RAD}^c = P_{RAD}/P_{OHM}$ , is increased, the non-radiative (*i.e.*, intrinsic) confinement time,  $\tau_E^{NR}$ , is expected to increase according to  $\tau_E/(1 - f_{RAD}^c)$ .

A preliminary test of this hypothesis that energy loss channels can be adjusted to maintain a constant plasma energy content was performed on ZT-40M by adding trace quantities of krypton impurities to the plasma [12]. The radiation loss,  $P_{RAD}$ , increased, the beta remained relatively constant, and the ohmic input power,  $P_{OHM}$ , increased only slightly. The data for the krypton-injection experiment shown on Figure 1.2-4 are in quantitative agreement with this prediction and offer the potential for the beta-limited RFP to radiate (more-or-less uniformly) a large fraction of its energy without significantly reducing the global energy confinement time.

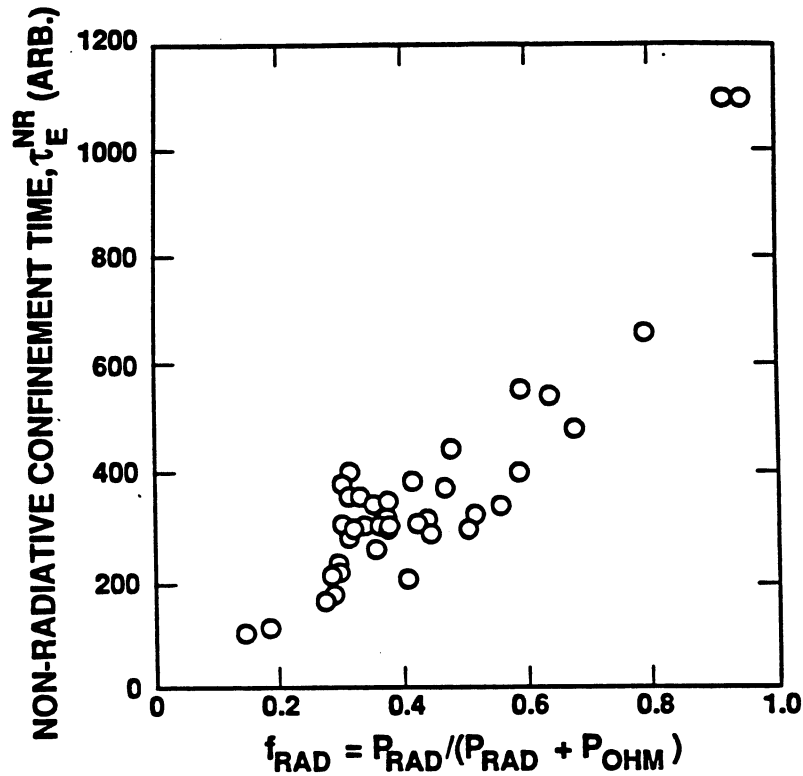


Figure 1.2-4. Scaling of the non-radiative energy confinement time with the fractional radiative power loss in the ZT-40M experiment [12].

This potential for highly radiative plasmas is important for the compact, high-MPD reactor embodiment in order to control and distribute the expected high heat fluxes uniformly over the first wall and to reduce the heat flux to the divertor plates. Generally, a highly radiative plasma regime that does not degrade the overall confinement is not available to the tokamak plasma; radiation loss is added to intrinsic losses and degrades the overall confinement.

One-dimensional (radial) plasma simulations were performed to determine achievable values of  $f_{RAD}^c$  for a given kind and quantity of injected impurity (Section 5.3). For these calculations, the local beta limit described above in terms of  $f(\beta_\theta)$  is imposed. This limit enhances the local electron perpendicular thermal conductivity and the particle diffusivity by large factors above classical values, especially in the central plasma region when the on-axis beta exceeds a critical limit. For ohmically heated plasmas with small radiation losses, these assumptions lead to a global scaling of the form given above with  $\nu \simeq 1.5$ .

The 1-D plasma simulations were performed assuming a uniform impurity concentration and a coronal equilibrium model. The values of the core-plasma radiation fraction,  $f_{RAD}^c$ , and the resultant  $Z_{eff}$  are estimated as functions of the impurity concentration for several impurity species and the results are given in Figure 1.2-5. High- $Z$  impurities are preferred because a high value of  $f_{RAD}^c$  can be achieved for minimum  $Z_{eff}$  (to minimize  $V_\phi$  and the OFCD requirements). Combined with similar estimates of the edge-plasma and divertor radiation fractions, a total radiation fraction of  $f_{RAD}^{TOT} = 0.97$  is possible for the Xe impurity concentrations given on Table 1.2-I.

As for most fusion reactor designs, the specifications of the net-electric power (*i.e.*, total fusion power), plasma power balance, and neutron wall loading give the global energy confinement time. Because the value of neutron wall loading is determined by the minimization of COE in TITAN, the above value of  $\tau_E$  represents an “economic” confinement time,  $\tau_E(\text{ECON})$ , that must be compared with experimental predictions,  $\tau_E(\text{PHYS})$ . The economic confinement required to achieve the minimum-COE design point for TITAN (Figure 1.1-1) is  $\tau_E(\text{ECON}) = 0.22$  s, or  $\chi_E = 0.32$  m<sup>2</sup>/s. For TITAN, this level of global energy confinement must be attained in a highly radiating core plasma (with a radiation fraction,  $f_{RAD}^c \simeq 0.7$ ) with a poloidal beta of  $\beta_\theta = 0.23$  (including a beta increment of  $\sim 0.03$  for energetic alpha particles). A comparison of the TITAN confinement requirement with the present RFP data base is given in Figure 1.1-6.

The TITAN systems code, as well as the plasma engineering effort, has used a physics scaling of the form  $\tau_E(\text{PHYS}) = 2(1/\tau_{Ee} + 1/\tau_{Ei})^{-1}$  with  $\tau_{Ee} = C_\nu I_\phi^\nu r_p^2 f(\beta_\theta)$  and  $\tau_{Ei} \simeq 4\tau_{Ee}$ . The current exponent  $\nu = 0.8$  to 1.5 represents a range of fits to the global confinement observed in experiments after corrections for radiative loss have been applied. The function  $f(\beta_\theta)$  reflects an attempt to model a beta limit that may exist in RFPs with  $f(\beta_\theta) = 1$  for low values of  $\beta_\theta$  and  $f(\beta_\theta) \rightarrow 0$  when  $\beta_\theta$  exceeds a critical value of beta, thereby giving considerable thermal stability to the burn.

Using the experimental scaling of the confinement time,  $\tau_{Ee} \propto I_\phi^\nu r_p^2 f(\beta_\theta)$ , the impact of the plasma current scaling exponent,  $\nu$ , on achieving the minimum-COE TITAN-I design is illustrated in Figure 1.2-6. For each respective constant  $\nu$  curve, the condition  $\tau_E(\text{ECON}) \leq \tau_E(\text{PHYS}) \equiv 2(1/\tau_{Ee} + 1/\tau_{Ei})^{-1}$  with  $\tau_{Ei} \simeq 4\tau_{Ee}$  is met to the right (*i.e.*, higher  $r_p$ ). The accessibility to minimum-COE designs depends on the value of  $\nu$ . In addition, for  $\nu$  values much below  $\sim 0.8$ , the demands on the OH-coil system during the ohmic-heating transient to ignition and burn can be serious. Also, it should be noted that the flexibility of operation of TITAN reactors at lower than nominal power (for load following or checkout) requires better intrinsic plasma confinement (*i.e.*, higher  $\nu$ ).

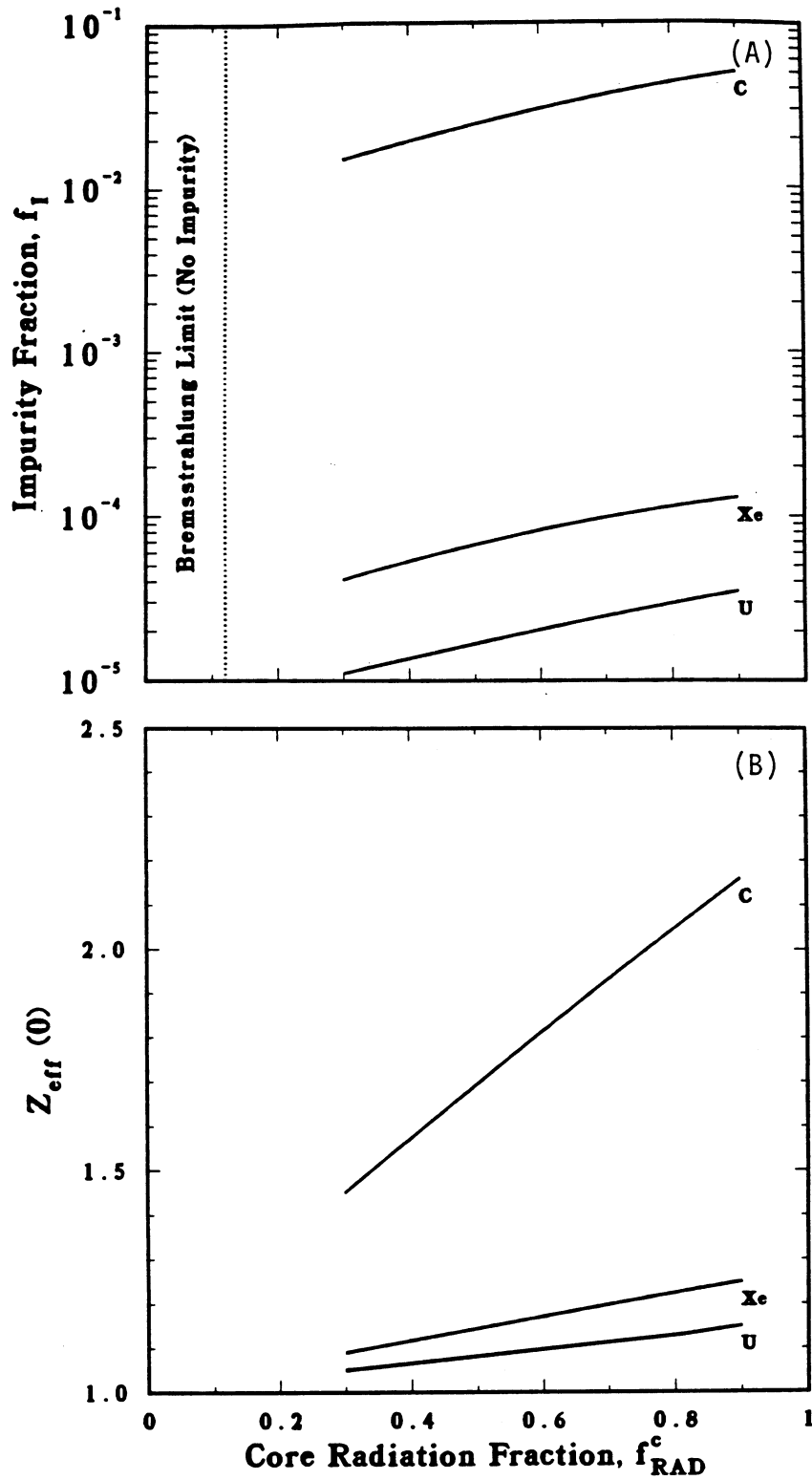


Figure 1.2-5. The required impurity fraction (A) and the resultant  $Z_{eff}$  (B) as functions of the core radiation fraction,  $f_{RAD}^c$ , for different impurities.

**Table 1.2-I.**  
**IMPURITY CONCENTRATION AND RADIATION FRACTIONS**  
**IN THE TITAN PLASMA**

Location	$n_{Xe}$ ( $10^{18} \text{ m}^{-3}$ )	$n_i$ ( $10^{20} \text{ m}^{-3}$ )	$f_{RAD} = P_{RAD}/P_{TOT}^{(a)}$
Core	0.289	8.9	0.695
Edge	0.289	1.7	0.232
Divertor	10.50	62.0	0.039

(a)  $P_{TOT} = P_{OHM} + P_{\alpha} = 552 \text{ MW}$ .

Several important points should be noted. (1) The above empirical scaling is derived from experiments with limited variations in both  $I_{\phi}$  and  $r_p$ . (2) In the present ohmically heated discharges,  $\beta_{\theta}$  and  $\tau_E$  (or  $\chi_E$ ) are inexorably coupled and it is not clear that the above empirical scaling of confinement will be applicable to fusion discharges where alpha-particle heating is dominant. (3) Zero-dimensional simulation of plasma start-up for TITAN reactors with the above scaling shows that the ignition is achieved at  $\beta_{\theta} \simeq 0.05-0.1$  ( $\tau_E \simeq 0.4 \text{ s}$ ) and the value of  $\beta_{\theta} \simeq 0.23$  is only reached at the steady-state burn condition. Since the above scaling is derived for the flat-top portion of experimental discharges with  $\beta_{\theta}$  being close to its limit, applicability of this scaling to TITAN start-up simulations is questionable.

Detailed analysis of the TITAN plasma equilibrium is reported in Section 5.2. These analyses were performed using a large-aspect-ratio approximation. Two distinct sets of  $\mu$  and  $p$  profiles have been used. For start-up and transient calculations, a standard set of profiles,

$$\mu(r) = \mu(0) \left[ 1 - (r/r_p)^8 \right], \quad (1.2-5)$$

$$n(r) = n(0) \left[ 1 - (r/r_p)^{2.5} \right], \quad (1.2-6)$$

$$T(r) = T(0) \left[ 1 - (r/r_p)^4 \right], \quad (1.2-7)$$

are used. At steady-state full-power operation, the TITAN plasma is deliberately doped with a trace amount of Xe impurity to enhance core-plasma radiation and to reduce the

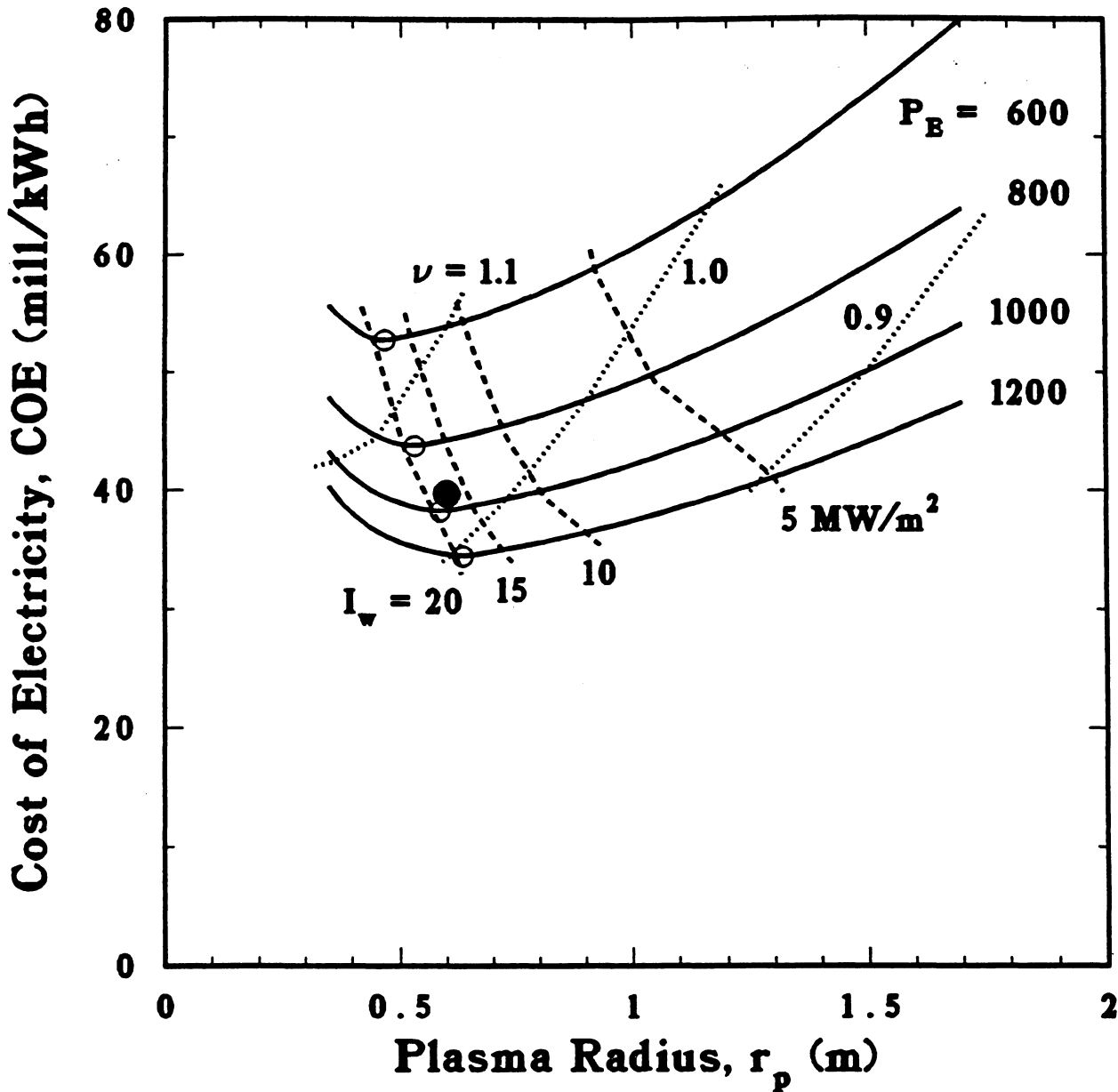


Figure 1.2-6. Parametric trade-off of TITAN-I cost with level of confinement required ( $\tau_{Ee} = C_\nu I_\phi^\nu r_p^2 f(\beta_\theta)$ ,  $\tau_{Ei} = 4\tau_{Ee}$ ), expressed as the magnitude of exponent  $\nu$  required for  $\tau_E(\text{ECON}) \leq \tau_E(\text{PHYS}) = 2(1/\tau_{Ei} + 1/\tau_{Ee})^{-1}$ . Accessible design points are to the right of curves of constant  $\nu$ . Minimum-COE design points with  $\tau_E(\text{OPT}) = \tau_E(\text{ECON})$  for fixed net power output  $P_E$  are indicated by open circles. The near-minimum-COE TITAN-I reference design at  $P_E = 970$  MWe and  $I_w = 18.1$  MW/m<sup>2</sup> is denoted by a filled circle.

heat load on the divertor target plates. One-dimensional transport analysis (Section 5.3) has been performed and the following plasma profiles were obtained:

$$\mu(r) = 2.843 \left[ 1 - 0.44(r/r_p)^6 - 0.56(r/r_p)^8 \right], \quad (1.2-8)$$

$$T_e(r) = \begin{cases} 14.40 - 46.94(r/r_p)^{2.8504} & (0 < r/r_p < 0.25) \\ 16.07 - 10.29(r/r_p) & (0.25 < r/r_p < 0.833) \\ 8.111 - 7.886(r/r_p)^{14.025} & (0.833 < r/r_p < 1) \end{cases}, \quad (1.2-9)$$

$$n(r) = 1.23 \times 10^{21} \left[ 1 - 0.8577(r/r_p)^{3.44} \right]. \quad (1.2-10)$$

These profiles have been used in the burning-plasma simulations. Table 1.2-II compares the values of plasma profile factors and plasma internal inductances for both profiles. These equilibrium profiles and parameters are computed for  $\beta_\theta = 0.2$  and  $F = -0.1$ . Values of magnetic-field strength and current density are also given for  $r_p = 0.6$  m and  $I_\phi = 17.8$  MA. The above cylindrical equilibrium calculations have been used extensively for simulation of the TITAN plasma. Two-dimensional equilibrium analysis by the computer code NEQ [43] was also performed to substantiate the accuracy of such an approximation for the TITAN effort. The equilibrium parameters computed by NEQ are in good agreement with those reported in Table 1.2-II.

Detailed stability analyses of TITAN profiles were not performed. Rather, a poloidal beta of  $\beta_\theta = 0.23$  (corresponding to fuel ion beta of 0.2) was assumed, which is in the range of experimental achievements. The sensitivity of the reference design to achievable stable values of poloidal beta was also studied by the TITAN parametric systems model. The COE increases as  $\beta_\theta$  is decreased, as is shown in Figure 1.2-7, primarily because of the need to establish and drive more plasma current, as is reflected in increased OFCD power consumption and increased coil mass (reduced MPD). Values of  $\beta_\theta$  much below  $\sim 0.1$  result in substantial increases in COE.

Finally, the existence and role of a close-fitting conducting shell that surrounds the RFP strongly impacts all physics and engineering aspects of the design. The data base for RFP operation with resistive shells is summarized in Section 2.3.9. However, the need for and characteristics of a conducting shell with electrical breaks and its impact on RFP formation and start-up, confinement, current drive, and impurity control represent an important but inadequately mapped issue for the RFP. Because of the lack of data base, the TITAN study has circumnavigated this issue numerous times by assuming that the first wall and blanket would act as the conducting shell.

Table 1.2-II.

## EQUILIBRIUM PARAMETERS OF TITAN PLASMA

Parameter	Power Profiles <sup>(a)</sup>	Radiative Profiles <sup>(b)</sup>
Poloidal beta, $\beta_\theta$	0.2	0.2
Reversal parameter, $F$	-0.1	-0.1
Pinch parameter, $\Theta$	1.522	1.538
Safety factor, $q$		
On axis	0.110	0.109
At plasma edge	-0.011	-0.010
Field-line pitch, $P$		
On axis	0.430	0.423
At plasma edge	-0.039	-0.039
Plasma internal inductance per unit length (H/m)		
Poloidal, $l_{i,p}$	$1.136 \times 10^{-7}$	$1.140 \times 10^{-7}$
Toroidal, $l_{i,t}$	$3.724 \times 10^{-8}$	$3.824 \times 10^{-8}$
Total, $l_i$	$1.508 \times 10^{-7}$	$1.522 \times 10^{-7}$
Plasma-resistance profile factor, $g_{OHM}$	3.419	2.918
Poloidal field at plasma edge, $B_\theta(r_p)$ (T) <sup>(c)</sup>	5.93	5.93
Toroidal field <sup>(c)</sup>		
On axis, $B_\phi(0)$ (T)	11.69	11.85
At plasma edge, $B_\phi(r_p)$ (T)	-0.390	-0.386
Average, $\langle B_\phi \rangle$ (T)	3.90	3.86
Toroidal current density <sup>(c)</sup>		
On axis, $J_\phi(0)$ (MA/m <sup>2</sup> )	43.2	44.6
At plasma edge, $J_\phi(r_p)$ (MA/m <sup>2</sup> )	0.	1.90
Average, $\langle J_\phi \rangle$ (MA/m <sup>2</sup> )	15.7	15.7

(a) Profiles of plasma  $n$ ,  $T$ , and  $\mu$  are given in Equations 1.2-5 through 1.2-7.

(b) Profiles of plasma  $n$ ,  $T$ , and  $\mu$  are given in Equations 1.2-8 through 1.2-10.

(c) Values for  $r_p = 0.6$  m and  $I_\phi = 17.8$  MA.

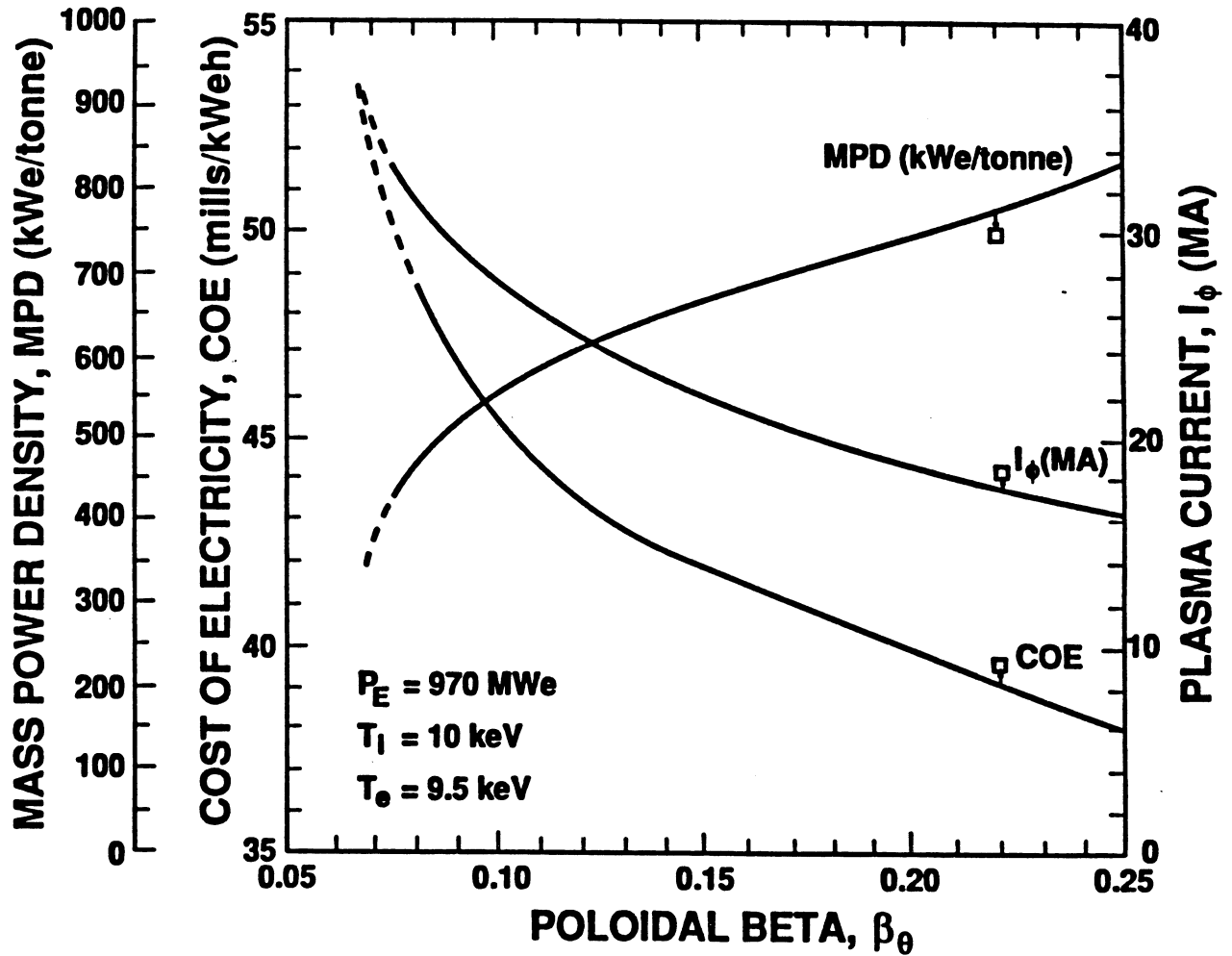


Figure 1.2-7. Dependence of minimum-COE TITAN-I design values on poloidal beta; the near-minimum-COE TITAN-I reference design values are also shown.

### 1.2.3. Magnetics

The detailed TITAN magnetics design is reported in Section 4. The magnet configuration consists of the following sets of coils: toroidal-field (TF), divertor-field (DF), and poloidal-field (PF) coils. The TITAN reactors operate at steady state using the oscillating-field current-drive (OFCD) system (Sections 1.2.7 and 7). Rather than using a separate coil set, the TF, DF, and PF coils are oscillated about their steady-state currents and used as the OFCD driver coils. Separate TF-, DF-, and PF-coil designs were produced for each TITAN fusion power core (FPC). The TITAN-I design uses the integrated-blanket-coil (IBC) concept [14], wherein poloidal currents are driven in the primary lithium coolant to produce the required toroidal magnetic field. The TITAN-II FPC design uses normal-conducting, Cu-alloy TF and DF coils.

The integrated-blanket-coil (IBC) concept combines the blanket functions of tritium breeding and high-temperature energy recovery (of both fusion and ohmic heating) with the coil function of magnetic-field production in a single component. The IBC resembles a conventional blanket sector, but the coolant also serves as the electrical conductor. Previous studies [14,44] indicate that adopting the IBC approach offers the following benefits: (1) The IBC dual functions of coil and blanket permit a closer placement of the coil to the plasma without sacrificing neutronics performance, which potentially increases the mass power density of the FPC. (2) Moving the coils closer to the plasma improves magnetic coupling as measured by inductance, thereby reducing current requirements in PF and DF coils. (3) For compact reactors especially, the IBC may simplify design and maintenance because fewer coolant lines and the associated connections are required.

Several combinations of materials for the coolant (conductor) and the structure are possible for the IBC. The TITAN-I IBC is based on liquid lithium and the vanadium alloy, V-3Ti-1Si (respectively, the coolant and structural material of the FPC). One concern with the IBC concept is the large electrical resistivity of lithium relative to copper. If the concept is to be economically attractive, the joule losses should be comparable to those with a conventional resistive magnet system. However, even when a 70% fill fraction is assumed for a wound coil, the resistivity of the IBC is about 13 times larger than that of a room-temperature copper coil. Part of this difference is negated by capturing the ohmic heat in the IBC, which serves as the main energy recovery component; therefore, about 40% of the resistive losses in the IBC reappear as electrical power, albeit added costs associated with added thermal-conversion capacity is incurred.

The IBC concept requires that the electrical and thermal hydraulic systems be physically connected, leading to relatively low-voltage, high-current (few-turn) coils. The coil

leads carry large currents and require careful design to minimize the error fields and the power consumption therein. The design of the low-voltage, high-current power supplies is the most critical engineering issue for the IBC. The engineering aspects of the TITAN IBCs are discussed in Section 10.5.

The TF coils provide the initial bias field,  $B_{\phi_0}$ , on which the initial RFP configuration is formed. These coils subsequently maintain the external reversed field,  $B_{\phi R}$ , with a minimum ripple,  $\Delta B_R/B_\theta$ , at the plasma edge. The major goal for the TF-coil design of RFPs is the achievement of minimal toroidal-field ripple. Toroidal-field ripple produces magnetic islands within the edge-plasma region. Particles and energy flow freely within this island structure, and plasma confinement is thereby degraded according to the island size. To ensure that confinement is not adversely affected by the TF ripple, the radial extent of the islands is required to be smaller than the radial distance between the reversal surface,  $r_r$ , and the plasma surface,  $r_p$ ; this region is perceived to be primarily responsible for confinement in an RFP [6].

An estimate of the magnetic-island size produced by TF ripple is given in terms of the radial thickness of an island [45]:

$$\Delta r = 4 \left[ \frac{r \Delta B_R}{n B_\theta (dq/dr)} \right]^{1/2}, \quad (1.2-11)$$

where  $r$  is the minor radius of the resonant surface,  $\Delta B_R$  is the amplitude of the radial magnetic-field perturbation,  $n$  is the toroidal mode number of the perturbation,  $B_\theta$  is the poloidal field at the resonant surface, and the derivative of the safety factor,  $dq/dr$ , is evaluated at the resonant surface. In the case of TF ripple, the toroidal mode number of the perturbation is equal to the number of TF coils,  $N_{TF}$ . The TF-coil designs for most RFP reactors [7] and experiments [13] strive for island widths  $\Delta r \leq r_p - r_r$  which are achieved with ripples,  $\Delta B_R$ , of a few mT produced by  $N_{TF} \geq 25$  TF coils.

The TITAN-I TF-coil design is shown in Figure 1.2-8 and described in Table 1.2-III. The amplitude of the ripple field was found to be a few  $\mu\text{T}$ , which in turn results in a magnetic-island width  $\Delta r \leq 0.1 \text{ mm}$  for  $N_{TF} \sim 10^3$  and is more than two orders of magnitude below the design constraint. Such a small ripple and, hence, island width is a result of the TF IBC being an excellent approximation to a toroidally uniform conducting shell. The deviation from a shell is only a function of the diameter of the coolant tubes used in a TF IBC design and the spacing between the tubes. A close packing of the tubes is achieved by varying the tube cross section from a circle in the outboard equatorial plane to an ellipse which preserves the radial build in the inboard equatorial plane (Section 10). The field error produced by the gap in the IBC needed to permit the ingress and egress

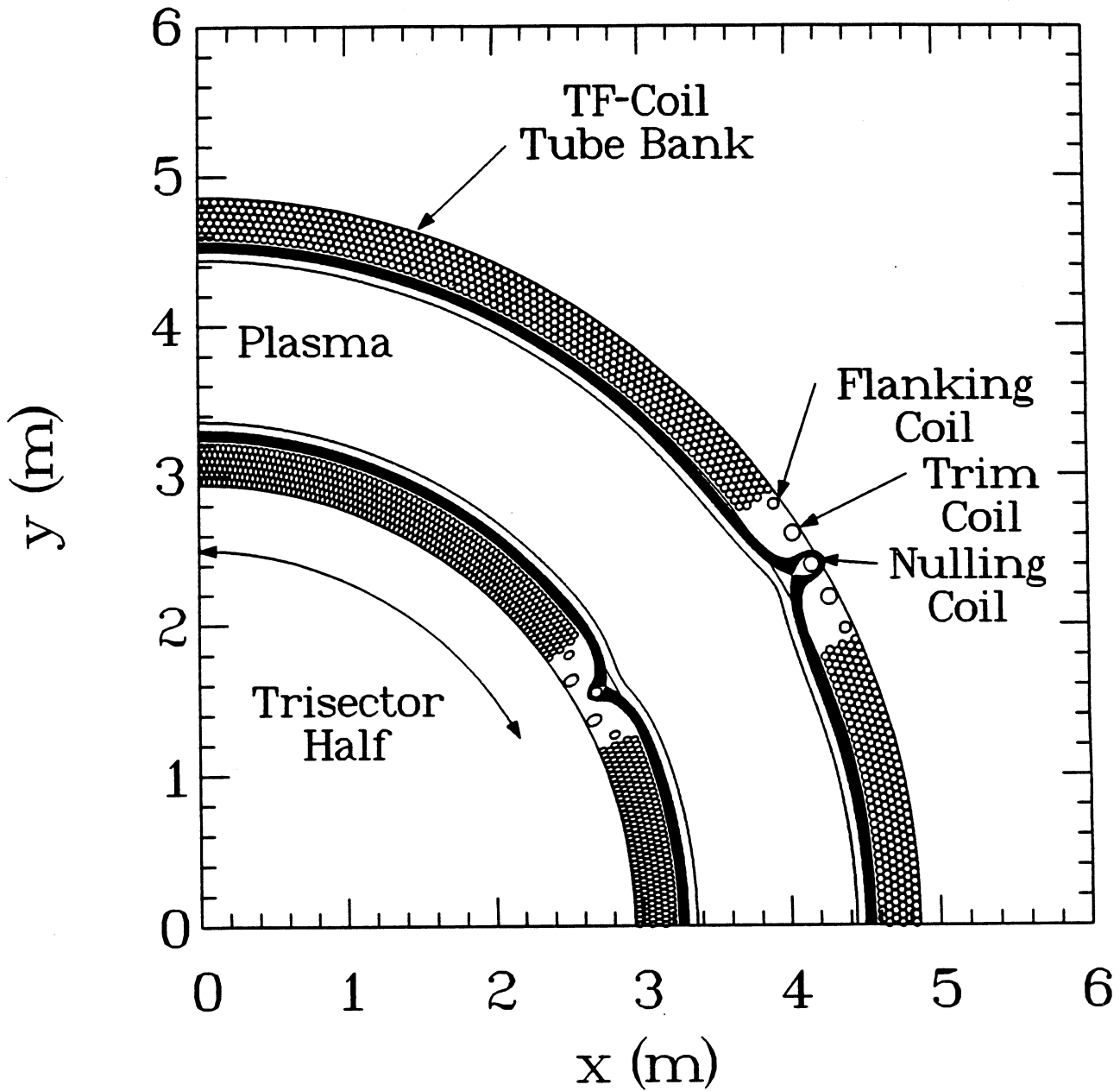


**Figure 1.2-8.** Equatorial-plane view of TF-IBC design with divertor. Also shown are field-line tracings at inboard and outboard minor radii of  $r = 0.5494, 0.5995, 0.6005, 0.6010, 0.6030, 0.6060, 0.6090, 0.6120, 0.6180, 0.6240, 0.6300, 0.6360, 0.6420, 0.6480, 0.6540, \text{ and } 0.6600$  m.

**Table 1.2-III.**  
**PARAMETERS OF TITAN-I TOROIDAL-FIELD COILS**

Current per trisector (MA)	2.08					
Reversed toroidal field, $B_{\phi R}$ (T)	0.36					
Number of tubes per trisector	975					
Average current per tube (kA)	2.13					
Tube inner diameter (mm) <sup>(a)</sup>	47.5					
Tube wall thickness (mm) <sup>(a)</sup>	2.5					
Tube inner area (m <sup>2</sup> )	$1.40 \times 10^{-3}$					
Average current density (MA/m <sup>2</sup> )	1.52					
Resistivity, $\eta$ ( $\mu\Omega$ -m)	0.353					
Total power, $P_{TF}^{\Omega}$ (MW)	24.0					
Blanket coverage	0.887					
<b>Tube data for row number:</b>	<b>1</b>	<b>2</b>	<b>3</b>	<b>4</b>	<b>5</b>	<b>6</b>
Poloidal radius, $r_{\theta c}$ (m)	0.706	0.752	0.797	0.843	0.888	0.934
Number per trisector	162	163	162	163	162	163
Current, $I_{\theta c}$ (kA)	2.22	2.19	2.15	2.11	2.08	2.04
Current density $\langle j_{\theta c} \rangle$ (MA/m <sup>2</sup> )	1.54	1.54	1.53	1.52	1.52	1.51

(a) Values evaluated at outboard equatorial plane and vary poloidally.

of the first-wall coolant channel and by the current leads to the TF IBC is about a few  $\mu\text{T}$  and does not appear to present a problem.

The TITAN-II geometry is specified to the point that the only degree of freedom in designing the TF coils is  $N_{TF}$ . The total TF-coil cross-sectional area is independent of  $N_{TF}$  because the magnetic field and the power dissipation are held constant near values suggested by the system code. The amplitude of the ripple field,  $\Delta B_R$ , was calculated over a range of  $N_{TF}$  values and found to decrease with increasing  $N_{TF}$  so that the magnetic island width,  $\Delta r$ , falls off faster than the explicit prediction of Equation 1.2-11 that  $\Delta r \propto N_{TF}^{-1}$ . Based on these calculations, a value of  $N_{TF} = 30$  was adopted for the TITAN-II TF-coil design, which is summarized in Table 1.2-IV and shown in Figure 1.2-9.

Table 1.2-IV.

PARAMETERS OF TITAN-II TOROIDAL-FIELD COILS

---

Number of TF coils, $N_{TF}$	30
Major radius, $R_{TF}$ (m)	3.898
Minor radius, $r_{TF}$ (m)	1.120
Radial thickness, $\delta_{TF}$ (mm)	70.4
Toroidal thickness, $\ell_{TF}$ (mm)	326.7
Magnetic-island width, $\Delta r$ (mm)	12.0
Field error, $\Delta B_R$ (mT)	14.14
Reversed toroidal field, $B_{\phi R}$ (T)	0.38
Current per coil, $I_{TF}/N_{TF}$ (kA)	247.0
Current density, $j_{TF}$ (MA/m <sup>2</sup> )	10.7
Steady-state peak coil field, $B_{\phi c}$ (T)	0.69
TF-coil mass, $M_{TF}$ (tonne)	35.5 <sup>(a)</sup>
Total ohmic power, $P_{TF}^{\Omega}$ (MW)	16.

---

(a) Assuming a coil density of 7.3 tonne/m<sup>2</sup>.

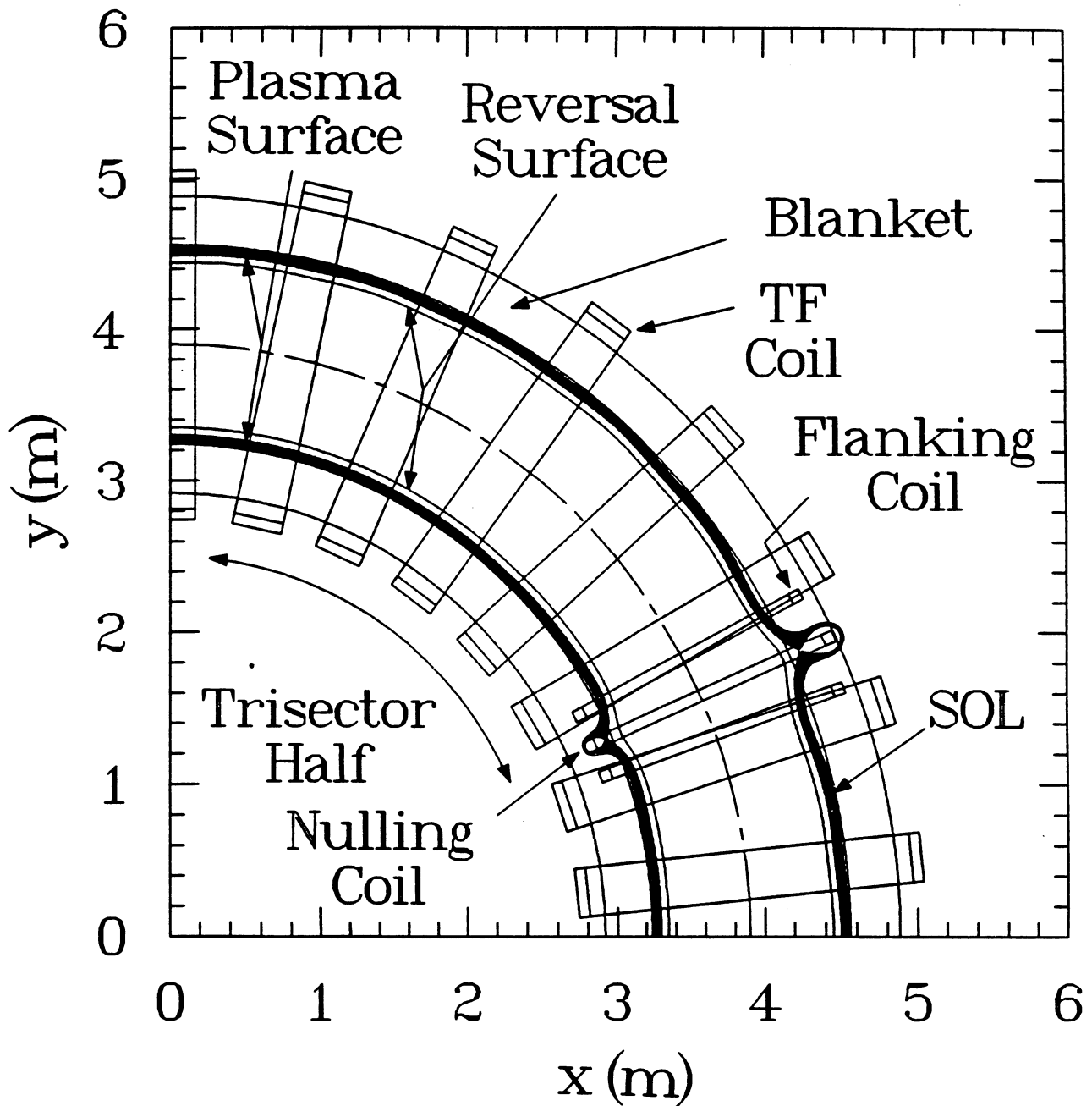


**Figure 1.2-9.** Equatorial-plane view of TITAN-II divertor design. Also shown are field-line tracings at inboard and outboard minor radii of  $r = 0.5494, 0.5995, 0.6005, 0.6010, 0.6030, 0.6060, 0.6090, 0.6120, 0.6180, 0.6240, 0.6300, 0.6360, 0.6420, 0.6480, 0.6540,$  and  $0.6600$  m.

The TITAN-II TF-coil design meets the magnetic-island constraint with only a small safety margin. The safety margin could be increased if so desired by slightly increasing the plasma-to-TF-coil clearance and the TF-coil minor radius. Note that the magnetic-island width predicted by Equation 1.2-11 is not valid because the resonant surface (where  $q(r) = N_{TF}^{-1}$ ) does not lie between  $r_r$  and  $r_p$ . Three-dimensional field-line tracings in the edge-plasma region with the TF and PF coils and plasma simulated under the same conditions of non-resonance of the TF ripple [46] are used to find the island width.

The TITAN designs use three toroidal-field divertors. The divertor nulls the minority toroidal field to minimize perturbations to the confining magnetic field in the plasma and to minimize the DF-coil currents required to produce a null. The toroidal-field null is a line poloidally encircling the plasma cross section upon which the toroidal field is zero, and is located on the plasma separatrix surface. The null is produced by a nulling coil (Figures 1.2-8 and 1.2-9). The nulling coils (one per divertor location) form a solenoid within the TF-coil solenoid; the nulling-coil solenoid nearly cancels the toroidal field over the volume of the inner solenoid. To localize the effect of the nulling coil, two flanking coils are positioned symmetrically about the nulling coil (Figures 1.2-8 and 1.2-9). The flanking coils carry a combined current equal to that in the nulling coil, but of opposite sign. In the case of the TITAN-I IBC divertor, the divertor assembly displaces a portion of the IBC TF-coil tube bank. A pair of trim coils is required to conduct a current equal to that of the displaced tube bank in order to control the TF ripple (Figure 1.2-8).

The TITAN divertors use an "open" geometry in which the divertor plate is positioned near the null. The flux expansion produced by the open divertor geometry results in a substantial decrease in the heat and particle fluxes incident upon the plate. Production of a higher flux-surface expansion factor requires (1) a larger nulling-coil minor radius resulting in a larger ohmic dissipation in the divertor coils, and/or (2) the plate to be located close to the null but at least several mean free paths (four for TITAN) away to prevent the neutral particles from entering the core plasma. Therefore, the divertor magnetics connection to edge-plasma modeling and target design was exercised iteratively to establish divertor performance criteria. The TITAN-I and TITAN-II target designs have different divertor plate heat-flux limits set by the choice of coolant, structural material, and configuration. The critical heat-flux limits translate into magnetics requirements that the TITAN-I divertor design produce a peak flux-surface expansion factor of  $\sim 2$  at a plate location 22.1 mm (four neutral mean free paths) from the null. The TITAN-II divertor design produces an expansion factor of  $\sim 3$ . Only three divertors are used in either design (Sections 1.2.4 and 5). The ohmic dissipation in the DF coils is affected by the angular spread between flanking and nulling coils which, in turn, affects the ripple

produced by the divertor that should be minimized. In addition, symmetrizing the edge-plasma region ( $r_r \leq r \leq r_p$ ) from inboard to outboard was found to play an important role in reducing divertor-introduced island widths and is imposed as an additional goal.

The TITAN-I DF coils are based on the IBC concept (Figure 1.2-8 and Table 1.2-V). An expanded view of the divertor region is shown in Figure 1.2-10. The angular spread between the flanking and nulling coils is  $5.7^\circ$  to achieve a peak flux expansion factor of  $\sim 2$  at the divertor plate and an ohmic dissipation of  $\sim 120$  MW. The ohmic dissipation is rather large because of the higher resistivity of Li relative to Cu and because the DF-coil cross-sectional area cannot be increased sufficiently to achieve a smaller ohmic dissipation.

The TITAN-II DF coils use Cu alloy as the conductor material (Figure 1.2-9 and Table 1.2-V). An expanded view of the divertor region is shown in Figure 1.2-11. The angular spread between the flanking and nulling coils is  $4^\circ$  to achieve a peak flux expansion factor of  $\sim 3$  at the collector plate and an ohmic dissipation of  $\sim 10$  MW. A maximum of 20 to 50 mm of shielding is possible inboard; this shield thickness increases to  $> 100$  mm outboard (Figure 1.2-11). A maximum of 120 mm of shielding is possible for the flanking coils. Shielding is not necessary, however, to protect the insulators (Section 10.2), but it is desirable for purposes of energy recovery.

The PF-coil set performs equilibrium and ohmic-heating (start-up) functions. The equilibrium function requires that a vertical field of appropriate magnitude,  $B_V$ , and index,  $\partial(\ln B_V)/\partial(\ln R)$ , corresponding to the values of the plasma current and beta [47], be imposed over the plasma cross section. The ohmic-heating function provides the poloidal-flux swing required to establish the steady-state plasma current, which is then subsequently sustained by OFCD. Since the ohmic-heating function is required only during start-up and the equilibrium function is required continuously, the PF-coil set is naturally, but not necessarily, separated into two sets of coils: equilibrium-field (EF) and ohmic-heating (OH) coils. This separation has also helped eliminate the need for on-site energy storage during the start-up procedure (Section 6).

Since the EF coils are continuously active, the recirculating power can be minimized by using superconducting EF coils. Superconducting EF coils, however, require  $\sim 1.5$  m of blanket and shielding between the coils and plasma compared to  $\leq 0.4$  to  $0.8$  m for normal-conducting EF coils; hence, more current is needed to produce the same field resulting in an increase in the stored energy and a more massive and expensive coil set. The trade-off between normal-conducting and superconducting EF coils was examined and found to weigh slightly in favor of superconducting EF coils (Section 3.4). Consequently, the use of superconducting EF coils is adopted for the TITAN reactor study.

Table 1.2-V.  
DF-COIL PARAMETERS FOR TITAN-I AND -II

	TITAN-I <sup>(c)</sup>		TITAN-II <sup>(b)</sup> (Final)	
	Nulling	Flanking	Trim	Nulling Flanking
Number per trisector	1	2	2	1 2
Toroidal angle (°)	0	5.717	2.935	0 4.011
Major radius (m)	3.946	3.945	3.9	3.963 3.940
Minor radius (m)	0.855	0.860	0.900	0.879 0.830
Current per coil (kA)	164.00	82.00	131.07	280.00 140.00
Current density <sup>(c)</sup> (MA/m <sup>2</sup> )	20 <sup>(d)</sup>	20 <sup>(d)</sup>	15 <sup>(d)</sup>	50 25
Average current density (MA/m <sup>2</sup> )	27.532 <sup>(c)</sup>	29.095 <sup>(e)</sup>	20.835 <sup>(e)</sup>	50 25
Resistivity, $\eta$ ( $\mu\Omega$ m)	0.35313	0.35313	0.35313	0.020 0.020
Power per coil (MW)	11.754	6.238	7.382	2.209 0.522
Conductor volume (10 <sup>-2</sup> m <sup>3</sup> )	3.2001	1.5229	3.5574	2.165 2.044
Coil volume (10 <sup>-2</sup> m <sup>3</sup> )	3.6206	1.8189	4.0147	3.093 2.920
Total average current density (MA/m <sup>2</sup> )		25.1		35.7
Conductor filling fraction, $\lambda$		0.874		0.7
Steady-state dissipated power (MW)		116.980		9.757
Inboard/outboard/average values at $r = 0.6005$ m				
Watershed-to-null distance, $L_N$ (m)		53.9/91.4/72.7		53.5/88.3/70.9
Watershed-to-plate distance, $L_P$ (m) <sup>(f)</sup>		55.2/94.0/74.6		55.9/91.6/73.8
Peak flux-surface expansion factor <sup>(f)</sup>		2.27/4.23/3.25		3.07/5.14/4.11

<sup>(a)</sup> Design plasma-surface field values:  $B_{\phi R} = 0.36$  T and  $B_{\theta}(r_p) = 5.6$  T.

<sup>(b)</sup> Design plasma-surface field values:  $B_{\phi R} = 0.38$  T and  $B_{\theta}(r_p) = 5.91$  T.

<sup>(c)</sup> Outboard equatorial-plane value.

<sup>(d)</sup> Current density obtained by averaging current over conductor and structure.

<sup>(e)</sup> Includes effect of variable coil cross section and constant structural cross-sectional area associated with 2.5-mm-thick walls.

<sup>(f)</sup> Values are measured at 22.1 mm from the null.

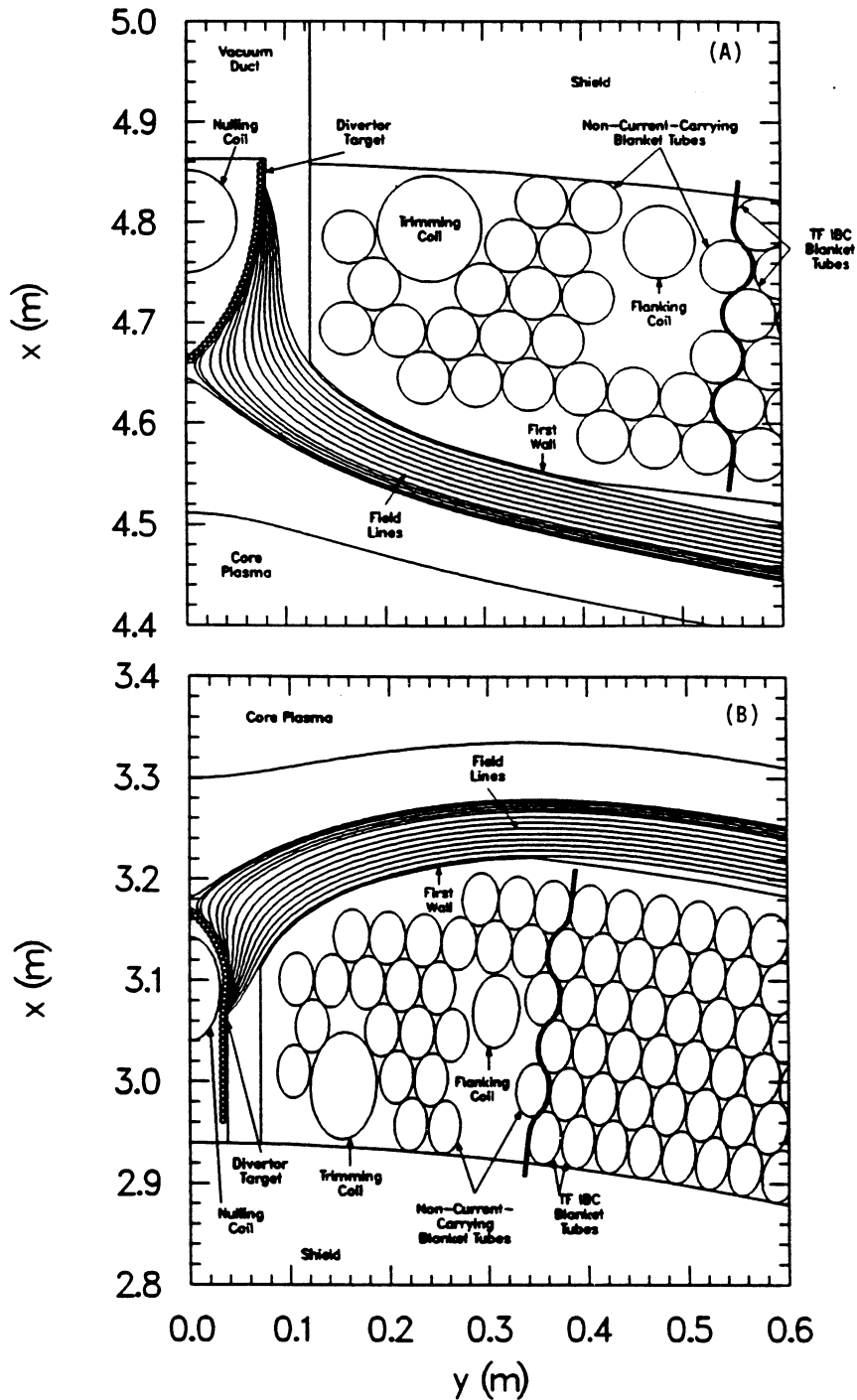


Figure 1.2-10. An expanded view of the TITAN-I divertor configuration outboard (A) and inboard (B) shown in Figure 1.2-8 and described in Table 1.2-V. The field lines are at  $r = 0.5449, 0.5995, 0.6005, 0.6010, 0.6030, 0.6060, 0.6090, 0.6120, 0.6180, 0.6240, 0.6300, 0.6360, 0.6420, 0.6480, 0.6540,$  and  $0.6600$  m.

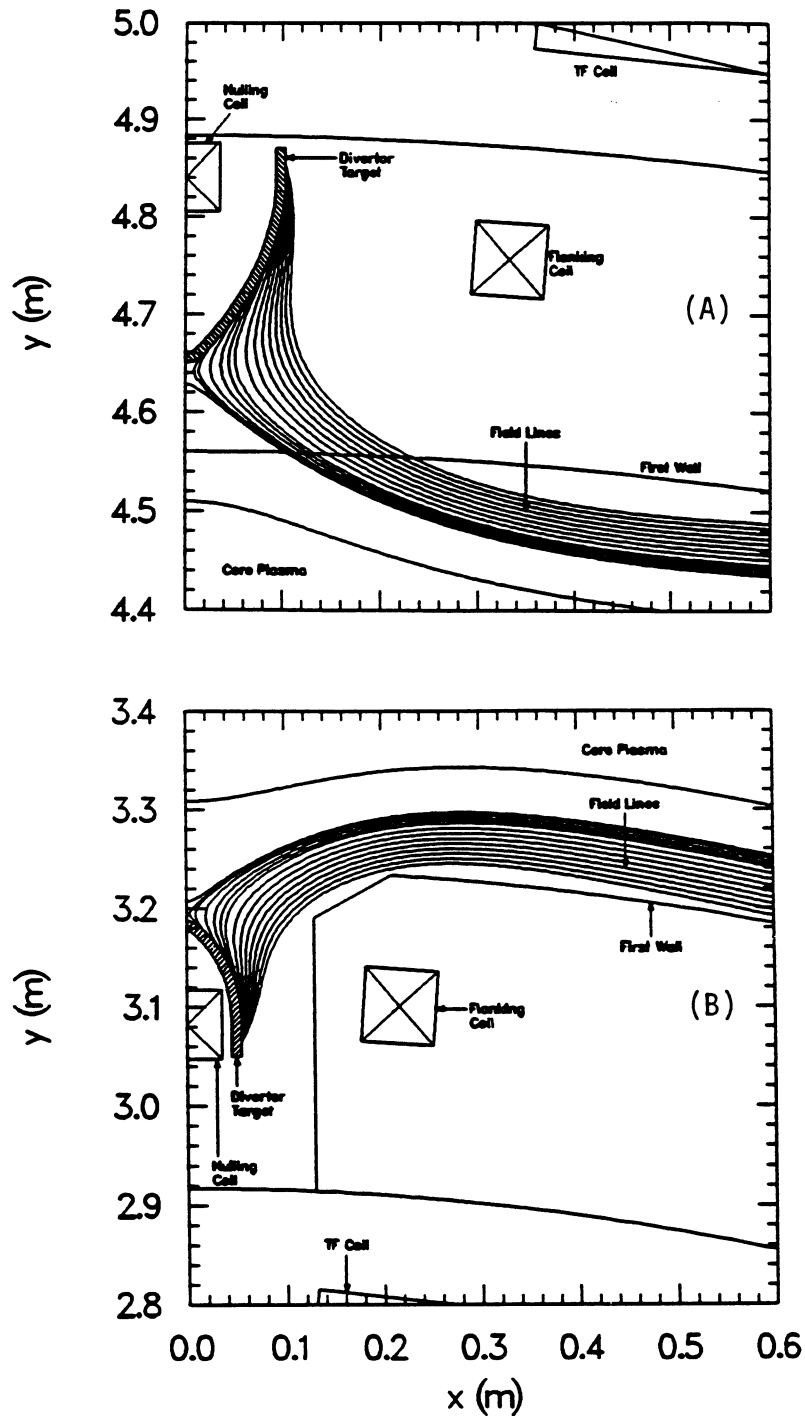


Figure 1.2-11. An expanded view of the TITAN-II divertor configuration outboard (A) and inboard (B) shown in Figure 1.2-9 and described in Table 1.2-V. The field lines are at  $r = 0.5494, 0.5995, 0.6005, 0.6010, 0.6030, 0.6060, 0.6090, 0.6120, 0.6180, 0.6240, 0.6300, 0.6360, 0.6420, 0.6480, 0.6450,$  and  $0.6600$  m.

This EF-coil set would be a life-of-plant item. The parameters of the PF-coil set are chosen such that the superconducting EF coils provide approximate equilibrium during the plasma start-up sequence without any need for highly controllable power supplies.

During the plasma start-up, an additional EF trim coil is required to ensure that the plasma remains in equilibrium (Sections 1.2.6 and 6). Furthermore, the reactive power associated with maintaining the plasma in equilibrium during OFCD is substantially reduced if the applied voltage is held fixed on the superconducting EF coil and the OFCD transient is followed with the EF trim coil (Sections 1.2.7 and 7). The current requirements of the trim coil are small ( $\sim 1$  MA), permitting a normal-conducting Cu-alloy trim coil. Furthermore, the equilibrium field and the decay index are relatively insensitive to the position of the trim coils. Consequently, the trim-coil positions are determined primarily by the requirements for vertical access.

The function of the OH coils is to provide the necessary volt-seconds for the start-up sequence. The desire to optimize the OH-coil performance, as measured by the electrical coupling between the OH coil and the plasma, conflicts with design-integration requirements for access to the TF coils, blanket, and vacuum chamber. Other magnet engineering issues such as stresses, cooling requirements, and the magnet support structure should also be considered. An important constraint is the maximum level of the stray vertical field produced by the OH coils. This constraint specifies the stray vertical field produced by the OH-coil set as a fraction of the initial toroidal field,  $B_{\phi_0}$ . In principle,  $B_{\phi_0}$  can be increased to ensure compliance with the stray-vertical-field constraint. Any increase in  $B_{\phi_0}$ , however, would result in increases in the OH-coil flux consumption as well as increases in the formation energy and power. Consequently, a maximum value of 2.45 mT for the stray vertical field is adopted. A secondary constraint is that the OH-coil set exhibit a field null within the plasma chamber. A field null provides a closed field line upon which to initiate a current channel.

The parameters of the TITAN-I and TITAN-II PF coils are given in Tables 1.2-VI and 1.2-VII. The PF coils are closer to the plasma in TITAN-II because of a thinner first wall, blanket, and shield ( $\sim 0.45$  m as opposed to  $\sim 0.75$  m for TITAN-I) and the OH-coil mass is larger in TITAN-II because of a lower current density as dictated by the parametric systems model of Section 3.2. The compliance of the final TITAN-I design with the constraints of a field null and the magnitude of the stray vertical field are demonstrated in Figure 1.2-12.

Table 1.2-VI.  
CIRCUIT PARAMETERS FOR TITAN PF-COIL DESIGNS<sup>(a)</sup>

	TITAN-I	TITAN-II
Self inductances ( $\mu\text{H}$ )		
· $L_p$	13.29	13.29
· $L_{OH}$	2.74	3.68
· $L_{EF}$	15.02	13.35
· $L_{Trim}$	18.36	19.35
Mutual inductances ( $\mu\text{H}$ )		
· $M_{OH,p}$	2.87	3.92
· $M_{OH,EF}$	2.26	3.04
· $M_{OH,Trim}$	2.99	4.03
· $M_{EF,p}$	3.86	4.12
· $M_{EF,Trim}$	8.69	8.22
· $M_{Trim,p}$	5.60	6.15
Current levels (MA-turn)		
· $I_\phi$	17.75	17.82
· $I_{EF}$	19.24	18.60
· $\Delta I_{OH}$	55.80	40.82
Magnetic fluxes (Wb)		
· Plasma	236.0	236.9
· EF coil	74.5	77.1
· OH coil	161.5	159.8

(a) Equivalent single-turn inductance values are given.

**Table 1.2-VII.**  
**PARAMETERS OF TITAN PF-COIL DESIGNS**

	TITAN-I	TITAN-II
EF-coil current (MA-turn) <sup>(a)</sup>	19.2	18.6
EF-coil volume (m <sup>3</sup> )	39.7	35.8
EF-coil mass (tonne)	289.7	261.4
EF-coil peak field (T) <sup>(a)</sup>	6.4	7.2
EF-coil current density (MA/m <sup>2</sup> ) <sup>(a)</sup>	19.8	19.4
Vertical field index, $n$	0.16	0.40
OH-coil current (MA-turn) <sup>(b)</sup>	27.9	20.4
OH-coil volume	39.5	51.5
OH-coil mass (tonne)	288.4	375.8
OH-coil joule losses (MW) <sup>(b)</sup>	103.	52.5
OH-coil von Mises stress (MPa) <sup>(b)</sup>	89.	33.4
OH-coil peak field (T) <sup>(b)</sup>	5.7	4.7
OH-coil current density (MA/m <sup>2</sup> ) <sup>(b)</sup>	12.5	7.8
OH-coil stray vertical field (mT) <sup>(b)</sup>	0.43 <sup>(c)</sup>	2.30 <sup>(c)</sup>

(a) Mean steady-state values.

(b) Back-bias values for a symmetric bipolar swing.

(c) Satisfies the stray-vertical-field constraint (< 2.45 mT, Section 6.2).

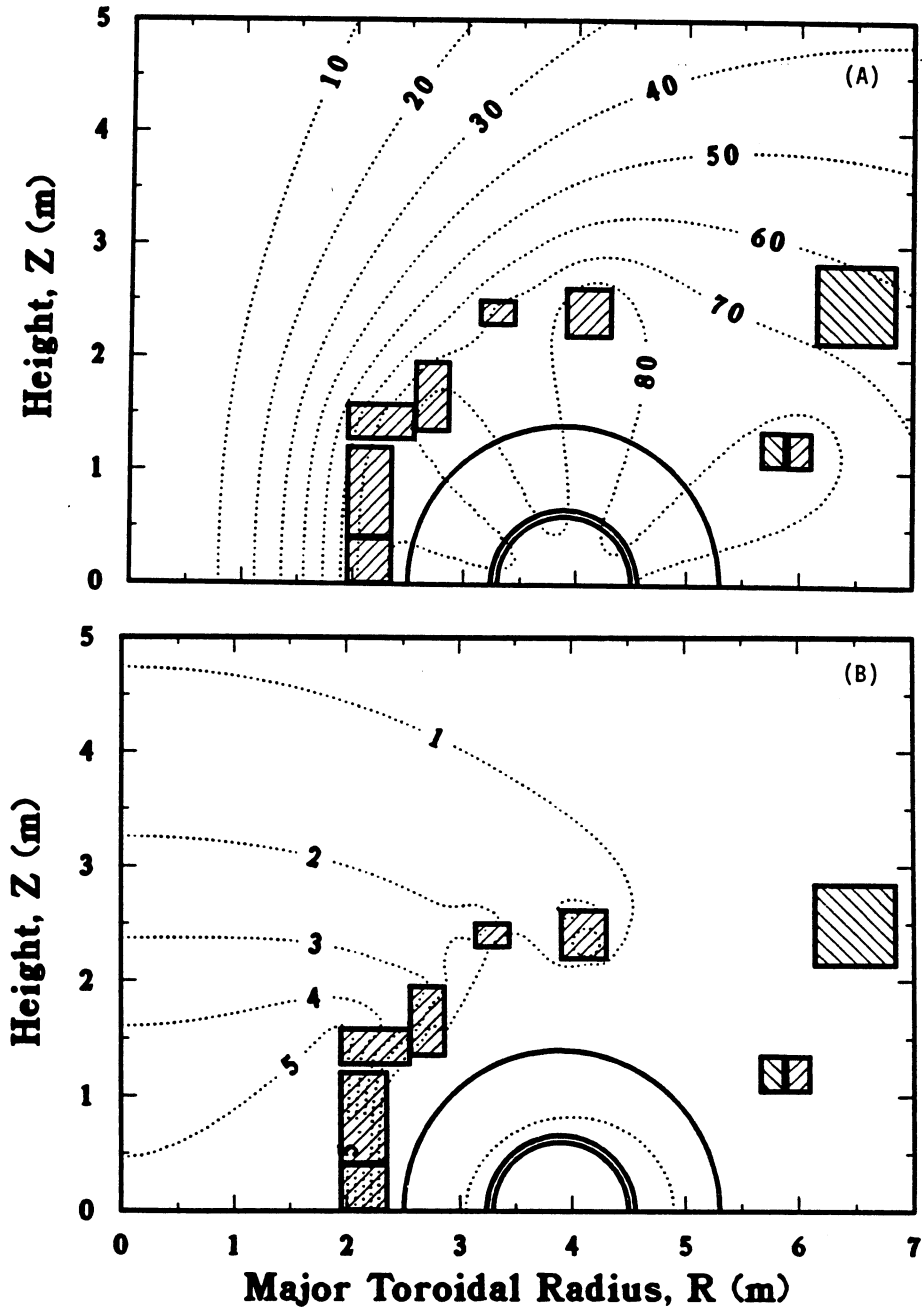


Figure 1.2-12. Contour plots of flux (A) and magnetic-field strength (B) for the final TITAN-I OH-coil design. The flux contours, labeled in weber, demonstrate the presence of a field null within the plasma chamber. The magnetic-field contours are labeled in tesla, except the 2.45-mT contour around the plasma chamber which corresponds to the stray-vertical-field constraint.

#### 1.2.4. Impurity Control

The characteristics of the edge plasma have been of major importance in the TITAN design, and extensive simulations of the edge plasma were undertaken (Section 5). The main objectives of these simulations were to predict the plasma conditions at the first wall and divertor target and provide specifications for the engineering design of these components (Sections 11 and 17), and to estimate the requirements for particle removal. To obtain a self-consistent view of the behavior of the plasma and neutral particles, this analysis has been coupled to the modeling of the core plasma and the neutral particle transport (Section 5).

The design of in-vessel components (divertor plate, limiter, first wall) is a critical issue for all reactors and poses a particularly severe constraint for high-power-density reactors such as TITAN. The key problem is to dispose of the steady-state plasma power (alpha-particle and ohmic) while maintaining acceptable heat fluxes and erosion rates on all components. The approach for TITAN reactors is to produce balanced radiation from the core plasma, the edge or scrape-off layer (SOL) plasma, and from the divertor plasma. The plasma is deliberately doped with a trace amount of a high- $Z$  xenon impurities to create strong radiative cooling and to spread the heat load uniformly over the largest possible area (first wall). This high-radiation regime of operation, which appears to be an essential ingredient for a high-power-density reactor, may be more easily achieved in RFPs than in tokamaks because experimental evidence suggests that RFPs operate with a soft  $\beta$  limit.

The edge-plasma analysis was carried out using the recently developed quasi-2-D transport code ODESSA [48,49]. The code retains the computational advantages of a 1-D radial transport code but incorporates important parallel physics. The localized nature of recycling at the divertor target allows two essential axial domains of interest, namely, the upstream or SOL zone and the downstream or recycling zone in the divertor (Figure 1.2-10) to be identified. By introducing suitable axial-averaging operators, a set of coupled 1-D time-dependent equations for the plasma parameters in the SOL and divertor zones is obtained that incorporates explicit radial variation and essential parallel-transport processes, as well as the sheath condition. The 1-D nature of the code is a major design virtue computationally because extensive parametric studies are possible and necessary to achieve a converged design. A detailed description of the model and numerical approach is given in References [48] and [49]. Recent modifications to the model [50] are the addition of a self-consistent neutral-atom recycling model in the divertor chamber and a high- $Z$  (xenon) impurity radiation model for radiative cooling at sub-200 eV temperatures.

The neutral density model is a simplified but reasonably accurate time-dependent model that assumes a radially flat neutral profile. However, the magnitude evolves self-consistently in time with changing plasma conditions in the divertor through temperature-dependent reaction rates and a prescribed pumping rate, which depends on such factors as geometry and pipe conductances. Prescribing the pumping time is believed to be more physical than the customary practice of fixing the recycling coefficient [51]. The recycling coefficient is then computed self-consistently from the relative amounts of ionization and leakage when the plasma reaches steady state. The flat profile assumption is justified on the grounds that charge-exchange-induced diffusion, which strongly dominates ionization at the low divertor temperatures encountered ( $T_e \sim 5 \text{ eV}$ ), smooths spatial gradients of neutral density. This behavior is also seen in Monte Carlo simulations of neutral transport in the divertor.

In the absence of reliable data for the radiative cooling rate of high- $Z$  elements at low plasma temperatures, a simple model is used to estimate the impurity radiation. Post's coronal equilibrium data [52] is extrapolated from the lower limit ( $\sim 80 \text{ eV}$ ), assuming a constant cooling rate to  $\sim 10 \text{ eV}$  followed by an exponential drop to zero temperature. The rate of decay was varied to give a reasonable physical model that was not constant to zero temperature on the one hand, and that did not trigger thermal instabilities on the other hand.

The impurity density profile was assumed radially uniform in the core and edge, and justified on the grounds that with an anticipated edge fueling of xenon, a flat profile was more reasonable than a constant fraction of the electron density. However, in the divertor, recycling of the impurities is likely to drive the impurity concentration to some fraction of the electron density. This fraction was made consistent with the upstream concentration.

Transport coefficients used were similar to those utilized for 2-D simulations of the NET/INTOR tokamak designs [51] ( $D = 1 \text{ m}^2/\text{s}$  and  $\chi = 4 \text{ m}^2/\text{s}$ ). Boundary conditions at the first wall and divertor target were also standard [51,53]. Extensive iterations with the core transport code were performed to ensure self-consistency at the core/edge boundary of heat and particle fluxes, and of plasma density and temperatures. The plasma computations were supplemented with 3-D Monte Carlo neutral-transport simulations in the relevant TITAN divertor geometry, using the DEGAS code [54].

Detailed field-line tracing calculations (Section 4.4) show the field-line connection length,  $L_{\parallel}$  (defined as the distance along the field line from the "watershed" point between divertors to the target), to be sensitive to the distance into the SOL, especially in the vicinity of the separatrix. However, since the resolution on transport scales is at best

an island width, a suitable average over the SOL width was taken for the ODESSA simulations, at a value  $L_{\parallel} = 69$  m.

The TITAN divertor design consists of three divertors and an SOL width of 6 cm. The choice of the number of divertors,  $N_D$ , reflects a compromise because as the number of divertors increases, the total area of the divertor targets increases, leading to a lower heat flux (but weaker than the expected  $1/N_D$  dependence) while the ohmic losses in the lithium divertor coils also increase. The choice of SOL width was also a trade-off; a small SOL thickness is desirable for reasons of plasma MHD stability, but it leads to higher plasma temperatures at the first wall with a consequent increase in erosion.

In the final converged stage between core- and edge-plasma codes, stable profiles of plasma density, temperature, and flow velocity in the SOL and divertor were obtained for  $\sim 150$  MW of power flowing into the SOL at a particle throughput of  $\sim 10^{22}$  s $^{-1}$ . In the global-plasma power balance,  $\sim 70\%$  of the steady-state heating power was radiated in the core plasma,  $\sim 23\%$  in the SOL, 4% in the recycling zone, and 3% was deposited on the target through the plasma sheath.

Figure 1.2-13 depicts the radial upstream and downstream ion and electron temperature and density profiles. High separatrix density ( $\sim 2 \times 10^{20}$  m $^{-3}$ ) and temperatures ( $T_e \sim 220$  eV,  $T_i \sim 380$  eV) are achieved, with the latter decaying strongly to  $\sim 2$  eV at the first wall. Intense recycling (global recycling coefficient,  $R = 0.995$ ) is achieved at the divertor target based on the simple neutral-particle model in ODESSA, which is borne out by more detailed Monte Carlo simulations. This is characterized by high density ( $\sim 10^{21}$  m $^{-3}$ ) and low temperature ( $T_e \simeq T_i \simeq 5$  eV) in the divertor plasma.

In view of the considerable uncertainty in many of the assumptions used in the edge-plasma analysis, an extensive sensitivity study was undertaken in an effort to determine how the divertor design might change as the edge-plasma conditions change. Fairly substantial changes (factor 2-3) in the transport coefficients and in the neutral pumping time lead to relatively small changes in the average heat flux on the divertor target of less than 10% to 12%. Note that the profile of heat flux in the plasma may vary quite noticeably, particularly as the transport coefficients are adjusted, but the total power flow to the target (or, equivalently, the average heat flux) is less sensitive. The results are somewhat more sensitive to the parameters in the impurity radiation model, since 20% changes in the input variables yield changes in the heat flux of up to 10%. The connection length makes little difference to the heat flux (verifying that including a different value for each field line is not important), and there is also little sensitivity to the SOL thickness. The strongest sensitivity occurs with the core plasma-radiation fraction, where the average heat flux varies approximately as  $(1 - f_{RAD}^c)^{-1}$ . This sensitivity could

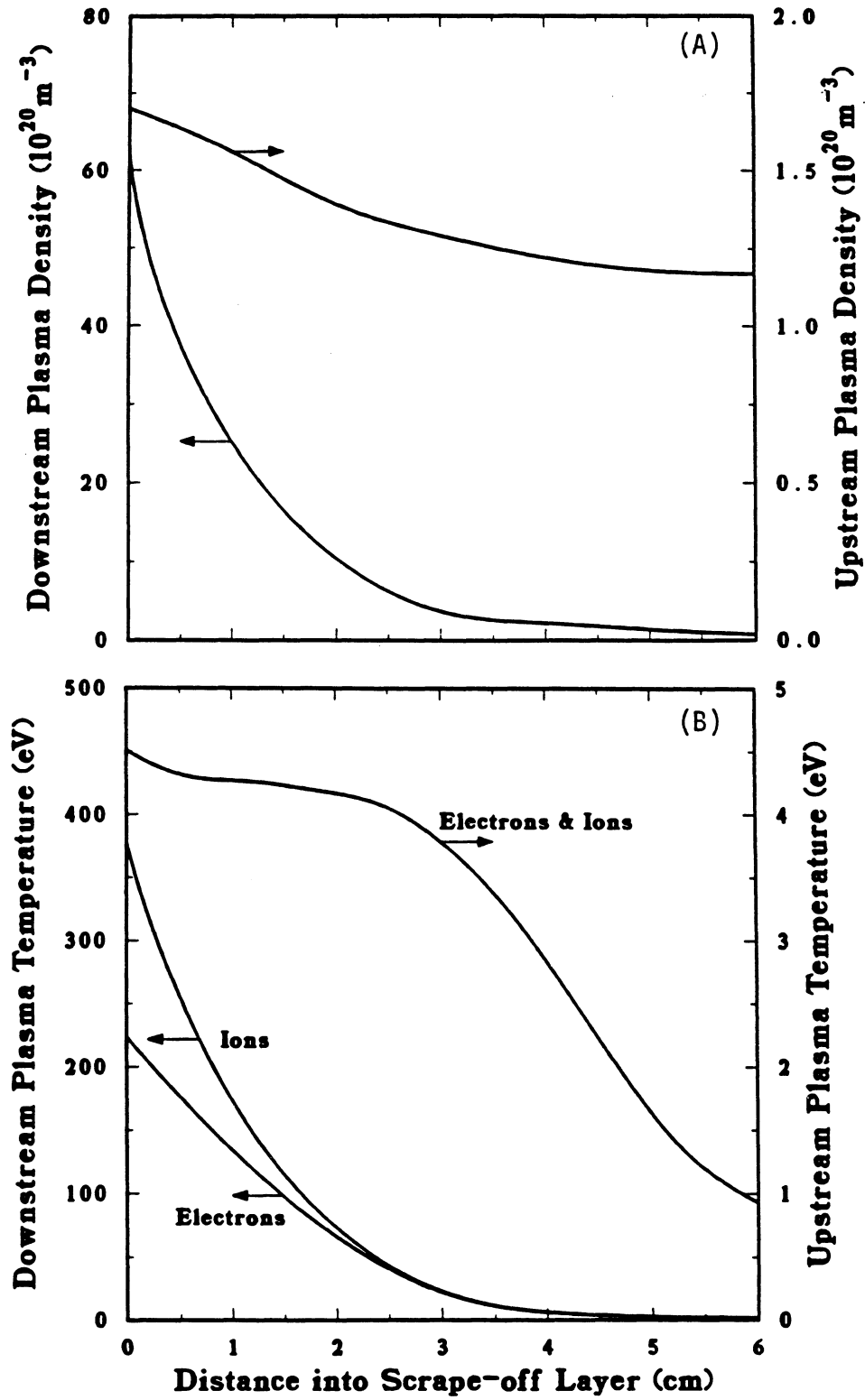


Figure 1.2-13. Radial profiles of plasma temperature (A) and density (B), in upstream (SOL) and downstream (divertor) zones.

be utilized to adjust for any uncertainties in other parameters (especially the radiation model, which is probably the weakest aspect of the model) by varying the impurity density to ensure that the heat flux on the divertor is acceptable.

Detailed neutral-transport modeling was performed by using DEGAS, a fully 3-D Monte Carlo transport code [54], which uses the most recent and thorough data base of cross sections and reflection coefficients. The geometry of the TITAN-I toroidal-field divertor was modeled using an equatorial-plane cross section of the divertor plasma and duct region. The pumping duct leading from the divertor to the vacuum tank, which is located over the outboard  $90^\circ$  in poloidal angle only, was modeled by an absorbing wall in this region.

The neutral transport results show that the global recycling coefficient,  $R$ , lies in the 0.95 to 0.98 range. Because of high plasma density ( $\sim 10^{21} \text{ m}^{-3}$ ) near the divertor target, the neutral densities fall very sharply away from the divertor target so that the flux of neutral particles across the separatrix and into the core plasma is negligible (Figure 1.2-14). The densities are high in the duct region and, for atomic D, fairly constant throughout the duct region, with pressures of about 15 to 75 mtorr depending

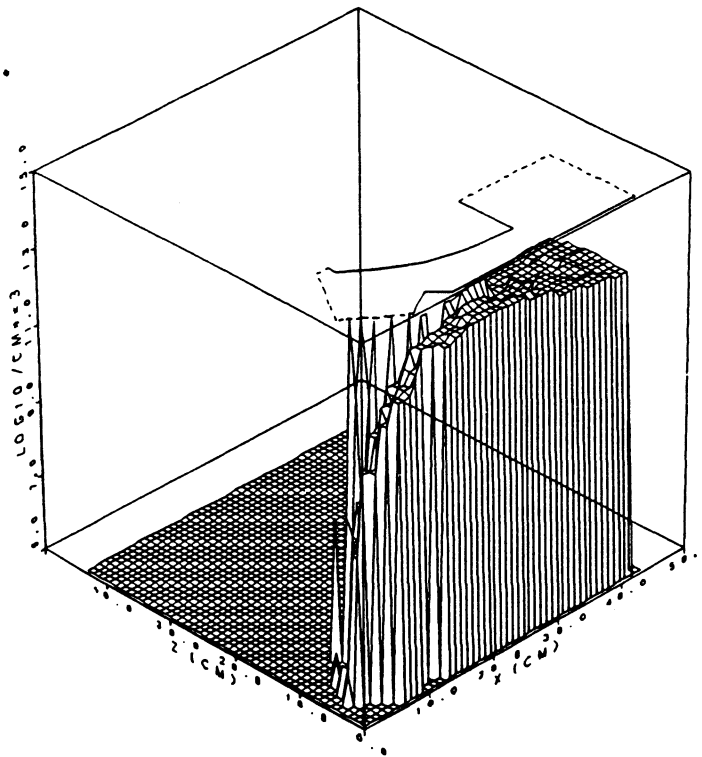


Figure 1.2-14. Poloidally averaged density of atomic D for TITAN-I divertor geometry.

on the poloidal location. An effective pumping speed of  $250 \text{ m}^3/\text{s}$  at the back of divertor pumping duct is found to be sufficient to achieve the required helium removal rate.

The neutral particle pressure shows a marked asymmetry in poloidal angle because of the presence of the pumping duct only on the outboard side of the divertor. This poloidal asymmetry, however, was found to have little effect on the edge-plasma properties. The fluxes of neutral particles escaping into the pumping duct were found to be significantly different from the plasma fluxes on the divertor target, specifically the neutral gas was enriched in D and He relative to T. For the assumed case of equal target fluxes of D and T, and for an He plasma flux of 5% that of DT, the neutral gas escaping was enriched in He relative to DT by a factor of  $\sim 3$  and in D relative to T by a factor of 3.7.

The DEGAS neutral-transport code was used to estimate erosion on the first wall of TITAN; the wall material chosen was vanadium (TITAN-I) but the results should be similar for the ferritic steel proposed for TITAN-II. Sputtering due to both ions and charge-exchange (C-X) neutrals was considered, using the upstream plasma profiles provided by ODESSA. The DT ion flux on the wall was estimated at  $2 \times 10^{21} \text{ m}^{-2}\text{s}^{-1}$ , with a 5% He ion fraction. Because the edge-plasma models contain a fairly large degree of uncertainty, a sensitivity study was performed to estimate the erosion rate for different values of the plasma temperature at the first wall. Since it is not clear whether a sheath will form at the wall, cases with and without the presence of a negative sheath were considered. Table 1.2-VIII shows the results of this analysis in which redeposition was ignored. For the reference case (plasma temperature of  $< 2 \text{ eV}$  at the first wall), there is negligible ion erosion since the ion energies are below the threshold for sputtering. Furthermore, the high plasma density near the first wall prevents the neutral particles released from the wall from penetrating to regions of high plasma temperature and then returning to the wall to pose a sputtering problem.

Since the engineering design of the first wall provides for a 0.25-mm allowance for erosion, these results imply that a plasma temperature of  $\sim 6 \text{ eV}$  is acceptable if a sheath exists at the wall, while the temperature is allowed to rise to  $\sim 10\text{-}20 \text{ eV}$  if there is no sheath; the limits would be increased further if redeposition were taken into account. ODESSA predicts a temperature of  $\leq 2 \text{ eV}$  so it appears that there is a large safety margin in the first-wall design from considerations of erosion.

Erosion of the divertor target was calculated from the DT and He ion fluxes, allowing for acceleration through the plasma sheath. The location chosen for the calculation was a point close to where the separatrix strikes the divertor target, where the particle flux and temperature have their highest values (DT ion flux of  $\sim 9 \times 10^{23} \text{ m}^{-2}\text{s}^{-1}$  with a 5% He ion fraction). Vanadium (TITAN-I first-wall material) sputtering due to He bombardment

**Table 1.2-VIII.**  
**SENSITIVITY STUDY FOR FIRST-WALL EROSION RATE<sup>(a)</sup>**

First-Wall Temperature (eV)	DT Ions	DT C-X Neutrals	He Ions	Total
1.7	0.00 (0.00)	0.01 (0.01)	0.00 (0.00)	0.01 (0.01)
6.0	0.00 (0.03)	0.01 (0.01)	0.00 (0.25)	0.01 (0.29)
10.0	0.02 (1.02)	0.02 (0.02)	0.02 (0.78)	0.06 (1.82)
20.0	0.75	0.09	0.22	1.06
30.0	2.55	0.21	0.54	3.30

(a) Erosion rate in mm/y without (with) a sheath.

was found to be excessive ( $\sim 5\text{-}10\text{ mm/y}$ ) even at the low plasma temperature of 4 eV. Therefore, a layer of tungsten (alloyed with rhenium to improve its ductility) armor is used to protect the cooled divertor plate.

Helium and DT sputtering on tungsten are negligible for the TITAN-divertor plasma conditions. Based on considerations of the expected concentration of xenon impurities in the divertor plasma, the total Xe flux onto the target was estimated at  $\sim 10^{20}\text{ m}^{-2}\text{s}^{-1}$ . Many uncertainties exist regarding the behavior of the recycling Xe impurity, especially with respect to the flow speed and charge state when it strikes the target. There is a tendency for the impurity to be frictionally accelerated by the drifting background plasma such that it can be flowing at close to the sonic velocity of the DT ions. However, the mean free path for ionization of the neutral Xe atoms emitted from the target is short at these high plasma densities and there is little distance for the impurity to be accelerated to a high velocity before returning to the target. It is assumed that the recycling Xe has a flow speed of one-tenth that of the DT plasma ions, but that the primary Xe flux has the same flow speed as the background plasma. If these species have charge states of, respectively, 2 and 4, then the erosion rate is less than 2 mm/y even if redeposition is ignored. Strong redeposition near the divertor target may dominate the net erosion rate, implying that higher charge states and flow speeds could be tolerated. Acknowledging the

great uncertainties regarding erosion estimates for the divertor target, the specification for the divertor design was that a 2-mm-thick layer of tungsten should be provided to give a lifetime of one full-power year. Further investigations into the effects of heavy impurities on the erosion rate of divertor targets clearly are required.

Significant erosion can occur on the wall facing the divertor plate from charge-exchange neutrals originating from the divertor target. Orienting this wall at a relatively oblique angle to the target can reduce this erosion but it may be necessary to protect the surface with a thin layer of an armor material such as tungsten. Since this region of the wall is shadowed from the core plasma and receives a small heat load, this protection should not lead to thermal problems in the structure.

### 1.2.5. Fueling

The TITAN fueling system is described in Section 5.6. The TITAN external fueling rate balances the combined DT exhaust and fusion burnup in steady state. The TITAN-I tritium burnup is 0.353 kg/d at a fractional burnup of 0.24, such that the tritium throughput rate is 1.5 kg/d. The performance of TITAN-II is similar. Assuming that the confinement times of deuterium and tritium in the plasma are equal ( $\tau_{pi} \simeq 3.6$  s), the fueling stream can maintain the nominal composition of the plasma (including Xe impurities), subject to isotopic separation and removal of the alpha-particle ash.

Edge refueling is presumed to be inappropriate in TITAN because particles introduced at the first wall will tend to be swept out along the scrape-off layer (outside the separatrix) to the divertor plate and vacuum ducts and, therefore, will be unavailable to refuel the core plasma. Pellet fueling [55,56] using cryogenic pellets ( $\rho_o \simeq 250$  kg/m<sup>3</sup>) is the fueling option of choice. The RFP plasma confinement is provided largely near the reversal surface ( $r_r \simeq 0.55$  m for TITAN with  $r_p = 0.60$  m), with turbulent mixing of particles assumed to occur within the core plasma. It is assumed, therefore, that the pellet inventory needs to be deposited mostly just inside the reversal surface. Deep penetration to the central plasma is not required in an RFP, so ultra-high pellet injection speeds ( $> 3$  km/s) or advanced acceleration technologies [57], beyond the presently available pneumatic or centrifugal approaches [56], should not be required in the TITAN case.

Ablation of the pellet while traversing the scrape-off region between the first wall and separatrix, although typically small, is included in the present calculation. Ablation of the pellet, as the pellet penetrates the plasma, contributes to the local plasma particle inventory. The model assumes that the radial plasma-transport time ( $\tau_D \simeq 20$  ms) is

much longer than the parallel-transport time ( $\tau_{\parallel} \simeq 240 \mu\text{s}$ ), which in turn is much longer than the time for a pellet to cross the flux surface ( $\tau_{\text{pel}} \simeq 5 \mu\text{s}$ ). The pellet, therefore, first ablates, then the particles spread out along the flux surface, and finally particles diffuse radially. Larger initial pellet radius or higher injection speed allows deeper penetration into the plasma. It is desirable to limit the individual-pellet particle inventory to a small fraction,  $g$ , of the nominal plasma particle inventory to reduce fluctuations in the plasma density and fusion power during refueling. Ablation caused by fusion-product alpha particles is ignorable for the shallow penetration case of interest to TITAN. If deep penetration is required, incremented injection speed must be provided to overcome the additional ablation from energetic alpha particles, although the magnitude of this effect is not well known and may, in fact, be negligible.

An advanced pellet-ablation model [58] has been applied in the TITAN study. In this model, all energy reaching the pellet surface is assumed to result in evaporation rather than bulk heating of the pellet (*i.e.*, energetic runaway electrons are ignored). It is found that fueling of the TITAN RFP reactor appears to be relatively straightforward. A pellet injector based on present technology can inject 2-km/s pellets past the reversal radius ( $r_r \simeq 0.55 \text{ m}$ ). Presently available injector frequencies ( $\sim 6 \text{ Hz}$ ) will have to be increased to  $\sim 25 \text{ Hz}$  for TITAN applications. Pellets composed of TT penetrate slightly deeper than DD pellets ( $d = 0.13 \text{ m}$  versus  $0.12 \text{ m}$  for  $u = 21 \text{ km/s}$  1.75-mm pellets), but the difference does not justify DT isotopic separation and, therefore, TT pellets are not used for the TITAN reactors. Future work should self-consistently incorporate the pellet-refueling source profiles into the temporal 1-D, core-plasma transport description to evaluate the profile effects on global plasma characteristics. Also, a model [59] of asymmetric pellet ablation (Section 2.3.3) remains to be applied to RFP reactors.

It is assumed that TITAN will be provided with two injection systems (5 M\$ each) for redundancy. The injectors themselves can be placed relatively remote from the TITAN FPC (*e.g.*, outside the vacuum task for TITAN-I or well above the TITAN-II FPC to avoid penetrations through the water pool enclosure.) Each injector would occupy an essentially cubic box with a volume of approximately one cubic meter [56]. An evacuated drift tube would connect each injector to the FPC in the vicinity of the divertors to avoid penetrations through the blanket/shield subsystems.

### 1.2.6. Start-Up and Shutdown

It became evident towards the end of the early RFP reactor studies [7] and during the scoping phase of the TITAN study [1] that the design limits for both the toroidal-

and poloidal-field-coil systems would be determined more by the plasma breakdown, formation, and ramp-up transients than by the steady-state operational phase. Therefore, extensive simulations of TITAN plasma-transient operations were performed (Section 6).

A typical reversed-field-pinch (RFP) experimental discharge can be divided into four phases: (1) breakdown and formation, (2) current ramp-up, (3) sustainment, and (4) termination. A representative time history of an RFP discharge, taken from ZT-40M experiments [61], is shown in Figure 1.2-15. Ignition and fusion burn in a reactor are achieved during the current ramp-up phase, and operation of the current-drive system is required during the sustainment phase. The breakdown and formation phase encompasses the time from the start, which begins by establishing a toroidal magnetic field inside the discharge chamber in the absence of the plasma, to the formation of a "seed" RFP plasma. At the time of peak toroidal magnetic field, poloidal-field windings are activated to produce a flux change through the center of the torus and, consequently, a toroidal voltage around the discharge chamber. This voltage typically ionizes the gas in a few microseconds and the toroidal current is initiated in the resulting plasma. The toroidal plasma current and the toroidal magnetic field within the plasma increase while the toroidal magnetic field at the wall decreases, keeping the average toroidal field (and the toroidal flux) in the chamber almost constant. Eventually the toroidal magnetic field at the wall changes sign and is crowbarred in the reverse direction relative to the back-biased condition of the breakdown and formation phase. The plasma current is then increased to the peak value during the current ramp-up phase. The poloidal-field (PF) coil system provides the poloidal flux and the majority of toroidal flux contained within the full-current plasma by the RFP dynamo.

The existing RFP experimental data base for RFP formation and start-up is reviewed in Sections 2.3 and 6.2. Several constraints have been identified, such as: (1) ratio of toroidal electric field to initial gas fill pressure, (2) ratio of stray vertical field to the initial toroidal field, (3) minimum plasma current density, (4) impurity burn-through in terms of the ratio of plasma current density to the plasma density, (5) density pump-out in terms of minimum density as a function of initial bias field, (6) poloidal beta, and (7) avoidance of electron runaway regime. Applying these constraints to the formation of the TITAN plasma, it was found that the conditions for plasma breakdown and subsequent RFP formation for the TITAN reactors are expected to differ little from the conditions in present and planned RFP experiments [34]. Likewise, the conditions of the seed RFP plasma required to start up the TITAN reactor, except for plasma size, are similar to present-day RFP parameters ( $I_\phi = 0.2$  to  $0.4$  MA,  $n = 1$  to  $3 \times 10^{19} \text{ m}^{-3}$ ,  $T = 0.1$  to  $0.4$  eV). For the reference formation scenario, loop voltage in the range of 200 to 500 V

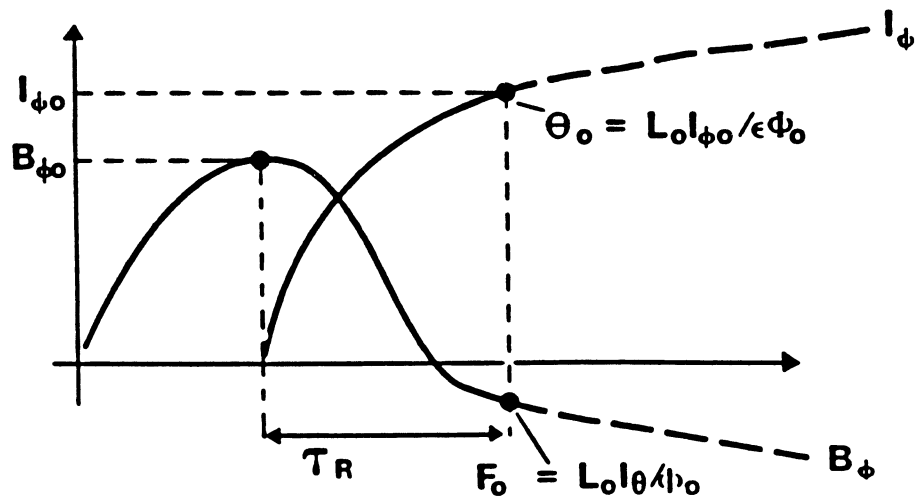
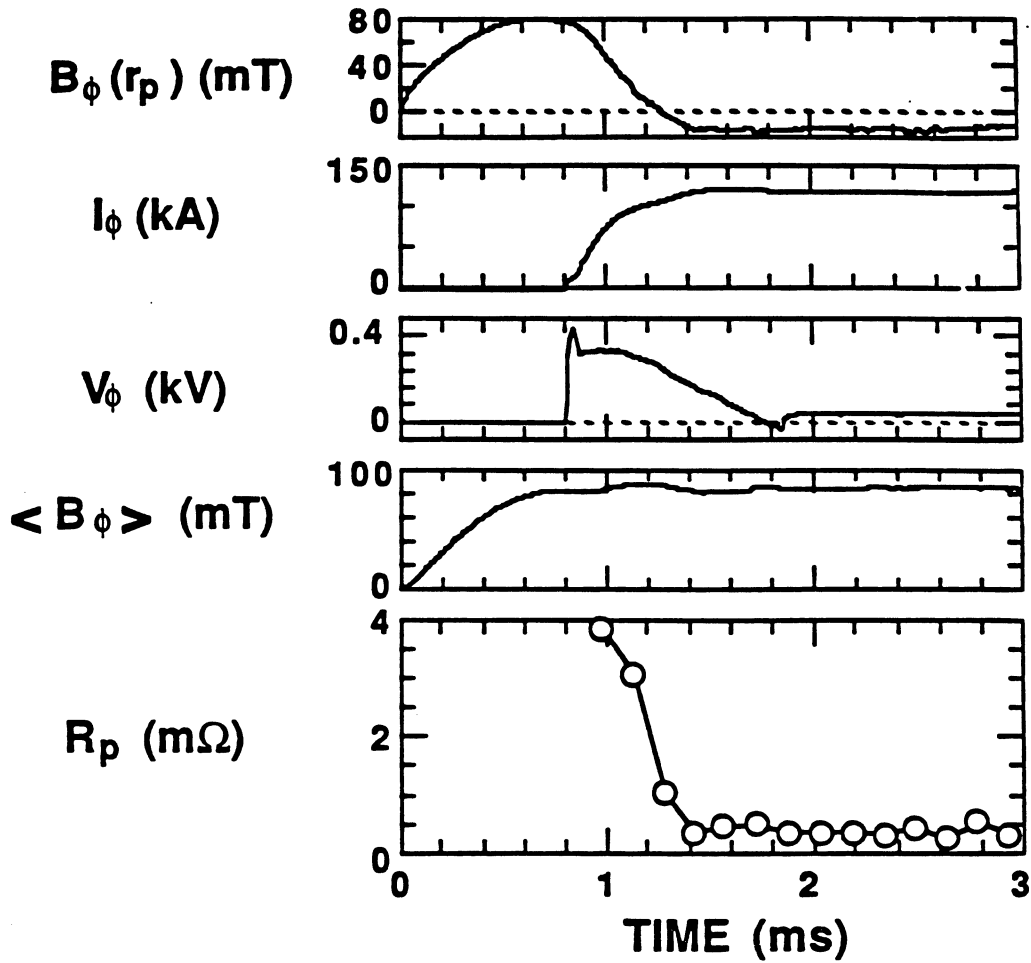


Figure 1.2-15. Typical matched-mode RFP formation for ZT-40M leading to the values of  $\Theta_0$ ,  $F_0$ , and  $I_{\phi_0}$  [61] used as initial conditions for start-up, ignition, and burn simulations.

is necessary to ensure short formation time and acceptable resistive flux consumption and formation energy. The scaling of plasma resistivity during the formation phase is an important issue that may be resolved with data from larger RFP experiments. Better density and impurity control during the breakdown and formation process may also be required.

The steady-state analysis of global plasma-power balance provides useful information for the optimization of plasma approach to ignition. Results of this type of analysis for auxiliary-heated fusion devices are usually presented in the form of required auxiliary power for power balance as a function of plasma density and temperature. This information is then used to identify the path to ignition that requires minimum auxiliary heating power. Similar analysis can be applied to compact RFP reactors in which the plasma is heated to ignition by ohmic heating alone (no auxiliary heating).

Addition of the ion and electron power-balance equations for steady state results in

$$\frac{3}{2} \left( \frac{n_e T_e}{\tau_{Ee}} + \sum_j \frac{n_j T_j}{\tau_{Ej}} \right) = P_\alpha + P_{OHM} - P_{RAD}, \quad (1.2-12)$$

where  $P_\alpha$  and  $P_{OHM}$  are, respectively, the alpha-particle and ohmic heating power and  $P_{RAD}$  is the radiative (bremsstrahlung) losses. Equation 1.2-12 can be solved for the required plasma current for power balance,  $I_\phi$ , as a function of density and temperature for a given plasma size, ion mixture, plasma profiles ( $n$ ,  $T$ , and  $\mu$ ),  $F$  or  $\Theta$  values, and the scaling of  $\tau_E$  as given by Equation 1.2-4. Because of the high density of RFP plasmas, the electron/ion energy-equilibration time,  $\tau_{ei}^{eq}$ , is short resulting in  $T_e \simeq T_i \simeq T$ .

Results of this analysis for the TITAN plasma ( $r_p = 0.6$  m) are shown in Figure 1.2-16 for a 50:50 DT mixture,  $n_e \simeq n_i \simeq n$  ( $Z_{eff} = 1$ ), plasma power profiles (Equations 1.2-5 through 1.2-7), and  $F = -0.1$ . A current exponent of  $\nu = 1.05$  and a soft  $\beta$  limit of  $\beta_{\theta c} = 0.23$  are used. Figure 1.2-16(A) shows a "ridge" in the  $I_\phi$ - $n$ - $T$  space above which the path to ignition and burn should be located (similar to corresponding diagrams for auxiliary heated devices where a ridge for auxiliary heating exists). The optimum ignition scenario attempts to pass over the ridge at its lowest height (saddle point). This saddle point is at  $T \simeq 7$  keV and  $n \simeq 3 \times 10^{20} \text{ m}^{-3}$  with a current of  $I_\phi \simeq 16$  MA. The TITAN start-up path through ignition and burn, shown as solid line in Figure 1.2-16, passes close to this saddle point.

The corresponding contours of constant  $I_\phi$  are shown in Figure 1.2-16(B). The chain dashed line in this figure is the contour of  $\beta_\theta = 0.2$  and the points above this line all have  $\beta$  values of  $\sim 0.2$  because of the assumption of the  $\beta$ -limited confinement. The  $\beta_\theta$  value for the saddle point is about 7%.

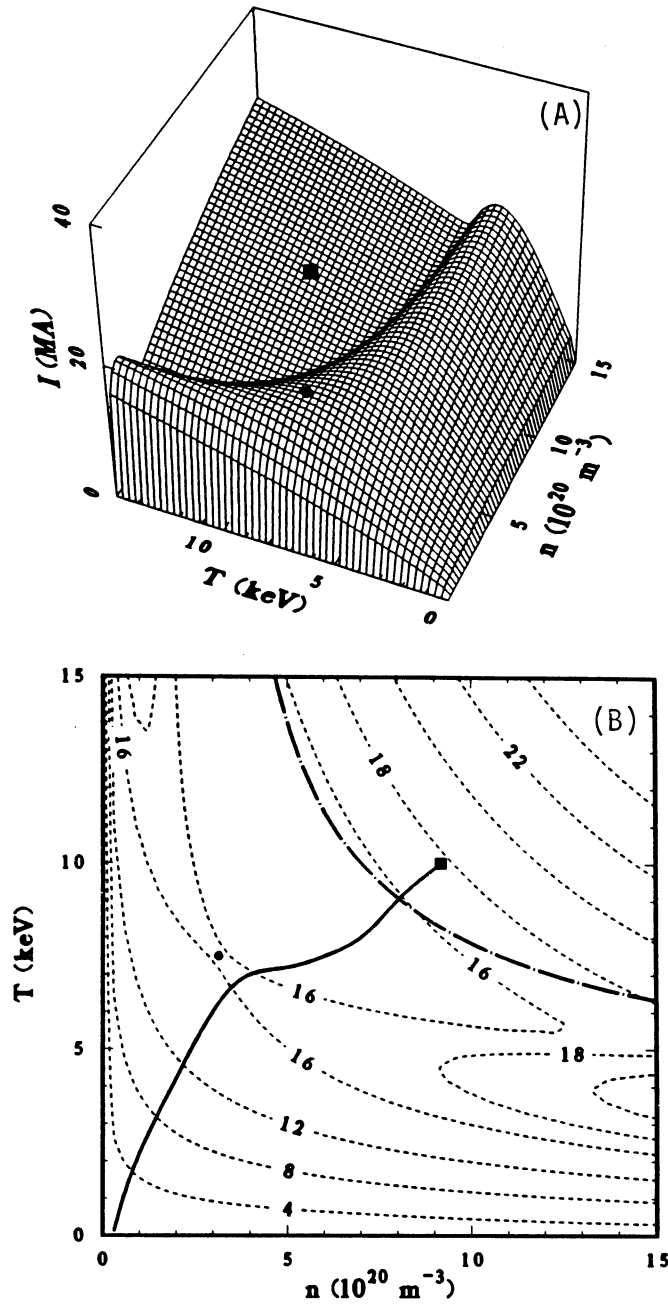


**Figure 1.2-16.** The required current for power balance as a function of TITAN plasma density and temperature (A) and the corresponding contour plot (B). The steady-state TITAN plasma is denoted by a filled square and the saddle point by a filled circle. The TITAN start-up path to ignition and burn, shown as a solid line, is located above this surface and passes close to the saddle point.

The sensitivity of the structure of the  $I_\phi$ - $n$ - $T$  ignition surface to the various assumptions has been also studied. The  $\beta$ -limited confinement assumption does affect the ridge structure and only changes the current values above the chain-dashed line of Figure 1.2-16. If the confinement scaling is more favorable with current (higher  $\nu$  values), the saddle point moves towards lower currents and slightly lower densities. For example, for  $\nu = 1.2$ , the current is reduced to 12 MA. Increasing  $Z_{eff}$  from 1.0 to 1.7, increases the current by about 10% and electron density by 50% (note that line radiation is ignored).

The current in the TITAN plasma is initiated and then ramped to full value through induction by the PF-coil system. In addition to producing the required flux change, the PF system must also generate the necessary equilibrium-field distribution. The most efficient way to produce a net flux change is through bipolar operation of the coil system since the stored energy, magnetic-field strength, coil stress, and joule losses would be minimized. Plasma equilibrium depends on the magnitude of the plasma current and the equilibrium field produced by the PF coils should closely match the required vertical field for equilibrium.

For the TITAN designs, the PF-coil system is divided into two sets of coils: the ohmic-heating (OH) coil set, which produces most of the flux swing but does not produce any equilibrium (vertical) field; and the equilibrium-field (EF) coil set, which produces the necessary vertical field and may or may not contribute to the flux swing. This approach allows the OH coils to be operated independently of the magnitude of the plasma current. The magnetic properties of the OH- and EF-coil sets and the start-up switching sequence have been chosen (Section 6.3) such that the EF coil produces the required vertical field approximately. The PF-coil system includes a pair of small, normal-conducting trim coils to maintain exact equilibrium during the start-up sequence. Using this approach, only the power supplies for the EF trim coils have to be feedback controlled to ensure proper equilibrium. The EF trim coils are also used during the steady-state operation for plasma equilibrium control and OFCD (Sections 1.2.7 and 7).

The TITAN-I start-up scenario is chosen such that the start-up power is directly extracted from the power grid without requiring an on-site power-storage system (other than the coils themselves). The start-up switching sequence is shown in Figure 1.2-17. The TITAN start-up sequence uses a bipolar swing of the OH-coil currents and begins with charging the OH coils to their full back-bias values. The OH coils are then discharged into a transfer resistor, while the EF coils are connected in parallel to the OH coils ("formation and fast discharge" phase in Figure 1.2-17). The value of the transfer resistor is set by the constraint on the maximum voltage across the superconducting EF coils. The fast-discharge phase lasts about 1 to 2 seconds.

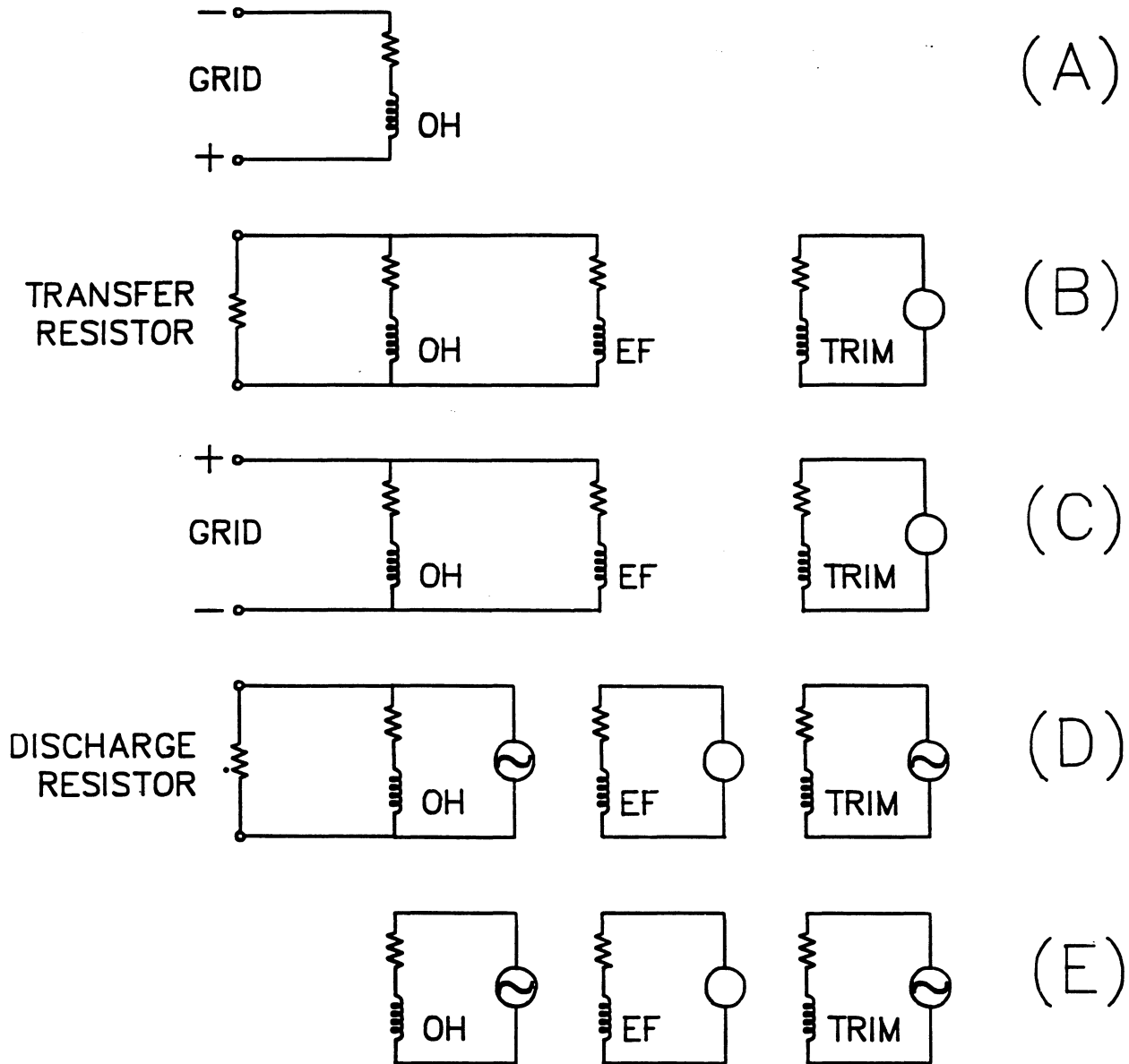


**Figure 1.2-17.** Start-up sequence for the TITAN reactors: (A) Charge-up – OH coils are charged to full back-bias value, (B) Formation and fast discharge – OH coils are discharged through a transfer resistor (EF coils are connected in parallel to the OH coils), (C) Slow ramp – grid power drives the OH coils to full forward bias current and the EF coils to their steady-state value, (D) Transition – the OH coils are slowly discharged while OFCD is initiated, and (E) Steady state – current-drive system is fully operational. Initiation of OFCD operation during the slow-ramp phase is advantageous.

As the OH coils are discharging, the voltage across the circuit drops. When the voltage across the OH coils reaches that of the grid power supply, the transfer resistor is disconnected from the circuit and the grid power supply is directly applied to the OH and EF coils ("slow-ramp" phase). The OH coils are driven to their full, forward-bias current value and the EF coils and the plasma to their respective steady-state currents. The voltage of the grid power supply is usually a few kilovolts and its value is determined by the maximum power from the grid. The current-drive system begins operation during this phase and will be fully operational at the burn phase, maintaining the steady-state current in the plasma. After achieving the steady-state burn condition, the OFCD system is initiated while the OH coils are discharged slowly, from the full forward-bias current value to zero, in order to minimize the recirculating power and the coil-cooling requirements. Initiation of OFCD operation during the slow-ramp phase is advantageous.

The evolution of the TITAN plasma through current ramp, ignition, and burn transients is investigated by using a 0-D, profile-averaged plasma-circuit code. This code solves the ion and electron power-balance equation and the Fokker-Planck equation for fusion  $\alpha$  particles using an implicit time-differencing scheme. The desired evolution of the plasma density, obtained from the above ignition requirement analysis, is used together with the particle balance equation to determine the required fueling rate. Between each time step, a circuit analysis package integrates the circuit equations. At the start of the analysis and for the given FPC geometry and external coil sets, the code divides the FPC into small sectors and models each as an eddy-current circuit element. The self- and mutual inductances of the various circuit elements are then calculated, and the overall inductance matrix is constructed.

Figures 1.2-18 through 1.2-20 show the evolution of the TITAN-I plasma during the start-up sequence for a back-bias OH-coil current of  $I_{OH}^- = 50$  MA-turn, ignoring the eddy currents that may be flowing in the FPC. Figure 1.2-18 shows the time histories of the plasma and PF circuit currents. Because of the effect of plasma resistance, the EF-coil current reaches its final value before the plasma current and is crowbarred first. These figures also show the current required for the EF trim coil to achieve the exact equilibrium throughout the discharge. The vertical field provided by the superconducting EF coil is shown in Figure 1.2-19(A) and is compared to the required value from the Shafranov formula [47]. The vertical field provided by the EF trim coil to produce the exact equilibrium is also shown. An analytical estimate for the evolution of currents, voltages, and power flow during the start-up sequence has also been worked out (Section 6.5) and found to be comparable to the values found from the simulation code.

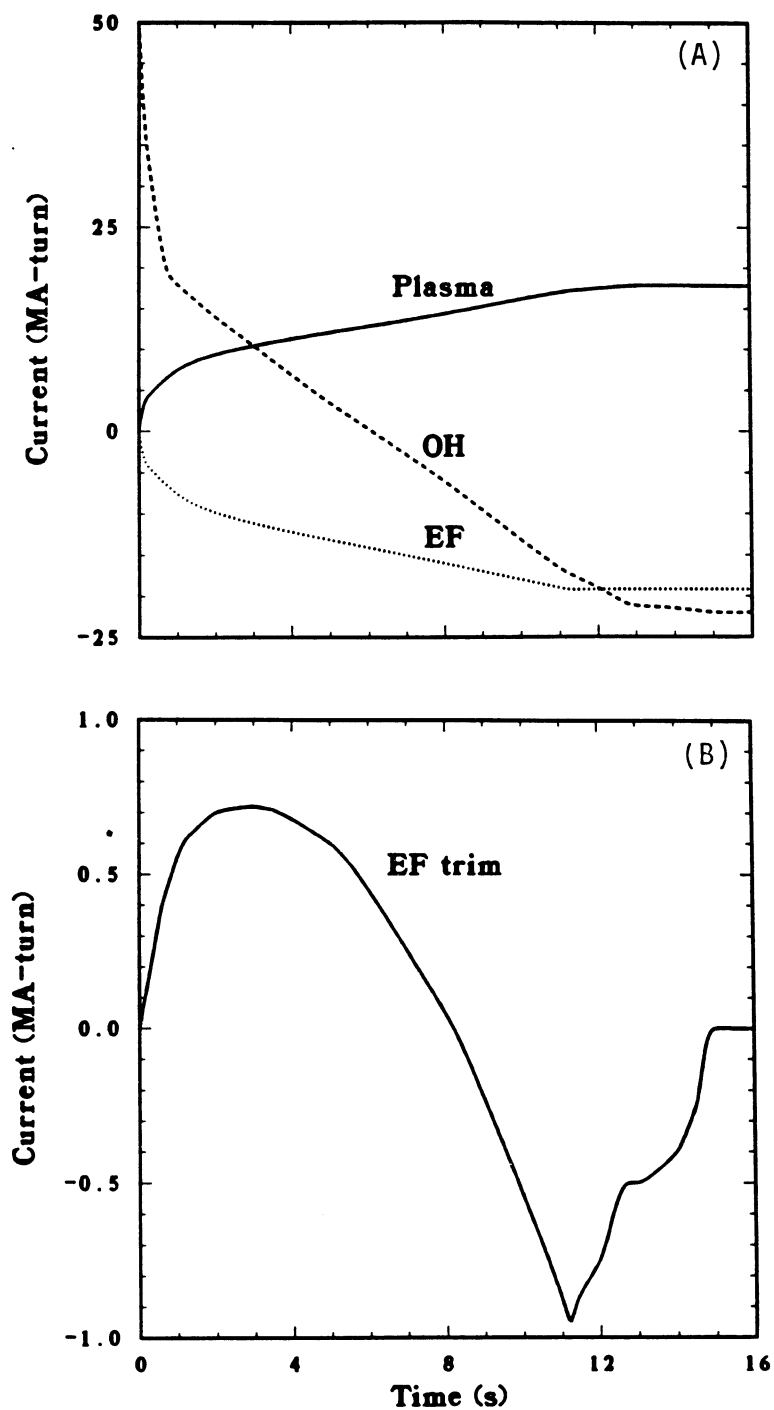


Figure 1.2-18. The TITAN-I start-up simulation results for the evolution of the current in (A) the plasma, superconducting EF coil, and OH coil; and (B) the EF trim coil.

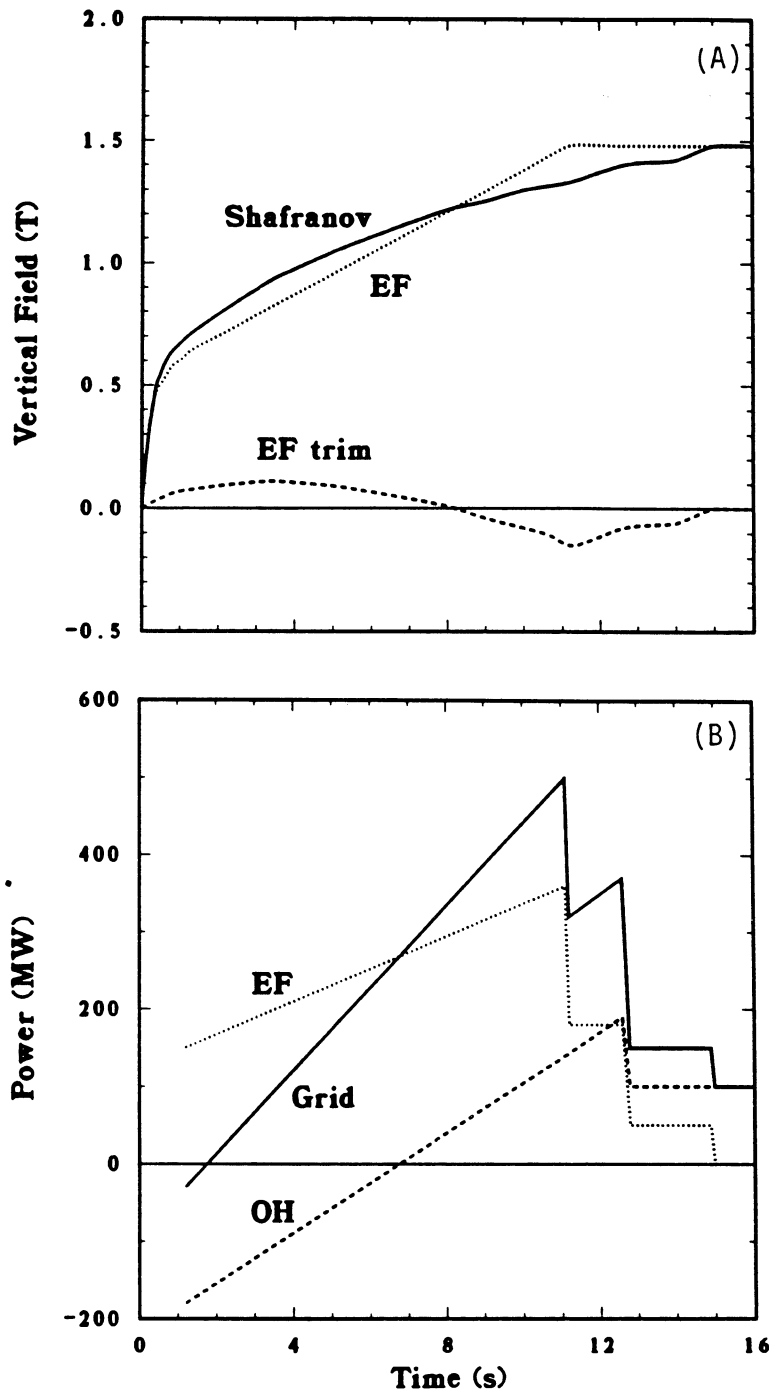


Figure 1.2-19. The TITAN-I start-up simulation results for the evolution of (A) vertical fields produced by the superconducting EF and EF trim coils and the required vertical field from the Shafranov formula; and (B) power deposited in the superconducting EF coil, OH coil, and the total power extracted from the grid.

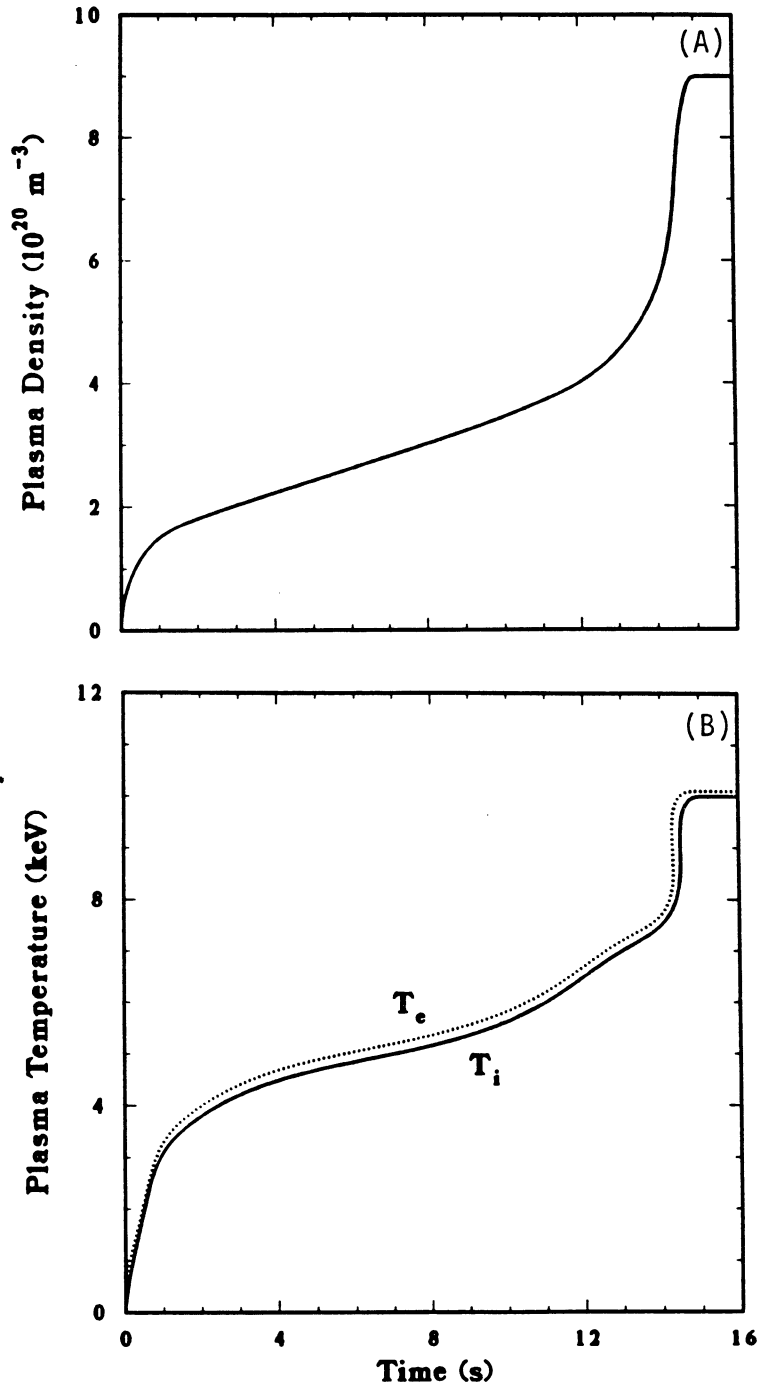


Figure 1.2-20. The TITAN-I start-up simulation results for the evolution of plasma density (A) and temperature (B).

Figure 1.2-19(B) shows the total power extracted from the grid and the power delivered to the OH and EF coils during the start-up sequence. At  $t \simeq 11$  s, final EF-coil current is achieved and the EF coils are crowbarred resulting in a drop in EF-coil (and grid) power. Since the plasma and OH-coil currents are still changing, power has to be supplied to the EF coil in order to maintain the EF-coil current. Full plasma current is achieved at  $t \simeq 13$  s and OH coils are crowbarred, resulting in decreases in OH- and EF-coil powers. Between  $t \simeq 13$  and 15 s, the poloidal beta and, therefore, plasma inductance are changing rapidly. During this period, the trim-coil current is also dropping to zero. Some power still has to be applied to the EF coil to counter the two effects. The OH-coil power after  $t \simeq 13$  s is mostly due to joule heating in the OH coils. It should be noted that the current, voltage, and power to the EF trim-coil circuit is calculated to keep the plasma in exact equilibrium (no shift in magnetic axis). Permitting small shifts in the plasma position will greatly reduce the power required for the EF trim-coil circuit.

Figure 1.2-20 shows the evolution of plasma density and temperature during the start-up sequence. The evolution of plasma density and temperature in the ignition  $I_\phi$ - $n$ - $T$  space is shown in Figure 1.2-16. The ion density evolution is an input to the plasma-circuit code and was adjusted to ensure that the start-up path is located close to the ignition saddle point, and also that the plasma streaming parameter remains small and the electron runaway condition is avoided. The corresponding fueling rate is calculated from the particle balance equation. The plasma ignition is achieved at  $\beta_\theta$  values of about 8% and the final value of  $\beta_\theta$  is achieved only after ignition.

The impact of the eddy currents on the start-up sequence has also been studied. The TITAN-I FPC is located in a thick vacuum tank with no resistive break. However, resistive breaks are used in the FPC itself. As a result, the eddy currents in the tanks produce the dominant effect on the start-up. Because the magnitudes of the eddy currents are small, the evolution of the plasma current is not affected. The vertical fields produced by the eddy currents, even though small, affect the plasma equilibrium during the fast-discharge phase and programming voltage to the EF trim coils should be modified to keep the plasma in exact equilibrium. However, the power requirement for the EF trim-coil power supplies is not increased by the presence of eddy currents.

In RFPs and tokamaks, in addition to the plasma thermal energy, a significant amount of energy is stored in the poloidal magnetic field. At full operational conditions, the stored energy in TITAN-I plasma includes 0.1 GJ of kinetic (thermal) energy and  $W_M \sim 4.3$  GJ of magnetic energy ( $\sim 5.2$  GJ for OH coils with full forward-bias current). The magnetic energies internal to the plasma are 0.3 MJ in the toroidal field and 0.4 GJ in the poloidal field. The magnetic energies outside the plasma are  $< 2$  MJ in the toroidal field and

3.6 GJ in the poloidal field. Any rapid release of these stored energies (*e.g.*, similar to disruptions in tokamaks) may lead to severe consequences.

Operating RFP experiments usually end with a "current termination" phase where the plasma current is rapidly reduced to approximately zero. Current termination is characterized by the loss of toroidal-field reversal and is accompanied by a positive voltage spike (as opposed to a negative voltage spike for tokamak disruptions) and large density and magnetic-field fluctuations. A number of variables, such as plasma density, toroidal-field reversal, magnetic-field errors, and impurities appear to affect RFP terminations. A complete and satisfactory explanation of RFP current terminations is not yet available. Evidence, however, suggests that the onset of termination may be related to a loss of density, possibly leading to a streaming parameter that exceeds a critical value for runaway electrons. Since the value of the streaming parameter for the TITAN plasma is only a percent of the critical value for runaway electrons, a current termination is not expected during normal, steady-state operation of the TITAN reactor; rather only failure of plasma support technologies leading to an uncontrolled ramp-down of the plasma current will result in a current termination.

A method of controlled current ramp-down has been tested on the HBTX1B experiment in which the TF-coil circuit is controlled so that the pinch parameter (and the field reversal) is maintained at a given value as the current is decreased to a relatively low level [62]. Maintaining the field reversal in this way is found to delay termination, and the current can be reduced to between 10% and 20% of the maximum value (and the stored magnetic-field energy reduced to 1% to 4% of the maximum value) before the termination occurs. Controlled ramp-downs of this kind forestall the loss of toroidal-field reversal as long as possible and are required for the reactor.

During normal, steady-state operation of the TITAN reactors, the following plasma support technologies are operational: (1) fueling, (2) current-drive, (3) toroidal-field, (4) divertor-field, and (5) equilibrium-field systems. Consequences of failure of each of these systems were studied. It was found that the failure of the equilibrium-field system appears to be the most severe plasma-related accident for the TITAN reactor (and for any current-carrying toroidal system).

The TITAN plasma shutdown procedures are guided by the above observations to ensure that (1) plasma current is reduced through a controlled ramp-down in order to forestall current termination, (2) plasma equilibrium is maintained during current ramp-down, (3) failure of the equilibrium-field system (*i.e.*, quench of the superconducting EF coils) will automatically lead to an emergency shutdown, and (4) most of the magnetic energy stored in the plasma is removed during the shutdown.

The plasma shutdown scenarios envisioned for the TITAN plasma, therefore, start with terminating fueling and current-drive operations and simultaneously discharging the EF coils. For the standard shutdown procedure, the duration of the EF-coil discharge can be on the order of a few to tens of seconds. During the emergency shutdown procedure, however, the EF coils are discharged rapidly ( $\sim 0.1$  s) through a resistor that can be combined with the quench protection system for the EF coils. Therefore, failure of the equilibrium-field system will automatically initiate the emergency shutdown procedure.

Because of the strong magnetic coupling between the plasma and EF and OH coils in TITAN, a fast discharge of the EF coils results in a rapid decrease in the plasma current; that is, the plasma stored magnetic energy is removed through the EF-coil circuit rather than appearing as heat on the first wall. The parameters of the EF- and OH-coil circuits, however, are chosen such that the plasma equilibrium is approximately maintained during this discharge without any need for an equilibrium control system. The large time constant of the IBC TF coils for field penetration is also utilized to ensure maintenance of the field reversal during the shutdown in a manner similar to the controlled current ramp-down [62].

A series of simulations with the plasma-circuit code has been performed to assess the effects of plasma termination and the effectiveness of the above procedures in reducing the impact of termination. In these simulations, full plasma parameters are assumed at time  $t = 0$ . The effect of current termination is simulated by an exponential increase in the value of the plasma resistance with the growth time of resistive MHD modes perceived to be responsible for loss of reversal and termination ( $\sim 10$  ms for TITAN).

Simulations were performed for two sets of conditions: (1) the EF coils remain at full current and (2) at the initiation of the accident, the superconducting EF coils discharge rapidly in a resistor that can be combined with the quench protection system for the EF coils. The evolution of circuit currents and the corresponding heating power in the plasma for the second case are shown in Figure 1.2-21. It can be seen that the major part of the magnetic stored energy in the system is removed through the discharge of the EF coils. The total energy that appears as heat in the plasma (and, therefore, on the first wall) is  $\sim 400$  MJ, representing a factor of 10 reduction compared to plasma stored energy. The peak heating rate and the plasma loop voltage are also reduced tenfold. Because the TITAN PF-coil system is designed to provide approximate equilibrium during the start-up phase, approximate equilibrium is also maintained during the fast discharge of the EF coils as shown in Figure 1.2-22. The change in the plasma position, because of the mismatch between the vertical field and the required field from Shafranov formula, is small during most of the termination simulation. The eddy-current effects have also

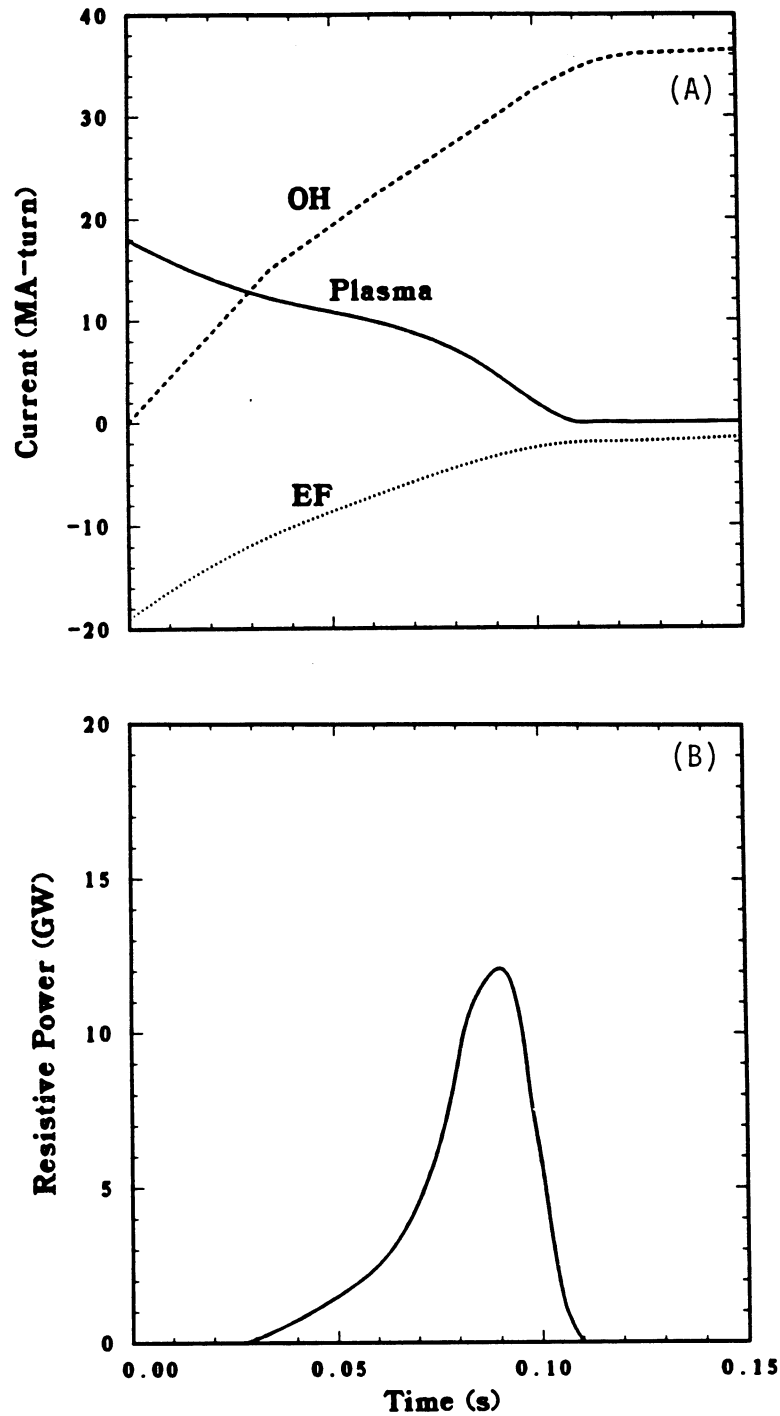


**Figure 1.2-21.** The TITAN-I termination simulation results for the evolution of (A) the plasma, EF-coil, and OH-coil currents; and (B) the heating power in the plasma. Note that heating power is reduced tenfold in this case.

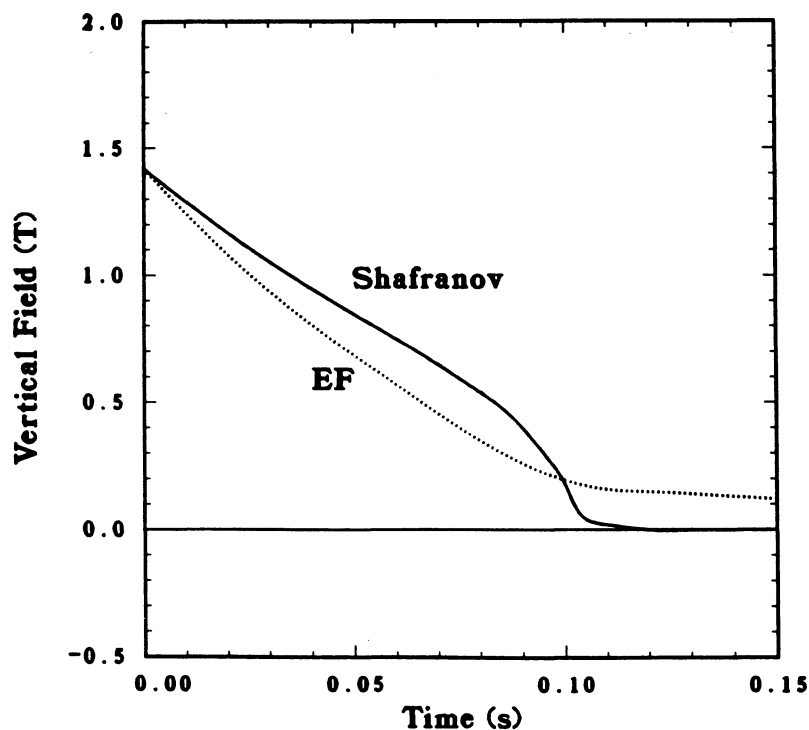


**Figure 1.2-22.** The TITAN-I termination simulation results for the evolution of vertical fields produced by the superconducting EF-coil current and the required vertical field from the Shafranov formula.

been investigated and, although small, found to improve the situation (*i.e.*, smaller energy appears in the plasma and less mismatch occurs between the required vertical field and that produced by the EF coils).

These preliminary simulations of the TITAN emergency shutdown procedure appear to indicate that most of the stored magnetic energy is removed from the system and dumped through the discharge resistor. Only about 200 MJ of energy is transferred to the first wall in a time scale of 50 to 100 ms, resulting in an average temperature rise in the first wall of about 300 °C; therefore, failure of the first wall is not expected.

Despite these favorable results, the RFP theoretical and experimental data base is not very extensive. In particular, no experimental data on high-current, high-temperature, diverted RFP plasmas exist. Furthermore, a complete and satisfactory explanation of current termination in RFPs is not yet available. The safety impact of plasma accidents, therefore, should be further investigated and the shutdown procedures, such as those envisioned for the TITAN plasma, should be experimentally explored.

### 1.2.7. Current Drive

Because of the large plasma resistance in the TITAN designs, an inductively pulsed burn would be sustained for a pulse length of the order of  $L_p/R_p \simeq 200\text{-}400$  s. Therefore, steady-state operation is essential considering issues such as the total power balance, thermal cyclic fatigue in a high-power-density environment, as well as the costs of on-site energy storage (frequent grid-assisted start-up seems unlikely) and thermal storage. An inductively pulsed RFP reactor is a possibility [63]. The parameters of such a reactor, however, should be optimized to minimize the plasma resistance, which results in larger plasmas, lower power density, and possibly the use of superconducting coils throughout the fusion power core.

The detailed analysis of the TITAN current-drive system is reported in Section 7. A number of current-drive options for the RFP have been considered. Although the use of fast-wave current-drive schemes has not been fully explored for the RFP, the high plasma density ( $n \sim 9 \times 10^{20} \text{ m}^{-3}$  in TITAN) and currents relative to those for the tokamak indicate problems with the efficiency of radio-frequency (RF) current-drive schemes. On the other hand, because of the relaxation processes in RFPs, there is no need to drive the current at the plasma center and some of the issues related to wave penetration may be negated. Bootstrap current is also expected to be low, if such current exists at all in RFPs, since  $\beta_\theta$  and  $\epsilon = r_p/R_T$  are small relative to the tokamak.

The close coupling of poloidal and toroidal currents and magnetic fields that determine the near-minimum-energy states of the RFP offers the possibility of a current-drive method based on “magnetic helicity injection” because the resistive decay of plasma current can be viewed as a dissipation of magnetic helicity [9]. Current drive through “electrostatic helicity injection” has been experimentally demonstrated in spheromaks [40], which are also relaxed-state systems like RFPs. Another helicity-injection technique is the oscillating-field current drive (OFCD) [9,41]. In this scheme, audio-frequency oscillating voltages are applied to the toroidal and poloidal circuits in the appropriate phase ( $\delta = \pi/2$ ) to drive a DC toroidal current in the plasma with the plasma, in effect, behaving as a nonlinear rectifier. As originally proposed [9], OFCD is based on the premise that maintenance of the RFP configuration simply requires the supply of magnetic helicity at a rate equal to its dissipation. The helicity balance is given by [9,64]

$$\frac{dK}{dt} = 2\phi V_\phi - 2 \int \mathbf{E} \cdot \mathbf{B} dV_p, \quad (1.2-13)$$

where the integral gives the rate of helicity dissipation throughout the plasma volume and the remaining product of toroidal flux and voltage gives the rate of helicity injection

or ejection through the plasma surface. Helicity is effectively injected into the plasma if  $\Phi$  and  $V_\phi$  are sinusoidal and are oscillated in phase with each other (*e.g.*,  $V_\theta = -\dot{\Phi}$  and  $V_\phi$  are in quadrature), even though the time-averaged electric fields are zero. Hence, with the  $F$ - $\Theta$  diagram providing the required connection between  $V_\theta$  and  $V_\phi$ , a noninvasive and potentially efficient means to drive currents in high-density fusion plasma is possible.

Experimental data on OFCD in RFPs are reviewed in detail in Section 2.3.8 [10, 41]. Low-power OFCD tests ( $\sim 7$  MVA,  $I_\phi \simeq 60$  to 70 kA), shown on Figure 1.2-23, were conducted on ZT-40M. These ramped discharges were at low temperature and, hence, a high plasma resistance. With optimal phasing ( $\delta \simeq \pi/2$ ), an approximately 5% increase in poloidal flux was observed when OFCD was applied. While a clear demonstration of substantial current drive by OFCD must await RFPs operating with hotter plasmas and reduced wall interaction [34], the strong dependence of the plasma response on  $\delta$  and the spatial and temporal behavior of the mean magnetic fields are in general agreement with magnetic helicity models and simulations.

For the TITAN reactors, helicity injection by the OFCD technique has been selected as the means to sustain the toroidal plasma current. A circuit model was developed that simulates the major elements associated with OFCD in order to determine the injected and/or dissipated powers. The model was used to quantify the need for toroidal and poloidal gaps or insulating breaks in structures such as the first wall, which will have currents induced by the OFCD. The plasma is described in terms of the plasma magnetic helicity,  $K$ , toroidal flux,  $\phi$ , and magnetic energy,  $W_M$ . The relationship between these parameters and the circuit variables (*i.e.*, resistances, inductances, currents, voltages) constitutes the overall current-drive model. Power flow in the OFCD system can be described by energy balance [41] rather than helicity balance. A power balance imposed at the plasma interface, together with the definition of the plasma internal magnetic energy and a positive Faraday's law,  $V_\theta = d\phi/dt$ , results in

$$V_\phi = I_\phi R_p + \left( L_p + \frac{\Theta}{2} \frac{dL_p}{d\Theta} \right) \dot{I}_\phi + \left( \frac{1-F}{\epsilon\Theta} - \frac{\epsilon\Theta^2}{2L_o} \frac{dL_p}{d\Theta} \right) V_\theta, \quad (1.2-14)$$

where  $V_{\phi,\theta}$  are the toroidal and poloidal voltages applied to the plasma,  $R_p$  is the plasma resistance,  $L_p$  is the plasma internal inductance (not including the vacuum toroidal flux), and  $L_o$  is the vacuum toroidal inductance. If (1) the coupling of fields is sufficiently strong to make  $L_p$  a function of  $\Theta$ , and (2) if a mechanism exists to allow the perturbation to the near-minimum-energy state to be relaxed to some point in  $F$ - $\Theta$  space on a time scale of relaxation,  $\tau_R$ , then oscillations of  $V_{\phi,\theta}$  in proper phase at frequency less than  $\sim 2\pi/\tau_R$  can give a net time-averaged current,  $\langle I_\phi \rangle$ , with  $\langle V_\phi \rangle = 0$  (*i.e.*, no net flux change).

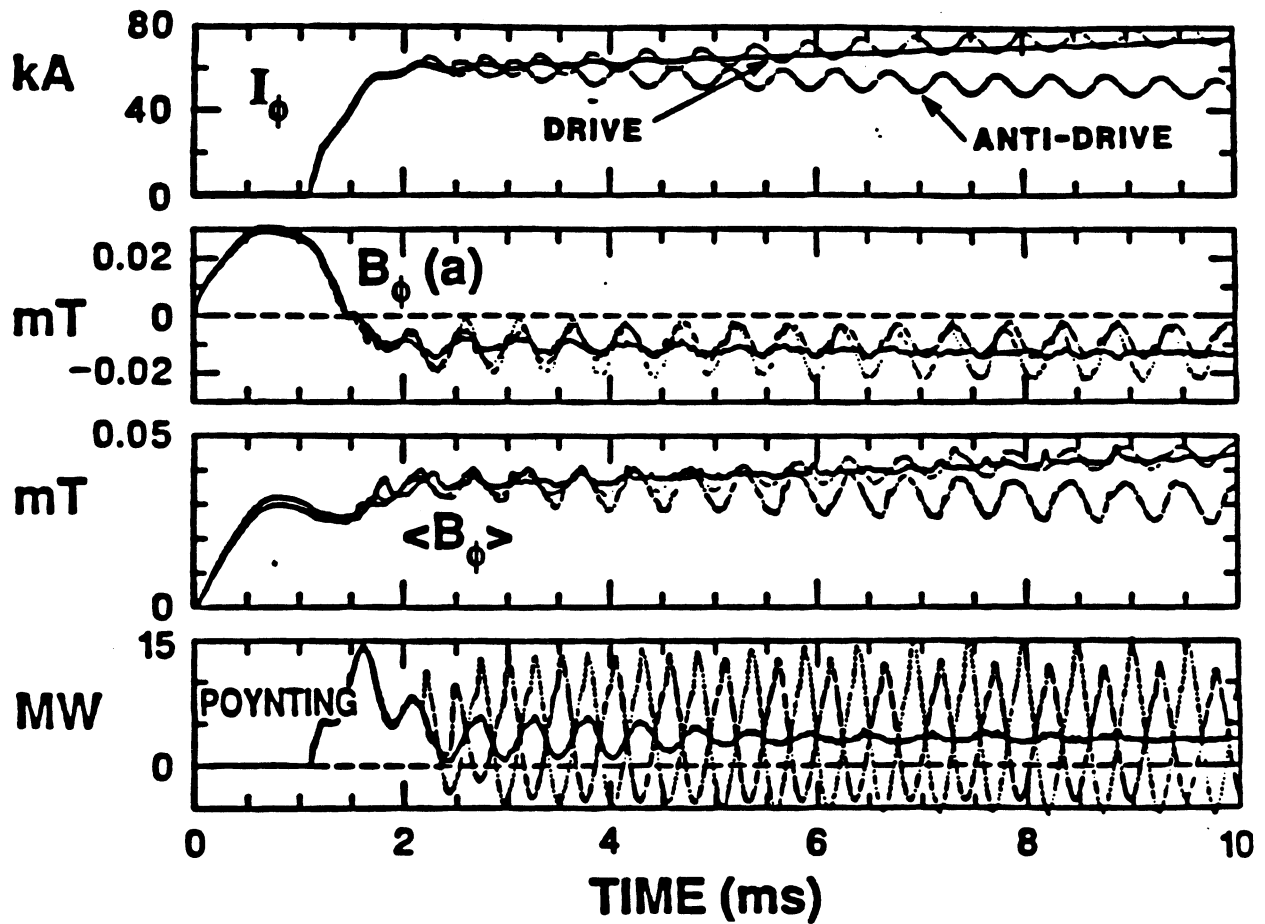


Figure 1.2-23. Low-power OFCD discharge results from Reference [10]. Shown are traces of current, edge toroidal field, toroidal flux, and Poynting vector for a standard discharge, a discharge with the optimal phase between toroidal and poloidal OFCD circuits for driving current, and a discharge with the optimal phase in the OFCD circuit for anti-drive.

In evaluating Equation 1.2-14 to determine the flux changes, field oscillations, and power flows, the relationship between  $F$  and  $\Theta$ , as well as the dependence of field and current profiles on  $\Theta$  in order to determine  $L_p$  and  $R_p$ , must be determined. A 1-D MHD model together with the  $\mu$ ,  $n$ , and  $T$  profiles (Equations 1.2-8 through 1.2-10) are used to produce the  $F$ - $\Theta$  curve and to compute  $L_p$  and  $R_p$  as functions of  $\Theta$ . The algorithm for finding a steady-state solution to Equation 1.2-14 fixes the value of  $\delta\phi/\phi_o$  and iterates on the value of  $\delta V_\phi/V_{\phi_o}$  of a sinusoidal toroidal-flux function until the plasma-current solution becomes periodic, *i.e.*,  $I_\phi(t) = I_\phi(t + 2\pi/\omega)$ . The plasma current is reset to the desired value at the beginning of each simulation period. In an outer loop, the time scale is adjusted to ensure that the mean current during a period is the same as the current at the beginning of the period.

The above-mentioned algorithm requires an initial guess for  $\delta V_\phi$ . The constraint that the time-averaged helicity is constant,  $\langle dK/dt \rangle = 0$ , can be used to estimate the magnitude of the field oscillations required to sustain a given toroidal plasma current. If the ohmic dissipations for both the induced and driven cases are similar, and if the induced case is characterized by  $\phi_o$  and  $V_{\phi_o}$ , then  $\langle dK/dt \rangle = 0$  results in

$$\left(\frac{\delta\phi}{\phi_o}\right) \left(\frac{\delta V_\phi}{V_{\phi_o}}\right) \simeq -2. \quad (1.2-15)$$

Because toroidal-flux oscillations much above  $\delta\phi/\phi_o \simeq 0.05$  are expected to seriously impact the RFP configuration (*i.e.*, loss of toroidal-field reversal), the AC toroidal voltage needed to drive a DC toroidal current with  $\langle dK/dt \rangle \simeq 0$  can be  $\sim 40$  times greater than the voltage needed to sustain an inductively driven RFP.

An assessment of OFCD efficiency requires the modeling of the circuit elements external to the plasma in addition to the plasma itself. The governing matrix circuit equation is written as follows:

$$\mathbf{L} \frac{d}{dt} \mathbf{I} + \mathbf{R} \mathbf{I} = \mathbf{V}, \quad (1.2-16)$$

where  $\mathbf{I}$  and  $\mathbf{V}$  are column vectors representing the currents and voltages, respectively,  $\mathbf{R}$  is a diagonal matrix of resistances,  $\mathbf{L}$  is the inductance matrix, and the inductances are assumed invariant in time. Separate matrix circuit equations are derived for poloidal,  $\theta$ , and toroidal,  $\phi$ , current paths and are labeled according to the current direction,  $\theta$  and  $\phi$ , respectively. The voltage on the TF coil is determined by requiring that the toroidal field at the plasma surface be produced by all the elements with continuous poloidal current paths. The voltage of the OH coil is derived from knowing the solution for  $I_\phi$  from Equation 1.2-14. In the case of the EF coil, the voltage is maintained at a constant value

corresponding to the mean equilibrium field. The EF trim-coil voltage is determined by requiring the trim coil to track the oscillating equilibrium-field requirement of the plasma. The current vector  $\mathbf{I}$  in Equation 1.2-16 has components corresponding to each circuit element. The plasma current in the toroidal-circuit version of Equation 1.2-16 is the  $I_\phi$  solution to Equation 1.2-14. The plasma current in the poloidal-circuit version of Equation 1.2-16 is a model artifact required for inductive transfer of magnetic-field energy to the plasma from the external elements and resembles a plasma skin current (physically, it is not a skin current).

A shell model is used to determine the inductances and the resistances used in the respective matrices. The circuit elements simulated are the plasma, first wall, the TF coils, a portion of the windings of the OH coils, a primary EF-coil set, a secondary EF trim-coil set, and the reflector and shield for the TITAN-I and the blanket for the TITAN-II. The TF-coil set for TITAN-I has been separated into six individual elements that physically correspond to the six radial rows of integrated-blanket-coil (IBC) tubes. This configuration is used because the tube rows are connected electrically in parallel and the current penetration skin depth at the frequencies considered ( $\sim 25$  Hz) is comparable to the tube diameter. Passive circuit elements with resistive breaks or gaps were modeled as consisting of an inner and outer current path and both toroidal and poloidal current flows were taken into account (Section 7).

Simulation of the TITAN-I OFCD with a continuous first wall showed that  $\sim 120$  MW of power is dissipated in the first wall. Efforts to reduce the dissipated power initially focused on varying the toroidal-flux swing,  $\delta\phi/\phi_o$ , and the drive frequency,  $f$ . It was found that the operating window for  $\delta\phi/\phi_o$  is bounded above and below for both frequencies because of a loss of field reversal. The upper bound is the result of too large oscillations in  $\phi$  at a shallow reversal ( $F = -0.1$ ). The lower bound is the result of too large oscillations in  $I_\phi$  ( $\geq 5\%$ ) and, hence,  $\Theta$ . This lower bound causes a loss of field reversal because adherence to an  $F$ - $\Theta$  curve is strictly enforced. The  $\delta\phi/\phi_o$  operating window shrinks with lower frequencies until completely disappearing at frequencies between 5 and 10 Hz. A drive frequency of 25 Hz was selected for the TITAN study because the  $\delta\phi/\phi_o$  operating window is relatively unrestricted in this region, power supplies at 25 Hz are commercially available, and the effect of frequency on dissipated power has nearly saturated at 25 Hz.

The OFCD simulations indicate that the only way to emulate an increased first-wall resistance while maintaining wall stabilization is by using gaps or insulating breaks. The effect of the first-wall gap is primarily a reduction of the dissipated power in the first wall and secondarily a reduction of the coil powers. The net effect of gaps is to increase the current-drive efficiency by a factor of 3.7 over that for a continuous (without gaps) first

wall. It was also found that using the EF trim coils to maintain the plasma equilibrium would result in a large reduction of  $\sim 7$  GW in the EF-coil reactive power and the power-supply cost.

The TITAN-I and TITAN-II OFCD design points summarized in Table 1.2-IX were selected from the middle of the  $\delta\phi/\phi_0$ -operating window to provide a maximum safety margin against the accidental loss of field reversal. The gaps in both TITAN-I and TITAN-II first walls must hold off  $\sim 2$  V in order to maintain the electrical-break effect; this condition could be met by using (1) an  $\sim 1$ -mm-wide vacuum gap or (2) an even thinner amount of electrical insulator. The small-amplitude ( $< 2\%$ ) plasma-current oscillations should not adversely affect the plasma stability or transport.

The power dissipated in the first wall of each design (with breaks) is the same because the first walls are physically the same. The power dissipated in the TITAN-I reflector and shield (R/S) is larger than in the TITAN-II blanket primarily because of a lower R/S resistance. Because the TITAN-I R/S is positioned outside of the TF IBCs, none of the poloidal-circuit elements couple to the R/S and no power is dissipated in the R/S from that circuit. The dissipated and reactive powers in the coils of the toroidal circuit (*i.e.*, OH, superconducting EF, and trim coils) are slightly larger for TITAN-II because the toroidal-circuit blanket inductance is larger for TITAN-II (*i.e.*, the blanket is less transparent to the power flowing through its surfaces).

The voltage waveforms for the TITAN-I and TITAN-II OFCD design points are shown in Figure 1.2-24. These waveforms indicate that the much larger TITAN-II blanket resistance causes a large ( $\sim 100$  V) induced voltage, which is not found in the TITAN-I design. The TITAN-II voltage waveforms more prominently display a phenomena common to both designs: the  $90^\circ$  phase shift between the toroidal and poloidal plasma voltages ( $V_\phi$  and  $V_\theta$ , respectively), which yields the optimal current-drive efficiency, is generated by a different phase shift between the toroidal ( $V_{OH}$  and  $V_{SEF}$ ) and poloidal ( $V_{TF}$ ) coil voltages. The phase shift between the coil voltages is dependent upon  $\delta\phi/\phi_0$  in addition to the TF-coil position.

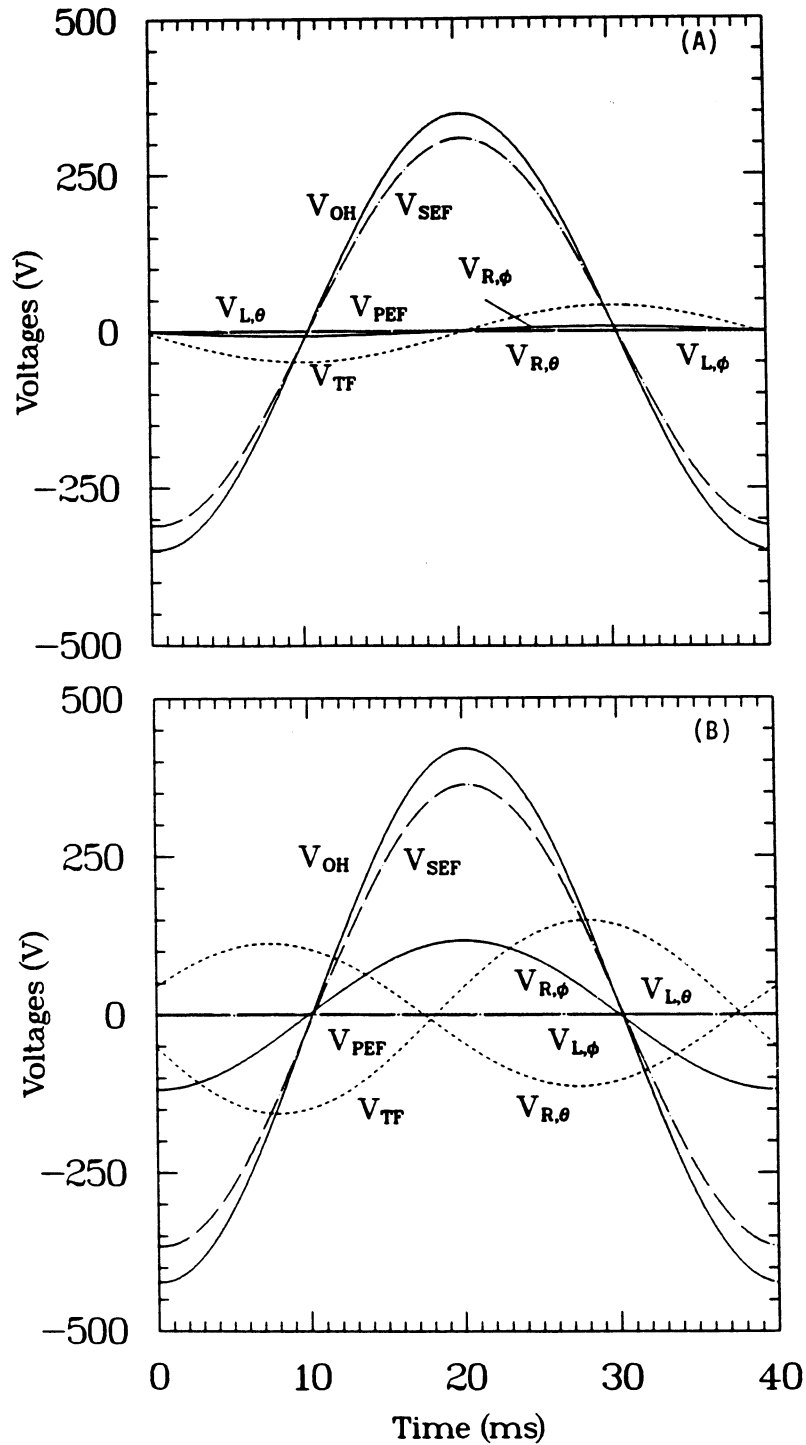
The current waveforms for the TITAN-I and TITAN-II OFCD design points are shown in Figure 1.2-25. Even though the superconducting EF coils are maintained at a constant (albeit negligible) voltage, the current in these coils oscillates with an amplitude of  $\leq 2$  MA. Furthermore, the EF-coil current oscillations are out of phase with the trim- and OH-coil oscillations. The TITAN-I and TITAN-II TF-coil current waveforms are nearly the same, even though the voltage waveforms are quite different because the plasma-current and, hence, the toroidal-field waveforms are required to be identical and because

Table 1.2-IX.  
COMPARISON OF OFCD IN TITAN DESIGNS

	TITAN-I	TITAN-II
Average plasma current, $I_\phi$ (MA)	17.82	17.82
Drive frequency, $f$ (Hz)	25.	25.
Toroidal-flux swing, $\delta\phi/\phi_0$	0.035	0.035
$\Theta$ variation	1.499 – 1.616	1.499 – 1.616
$F$ variation	-0.032 – -0.173	-0.032 – -0.173
Toroidal (poloidal) circuit power (MW):		
Plasma Poynting power, $P_P^*$	3959.99 (247.31)	3959.99 (247.31)
Plasma dissipation, $P_\Omega$	28.55 ( 0. )	28.55 ( 0. )
First-wall dissipation, $P_{FW}$	0.00 ( 0.01)	0.00 ( 0.01)
Blanket dissipation, $P_B$	1.04 ( 0. )	0.01 ( 0.17)
Terminal reactive power, $P_i^*$ (MW):		
TF coils	503.88	1413.77
OH coils	74.92	101.99
EF coils	~ 0.	~ 0.
Trim coils	113.44	147.16
Coil dissipation, $P_H$ (MW):		
TF coils	47.38	11.44
OH coils	0.13	0.17
EF coils	~ 0.	~ 0.
Trim coils	1.95	2.49
Real (lost) terminal power, $P_T$ (MW):		
TF coils	74.00	38.23
OH coils	1.62	1.15
EF coils	~ 0.	~ 0.
Trim coils	3.44	3.46
TF-coil DC power, $P_{H,\theta}^{SS}$ (MW)	29.15	9.34
Power-supply dissipation, $P_{PS}$ (MW) <sup>(a)</sup>	6.92	15.34
Total dissipation, $P_D$ (MW)	85.93	58.19
Current-drive power, $P_{CD}$ (MW)	56.83	48.85
Efficiency, $I_\phi/P_{CD}$ (A/W) <sup>(b)</sup>	0.33	0.36

(a) Assuming the power supplies are 99% efficient ( $Q_{PS} = 100$ ).

(b) Based on the total power consumed including driver efficiency and transmission losses.



**Figure 1.2-24.** The voltage waveforms for TITAN-I (A) and TITAN-II (B) design for one OFCD period. The voltages across OH coils ( $V_{OH}$ ), trim coils ( $V_{SEF}$ ), TF coils ( $V_{TF}$ ), first wall ( $V_{L,\phi}$  and  $V_{L,\theta}$ ), and across TITAN-I reflector and shield or TITAN-II blanket ( $V_{R,\phi}$  and  $V_{R,\theta}$ ) are shown.

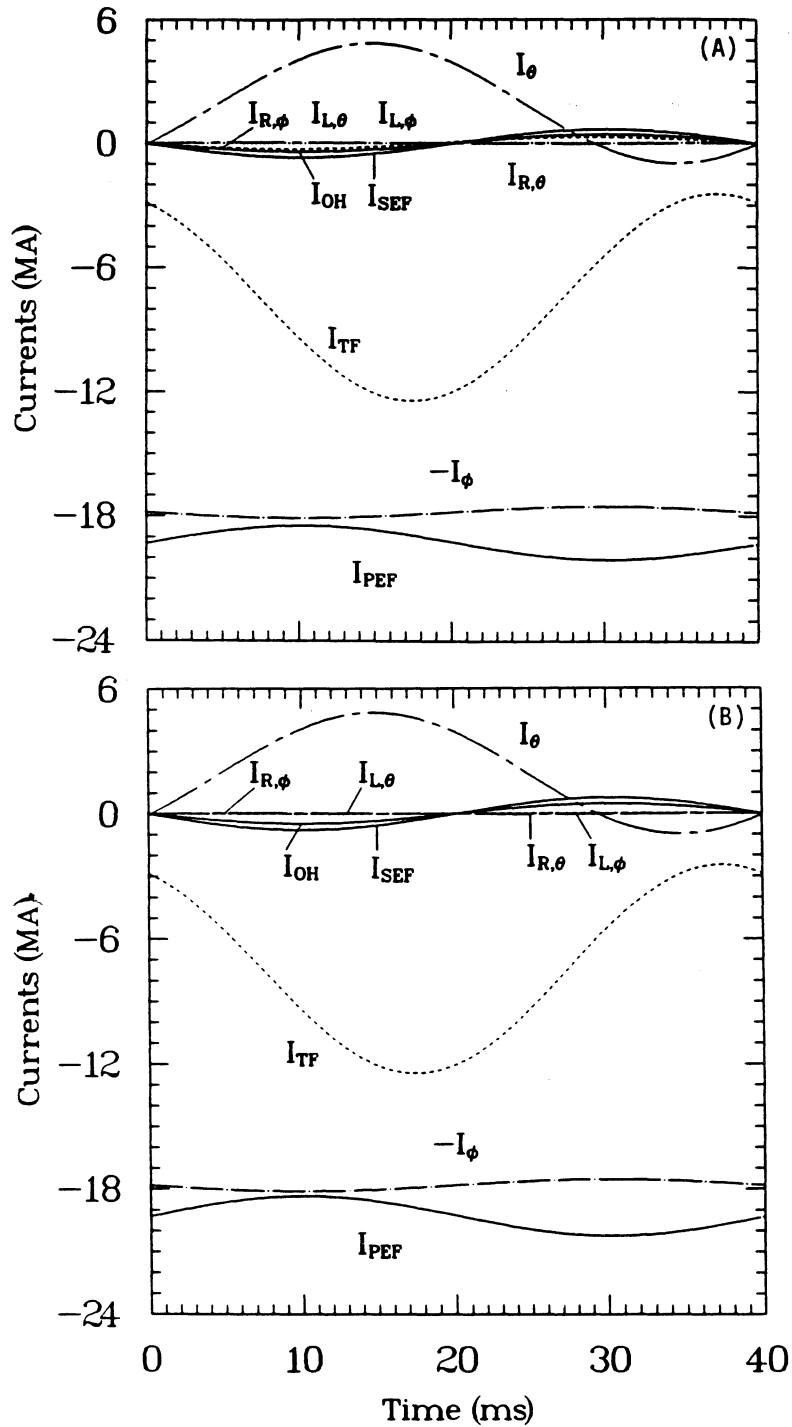


Figure 1.2-25. The current waveforms for TITAN-I (A) and TITAN-II (B) design for one OFCD period. The currents in the OH coils ( $I_{OH}$ ), trim coils ( $I_{SEF}$ ), superconducting EF coils ( $I_{PEF}$ ), TF coils ( $I_{TF}$ ), first wall ( $I_{L,\phi}$  and  $I_{L,\theta}$ ), and in TITAN-I reflector and shield or TITAN-II blanket ( $I_{R,\phi}$  and  $I_{R,\theta}$ ) are shown.

the toroidal field is determined primarily by the TF coils (the toroidal field is affected only slightly by the first wall and blanket).

Whereas the TITAN-II TF-coil current density is uniform, the TITAN-I TF-coil current density has a radial variation. The expected exponential decay of the current radially through the TF IBC tube bank occurs because the current-penetration skin depth is greater than the coil radial build. In addition the current from radial row to radial row incurs a phase shift. This radial non-uniformity of the TF IBC current gives rise to the differences in the TITAN-I and TITAN-II TF-coil dissipated powers. The TITAN-II design ultimately dissipates less power in the first wall, blanket, and coils than TITAN-I, but has a larger terminal reactive power because of the different TF-coil designs. When the efficiency of the power supplies ( $Q = 100$  assumed) is included in the current-drive efficiency, both designs operate at comparable efficiencies of  $\sim 0.35$  A/W. This frequency is based on the total power supplied to the system, including driver efficiency and transmission losses.

#### 1.2.8. Summary and Key Technical Issues

The TITAN plasma simulations incorporate the latest understanding and models developed for reversed-field pinches, as summarized in Section 2; in several cases, new and improved models had to be developed for the TITAN study. More detailed descriptions of the theoretical and experimental aspects of the RFP confinement concept are given in Section 2, and References [6,38,39] and the references contained therein. Because of the relative lack of theoretical and experimental data bases for RFPs, the sensitivity of the design point to various physics assumptions has also been investigated (Section 3.4.2). A detailed description of the plasma engineering for the TITAN reactors is given in Sections 4 through 7. A detailed description of the necessary R&D areas for compact RFP reactors has also been produced and is reported in Section 8.

The TITAN plasma simulations include analyses of the equilibrium and stability of the TITAN plasma (Section 5). These equilibrium analyses were performed using a large-aspect-ratio approximation. Two-dimensional equilibrium analysis, however, was also performed to substantiate the accuracy of such an approximation for the TITAN effort. The most important equilibrium and stability issue is the need for a conducting shell. The existence and role of a close-fitting conducting shell that surrounds the RFP strongly impacts all physics and engineering aspects of the design.

The TITAN magnet configuration consists of the following sets of coils: toroidal-field (TF), divertor-field (DF), and poloidal-field (PF) coils. The TITAN reactors operate

at steady state using the oscillating-field current-drive (OFCD) system. Rather than using a separate coil set, the TF, DF, and PF coils are oscillated about their steady-state currents and used as the OFCD driver coils. Separate TF-, DF-, and PF-coil designs were developed for the TITAN reactors to demonstrate that a range of designs are capable of efficient, high mass-power-density operation.

The impurity control and particle exhaust system consists of three high-recycling, toroidal-field divertors (Sections 5, 11, and 17). The TITAN designs take advantage of the beta-limited confinement observed in RFP experiments [12,13] to operate with a highly radiative core plasma, deliberately doped with a trace amount of high- $Z$  Xe impurities (Section 5). The highly radiative plasma distributes the surface heat load uniformly on the first wall ( $4.6 \text{ MW/m}^2$ ). Simultaneously, the heat load on the divertor target plates is reduced to less than about  $9 \text{ MW/m}^2$ . The ratio of impurity density to electron density in the plasma is about  $10^{-4}$ ,  $Z_{eff}$  is about 1.7, and 70% of the core plasma energy is radiated (an additional 25% of the plasma energy is radiated in the edge plasma).

The “open” magnetic geometry of the divertors (Section 4.4), together with the intensive radiative cooling, leads to a high-recycling divertor with high density and low temperature near the divertor target ( $n_e \simeq 10^{21} \text{ m}^{-3}$ ,  $T_e \simeq 5 \text{ eV}$ ) relative to the upstream separatrix density and temperature ( $n_e \simeq 2 \times 10^{20} \text{ m}^{-3}$ ,  $T_e \simeq 200 \text{ eV}$ ). The radial temperature profile is calculated to decay sharply to  $2 \text{ eV}$  near the first wall (Section 5). Negligible neutral-particle leakage from the divertor chamber to the core plasma and adequate particle exhaust are predicted. The first-wall and divertor-plate erosion rate is negligibly small because of the low plasma temperature and high density at that location.

It is found that fueling of the TITAN RFP reactor appears to be relatively straightforward. A pellet injector based on present technology can inject 2-km/s pellets past the reversal radius ( $r_r \simeq 0.55 \text{ m}$ ). Presently available injector frequencies ( $\sim 6 \text{ Hz}$ ) will have to be increased to  $\sim 25 \text{ Hz}$  for TITAN applications. The TITAN reactor will be provided with two injection systems (5 M\$ each) for redundancy.

The existing RFP experimental data base for RFP formation and start-up was reviewed in Section 2 and was then applied to the TITAN designs (Section 6.3). To summarize, the conditions for plasma breakdown and subsequent RFP formation for the reactor are expected to differ little from the conditions in present and planned RFP experiments [34]. Likewise, the conditions of the seed RFP plasma required to start up the TITAN reactor, except for plasma size, are similar to present-day RFP parameters ( $I_\phi = 0.2$  to  $0.4 \text{ MA}$ ,  $n = 1$  to  $3 \times 10^{19} \text{ m}^{-3}$ ,  $T = 0.1$  to  $0.4 \text{ eV}$ ). For the reference

formation scenario, loop voltage in the range of 200 to 500 V is necessary to ensure short formation time and acceptable resistive flux consumption and formation energy.

The ignition requirements for ohmically heated RFPs are studied (Section 6.4) in order to identify the optimum path for TITAN start-up. It was shown that the results of this analysis can be presented as the required current for power balance as a function of plasma density and temperature. Also, the resultant surface includes a "ridge" in the  $I_\phi$ - $n$ - $T$  space above which the path to ignition and burn should be located (similar to corresponding diagrams for auxiliary-heated devices where a ridge for auxiliary heating exists). The optimum ignition scenario attempts to pass over the ridge at its lowest height (saddle point). This saddle point for TITAN designs is located at  $T \simeq 7$  keV and  $n \simeq 3 \times 10^{20} \text{ m}^{-3}$  with a current of  $I_\phi \simeq 16$  MA. The TITAN start-up path through ignition and burn passes close to this saddle point. (Figure 1.2-16).

The TITAN start-up sequence (Section 6.5) through current ramp, ignition, and burn transients is chosen such that the start-up power is directly extracted from the power grid without requiring an on-site power-storage system. The evolution of the TITAN plasma during the start-up sequence is investigated by using a 0-D, profile-averaged plasma-circuit code. To summarize, the full plasma parameters can be achieved in  $< 12$  s by utilizing grid power supplies; no on-site storage facility is necessary. The TITAN PF coils are designed such that the superconducting EF coils provide an approximate equilibrium during the start-up sequence and a pair of small, normal-conducting EF trim coils maintain the exact equilibrium. Using this approach, only the power supplies for the EF trim coils have to be feedback controlled to ensure proper equilibrium.

Reversed-field-pinch discharges normally end abruptly and the plasma current decreases rapidly to zero. Current termination is a safety and economic concern because of large magnetic stored energy in the TITAN plasma. Techniques for control of current termination and plasma shutdown, leading to a "soft-landing," are discussed in Section 6.6. The preliminary simulations of the TITAN emergency shutdown procedure appear to indicate that by discharging the superconducting EF coils at the initiation of the accident, most (90%) of the stored magnetic energy is removed from the system and dumped through the discharge resistor. Only about 200 MJ of energy is transferred to the first wall in a time scale of 50 to 100 ms, resulting in an average temperature rise in the first wall of about 300 °C; therefore, failure of the first wall is not expected.

The TITAN RFP plasma operates at steady state using OFCD to maintain the 18 MA of plasma current. This scheme utilizes the strong coupling, through the plasma relaxation process which maintains the RFP profiles, between the toroidal and poloidal fields and fluxes in the RFP. Detailed plasma-circuit simulations have been performed that

include the effects of eddy currents induced in the FPC (Section 7). The calculated efficiency of the TITAN OFCD system is 0.3 A/W delivered to the power supply (0.8 A/W delivered to the plasma).

The performance projected for the TITAN reactor designs depends crucially on the physics areas. Given below are the key physics issues for the high-power-density RFP reactors and recommendations to the RFP experimental physics program.

**Confinement.** Determine spatially resolved profiles in non-transitory RFPs in order to resolve the scaling of intrinsic energy-confinement time with plasma geometry, current or current density, and  $F\text{-}\Theta$  value in hot plasmas with low values of  $\xi = v_D/v_{THe}$  and  $Z_{eff}$ . Special emphasis should be placed on investigating radiation-dominated operation and the limits of beta and intrinsic (non-radiative) confinement.

**Current drive.** Investigate both DC and AC techniques for helicity injection in hot RFPs with separatrices and minimal modulation-induced plasma-wall interaction. The impact and management of high levels of reactive power require better resolution. Other means of current drive should also be investigated.

**Impurity control.** Emphasize plasma operation with a toroidal-field separatrix in order to minimize plasma-wall interaction in a highly radiating plasma, eventually leading to high-recycling divertor operation and an easing of OFCD with a fixed separatrix position.

**Formation and start-up.** Clearly resolve the scaling of plasma resistance with current ramp rate, current, geometry, and  $F\text{-}\Theta$  values in plasmas with low values of electron streaming parameters, and minimal and/or controllable plasma-wall interactions.

Clearly, these key issues and the conditions needed and/or assumed for the compact RFP reactor designs are interrelated and symbiotic. The existence and role of a close-fitting electrically conducting shell that surrounds the RFP has strong impact on these physics issues. Hence, as a fifth, but highly integrating recommendation: resolve the need for and characteristics of a conducting shell with electrical breaks on the formation and start-up, confinement, current drive, and impurity control which represents, at present, an inadequately mapped issue for the RFP. This is an issue that the TITAN study

circumnavigated numerous times in its overall quest to resolve physics and engineering-systems issues for cost-effective and technologically attractive, high-power-density fusion reactors.

Finally, current termination is a safety and economics concern because of the large magnetic stored energy in the TITAN plasma. Experimental techniques for control of current termination and plasma shutdown, leading to a "soft-landing," especially by passive means, are essential for achieving a high degree of safety and environmental attractiveness for RFP reactors.

### **1.3. OVERVIEW OF TITAN-I FUSION POWER CORE**

#### **1.3.1. Configuration**

An overview of the TITAN-I FPC is given in Section 9 and detailed subsystem designs are given in Sections 10 through 14. The parameters of the TITAN-I reference design point, based on detailed subsystem design, are included in Appendix A and follows the DOE/OFE standard reporting format. Appendix A also includes detailed cost tables and parametric systems code predictions of subsystem parameters for comparison with DOE/OFE tables. The elevation view of the FPC is shown in Figures 1.3-1. Figures 1.1-1 and 1.1-2 show the general arrangement of the TITAN-I reactor.

One of the unique features of the TITAN-I design is that the entire FPC operates inside a vacuum tank, made possible because of the small physical size of the reactor (Figure 1.3-1). The vacuum-tank concept moves the vacuum boundary well away from the harsh radiation and thermal environment allowing for a more robust and reliable design. During maintenance of the FPC, the weld at the lid of the vacuum tank must be cut and then re-welded after the maintenance is completed. Although a design with individual vacuum ducts leading to each of the three divertor chambers was considered and is possible, remote cutting and welding of that complex geometry is expected to be much more difficult.

The TITAN-I vacuum tank also provides an additional safety barrier in the event of an off-normal incident. The entire primary-coolant system is enclosed within the containment building, which is filled with argon as a cover gas in order to reduce the probability of a lithium fire in case of major rupture of coolant pipes. Drain tanks are provided below the FPC (Figure 1.3-1) to recover and contain any lithium spilled in the vacuum tank or the reactor building. The drain-tank system connected to the vacuum

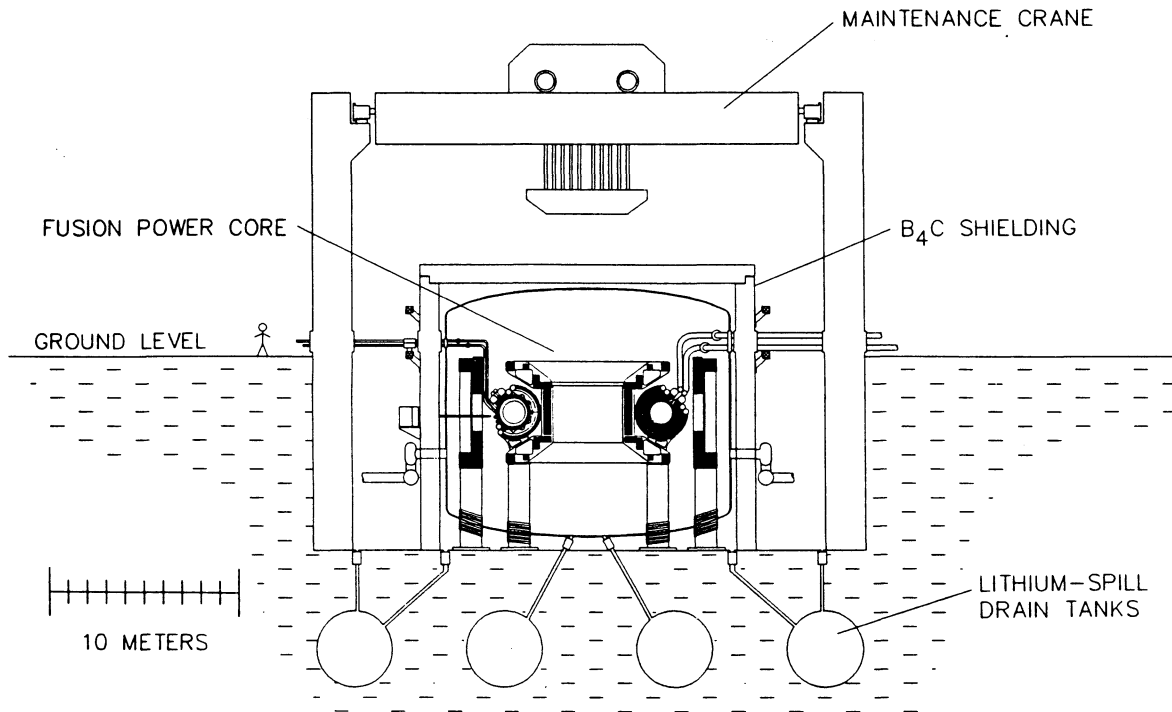


**Figure 1.3-1.** Elevation view of the TITAN-I reactor building through the reactor centerline showing the reactor vault, the maintenance crane, and the vacuum tank.

tank is evacuated during normal operation. The entire primary-coolant system is located above the FPC in order to eliminate the possibility of a complete loss-of-coolant accident (Figures 1.1-1).

The TITAN plasma is ohmically heated to ignition by using a set of normal-conducting ohmic-heating (OH) coils and a bipolar flux swing. The TITAN start-up requires minimum on-site energy storage, with the start-up power directly obtained from the power grid (maximum start-up power is 500 MW). An important safety design guideline for TITAN-I allows no water inside the containment building and vacuum vessel, in order to reduce the probability of lithium-water reactions (Section 13). As a result, the OH coils are cooled by helium gas. A pair of relatively low-field superconducting equilibrium-field (EF) coils produce the necessary vertical field and a pair of small, copper EF trim coils provide the exact equilibrium during the start-up and OFCD cycles. The poloidal-field-coil arrangement allows access to the complete reactor torus by removing only the upper OH-coil set.

Another unique feature of the TITAN-I design is that the divertor and the toroidal-field (TF) coils are based on the integrated-blanket-coil (IBC) concept [14]. The IBC concept utilizes the poloidally flowing lithium coolant of the blanket as the electrical conductor for the divertor and TF coils. Although lithium is about 20 times more resistive than copper, the low toroidal-field requirement of RFPs, combined with the large cross-sectional area available to the IBC, results in acceptable power requirements for TF and divertor coils. The joule heating in the TITAN-I divertor and TF coils are, respectively, 120 and 24 MW. The IBC concept reduces the need to shield the coils significantly, improves neutronics efficiency and energy recovery, reduces the number of components in the FPC, reduces the toroidal-field ripple, and allows direct access to the blanket and shield assemblies, thereby easing the maintenance procedure.

Poloidal cross sections of the TITAN-I FPC through a divertor module and through a blanket section are shown, respectively, in Figures 1.3-2 and 1.3-3. The geometry, size, and configuration of the first wall, blanket, shield and the associated coolant channels are established primarily by thermal-hydraulic, structural, and neutronics considerations. The dominant magnetic field at the plasma edge (or first wall) in the RFP is poloidal. Since, the TITAN-I FPC is cooled by lithium, the coolant channels in the first wall and blanket are aligned with the poloidal field to minimize the induced MHD pressure drops.

The TITAN reactors operate with a highly radiative core plasma in order to distribute the plasma heat load uniformly on the first wall. Simultaneously, the heat load on the divertor target plates is reduced to manageable levels. As a result, the first wall intercepts the radiation heat flux of about  $4.6 \text{ MW/m}^2$ . The TITAN-I first wall is made of a bank of circular tubes. Tubular coolant channels with circular cross sections are suitable for the first wall, since a circular tube has the best heat-transfer capability (highest Nusselt number) and highest strength. In addition, tubes are easy to manufacture with small tolerances in size and wall thickness. To adjust for the shorter toroidal length on the inboard as compared to the outboard, the first-wall tubes slightly overlap on the inboard side of the torus, as is shown in Figure 1.3-4. Consequently, two sets of coolant tubes are used; one set has a slightly larger poloidal diameter than the other. The inside diameter and wall thickness of the first-wall coolant tubes are, respectively, 8 and 1.25 mm. The inside diameter of the first-wall tubes reflects a compromise between the total number of coolant tubes and the heat-transfer coefficient; reducing the diameter increases the number of tubes, which may result in a lower reliability but increases the heat-transfer coefficient. The tube wall thickness of 1.25 mm includes a 0.25-mm allowance for erosion (the first-wall erosion is estimated to be negligible).

The blanket and shield coolant channels are designed with the consideration of heat transfer, blanket energy multiplication, tritium breeding, and shielding requirements. The overall thickness of the blanket and shield is 75 cm. The 28-cm-wide IBC zone is located 1 cm behind the first wall and consists of 6 rows of tubular coolant channels with an inside diameter of 4.75 cm and a wall thickness of 2.5 mm. The primary reason for using tubular coolant channels for the IBC zone, which results in more void, is to reduce the number of load-bearing welded joints (associated with using square ducts) near the plasma. The IBC coolant channels have varying cross sections (Figure 1.3-4) in order to minimize the void fraction of this zone. As a result, the IBC zone consists of 18% structure, 72% lithium, and 10% void by volume.

The 45-cm-thick hot shield is located 1 cm behind the IBC and has two zones. The first zone is 30 cm thick and consists of 5 rows of square coolant channels with outer dimensions of 6 cm and a wall thickness of 5 mm. The inside corners are rounded and have a radius-to-wall-thickness ratio of unity. The structure volume fraction is 30%, the coolant volume fraction is 70%, and there is no void. The second zone of the hot shield is 15 cm thick and consists of 4 rows of rectangular channels with thick walls to increase the structure volume fraction in this zone. The structure volume fraction is 90% and the coolant volume fraction is 10%. The channels have outer dimensions of 11.25 cm by 3.75 cm and a wall thickness of 16.25 mm.

The coolant flow in both first wall and blanket are single pass and in the poloidal direction. Double-pass poloidal flow, however, is used in the hot shield. Lithium flows in through the first three square channels of the hot shield, makes a 180° turn at the inboard side, and exits through the last two square channels and the rectangular channels of the hot shield. This double-pass flow pattern allows the hot shield to be constructed of two separate units. During the annual FPC maintenance, the top half of the shield will be removed so that the torus assembly (including the first-wall, IBC, and divertor sections) can be replaced. The estimated lifetime of the shield component is four full power years and, therefore, this portion can be reinstalled after the completion of the annual maintenance.

The lifetime of the TITAN-I reactor torus (including the first wall, blanket, and divertor modules) is estimated to be in the range of 15 to 18 MWy/m<sup>2</sup> with the more conservative value of 15 MWy/m<sup>2</sup> requiring the change-out of the reactor torus on a yearly basis for operation at 18 MW/m<sup>2</sup> of neutron wall loading at 76% availability. The lifetime of the hot shield is estimated to be five years. To reduce the rad-waste, therefore, the TITAN-I hot shield is made of two pieces; the upper hot shield is removed during the maintenance procedures and then reused following replacement of the reactor torus.

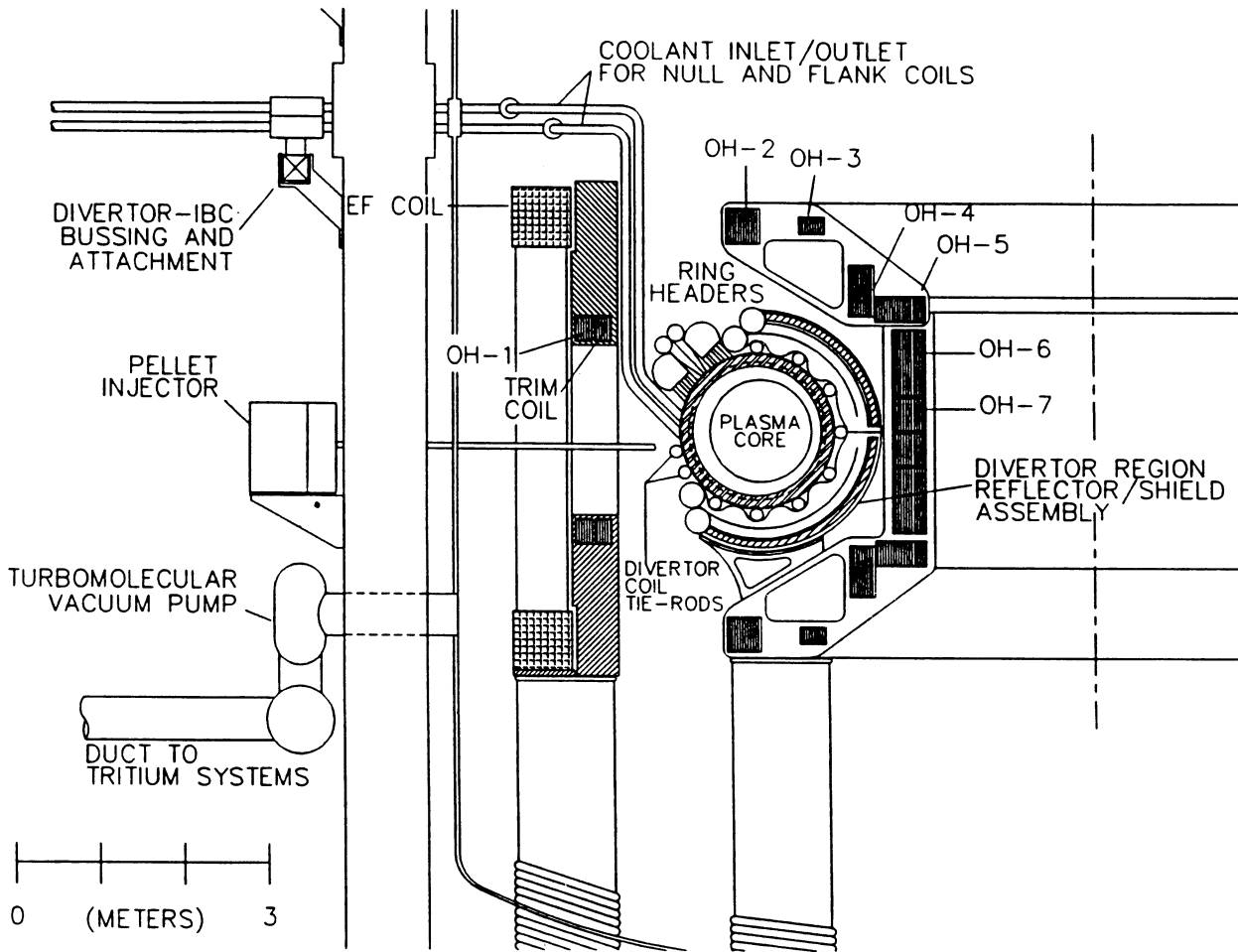


**Figure 1.3-2.** Poloidal cross section of the TITAN-I FPC through one of the divertor modules.

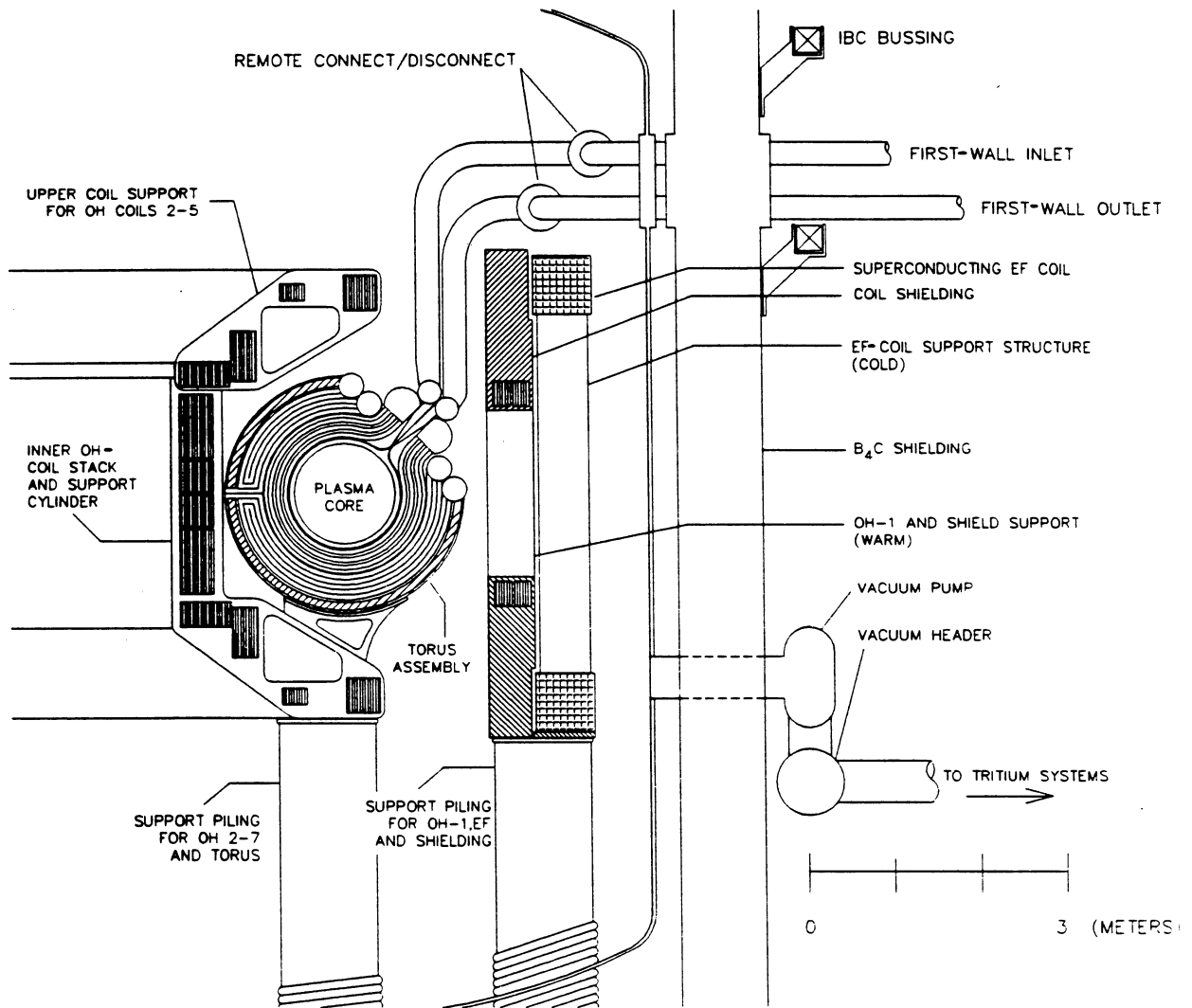
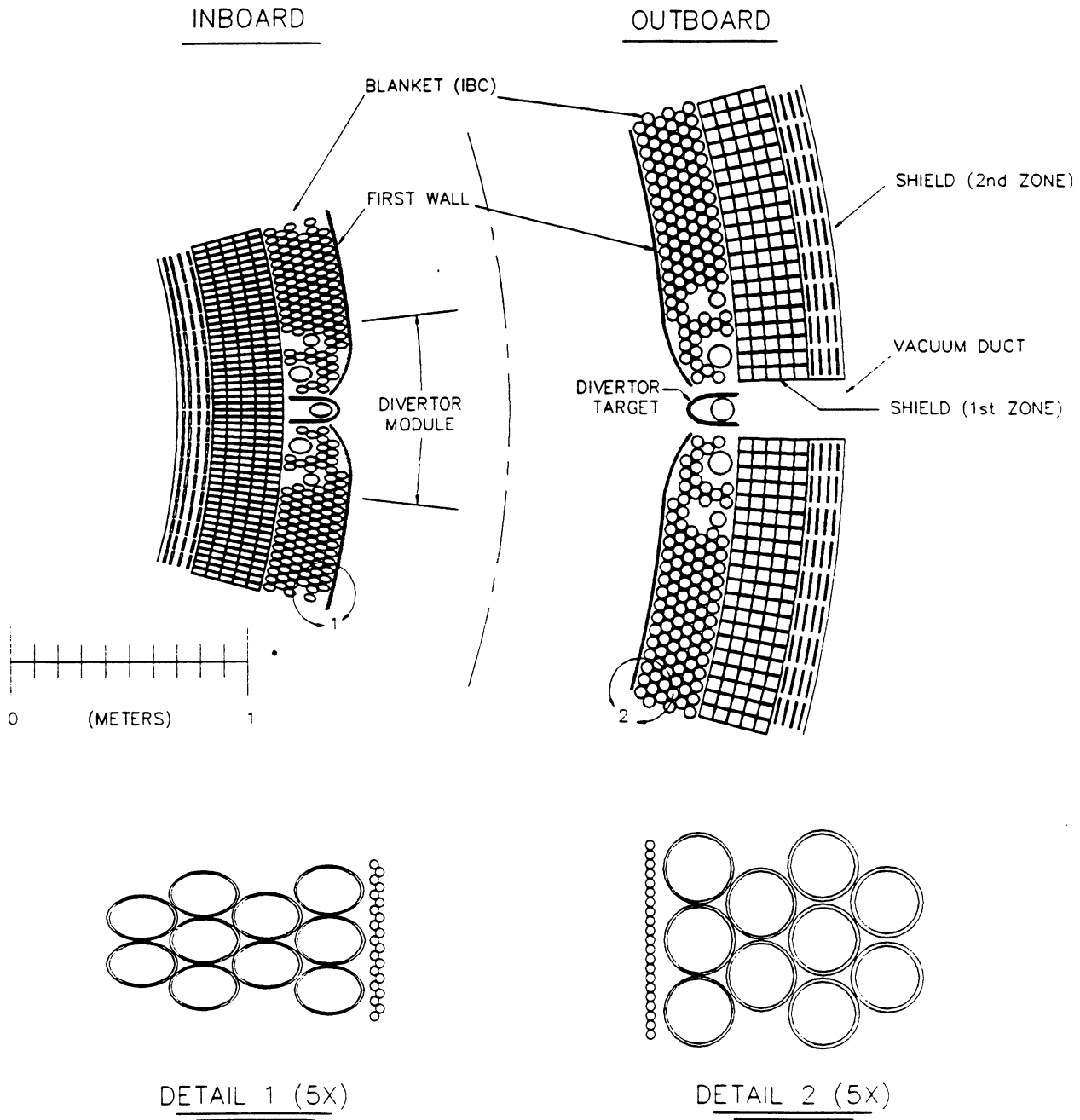


Figure 1.3-3. Poloidal cross section of the TITAN-I first-wall and blanket coolant channels.



**Figure 1.3-4.** Horizontal, mid-plane cross section of the TITAN-I FPC through blanket and divertor regions.

### 1.3.2. Materials

The advantage of vanadium-base alloys over others for fusion-reactor structural materials has been pointed out in previous publications [65,66]. In particular, when compared with ferritic-steel alloys, vanadium-base alloys exhibit better physical, mechanical, and nuclear properties. For example, compared to HT-9, vanadium-base alloys have a higher melting temperature, a lower thermal expansion coefficient, and a lower density. Furthermore, compared to ferritic alloys at  $1 \text{ MW/m}^2$  of neutron wall load, vanadium-base alloys have about one-half the nuclear-heating rate ( $\sim 25 \text{ W/cm}^3$ ), about a third of the helium-generation rate ( $\sim 57 \text{ He-appm/y}$ ), about half the hydrogen-production rate ( $\sim 240 \text{ H-appm/y}$ ), and lower long-term afterheat [65].

The high melting temperature of vanadium alloys ( $T_m = 1890^\circ\text{C}$ ) has significant bearing on safety related issues. The higher ultimate tensile strength ( $\sigma_u \sim 600 \text{ MPa}$  at  $600^\circ\text{C}$ ), the lower expansion coefficient, and the slightly higher thermal conductivity of vanadium-base alloys are reflected in higher thermal stress factors when compared to HT-9 [65]. The thermal stress factor is a measure of heat load capability. The high  $T_m$  coupled with a high thermal stress factor, promises high operating-temperature and high neutron-wall-loading capabilities. High  $T_m$  combined with a low helium-production rate is also desirable for fusion reactor materials, since below  $\sim 0.5T_m$  (in K), strength and ductility are retained and fracture remains transgranular [67] ( $0.5 T_m$ : vanadium  $\simeq 1082 \text{ K}$ , HT-9  $\simeq 846 \text{ K}$ ). Because helium embrittlement is directly related to the helium production rate, a low helium generation rate in vanadium-base alloys is a very favorable characteristic.

From the three candidate vanadium-base alloys, V-3Ti-1Si is chosen as the primary structural material for TITAN-I, primarily because of its irradiation behavior. It outperforms V-15Cr-5Ti and VANSTAR considering helium embrittlement, irradiation hardening, and swelling after exposure to a damage dose of 40 dpa by fast neutrons. However, V-3Ti-1Si has the lowest thermal-creep resistance of the three alloys (Section 10.2.1).

The effects of gaseous transmutations (*i.e.*, hydrogen and helium) on the mechanical properties of vanadium-base alloys were considered. Based on extrapolation of the limited available data to TITAN-I operating conditions, irradiation hardening and helium and hydrogen embrittlement of V-3Ti-1Si set an upper lifetime limit of approximately  $18 \text{ MWy/m}^2$  for the TITAN-I first wall. Irradiation-induced swelling of the V-3Ti-1Si alloy was also investigated and it was concluded that swelling would be negligible for the lifetime of the TITAN-I first wall (Section 10.2.1).

The modified-minimum-commitment method (MMCM) [68] was used to extrapolate the creep-rupture data and to establish the creep behavior during normal and off-normal operating conditions (Figure 1.3-5). From the limited creep data, it appears that V-3Ti-1Si will be able to operate satisfactorily at elevated temperatures (700°C). To include the effects of the irradiation hardening, helium-embrittlement data were used to estimate the maximum allowable design stress based on a 2/3 creep-rupture-stress criterion (Section 10.2.1). Further creep-rupture experiments are needed to develop more precise creep-rupture models for V-3Ti-1Si.

Compatibility of the vanadium-base alloys with lithium coolant was investigated. Recent test results were used to establish the anticipated degree of lithium attack on the V-3Ti-1Si alloy. Various lithium-attack processes were examined with particular attention given to the interaction between vanadium and non-metallic impurities such as oxygen, nitrogen, carbon, and hydrogen. The limited available data does indicate the possibility of a self-limiting corrosion rate on V-3Ti-1Si because of the formation of complex vanadium-titanium-nitride surface layers (Section 10.2.2). The effects of a bi-metallic loop containing liquid lithium were also investigated. Low-carbon, titanium-stabilized ferritic steel exhibits good resistance against lithium corrosion (Section 10.2.2).

In the TITAN-I design, the liquid-lithium coolant flows at a high velocity of 21 m/s in the first-wall channels. The effects of velocity on corrosion rate are complex and depend on the characteristics of the metal and the environment. Velocity affects corrosion by two distinct mechanisms: agitation of reaction constituents can increase reaction rates; and increasing momentum of fluid particles can lead to an increase in wear (*i.e.*, erosion). Increased reaction rates are generally found in aqueous solutions, where the concentration of cations and anions play a large role in corrosion rates. In general, liquid metals do not interact chemically with solid surfaces, therefore, the effects of velocity on corrosion rates of vanadium alloys in a liquid-lithium environment fall mostly into the second category.

Wear by erosion can be caused by intense pressure or shock waves traveling in the fluid. A literature search regarding erosion by liquid lithium showed that this issue has not been investigated in any detail, specifically for vanadium alloys. Most of the research regarding erosion deals with water-steel systems, and particularly distinguishes between particle-free or particle-containing water or slurry. From a very limited set of data on erosion of refractory metals by high-velocity liquid lithium and from the water-steel experience, it seems that lithium velocity of 20 to 25 m/s should not introduce unacceptable erosion rates (Section 10.2.2).

In TITAN-I reactor, electrically insulating materials are not used in direct contact with coolant; therefore coolant compatibility is not a major issue in selecting an insulating

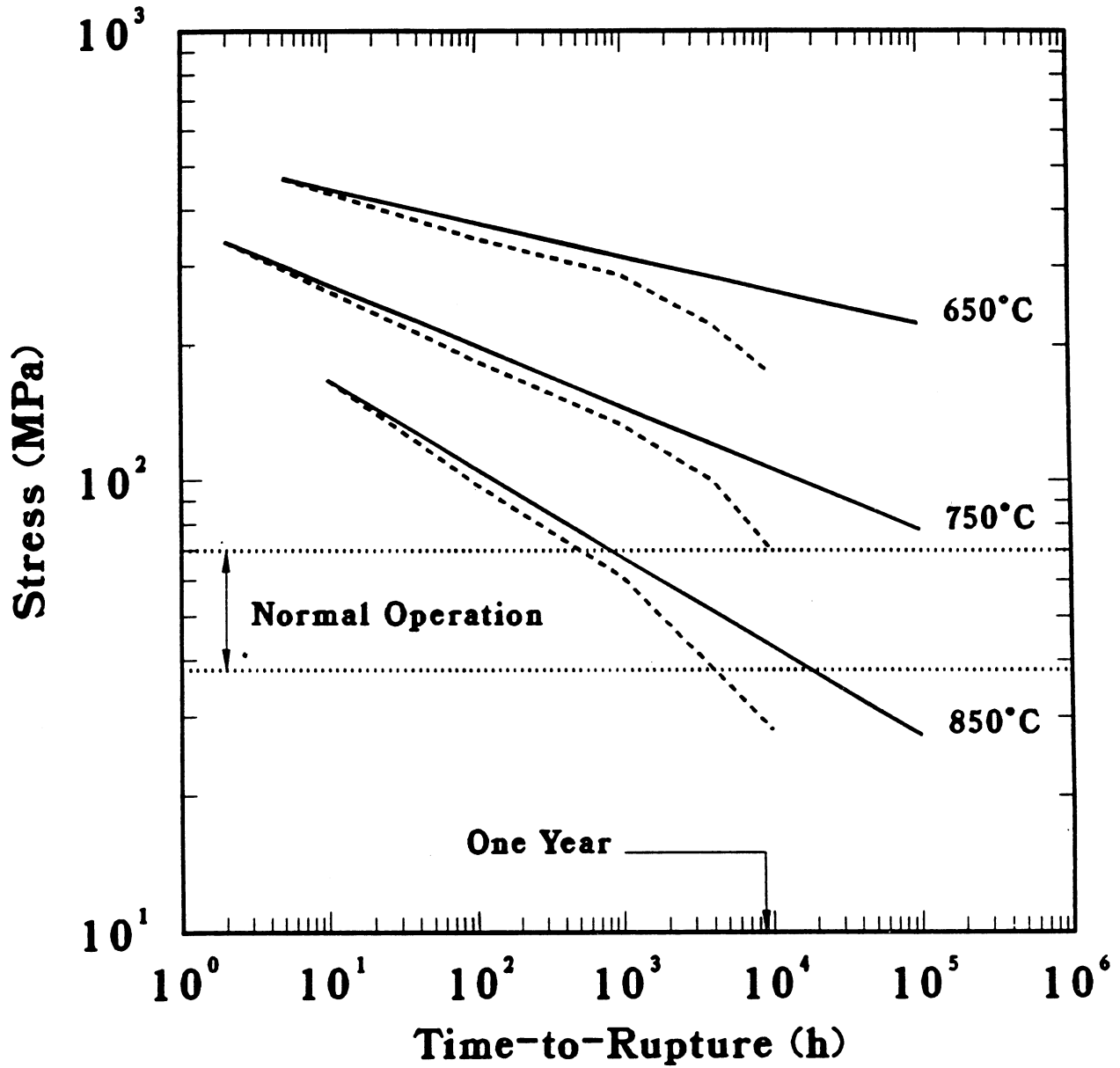
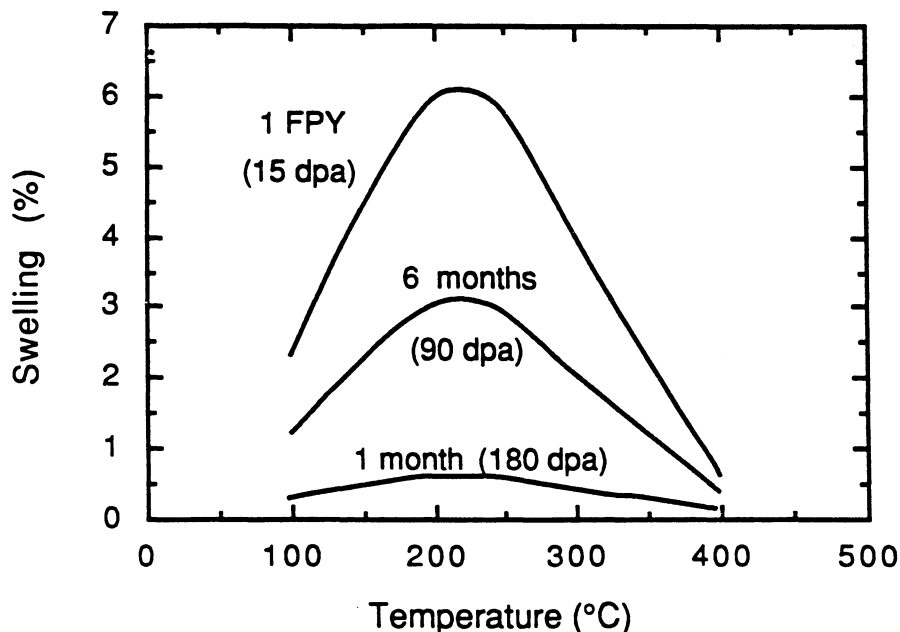


Figure 1.3-5. Creep-rupture-stress curves for V-3Ti-1Si at various temperatures estimated by modified-minimum-commitment method. Solid lines represent the creep behavior of unirradiated and dashed lines that of irradiated V-3Ti-1Si alloy. Also shown is the expected stress range during the normal operation of the TITAN-I design.

material. The selection criteria is based primarily on satisfying minimum irradiation-induced swelling, retention of strength, and minimum radiation-induced conductivity. Organic insulating materials generally do not meet high temperature requirements and suffer from rapid degradation of electrical resistivity when exposed to ionizing radiation. Ceramic insulating materials, on the other hand, possess high melting or decomposition temperatures ( $> 2000^{\circ}\text{C}$ ).

Spinel ( $\text{MgAl}_2\text{O}_4$ ) has been chosen as the primary electrical insulating material for the TITAN-I design, based on excellent resistance to radiation-induced swelling and retention (or increase) of strength (Section 10.2.3). A phenomenological swelling equation was developed as a function of temperature and damage dose. Figure 1.3-6 shows the estimated swelling of spinel at the first wall or divertor of TITAN-I as a function of temperature and exposure time at  $18\text{ MW/m}^2$  of neutron wall load. This swelling curve shows that operating spinel below  $150^{\circ}\text{C}$  or above  $300^{\circ}\text{C}$  ensures low swelling rates ( $< 5\%$ ). High operating temperatures may ensure a low swelling rate but could bring about dielectric breakdown of the insulator. Low-temperature operation ( $< 150^{\circ}\text{C}$ ) is, therefore, suggested (Section 10.2.3).



**Figure 1.3-6.** Swelling of spinel as a function of dpa (or exposure time under  $18\text{ MW/m}^2$  of neutron wall loading) and temperature.

### 1.3.3. Neutronics

The neutronics design of the blanket and shield for the TITAN reactors is unique because of the high neutron wall loading ( $18 \text{ MW/m}^2$ ). The other unique aspect of the TITAN reactors is the use of normal-conducting coils in the toroidal-field, divertor, and ohmic-heating (OH) magnets. The neutron-fluence limit of the TITAN-I OH magnets is set by the spinel-insulator lifetime and is 3 to 4 orders of magnitude larger than that of a superconductor magnet ( $1 \times 10^{23} \text{ n/m}^2$ ) [69]. The use of normal-conducting coils with ceramic insulators implies a 0.6 to 0.8 m reduction in the shielding space, and helps maintain the compactness of the FPC design.

Tritium breeding, blanket energy multiplication, afterheat, radiation damage to the structural materials and the OH magnets, annual replacement mass (and cost) of blanket and shield, and the waste-disposal ratings are some of the important parameters that were considered for the neutronics optimization of the TITAN-I design. Neutronics calculations were performed to investigate each of the above parameters based on a 1-D blanket and shield model in a cylindrical geometry, with the center of the poloidal cross section of the plasma located on the centerline of the cylinder. The neutron and gamma-ray transport code, ANISN [70], is used with the cross-section library ENDF/B-V-based MATXS5, processed with the NJOY system at Los Alamos National Laboratory [71].

Scoping calculations were performed for several combinations of blanket and shield thickness with varying amount of structure and different levels of  $^6\text{Li}$  enrichment in the lithium coolant (Section 10.3). It was found that:

1. Most of blankets considered achieved an adequate tritium-breeding ratio ( $\text{TBR} > 1.2$  from 1-D full-coverage calculations). Enrichment level of  $^6\text{Li}$  can be used to control the TBR.
2. Manganese stainless-steel shield can increase the blanket energy-multiplication ratio but would impose a potential safety problem because of higher levels of decay afterheat.
3. The energy-multiplication ratio for blankets with a vanadium shield ranges from 1.1 to 1.2. Afterheat levels, however, are considerably lower than those with a manganese shield.
4. A highly enriched  $^6\text{Li}$  coolant (75%) reduces the afterheat level by a factor of  $\sim 8$  for about one hour after shutdown.

5. The atomic displacement in the shield and magnets decreases dramatically as the  ${}^6\text{Li}$  enrichment increases which reduces the annual replacement mass.

The neutronics scoping studies resulted in the reference blanket and shield design of the TITAN-I illustrated in Figure 1.3-7. The neutronics performance of the reference design with a vanadium-alloy shield is given in Table 1.3-I. The tritium-breeding ratio is 1.33 and the total nuclear heating is 16.05 MeV per DT neutron resulting in a blanket energy multiplication of 1.14. The maximum fast-neutron fluence at the OH magnet after 30 full-power years (FPY) of operation at 18 MW/m<sup>2</sup> of neutron wall loading is found to be  $7 \times 10^{26}$  n/m<sup>2</sup>, and is substantially lower than the estimated lifetime limit of  $2 \times 10^{27}$  n/m<sup>2</sup> for the spinel insulator.

The  ${}^6\text{Li}$  enrichment of 30% was selected for the reference design because of the improved afterheat and magnet protection performance and the acceptable enrichment cost. Future optimization of the TITAN-I design may be possible by considering different low-activation reflector materials to reduce cost and by performing very detailed trade-off studies between  ${}^6\text{Li}$  enrichment, cost, annual-replacement-mass, and waste-disposal issues.

The final design parameters were verified by a set of 3-D neutronics calculations with the Monte Carlo code, MCNP [72], taking into account the toroidal geometry and the divertor modules. Non-IBC blanket tubes are incorporated in the space around the divertor and target plates. The hot-shield is extended behind the divertor coils except that a 90° opening in the poloidal direction is provided on the outboard divertor region for pumping (Figure 1.3-4). The tritium-breeding ratio for the 3-D model of the reference design is 1.18 and the maximum fast-neutron fluence at the OH magnet in the inboard region is  $1.6 \times 10^{27}$  n/m<sup>2</sup>, which is well below the assumed lifetime limit for the spinel insulator.

#### 1.3.4. Thermal and Structural Design

The TITAN-I FPC is cooled by liquid lithium. One of the issues for liquid-metal coolants in fusion reactors is the MHD-induced pressure drop. In an RFP fusion reactor such as TITAN, the toroidal magnetic field at the first wall is small; thus the MHD pressure drop can be kept low by alignment of the coolant channels primarily in the poloidal direction.

The TITAN designs operate with a highly radiative core plasma, in order to distribute the surface heat load uniformly on the first wall (4.6 MW/m<sup>2</sup>) and to keep the heat

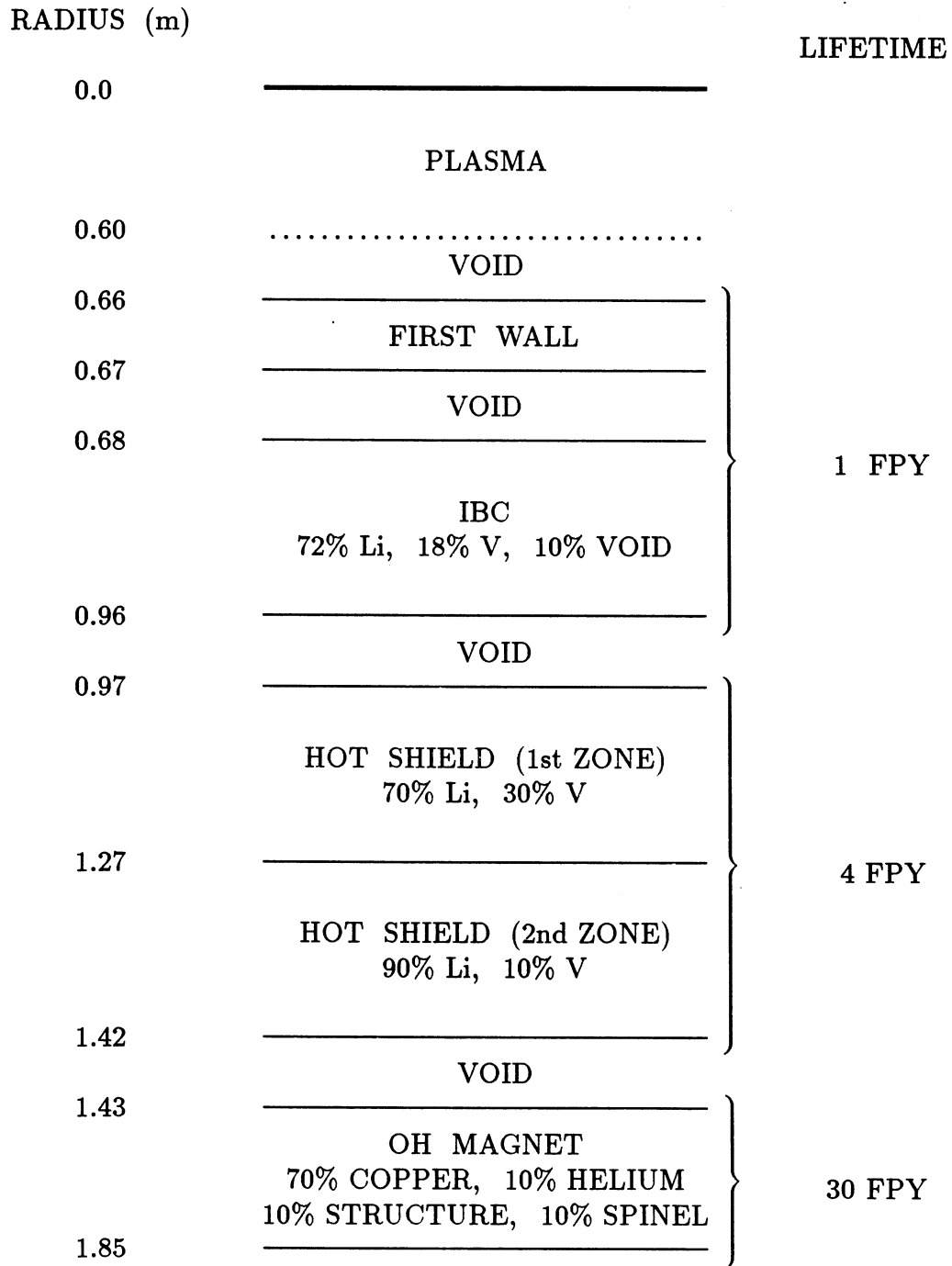


Figure 1.3-7. Schematic of the blanket and shield for the TITAN-I reference design.

**Table 1.3-I.**  
**NUCLEAR PERFORMANCE**  
**OF THE TITAN-I REFERENCE DESIGN<sup>(a)</sup>**

---

• <sup>6</sup> Li enrichment		30%	
• Tritium-breeding ratio:			
<sup>6</sup> Li (n,α)		1.084	
<sup>7</sup> Li (n,n',α)		0.247	
TOTAL		1.33	
• Blanket energy multiplication, <i>M</i>		1.14	
• Nuclear heating (MeV per DT neutron):			
	<u>Neutron</u>	<u>Gamma Ray</u>	<u>Sum</u>
First wall	0.341	0.183	0.524
Blanket	7.382	2.603	9.985
Shield (1st zone)	3.148	1.595	4.743
Shield (2nd zone)	0.235	0.560	0.795
TOTAL	11.106	4.941	16.047
OH coils	0.038	0.438	0.476

---

(a) From 1-D ANISN calculations.

load on the divertor target plates at a manageable level. Cooling of the high-heat-flux components, such as the first wall and divertor target plates, represents one of the critical engineering aspects of compact fusion reactors. The use of a highly radiative core plasma and the resulting distribution of the heat fluxes over the first wall is central to the solution to this problem. The main thermal-hydraulic design features of the TITAN-I FPC are:

1. First-wall sputtering is almost negligible as a result of the operation with a high-recycling divertor.
2. Small-diameter, thin-walled, circular coolant tubes are used for the first wall.
3. First-wall and blanket coolant circuits are separated.
4. Coolant channels are aligned with the dominant, poloidal magnetic field.
5. Turbulent-flow heat transfer is used to remove the high heat flux on the first wall.

For a given size for the first-wall coolant tubes, the maximum wall-temperature constraint would result in a maximum limit on the surface heat flux. Turbulent coolant flow, which is accompanied by a higher Nusselt number ( $Nu$ ), allows a higher surface heat flux compared with laminar coolant flow. The magnetic field, generally, tends to suppress turbulence in the flow of an electrically conducting fluid, and the onset of turbulence would occur at higher Reynolds numbers compared with non-MHD pipe flow.

A few studies on the turbulent heat transfer in liquid metals in the presence of a magnetic field [73-75] are available. Kovner *et al.* [73] performed experiments on the effect of a longitudinal magnetic field on turbulent heat transfer in liquid-galium flow in a tube. The following empirical correlation for Nusselt number was then proposed:

$$Nu = 6.5 + \frac{0.005Pe}{1 + 1890(Ha_{\parallel}/Re)^{1.7}}, \quad (1.3-1)$$

where  $Re$  is the Reynolds number,  $Ha_{\parallel}$  is the parallel Hartmann number,  $Pe = Re Pr$  is the Peclet number, and  $Pr$  is the Prandtl number. Even though Equation 1.3-1 is based on experimental data up to  $Ha_{\parallel} = 550$ , it is expected to hold beyond this range. Other experimental data and numerical studies show similar dependence [74,75]. Figure 1.3-8 shows the variation of the Nusselt number with Peclet number for  $B = 0$ ,  $Ha_{\parallel} = 1000$ , and  $Ha_{\parallel} = 3040$  (the expected  $Ha_{\parallel}$  in the TITAN-I first wall). The range of the experimental data is also shown in this figure.

The nonuniform circumferential heat flux on the first-wall coolant tubes will reduce the turbulent Nusselt number at the point of higher heat flux, as is shown for the case of

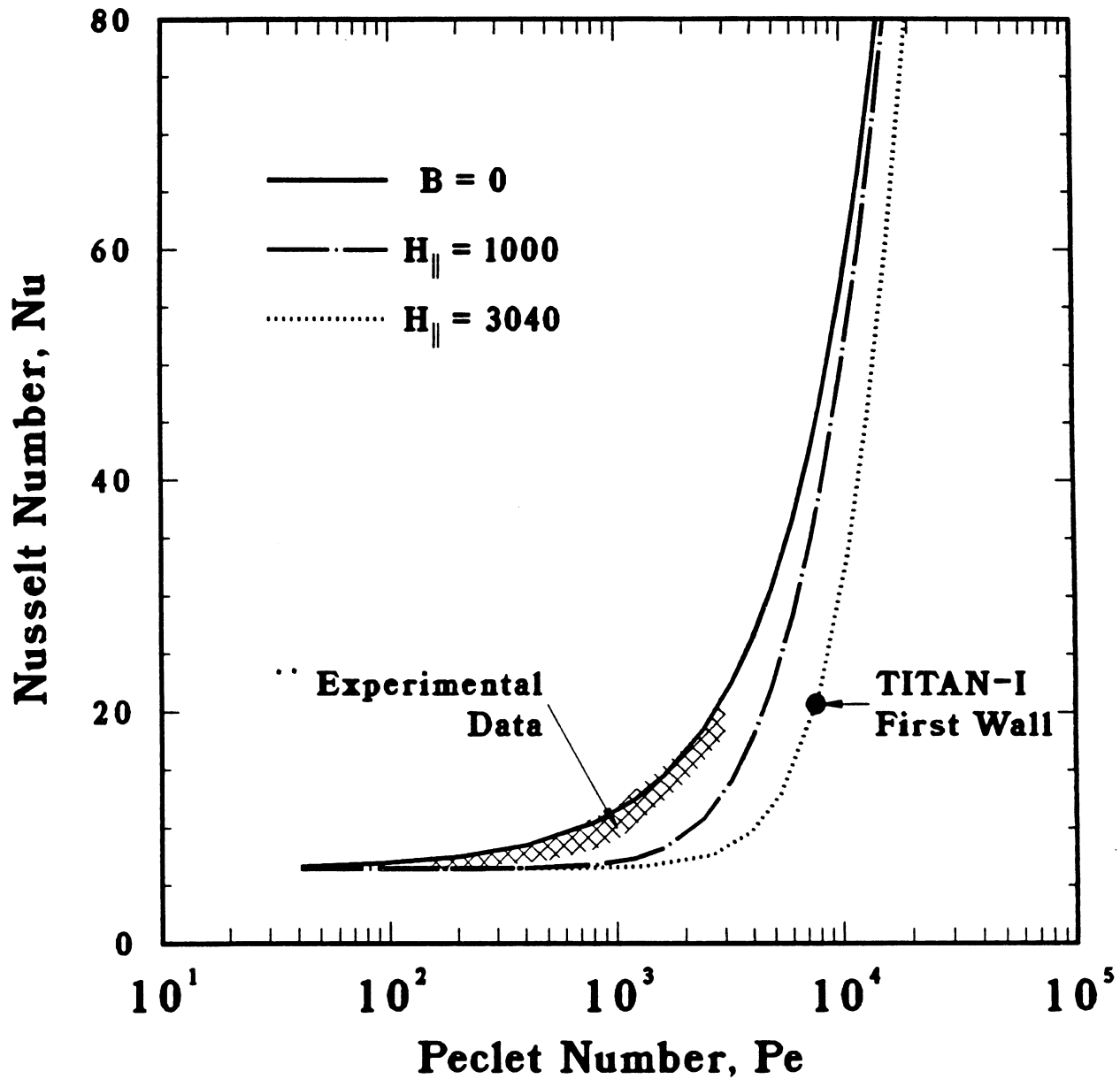


Figure 1.3-8. Variation of the Nusselt number,  $Nu$ , with the Peclet number,  $Pe$  for turbulent flow as predicted by Equation 1.3-1. The range of experimental data as well as the operating point of the TITAN-I first wall are also shown. The Nusselt number from this graph should be halved to account for nonuniform heat flux on the TITAN-I first wall.

laminar flow (Section 10.4.3). For the TITAN-I design, the  $Nu$  given by Equation 1.3-1 is reduced by a factor of two to account for this nonuniform circumferential heat flux until further data becomes available. The MHD pressure drops were calculated by various correlations appropriate for TITAN-I design (Section 10.4).

In order to complete the thermal-hydraulic design, pressure and thermal stresses in the FPC coolant channels were estimated by 1-D equations (along  $r$ , radial direction in the tube) for a thick-walled tube. Two-dimensional thermo-mechanical analyses of the TITAN-I FPC were also performed using the finite-element code, ANSYS [76], which verified the 1-D analysis (Section 10.4.7).

A thermal-hydraulic design window for compact, liquid-lithium-cooled RFP reactors was found based on certain design constraints such as the maximum allowable temperature of the structure ( $750^{\circ}\text{C}$ ), the maximum allowable pressure and thermal stresses in the structure (respectively, 108 and 300 MPa), and the maximum allowed pumping power (5% of plant output). The maximum allowable temperature of the structure corresponds to a maximum value for the average coolant exit temperature for a given heat flux. The maximum allowable stress and the maximum allowed pumping power would result in minimum values for the average exit temperature of the coolant. The design window for the coolant exit temperature is then located between these limits. Other parameters impacting the design window are the neutron wall loading, the coolant channel size, and the coolant inlet temperature.

Figure 1.3-9 illustrates the thermal-hydraulic design window for the TITAN-I first wall and shows that a design with a radiation heat flux on the first wall of  $4.9\text{ MW/m}^2$  is possible (corresponding to  $20\text{ MW/m}^2$  of neutron wall load at 95% total radiation fraction). The sudden change in the slope of the top curve in Figure 1.3-9 is caused by the change from laminar to turbulent flow. The flow in blanket and shield is always laminar. The total pumping-power limit of 5% of electric output is more restrictive than the pressure stress of 108 MPa. The thermal-stress limit is not reached up to the maximum heat flux on the first wall.

The main results of the thermal-hydraulic analysis of the TITAN-I first wall are given in Table 1.3-II. The coolant flow velocity in the TITAN-I first-wall tube is 21 m/s and the maximum pressure drop is 10 MPa. The coolant velocities in the 1st and 6th (last) rows of the IBC coolant channels are, respectively, 0.5 and 0.2 m/s. The pressure drops in the 1st and 6th rows are 3.0 and 0.5 MPa, respectively. The maximum pressure drop in the divertor coolant circuit is 12 MPa. In order to simplify the design, the first-wall and divertor coolants are supplied from the same circuit with a delivery pressure of 12 MPa. One single orifice is used to reduce the lithium pressure to 10 MPa for the first-wall circuit.

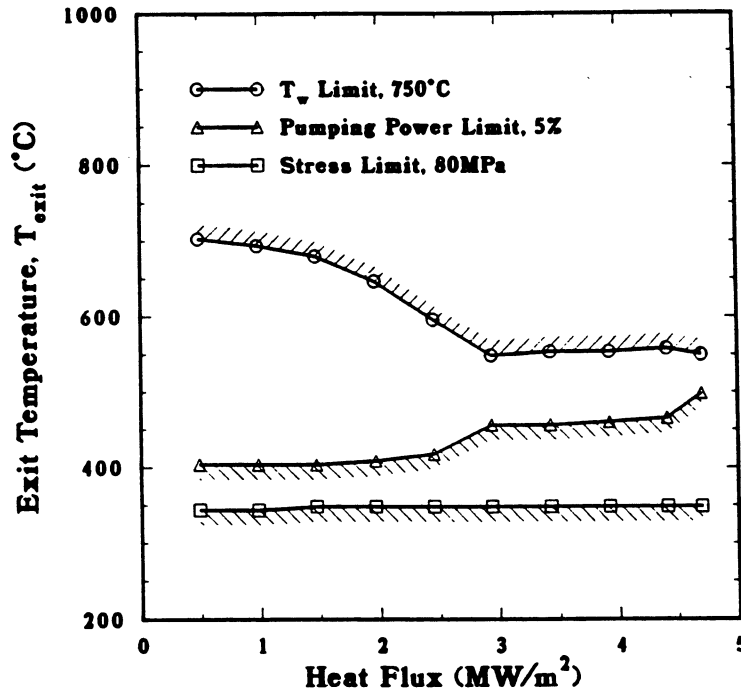


Figure 1.3-9. The thermal-hydraulic design window for the TITAN-I FPC.

Additional orifices are used, wherever necessary, in order to reduce the coolant pressure from 12 MPa to the required inlet pressure of the individual rows of divertor coolant tubes. The supply pressure of the blanket coolant pump is 3 MPa. Orifices are used to reduce the pressure to the required values at the inlet of each row of IBC channels.

### 1.3.5. Magnet Engineering

Three types of magnets are used in the TITAN-I design (Figure 1.3-3). The ohmic-heating (OH) and the equilibrium-field (EF) trim coils are normal-conducting with copper alloy as the conductor, spinel as the insulator, and gaseous helium as the coolant. The main EF coils are made of NbTi conductor and steel structural material. These poloidal-field (PF) coils are designed to last the life of the plant. Because of their simple geometry, the robust support structure, and the relatively low field produced by these coils, little or no extrapolation of current technology should be required.

The divertor and the toroidal-field (TF) coils of the TITAN-I design are based on the integrated-blanket-coil (IBC) concept [14]. The IBC as applied to TITAN-I also acts as the toroidal-field driver coil for the oscillating-field current-drive system, OFCD (Section 7). The toroidal-field (TF) coils of TITAN-I oscillate at 25 Hz with currents

Table 1.3-II.

## THERMAL-HYDRAULIC DESIGN OF TITAN-I FIRST WALL

---

Pipe outer diameter, $b$	10.5	mm
Pipe inner diameter, $a$	8.0	mm
Wall thickness, $t$	1.25	mm
Erosion allowance	0.25	mm
Structure volume fraction	0.400	
Coolant volume fraction	0.375	
Void volume fraction	0.225	
Coolant inlet temperature, $T_{in}$	320	°C
Coolant exit temperature, $T_{ex,FW}$	440	°C
Maximum wall temperature, $T_{w,Max}$	747	°C
Maximum primary stress	50	MPa
Maximum secondary stress	288	MPa
Coolant flow velocity, $U$	21.6	m/s
Pressure drop, $\Delta p$	10	MPa
Total pumping power <sup>(a)</sup>	37.7	MW
Reynold's number, $Re$	$1.90 \times 10^5$	
Magnetic Reynold's number, $Re_m$	0.48	
Parallel Hartmann number, $H_{\parallel}$	$3.04 \times 10^3$	
Perpendicular Hartmann number, $H_{\perp}$	$2.01 \times 10^2$	
Parallel magnetic interaction parameter, $N_{\parallel}$	48.6	
Perpendicular magnetic interaction parameter, $N_{\perp}$	0.21	
Nusselt number, $Nu$	10.35	
Prandtl number, $Pr$	$4.08 \times 10^{-2}$	
Peclét number, $Pe$	$7.76 \times 10^3$	

---

(a) A pump efficiency of 90% is assumed.

ranging between 30% to 170% of the mean steady-state value of 7.0 MA-turns (including the currents in the divertor trim coils). The PF coils also oscillate at 25 Hz. It is also necessary to oscillate the divertor coils to maintain the plasma separatrix at the proper location.

The IBC design encounters several critical engineering issues: (1) steady-state and oscillating power-supply requirements for low-voltage, high-current coils; (2) time-varying forces caused by the OFCD cycles; (3) integration of the primary heat-transport system with the electrical systems; (4) sufficient insulation to stand off induced voltages; and (5) suitable time constants for various components to permit the coil currents to oscillate at 25 Hz. Heat removal is not an issue for IBC because the joule heating is produced directly in the primary coolant.

Design of the power supplies is one of the critical issues for IBC. The low number of electrical turns available (12 for the TITAN-I design) results in low-voltage, high-current coils (3.85 V, 520 kA per coil). Power supplies rated for such conditions would be expensive and would exhibit high internal-power losses if based on technology that is currently available. Connecting all 12 IBCs of TITAN-I in series would raise the voltage of the power supply to a more manageable value. However, the IBC approach requires that the electrical and hydraulic systems be physically connected, and that the intermediate heat exchangers (IHXs) and coolant pumps should be grounded (*i.e.* no electric current flowing through the IHXs and pumps).

Figure 1.3-10 illustrates the electrical and hydraulic lay-out of the TITAN-I IBC system. The TITAN-I FPC consists of three sectors which are connected to each other through the divertor modules. To increase the power-supply voltage, the four IBCs in each sector are electrically connected in series in the TITAN-I design and allow a better match of current and voltage for the power supply (15.4 V, 541 kA). This circuit, however, requires two IHXs per sector for the IBC cooling circuit. Figure 1.3-10 shows that because of the series connection of the IBCs and grounding of the pumps and heat exchangers, a leakage current would flow through the cold and hot legs. The leakage current is small, but results in unequal coil currents and necessitates a small balancing power supply to accompany each main power supply, as is indicated in Figure 1.3-10. The balancing power supplies have much smaller current loads than the main power supply (7.7 V and 27 kA) which leak through the cold legs to ground.

The impurity-control system of the TITAN-I design consists of three toroidal-field divertors. Each divertor consists of one nulling coil and two flanking coils to produce the local effects necessary for field nulling. Because of the loss of coverage of TF IBCs in the divertor region, a pair of trim coils is added to each divertor in order to localize

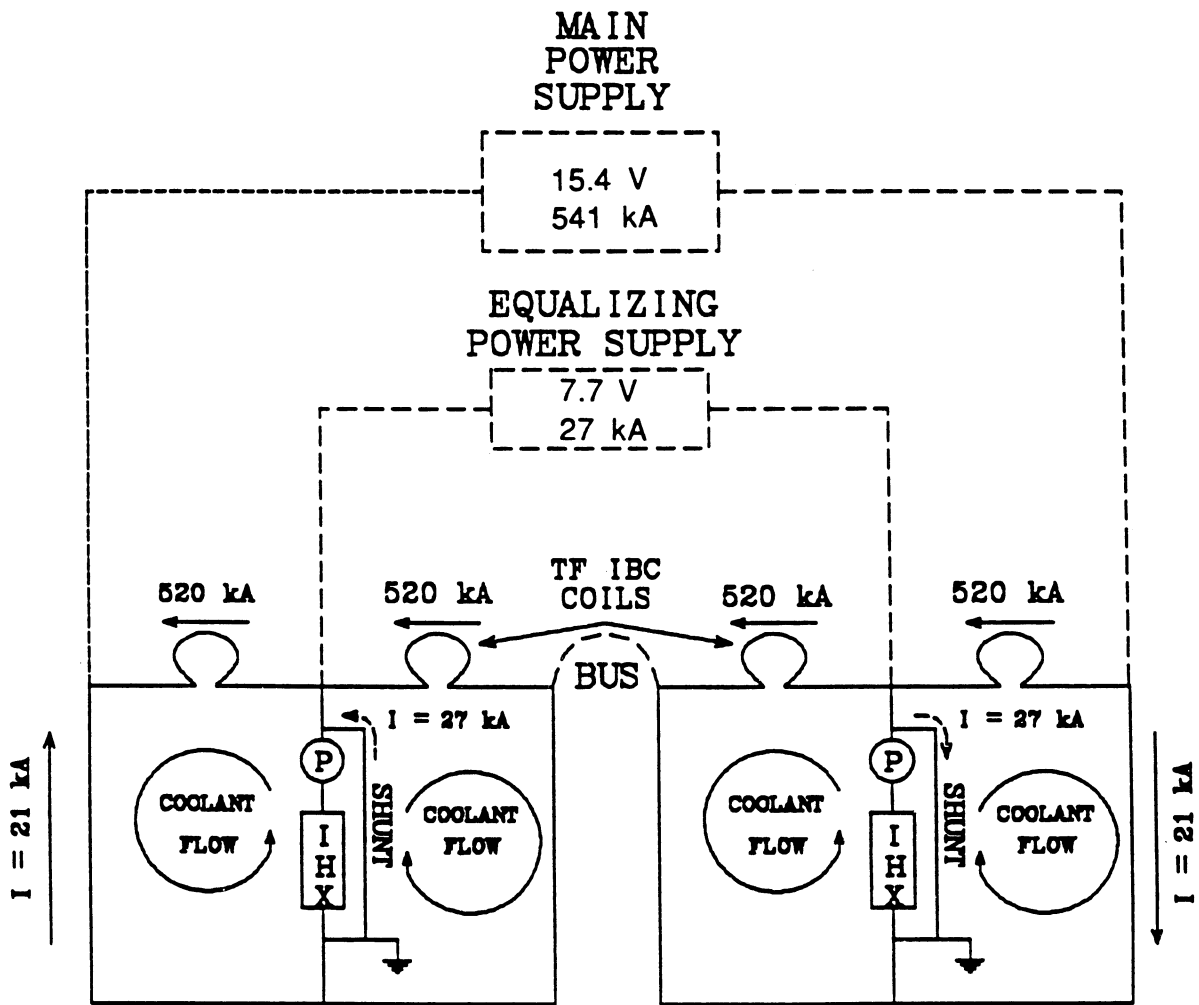


Figure 1.3-10. Schematic of the electrical and hydraulic layout of TITAN-I TF IBCs.

the toroidal-field ripple. The divertor IBCs operate at relatively higher current densities than the TF coils, thereby, require much greater voltages. Furthermore, the current in each nulling coil is exactly equal to that of the two flanking coils. The divertor IBCs are connected in order to take advantage of the symmetric currents and larger voltages. Furthermore, equalizing power supplies are not needed for the divertor IBCs – two power supplies would be required per divertor module. The total joule losses in the divertor IBCs (three divertors) is 117 MW with additional 3.5-MW losses in the hot legs.

Because of the large impedance of the toroidal-field circuit during the OFCD cycles (about  $0.1\text{ m}\Omega$  for each TF coil), the oscillating voltage on each TF coil ( $\sim 50\text{ V}$ ) is much larger than the steady-state value of about  $3.8\text{ V}$ . Detailed analyses of the OFCD power supplies and the leakage currents were not performed because the results are sensitive to the impedances of the hot and cold legs which in turn depend on the piping arrangement. Instead, the leakage currents were calculated based on simple estimates of the internal inductances of coolant pipings. The joule losses in the TF coils during the OFCD cycle are estimated to be 25.6 MW for the steady-state portion (24 MW in the coil and 1.6 MW in the hot and cold legs) and 16 MW for the oscillating voltages (15 MW in the coils and 1 MW in the hot and cold legs).

It is also necessary to oscillate the divertor coils during the OFCD cycle to maintain the plasma separatrix at the proper location. Since the magnitude of oscillation of the toroidal flux was found to be small, the strength of the toroidal field on the plasma surface would be directly proportional to the reversal parameter and the magnitude of the current oscillations in the divertor coils would be about  $2/3$  of the steady-state value. The voltage oscillations applied to the divertor coils are roughly equal to the steady-state values, in contrast to the TF coils, because the divertor coils operate at much higher current densities and have higher resistances. The oscillating losses in the divertor IBCs are estimated at 26 MW in the coils and 0.8 MW in the hot and cold legs.

Interaction of the current in the IBC with the reactor magnetic fields produces forces on the TF and divertor coils. These forces are much lower than the corresponding forces in tokamaks since the coil currents are much lower in RFPs. The magnitudes of the forces on the TITAN-I IBCs vary over time as the currents oscillate during the OFCD cycle. Hence, structural supports are designed for the peak loads (Section 10.5.3). Dynamic structural analysis also shows that failure will not occur as a result of these cyclic forces.

### 1.3.6. Power Cycle

One of the advantages of using liquid lithium as the coolant for TITAN-I is the ability to remove the thermal energy from the reactor at a high thermal potential so that a high power-cycle efficiency can be realized. An important feature of the thermal-hydraulic design of the TITAN-I first wall and blanket is the separation of the coolant circuits for these components in order to handle the high surface-heat flux on the first wall. As a result, the first-wall coolant has a much lower exit temperature (440 °C) than the blanket and shield coolant (700 °C). The divertor coolant also has a different exit temperature (540 °C). The inlet temperatures to all three circuits are kept the same primarily for simplicity. Since the thermal power in the divertor circuit is very small (1% of total thermal power), the first-wall and divertor coolants are mixed at exit, leading to two separate streams of the primary coolant which remove, respectively, 765 and 2170 MWt of power with exit temperatures of 442 and 700 °C.

The TITAN-I reference design uses two separate power cycles: one for the first-wall and divertor stream and the other for the IBC and shield stream (Section 10.6.2). Each of these two power cycles has a separate IHX, steam generators, and turbine-generator set. The TITAN-I FPC consists of three toroidal sectors. One IHX and one steam generator are required per sector for the first-wall and divertor coolant stream. The steam produced, in these three steam generators is mixed and fed to a single turbine-generator set. For the IBC and shield stream, two IHXs are used per sector, based on electrical engineering requirements of the IBCs. The secondary coolants of each pair of these heat exchangers are mixed and fed to one steam generator (per sector). As in the first-wall and divertor cycle, the steam from all three steam generators is mixed and fed to a single turbine-generator set.

The power cycle analysis is performed by the computer code PRESTO [77]. The pinch-point temperature difference in the steam generators of each of these power cycles is kept above 20 °C. For both the first-wall and divertor cycle and the IBC and shield cycle, the temperature loss in the IHXs is set at 20 °C. The first-wall and divertor power cycle is a superheat Rankine cycle with four stages of feed-water heating. Reheat of the steam after expansion through the high-pressure turbine is not used. The total thermal power in the first-wall and divertor power cycle is 765 MWt and the gross thermal efficiency is 37.0%. The IBC and shield power cycle is a superheat Rankine cycle with two reheat stages and seven stages of feed-water heating. The superheater and the reheaters are arranged in series. The total thermal power in this cycle is 2170 MWt, and the gross thermal efficiency of this cycle is 46.5%.

The main results and parameters of the first-wall and divertor cycle and the IBC and shield cycle are given in Table 1.3-III. The overall gross thermal efficiency for the TITAN-I design, by combining the efficiencies of the two cycles, is 44%.

### 1.3.7. Divertor Engineering

The design of the impurity-control system poses some of the most severe problems of any component of a DT fusion reactor and for a compact or high-power-density device these problems can be particularly challenging. The final TITAN-I divertor design represents the result of extensive iterations between edge-plasma analysis, magnetic design, thermal-hydraulic and structural analysis, and neutronics.

A summary of the results of the edge-plasma modeling is given in Table 1.3-IV and is described in detail in Section 5.4. The plasma power flow is controlled by the injection of a trace amount of a high- $Z$  material (xenon) into the plasma which causes strong radiation from the core, scrape-off layer, and divertor plasmas. About 95% of the steady-state heating power (alpha particle and ohmic heating by the current-drive system) is thereby radiated to the first wall and divertor plate, although only about 70% is radiated from the core plasma (*i.e.*, inside the separatrix). This intense radiation reduces the power deposited on the divertor target by the plasma to an acceptably low level. Preliminary experimental results [12,13] suggest that beta-limited RFP plasmas can withstand a high fraction of power radiated without seriously affecting the global confinement (Section 5.3). The radiative cooling also reduces the electron temperature at the first wall and divertor target (also assisted by recycling) which, in turn, reduces the sputtering and erosion problems.

To satisfy the requirement for a high- $Z$  material for the plasma-facing surface of the divertor target, a tungsten-rhenium alloy (W-26Re) is used. The high rhenium content provides the high ductility and high strength necessary for the severe loading conditions. A bank of lithium-cooled vanadium-alloy coolant tubes removes the heat deposited on the target. These tubes are separated from the tungsten-alloy armor by a thin, electrically insulating layer of spinel, to avoid an excessive MHD pressure drop. Fabrication of the divertor target is based on brazing the tungsten-alloy plate (produced by powder-metallurgy techniques) to the bank of coolant tubes, with the spinel layer deposited by the chemical-vapor-deposition (CVD) process. As a second technique, a unique manufacturing process using CVD (instead of brazing) is proposed to enhance bond strength of the tungsten-spinel-vanadium interfaces.

Table 1.3-III.

## PARAMETERS OF THE TITAN-I POWER CYCLE

---

<b>First-Wall and Divertor Power Cycle:</b>		
Total thermal power in the primary coolant	765	MW
Primary-coolant inlet temperatures	320	°C
Primary-coolant exit temperatures	442	°C
Secondary-coolant inlet temperatures	300	°C
Secondary-coolant exit temperatures	422	°C
Throttle steam temperature	396	°C
Throttle steam pressure	10.7	MPa
Steam flow rate	326	kg/s
Condenser back pressure	$6.76 \times 10^3$	Pa
Stages of feed-water heating	4	
Feed-water inlet temperature	169	°C
Gross thermal efficiency	37.0%	
<b>IBC and Shield Power Cycle:</b>		
Total thermal power in the primary coolant	2170	MW
Primary-coolant inlet temperatures	320	°C
Primary-coolant exit temperatures	700	°C
Secondary-coolant inlet temperatures	300	°C
Secondary-coolant exit temperatures	680	°C
Steam temperature after 1st reheat	565.6	°C
Steam temperature after 2nd reheat	550.0	°C
Throttle steam pressure	21.4	MPa
Steam flow rate	703	kg/s
Condenser back pressure	$6.76 \times 10^3$	Pa
Stages of feed-water heating	7	
Feed-water inlet temperature	258	°C
Gross thermal efficiency	46.5%	
Overall gross thermal efficiency	44.0%	

---

Table 1.3-IV.

## SUMMARY OF TITAN-I EDGE-PLASMA CONDITIONS

---

Number of divertors	3
Scrape-off layer thickness	6 cm
Peak edge density	$1.7 \times 10^{20} \text{ m}^{-3}$
Peak edge ion temperature	380 eV
Peak edge electron temperature	220 eV
Plasma temperature at first wall	1.7 eV
Peak divertor density	$6 \times 10^{21} \text{ m}^{-3}$
Peak divertor plasma temperature	4.5 eV
Divertor recycling coefficient	0.995
Throughput of DT	$6.7 \times 10^{21} \text{ s}^{-1}$
Throughput of He	$8.2 \times 10^{20} \text{ s}^{-1}$
Vacuum tank pressure	20 mtorr

---

The TITAN-I impurity-control system is based on the use of toroidal-field divertors to minimize the perturbation to the global magnetic configuration (toroidal-field is the minority field in RFPs) and to minimize the coil currents and stresses. The TITAN divertor uses an "open" configuration, in which the divertor target is located close to the null point and faces the plasma, rather than in a separate chamber. This positioning takes advantage of the increased separation between the magnetic field lines (flux expansion) in this region, which tends to reduce the heat loading on the divertor plate because the plasma flowing to the target is "tied" to the field lines. The high plasma density in front of the divertor target ensures that the neutral particles emitted from the surface have a short mean free path; a negligible fraction of these neutral particles enter the core plasma (Section 5.5).

The final magnetic design includes three divertor modules, located 120° apart in toroidal direction (Figure 1.2-10). The magnetic field lines are diverted onto the divertor

plate using a nulling coil and two flanking coils which localize the nulling effect. For the TITAN-I design, the divertor IBC assembly displaces a part of the TF IBC tube bank. Therefore, a pair of trim coils is also required to control the toroidal-field ripple. Also shown on the outboard view of Figure 1.2-10 is the pumping aperture which leads to the vacuum tank surrounding the torus. This aperture is present for only the outboard  $90^\circ$  in the poloidal angle; elsewhere there is shielding material to protect the OH coils.

The low value of the toroidal field in the RFP allows high coolant velocities to be achieved without prohibitive MHD pressure drops, thus permitting operation in the turbulent flow regime with the associated high heat-transfer coefficients. Despite the intense radiation arising from the impurities injected into the plasma, careful shaping of the divertor target, as shown in Figure 1.2-10, is also required to maintain the heat flux at acceptable levels at all points on the plate. Figure 1.3-11 shows the distribution of the various components of the surface heat flux along the divertor target for the inboard and outboard locations. The heat flux on the inboard target ( $\sim 9.5 \text{ MW/m}^2$ ) is significantly higher than that on the outboard ( $\sim 6 \text{ MW/m}^2$ ), because of the toroidal effects.

The temperature distribution of the target plate coolant and structure is shown in Figure 1.3-12. The same coolant inlet temperature of  $320^\circ\text{C}$  as for the first wall is used, allowing both coolant loops to be fed from the same circuit. The maximum temperature of the vanadium-alloy tubes does not exceed  $750^\circ\text{C}$ . The maximum temperature of the tungsten-rhenium armor is about  $930^\circ\text{C}$ , at which level the alloy retains high strength and the thermal stresses are within allowable levels.

A total pressure drop of 12 MPa was used for the divertor-coolant circuit. The maximum allowable coolant velocity was set at 25 m/s for this analysis, based on considerations of physical erosion. Figure 1.3-12 also shows the components of the pressure drop in the divertor-coolant tubes. Flow orificing is used extensively to tailor the coolant velocity distribution. In low-field regions, the large pressure head of 12 MPa would otherwise cause the velocity to exceed the 25 m/s limit. Near the outside of the plate, orificing allows the coolant outlet temperature to be adjusted so as to maintain an approximately constant level across the plate.

A detailed finite-element analysis of the steady-state temperatures and stresses in the divertor was made using the finite-element code, ANSYS [76], which has verified the design of the target plates (Section 11.5). A 2-D finite-element structural analysis also indicated that stress concentrations will occur at the edge of the interface between the different materials of the target. This aspect requires further analysis and experimental investigation to assure the viability of the design.

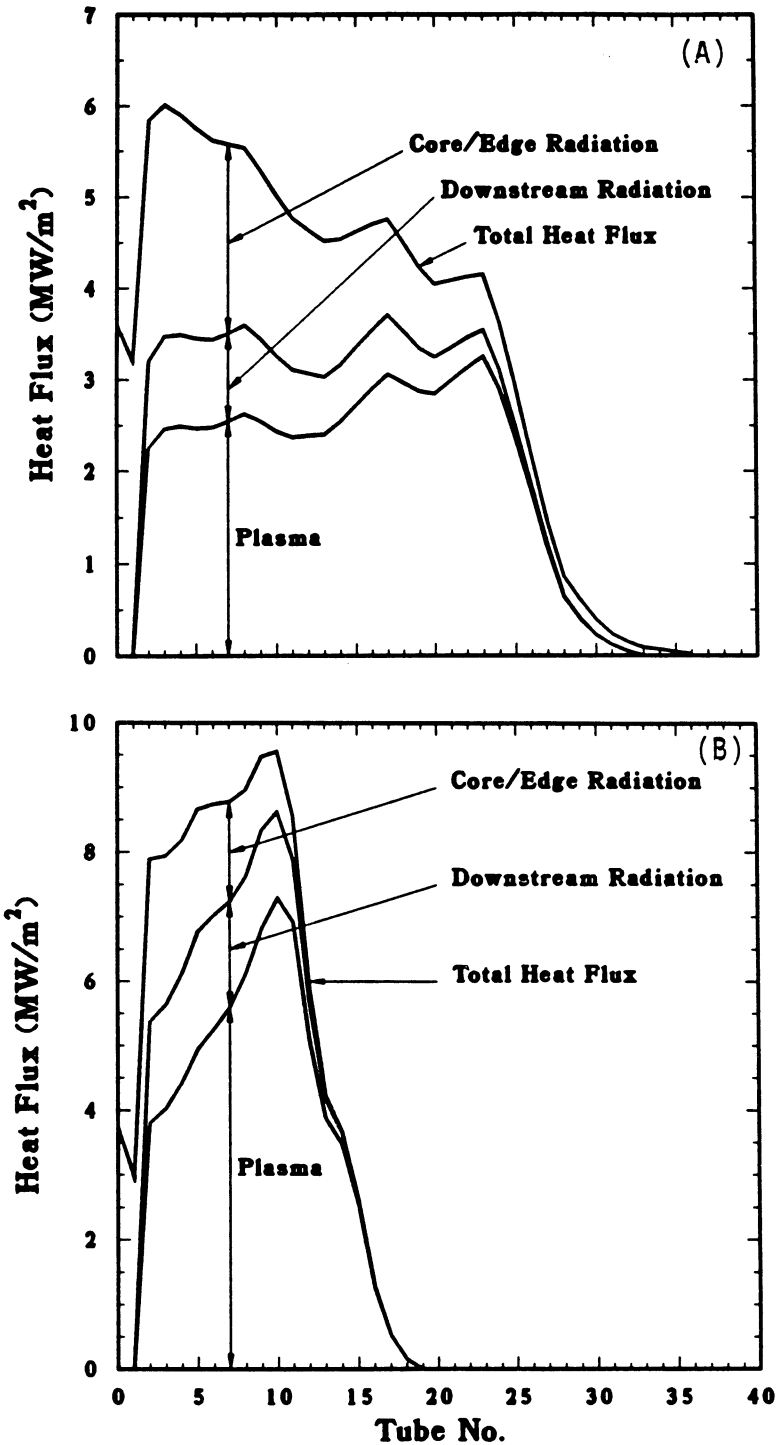


Figure 1.3-11. Heat flux distribution on outboard (A) and inboard (B) sections of divertor target. Coolant tubes are numbered from the apex or symmetry point of the target between the nulling coil and the core plasma.

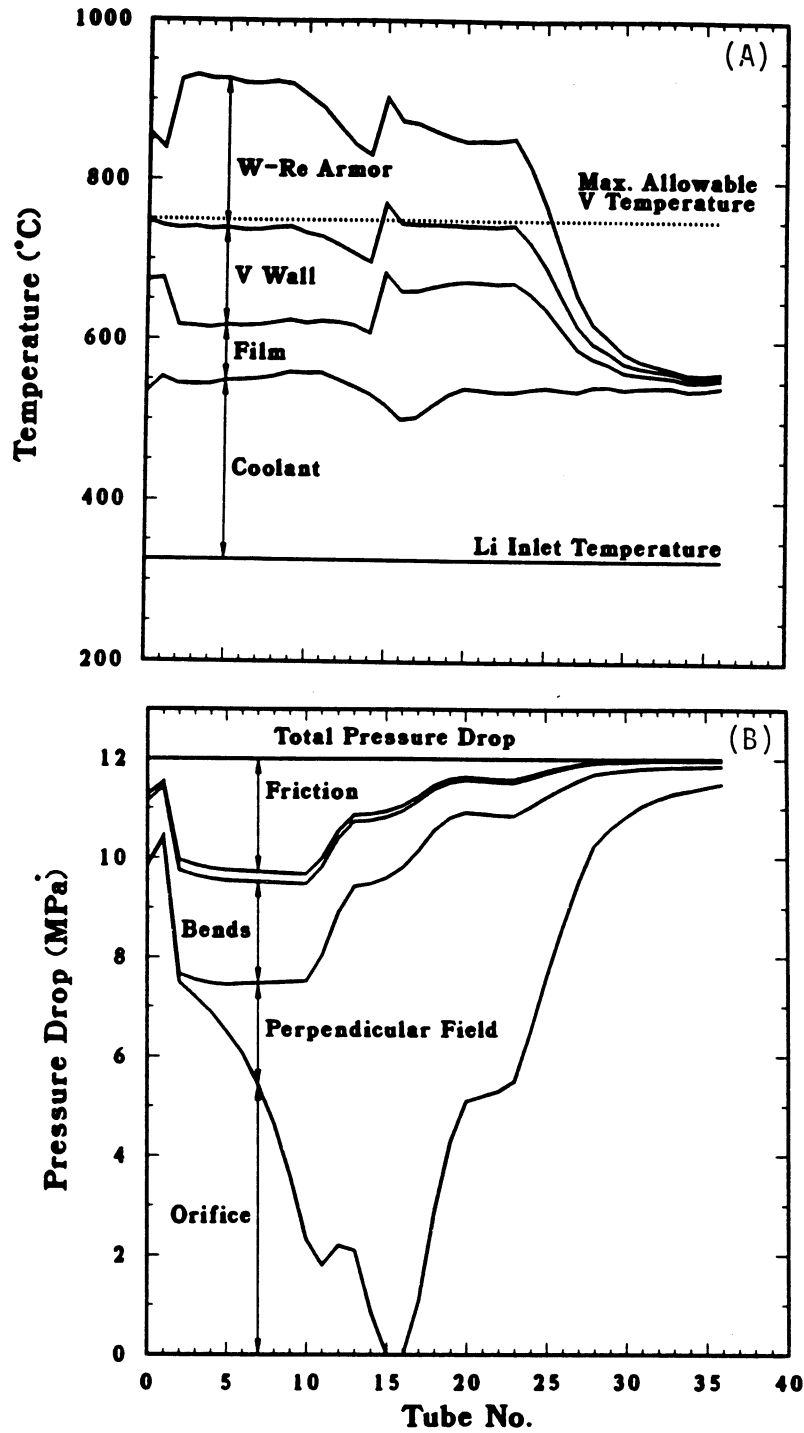


Figure 1.3-12. Coolant and structural temperatures at the coolant outlet (A) and components of the coolant pressure drop (B) for coolant tubes in the divertor target. Coolant tubes are numbered from the apex or symmetry point of the target between the nulling coil and the core plasma.

The vacuum system is based on the use of a large vacuum tank encompassing the entire torus, and connected to the divertor region by a duct located at each of the three divertor locations. It is proposed to employ lubricant-free magnetic-suspension-bearing turbo-molecular pumps for the high-vacuum pumps to avoid the possibility of tritium contamination of oil lubricants.

### 1.3.8. Tritium Systems

The major units in the tritium system of a fusion reactor are: (1) the plasma-processing system, (2) the breeder tritium-recovery system, (3) the atmospheric-tritium system, and (4) the secondary containment systems. The complete tritium system has to be designed under the constraints of tritium inventory, system cost, and tritium leakage rate. Significant relaxation of any one of the constraints will have a major impact on the overall design of the complete system.

In the TITAN design, the separation of the D and T of the plasma exhaust is not required. Therefore, only about 1% of the plasma exhaust will be required to pass through the cryogenic distillation system to separate protium generated by the DD reaction. The capacity and cost of the plasma-exhaust processing is thus much reduced. Since the cost of the plasma-exhaust-processing system is so low, a redundant unit is affordable. A double plasma-exhaust-processing system can significantly improve the reliability of the system and the reactor tritium storage can be reduced.

A molten-salt recovery process [78] is selected for tritium recovery from the lithium blanket, in which the liquid lithium and a molten salt are in contact, and LiH is preferentially distributed to the salt phase. The salt is then electrolyzed to yield hydrogen which is removed by sweeping the porous stainless-steel hydrogen electrode with a circulating stream of inert gas. The tritium is subsequently recovered from the inert gas with a getter. The molten-salt recovery process has been demonstrated on a laboratory scale to recover tritium from lithium down to 1 wppm. Therefore, the tritium inventory in the blanket would be moderate. The parameters of TITAN-I blanket tritium-recovery system is shown in Table 1.3-V.

Most reactor designs selected sodium as the intermediate coolant [66]. For the TITAN-I design, lithium is also used as the intermediate coolant to avoid using two separate technologies (sodium and lithium). Since, tritium solubility is much higher in lithium than in sodium, the TITAN-I design has a moderate amount of tritium inventory in the secondary loop. A unique advantage of using lithium as the primary coolant and

Table 1.3-V.

**ANALYSIS OF MOLTEN-SALT EXTRACTION SCHEME FOR  
A LIQUID-LITHIUM BLANKET SYSTEM**

Breeding rate	420 g/d <sup>(a)</sup>			
Recovery rate	520 g/d <sup>(a)</sup>			
Lithium exit temperature	556 °C <sup>(b)</sup>			
Extraction system temperature	556 °C <sup>(b)</sup>			
Estimated blanket inventories				
Lithium	2.12 × 10 <sup>8</sup> g			
Tritium	212 g (1 wppm)			
Tritium recovery efficiency, $\epsilon$	90%			
Capacity per extractor unit	23 m <sup>3</sup> /h			
Electrical power per unit	3.7 kW			
<hr/>				
Tritium Concentration (wppm)	Effective Distribution Coefficient ( $D_v\eta$ )	Lithium Processed per Hour (kg/h)	Number of Units	Required Electrical Power (kW)
1	4	22,000	7	26
1	1	88,000	28	104 <sup>(c)</sup>
<hr/>				

(a) Based on a tritium-breeding ratio of 1.2 and 100 g/d of PDP.

(b) Parameters of the Scoping Phase design,  
the blanket and first-wall coolant were mixed in the outlet.

(c) Reference case.

as the breeder is associated with the high tritium solubility in the lithium. The tritium partial pressure is very low. For a tritium concentration of 1 wppm, the tritium partial pressure is only  $10^{-7}$  Pa. With such low tritium partial pressure, tritium containment is usually not a severe problem. This reduces the required capacity of the room-air-detrification system and the secondary containment systems. The tritium inventories in TITAN-I components are shown in Table 1.3-VI. The TITAN-I tritium inventory (1650 g) and leakage rate (7 Ci/d) are very reasonable.

A potential problem facing TITAN-I is the plasma-driven permeation (PDP) of low-energy tritons through the permeable vanadium-alloy first wall. The extent of PDP depends on the ability of the small fraction of high-energy plasma ions to adequately clean the first-wall surface, which is uncertain. The problem of PDP is not unique to

Table 1.3-VI.

## TRITIUM INVENTORIES IN TITAN-I REACTOR

Unit	Tritium Inventory (g)
Storage	1,100
Primary-coolant loop	212
Secondary-coolant loop	300
Molten-salt extraction	10
Fuel processing	20
First wall:	
typical case	0.72
excessive PDP	4.53
Integrated blanket coil	2.20
Hot shield, zone 1	0.14
Hot shield, zone 2	0.25
Divertor shield	0.08
Divertor	< 0.01
Out-of-blanket piping	≪ 0.01
Total TITAN-I inventory	1,650

compact RFP designs. Any fusion reactor design with a combination of a low edge temperature and a vanadium-alloy first wall must consider this problem. Experiments are needed to determine the extent of PDP and the sputtering rate of the first-wall structure at low edge-plasma temperatures. In the TITAN-I design, a tungsten-rhenium alloy (W-26Re) is chosen for the divertor plates. Because tungsten is very resistant to permeation, PDP through the divertor plate is not a concern.

### 1.3.9. Safety Design

Strong emphasis has been given to safety engineering in the TITAN study. Instead of an add-on safety design and analysis task, the safety activity was incorporated the process of design selection and integration from the beginning of the study. The safety-design objectives of the TITAN-I design are: (1) to satisfy all safety-design criteria as specified by the U. S. Nuclear Regulatory Commission on accidental releases, occupational doses, and routine effluents; and (2) to aim for the best possible level of passive safety assurance.

The elevation view of the TITAN-I reactor is shown in Figure 1.3-1. The key safety features of the lithium self-cooled TITAN-I design are:

- The selection of a low-afterheat structural material, V-3Ti-1Si;
- The selection of a relatively high  ${}^6\text{Li}$  enrichment (30%) to aid in further reducing afterheat and radioactive wastes;
- The use of three enclosures separating the lithium and air: the blanket tubes, vacuum vessel, and the containment building which is filled with argon cover gas;
- Locating all coolant piping connections at the top of the torus to prevent a complete loss of coolant in the FPC in case of a pipe break;
- The use of lithium-drain tanks to reduce the vulnerable lithium inventory should a pipe break occur;
- The use of steel liner to cover the containment-building floor to minimize the probability of lithium and concrete reactions.;
- Excluding water from the containment building to prevent the possibility of lithium-water reaction.

Two of the major accidents postulated for the fusion power core are the loss-of-flow accident (LOFA) and the loss-of-coolant accident (LOCA). Thermal responses of the TITAN-I FPC to these accidents are modeled using a finite-element heat-conduction code, TACO2D [79]. Figure 1.3-13 shows the resulting temperatures during a LOFA. At 12.8 hours after the initiation of the accident, the first wall reaches its peak temperature of 990 °C which is well below the recrystallization temperature of the V-3Ti-1Si alloy. The first-wall peak temperature is also well below  $\sim 1300$  °C, the on-set of volatilization of radioactive products (CaO, SrO) in the vanadium alloy (more experimental data is needed to clarify the on-set temperature and the extent of the release of these radioisotopes). The heat capacity of the static lithium accounts for the moderate temperature excursion. No natural convection of the coolant is assumed even though the emergency plasma shutdown procedure is accompanied by the discharge of all magnets and no MHD retarding force is expected on the coolant. If natural convection develops, the temperature excursions would be considerably smaller than those predicted by Figure 1.3-13.

Thermal creep-rupture behavior of the TITAN-I first wall during accidents is estimated using the modified-minimum-commitment method (MMCM) [68]. For the materials and loadings expected in the TITAN-I first wall during a LOFA, the thermal stresses

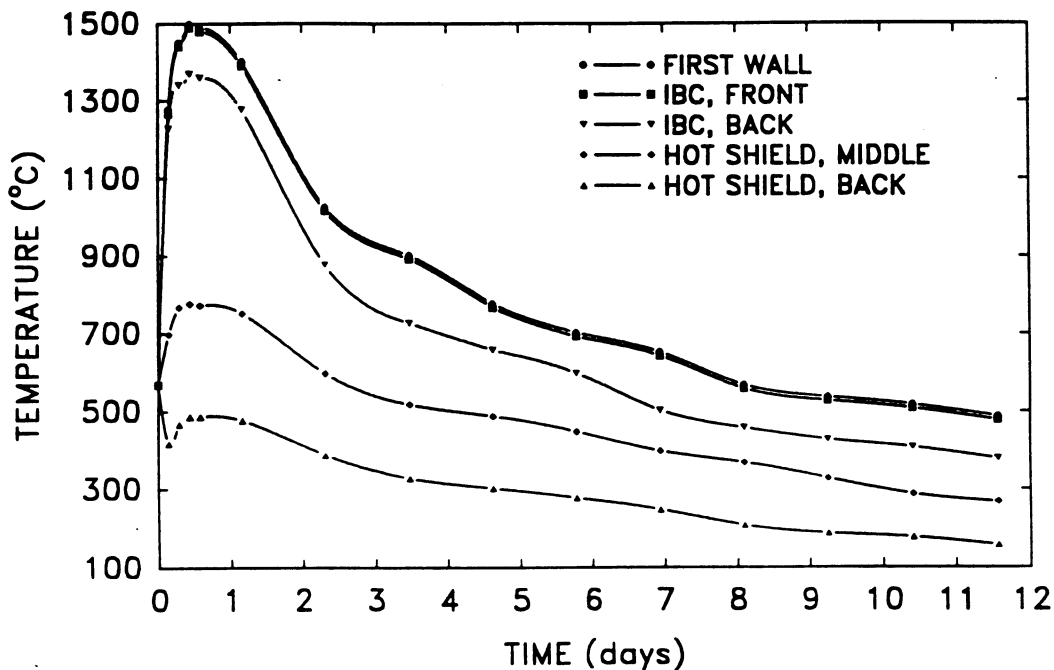


Figure 1.3-13. The thermal response of the TITAN-I FPC to a complete LOFA as a function of time after the initiation of the accident.

have a negligible influence on the rupture time relative to the pressure stresses. The predicted rupture times for several primary stresses at 1000°C are given in Table 1.3-VII. Since the coolant pressure is lost during off-normal conditions, the expected primary stress in the TITAN-I design during a LOFA is below 2 MPa and is caused by the hydrostatic pressure load inside the coolant piping. Table 1.3-VII shows that creep-rupture would not occur even if the structure is kept at elevated temperatures (1000°C) for a prolonged period of time – a LOFA would not lead to a LOCA. High-temperature creep-rupture data above 850°C are necessary to gain more confidence in the creep-rupture behavior at these higher temperatures.

Higher afterheat is expected in the tungsten plate of the divertor. During a LOFA, the peak temperature in the divertor vanadium cooling tube is 1117°C, close to recrystallization temperature of the V-3Ti-1Si. This may result in shortening the lifetime of the divertor modules, but failure that would lead to a LOCA is unlikely.

In the event of major primary-pipe breaks and failure of the containment building and vacuum vessel, air could enter the vacuum chamber and start a lithium fire. The TITAN-I reactor is configured so as (1) to ensure that a lithium fire would be a low probability event, and (2) to minimize the consequences of lithium fire if it occurs. In order to reduce the probability of lithium fires, three barriers (primary-coolant pipes, the vacuum tank, and the containment building) exist between the primary-coolant lithium and air. The containment building is also filled with argon cover gas. In order to reduce

Table 1.3-VII.

CREEP-RUPTURE TIME FOR TITAN-I FIRST WALL

Primary Stress, $\sigma_p$ (MPa)	Rupture Time, $t_r$ (h)
10	3200
20	360
30	101
40	41
50	20

the consequences of a lithium spill, two sets of lithium-drain tanks are provided to drain the maximum amount of lithium in less than 30 seconds.

For the perceived worst-accident condition of a lithium fire with breach of all barriers and no argon cover gas, the maximum combustion-zone temperature is found to be less than 1000°C. The tritium release in this case would be about 60 Ci which is quite acceptable under this worst-accident scenario. Of critical concern in the lithium-fire scenario is the formation and release of vanadium oxide  $V_2O_5$ . Further measurement of vanadium-oxide formation and its vapor pressure with temperature, and the calculation of potential releases to the public based on the TITAN-I configuration and accident scenarios should be performed.

The total tritium inventories in the lithium primary and secondary loops are 344 and 300 g, respectively. These are acceptable inventories when passive drain tanks are used to control the amount of possible tritium releases. The tritium inventory in the blanket structure is less than 10 g, which is also acceptable. The tritium-leakage rate from the primary loop was estimated to be 7 Ci/d which is within the 10 Ci/d design goal.

Plasma-accident scenarios need to be further evaluated as the physics behavior of RFPs becomes better understood. Preliminary results indicate that passive safety features can be incorporated into the design, such that the accidental release of plasma and magnetic energies can be distributed without leading to major releases of radioactivity. Research activities in this area need to be continued, especially for high-power-density devices.

Based on the analyses summarized above, TITAN-I does not need to rely on any active safety systems to protect the public. A LOFA will result in no radioactive release and will not lead to a more serious LOCA. A complete LOCA from credible events is not possible. Only the assurance of coolant-piping and vacuum-vessel integrity is necessary to protect the public. The TITAN-I design, therefore, meets the definition of level 3 of safety assurance, "small-scale passive safety assurance" [15,16]. Pending information on the vanadium-oxide formation and release from the TITAN-I vacuum chamber under the lithium-fire accident scenario, the qualification of TITAN-I as a level-2 of safety assurance design, "large-scale passive safety assurance," may also be possible.

#### 1.3.10. Waste Disposal

The neutron fluxes calculated for the reference TITAN-I reactor were used as input to the activation calculation code, REAC [80]. These results were analyzed to obtain the

allowable concentrations of alloying and impurity elements in TITAN-I FPC components. Waste-disposal analysis has shown that the compact, high-power density TITAN-I reactor can be designed to meet the criteria for Class-C waste disposal [81]. The key features in achieving Class-C waste in the TITAN-I reactor are attributed to: (1) materials selection and (2) control of impurity elements.

The materials selected for the TITAN-I FPC are the vanadium alloy, V-3Ti-1Si, and lithium. The main alloying elements of V-3Ti-1Si do not produce long-lived radionuclides with activity levels exceeding the limits for Class-C disposal (no limit on the concentration of vanadium and titanium and 23% allowable concentration of silicon which is much larger than 1% content of Si in V-3Ti-1Si). The allowable concentrations of various impurities in the vanadium structural material of the TITAN-I reactor are listed in Table 1.3-VIII. Some of these impurity elements, mainly niobium and possibly silver, terbium, and iridium, need to be controlled in the vanadium alloy below appm levels.

Table 1.3-VIII.

**MAXIMUM CONCENTRATION LEVELS OF IMPURITIES IN TITAN-I  
REACTOR COMPONENTS TO QUALIFY AS CLASS-C WASTE**

Element	Major Nuclide (Activity Limit) <sup>(a)</sup>	Components			Nominal Level
		FW & Blanket (1 FPY) <sup>(b)</sup>	Hot Shield (5 FPY) <sup>(b)</sup>	OH Magnets (30 FPY) <sup>(b)</sup>	
Nb (appm)	<sup>94</sup> Nb (0.2 Ci/m <sup>3</sup> )	5.	1.4	0.5	0.1
Mo (appm)	<sup>99</sup> Tc (0.2 Ci/m <sup>3</sup> ) <sup>94</sup> Nb (0.2 Ci/m <sup>3</sup> )	65.	100.	90.	1.0
Ag (appm)	<sup>108m</sup> Ag (3 Ci/m <sup>3</sup> )	1.3	1.5	0.7	1.0
Tb (appm)	<sup>158</sup> Tb (4 Ci/m <sup>3</sup> )	0.4	0.6	7.0	5.0
Ir (appm)	<sup>192m</sup> Ir (2 Ci/m <sup>3</sup> )	0.1	0.1	0.02	5.0
W	<sup>186m</sup> Re (9 Ci/m <sup>3</sup> )	5%	9%	100%	0.89%

(a) From Reference [80].

(b) Based on operation at 18 MW/m<sup>2</sup> of neutron wall loading with 76% availability.

Table 1.3-IX summarizes the TITAN materials and related quantities for Class-C disposal. The total weight in the FPC of the TITAN-I reactor is about 1363 tonnes, of which about 73% is from the magnet systems (OH and EF coils, and EF shield) that last the plant lifetime. The reactor torus (first wall, blanket, and the divertor module) is replaced annually and constitutes only 4% of the total weight of the FPC. The balance of the weight is from the shield which has a five-year lifetime. The average annual-replacement mass of the FPC is about 150 tonnes.

The TITAN-I divertor plates are fabricated with a tungsten armor because of its low sputtering properties. The waste-disposal rating of the divertor plates is estimated to be a factor of 10 higher than for Class-C disposal after one year of operation. The annual disposal mass of this non-Class-C waste is 0.35 tonnes, about 0.23% of the average annual discharge mass.

The conclusions derived from the TITAN-I reactor study are general, and provide strong indications that Class-C waste disposal can be achieved for other high-power-density approaches to fusion. These conclusions also depend on the acceptance of recent evaluations of specific activity limits carried out under 10CFR61 methodologies [82].

#### 1.3.11. Maintenance

The TITAN reactors are compact, high-power-density designs. The small physical size of these reactors permits each design to be made of only a few pieces, allowing a single-piece maintenance approach [7,8]. Single-piece maintenance refers to a procedure in which all of components that must be changed during the scheduled maintenance are replaced as a single unit, although the actual maintenance procedure may involve the movement, storage, and reinstallation of some other reactor components. In TITAN designs, the entire reactor torus is replaced as a single unit during scheduled maintenance. Furthermore, because of the small physical size and mass of the TITAN-I FPC, the maintenance procedures can be carried out through vertical lifts, allowing a much smaller reactor vault.

Potential advantages of single-piece maintenance procedures are identified:

1. Shortest period of downtime resulting from scheduled and unscheduled FPC repairs;
2. Improved reliability resulting from integrated FPC pretesting in an on-site, non-nuclear test facility where coolant leaks, coil alignment, thermal-expansion effects, *etc.*, would be corrected by using rapid and inexpensive hands-on repair procedures prior to committing the FPC to nuclear service;

Table 1.3-IX.

**SUMMARY OF TITAN-I REACTOR MATERIALS AND RELATED  
WASTE QUANTITIES FOR CLASS-C WASTE DISPOSAL**

Component	Material	Lifetime (FPY) <sup>(a)</sup>	Volume (m <sup>3</sup> )	Weight (tonnes)	Annual
					Replacement Mass (tonnes/FPY)
First wall	V-3Ti-1Si	1	0.4	2.5	2.5
Blanket (IBC)	V-3Ti-1Si	1	6.4	39.2	39.2
Shield (zone 1)	V-3Ti-1Si	5	15.5	95.6	19.1
Shield (zone 2)	V-3Ti-1Si	5	28.0	172.0	34.4
OH coils	Modified steel	30	3.8	34.0	1.1
	Copper		26.6	239.0	8.0
	Spinel		3.8	15.2	0.5
	Total		34.2	289.2	9.6
EF coils	Modified steel	30	43.0	315.0	10.5
EF shield	Modified steel	30	43.9	347.0	11.6
	B <sub>4</sub> C		18.8	47.0	1.6
	Total		62.7	394.0	13.2
Divertor shield					
zone 1	V-3Ti-1Si	1	2.3	14.2	14.2
zone 2	V-3Ti-1Si	5	6.7	41.2	8.2
TOTAL CLASS-C WASTE			199.	1363.	151.

(a) Based on operation at 18 MW/m<sup>2</sup> of neutron wall loading with 76% availability.

3. No adverse effects resulting from the interaction of new materials operating in parallel with radiation-exposed materials;
4. Ability to modify continually the FPC as may be indicated or desired by reactor performance and technological developments; and
5. Recovery from unscheduled events would be more standard and rapid. The entire reactor torus is replaced and the reactor is brought back on line with the repair work being performed, afterwards, outside the reactor vault.

The lifetime of the TITAN-I reactor torus (first wall, blanket, and divertor modules) is estimated to be in the range of 15 to 18 MWy/m<sup>2</sup>, and the more conservative value of 15 MWy/m<sup>2</sup> will require the change-out of the reactor torus on a yearly basis for operation at 18 MW/m<sup>2</sup> of neutron wall loading at 76% availability. The lifetime of the hot shield is estimated to be 5 years and, therefore, to reduce the rad-waste, the TITAN-I hot shield is made of two pieces with the upper hot shield removed during the maintenance procedures and reused in the next replacement of the reactor torus.

Seventeen principal tasks must be accomplished for the annual, scheduled maintenance of the TITAN-I FPC. These steps are listed in Table 1.3-X. The tasks which would require a longer time to complete in a modular design are also identified in Table 1.3-X (assuming the same configuration for the modular design as that of TITAN-I). Vertical lifts have been chosen for the component movements during maintenance. Lift limits for conventional bridge cranes is around 500 tonnes, with special-order crane capacities in excess of 1000 tonnes. The most massive components lifted during TITAN-I maintenance are the upper OH-coil set (OH coils 2 through 5) and the upper hot shield each weighing about 150 tonnes, which are easily manageable by the conventional cranes. The four major component lifts are illustrated in Figure 1.3-14.

An important feature of the TITAN design is the pretest facility. This facility allows the plant personnel to test fully the new torus assemblies in a non-nuclear environment prior to committing it to full-power operation in the reactor vault. Any faults discovered during pretesting can be quickly repaired using inexpensive hands-on maintenance. Furthermore, additional testing can be used as a shake-down period to reduce the infant mortality rate of the new assemblies. A comprehensive pretest program could greatly increase the reliability of the FPC, hence increasing the plant overall availability. The benefits of pretesting (higher reliability, higher availability) must be balanced with the additional cost associated with the pretest facility. The more representative the pretests are of the actual operation, the more duplication of the primary-loop components is required. A detailed list of pretests for the TITAN-I design is included in Table 1.3-XI.

**Table 1.3-X.**  
**PRINCIPAL TASKS**  
**DURING THE TITAN-I MAINTENANCE PROCEDURE**

---

1. Orderly shutdown of the plasma and discharge of the magnets;
2. Continue cooling the FPC at a reduced level until the decay heat is sufficiently low to allow cooling by natural convection in the argon atmosphere;
3. During the cool-down period:
  - a. Continue vacuum pumping until sufficient tritium is removed from the FPC,
  - b. Break vacuum (valve-off vacuum pumps and cut weld at vacuum tank lid),<sup>(a)</sup>
  - c. Remove vacuum-tank lid to the lay-down area,
  - d. Disconnect electrical and coolant supplies from the upper OH-coil set;
4. Drain lithium from the FPC;
5. Lift OH-coil set and store in the lay-down area;
6. Disconnect lithium-coolant supplies;<sup>(a)</sup>
7. Lift upper shield and store in the lay-down area;
8. Lift the reactor torus and move to the hot cell;<sup>(a)</sup>
9. Inspect FPC area;
10. Install the new, pretested torus assembly;<sup>(a)</sup>
11. Connect lithium supplies;<sup>(a)</sup>
12. Replace upper shield and connect shield-coolant supplies;
13. Replace the upper OH-coil set and connect electrical and coolant supplies;
14. Hot test the FPC;<sup>(b)</sup>
15. Replace vacuum-tank lid and seal the vacuum tank;<sup>(a)</sup>
16. Pump-down the system;<sup>(c)</sup>
17. Initiate plasma operations.

---

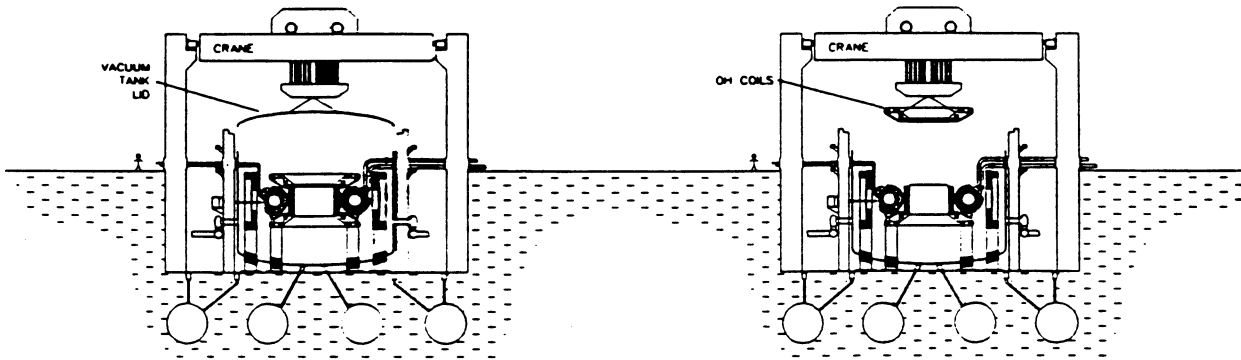
(a) The time required to complete these tasks is likely to be longer for a modular system than for a single-piece system, assuming similar configuration.

(b) The new torus assembly is pretested and aligned before commitment to service. Only minimal hot testing would be required.

(c) The TITAN-I reactor building is filled with argon gas and the replacement torus is also stored in argon atmosphere. Therefore, the pump-down time would be short.

(1) VACUUM TANK LID

(2) UPPER OH COILS



(3) UPPER HOT SHIELD

(4) TORUS ASSEMBLY

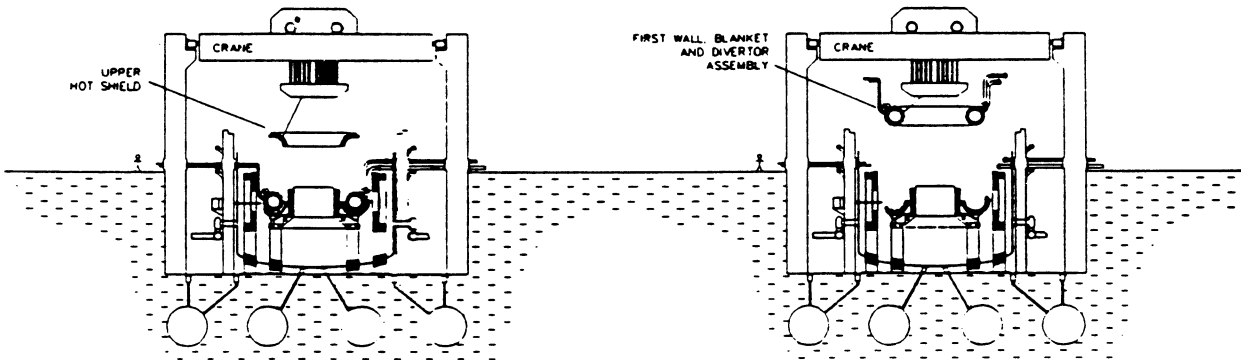


Figure 1.3-14. Four major crane lifts required for the TITAN-I maintenance.

Table 1.3-XI.

## MAIN PREOPERATIONAL TESTING OF THE TITAN-I FPC

Test	Sub-Module <sup>(a)</sup>	Module <sup>(a)</sup>	Full Torus <sup>(b)</sup>	
			No Plasma	Plasma <sup>(c)</sup>
<b>Mechanical</b>				
• Tube-bank vibration (first wall, blanket)	X	X	X	
• Tube-bank expansion (first wall, blanket)	X	X	X	
• Inter-module and full-torus deflection			X	
• Plasma chamber (shell)/coil displacement			X	
<b>Thermal Hydraulic</b>				
• Flow rates, pressure drops, leaks, ... :			X	
★ First wall, divertor, blanket, shield	X			
★ Coils			X	
★ Manifolds, headers			X	
• "Hot" FPC test, (pressure drops, vibrations, ...)			X	
★ Electrically heated coolant			X	
★ Plasma-driven heat fluxes				X
• Remote coupling, disconnects	X	X	X	
<b>Electrical</b>				
• Magnet test (forces, deflection, voltages, ...)			X	X
• Vacuum-field mapping (TF ripple, vertical field, ...)			X	
• Plasma transients				
★ RFP formation			X	X
★ Fast-ramp phase			X	X
★ Slow-ramp phase				X
• Current-drive (steady-state) phase				X
• Active feedback control			X	X
• Eddy currents (start-up, OFCD)				
★ First wall and shell			X	X
★ Blanket and shield			X	X
★ Coil casing, structure, pumps, ...			X	X
• Termination control/response				X
<b>Vacuum, Fueling, and Impurity-Control Systems</b>				
• Base vacuum			X	
• Full gas-load test			X	
• Pellet injection				X
<b>Neutronics</b>				
• Breeding efficiency				X
• Energy-recovery efficiency				X
• Shielding effectiveness, streaming				X

(a) Performed at factory site.

(b) Performed at plant site during operational year.

(c) Performed in the reactor vault during the scheduled maintenance.

### 1.3.12. Summary and Key Technical Issues

The TITAN-I design is a lithium, self-cooled design with a vanadium alloy (V-3Ti-1Si) structural material. Magnetohydrodynamics (MHD) effects had precluded the use of liquid-metal coolants for high-heat-flux components in previous designs (mainly of tokamaks), but the magnetic field topology of the RFP is favorable for liquid-metal cooling. In the TITAN-I design, the first wall and blanket consist of single pass, poloidal-flow loops aligned with the dominant poloidal magnetic field. Other major features are: separation of the first-wall and blanket coolant circuits to allow a lower coolant-exit temperature from the first wall; and use of MHD turbulent-flow heat transfer at the first wall, made possible by the low magnetic interaction parameter. The TITAN-I thermal-hydraulic design (Table 1.3-II) can accommodate up to  $5 \text{ MW/m}^2$  of heat flux on the first wall with a reasonable MHD pressure drop, a high thermal-cycle efficiency, and a modest pumping power of about 45 MWe. A molten-salt tritium-extraction technique is used.

A unique feature of the TITAN-I design is the use of the integrated-blanket-coil (IBC) concept [14]. With the IBC concept, the lithium coolant in the blanket circuit flowing in the poloidal direction is also used as the electrical conductor of the toroidal-field and divertor coils. The IBC concept eliminates the need for shielding the coils and allows direct access to the blanket and shield assemblies, thereby easing the maintenance procedure.

The general arrangement of the TITAN-I reactor is illustrated in Figures 1.1-1, 1.1-2, and 1.3-1 to 1.3-4. The operational (maintenance and availability), safety, and environmental issues have been taken into account throughout the design. For example, the entire FPC is contained in a vacuum tank to facilitate the remote making and breaking of vacuum welds. All maintenance procedures would be performed by vertical lift of the components (heaviest component weighs about 250 tonnes), reducing the size of the expensive containment building. The compactness of the TITAN designs would reduce the FPC to a few small and relatively low-mass components, making toroidal segmentation unnecessary. A "single-piece" FPC maintenance procedure, in which the first wall and blanket are removed and replaced as a single unit is, therefore, possible. This unique approach permits the complete FPC to be made of a few factory-fabricated pieces, assembled on site into a single torus, and tested to full operational conditions before installation in the reactor vault. The low cost of the FPC means a complete, "ready-for-operation" unit can be kept on-site for replacement in case of unscheduled events. All of these features are expected to improve the plant availability.

All of the FPC primary-coolant ring-headers are located above the torus for ease of access during maintenance. This arrangement also ensures that the coolant will remain in the torus in the event of a break in the primary piping. The most severe safety event will be a loss-of-flow accident (LOFA). The FPC and the primary coolant loop are located in an inert-gas-filled (argon) confinement building which, together with the blanket containers and the vacuum vessel, form three barriers to prevent air influx, thereby reducing the hazards of lithium fires and providing protection for the public from radioactive materials. Lithium-drain tanks are provided for both the reactor vault and the vacuum tank to reduce passively the vulnerable blanket-lithium inventory.

A low-activation, low-after-heat vanadium alloy is used as the structural material throughout the FPC in order to minimize the peak temperature during a LOFA and to permit near-surface disposal of waste. The maximum temperature during a first-wall LOCA and system LOFA (the most severe accident postulated for TITAN-I) is 990 °C. Lithium-fire accident scenarios and site-boundary dose calculations were performed to understand the potential release of radioactivity under major accident and routine release conditions. The safety analysis indicates that the liquid-metal-cooled TITAN-I design can be classified as passively safe, without reliance on any active safety systems. A high level of safety assurance [15,16] for the compact TITAN-I design, therefore, is expected.

The results from the TITAN study support the technical feasibility, economic incentive, and operational attractiveness of compact, high mass-power-density RFP reactors. The road towards compact RFP reactors, however, contains major challenges and uncertainties, and many critical issues remain to be resolved. The key engineering issues for the TITAN-I FPC have been discussed. In the area of materials, more data on irradiation behavior of V-3Ti-1Si, especially irradiation-induced swelling, are needed to confirm the materials prediction and to estimate accurately the lifetime of the TITAN-I first wall. Further creep-rupture experiments are also needed to develop more precise creep-rupture models for V-3Ti-1Si. Compatibility of vanadium-base alloy with lithium coolant and the effects of a bi-metallic loop also require more experimental data. Ceramic insulators offer the potential of minimum irradiation-induced conductivity, high melting and decomposition temperature, retention of strength, and minimum irradiation-induced swelling. Further experimental data on irradiation behavior of these insulators are needed.

The low value of the toroidal field in the RFP allows high coolant velocities to be achieved without prohibitive MHD pressure drops, thus permitting operation in the turbulent-flow regime, with the associated high heat-transfer coefficients. Further experimental data on turbulent-flow heat-transfer capability of liquid metals, especially in the TITAN-relevant operational regime of low magnetic field and high velocities, are

crucial to verify the TITAN-I thermal-hydraulic design. The combined effect, if any, of the parallel and perpendicular magnetic fields on flow transition and turbulent-flow heat transfer should also be investigated. The MHD pressure drop equations for bend, contraction, and a varying magnetic field need to be substantiated by further large-scale experiments and numerical and theoretical analyses. The effect of nonuniform heat flux on the heat-transfer capability (or Nusselt number) and volumetric nuclear heating in the coolant on the film temperature drop should be further studied.

The TITAN-I poloidal-field-coil system requires little or no extrapolation of current technology. But, the TITAN-I TF and divertor IBC design encounters several critical engineering issues. The most critical issue is the design of low-voltage, high-current power supplies for these coils. The requirement of oscillating voltages and currents for the OFCD compounds the IBC power-supply issues. The copper-coil option for both TF and divertor coils, similar to the TITAN-II design, is also possible.

The design of the impurity-control system poses some of the most severe problems of any component of a DT fusion reactor, and for a compact or high-power-density design these problems can be particularly challenging. Physics operation of high-recycling toroidal-field divertors in RFPs should be experimentally demonstrated and the impact of OFCD on the divertor performance studied. Cooling of the TITAN-I divertor plate requires experimental data on turbulent-flow heat transfer in liquid-metal systems, as outlined above. Fabrication of the tungsten divertor plate remains to be demonstrated and the degree of precision needed for target shaping and control of the position of the plasma separatrix are particularly difficult tasks.

The TITAN-I molten-salt tritium-recovery process needs large-scale demonstration. Any fusion reactor with vanadium first walls may encounter the problem of plasma-driven permeation (PDP) of tritium. The extent of PDP should be experimentally investigated.

The TITAN-I design uses many safety-design features to achieve a high level of safety assurance. Further detailed analysis of the response of the TITAN-I FPC to loss-of-flow and loss-of-coolant accidents, including lithium fires, are needed to confirm the findings. Data are needed on elevated temperatures of vanadium alloys such as the recrystallization temperature, the onset temperatures and the extent of volatilization of radioactive products in vanadium, and the formation and release of vanadium oxide,  $V_2O_5$ . In addition, in order to qualify for Class-C waste disposal, some of the impurity elements (mainly niobium and possibly silver, terbium, and iridium) need to be controlled in the vanadium alloy to below ppm levels.

## 1.4. OVERVIEW OF TITAN-II FUSION POWER CORE

### 1.4.1. Configuration

Detailed subsystem designs for the TITAN-II FPC are given in Sections 16 through 20. The parameters of the TITAN-II reference design point, based on detailed subsystem designs, are included in Appendix B and follow the DOE/OFE standard reporting format. Appendix B also includes detailed cost tables and parametric systems code predictions of subsystem parameters for comparison with DOE/OFE tables. The elevation view of the FPC is shown in Figure 1.4-1. Figures 1.1-4 and 1.1-5 show the general arrangement of the TITAN-II reactor.

The major feature of the TITAN-II reactor is that the entire primary loop is located at the bottom of a low-temperature, atmospheric-pressure pool of pure water (Figure 1.4-1). Detailed safety analyses have been performed (Section 19) which show that the TITAN-II pool can contain the afterheat energy of the FPC and will remain at a low enough temperature such that tritium or other radioactive material in the primary-coolant system will not be released.

The TITAN plasma is ohmically heated to ignition by using a set of normal-conducting ohmic-heating (OH) coils and a bipolar flux swing. The TITAN start-up requires minimum on-site energy storage, with the start-up power directly obtained from the power grid (maximum start-up power is 500 MW). The TITAN-II OH coils are cooled by pure water. A pair of relatively low-field superconducting equilibrium-field (EF) coils produce the necessary vertical field and a pair of small, copper EF trim coils provide the exact equilibrium during the start-up and OFCD cycles. The poloidal-field-coil arrangement allows access to the complete reactor torus by removing only the upper OH-coil set. The toroidal-field (TF) and divertor coils of TITAN-II are also composed of copper alloy.

The first wall and blanket of the TITAN-II design are integrated in the form of blanket lobes (Figure 1.4-2). The construction procedure for each blanket lobe is shown in Figure 1.4-3. The blanket lobe is made of two plates, called "J-plates" because one edge of each plate is rolled to the appropriate radius to form a J-section. Both J-plates are made of the low-activation, high-strength ferritic steel, 9-C [17]. The first-wall plate is thicker than the other plate, since it is subject to erosion. Two plates are then brazed or welded together to form a complete blanket lobe. A channel manifold ring completes the lobe and allows the coolant and breeder mixture to flow. This configuration will require a multistage pressing operation, perhaps even hot-pressing to achieve this shape.

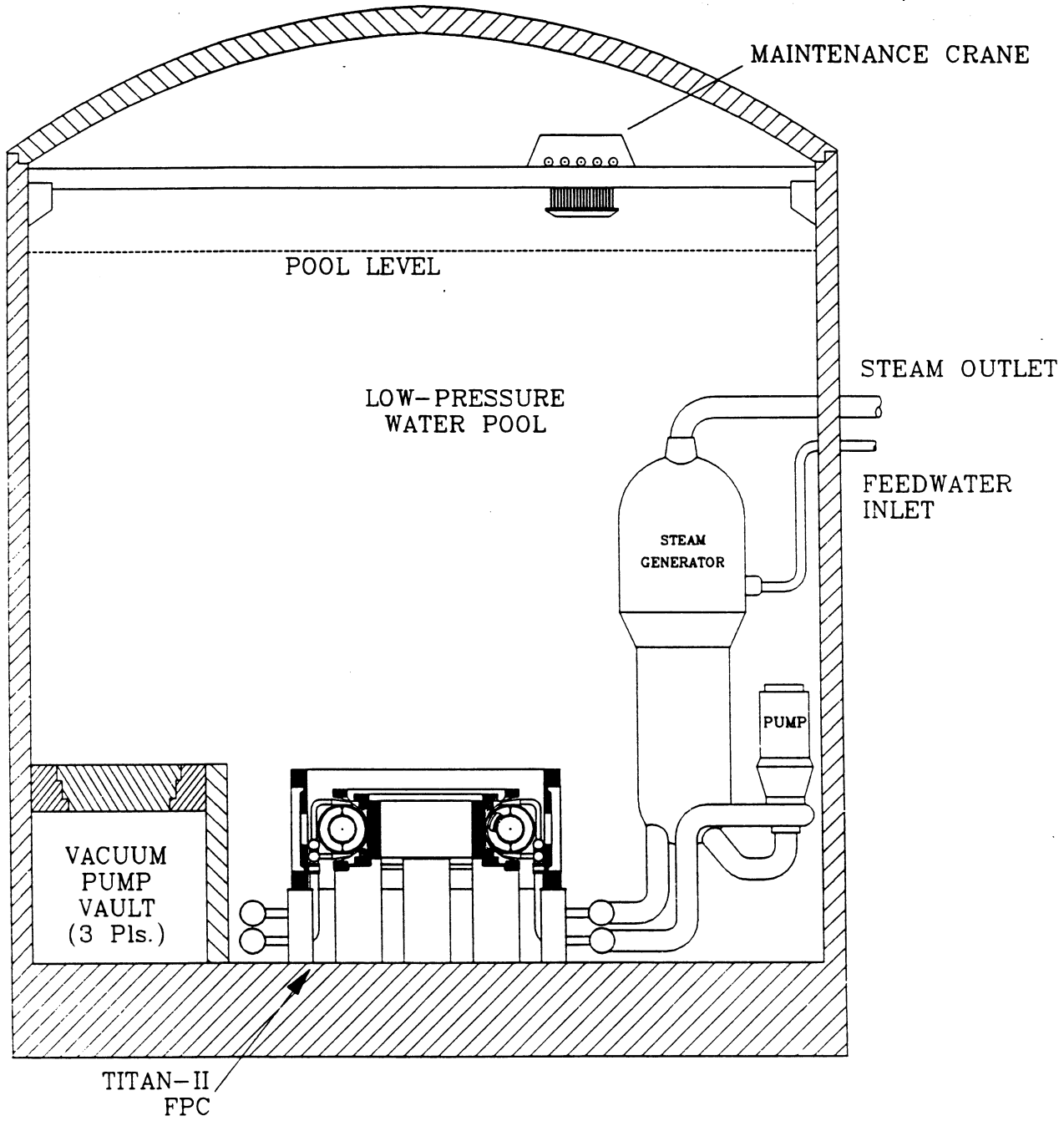


Figure 1.4-1. Elevation view of the TITAN-II reactor building through the reactor centerline showing the water pool and the maintenance crane.

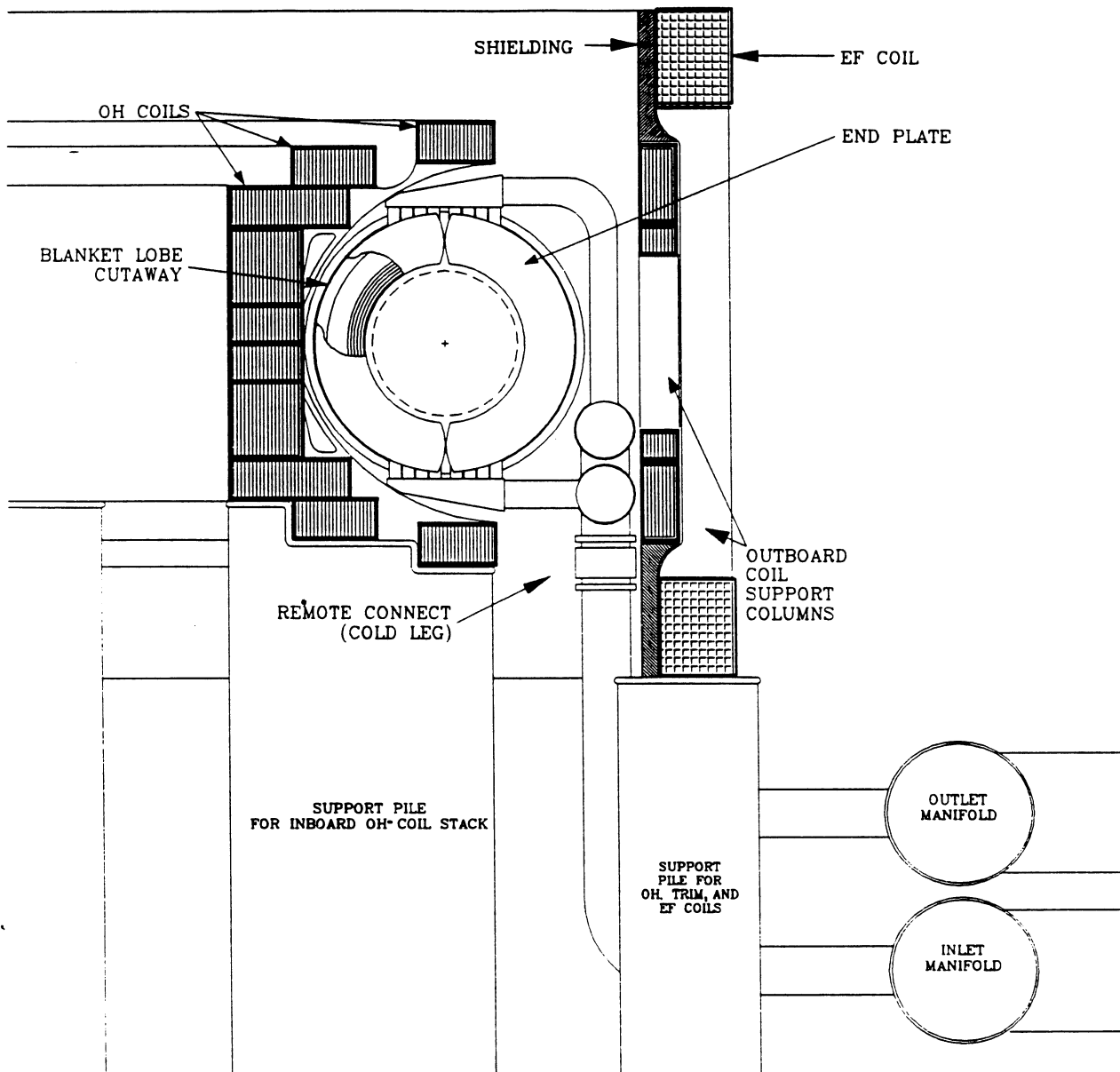


Figure 1.4-2. Poloidal cross section of the TITAN-II fusion power core.

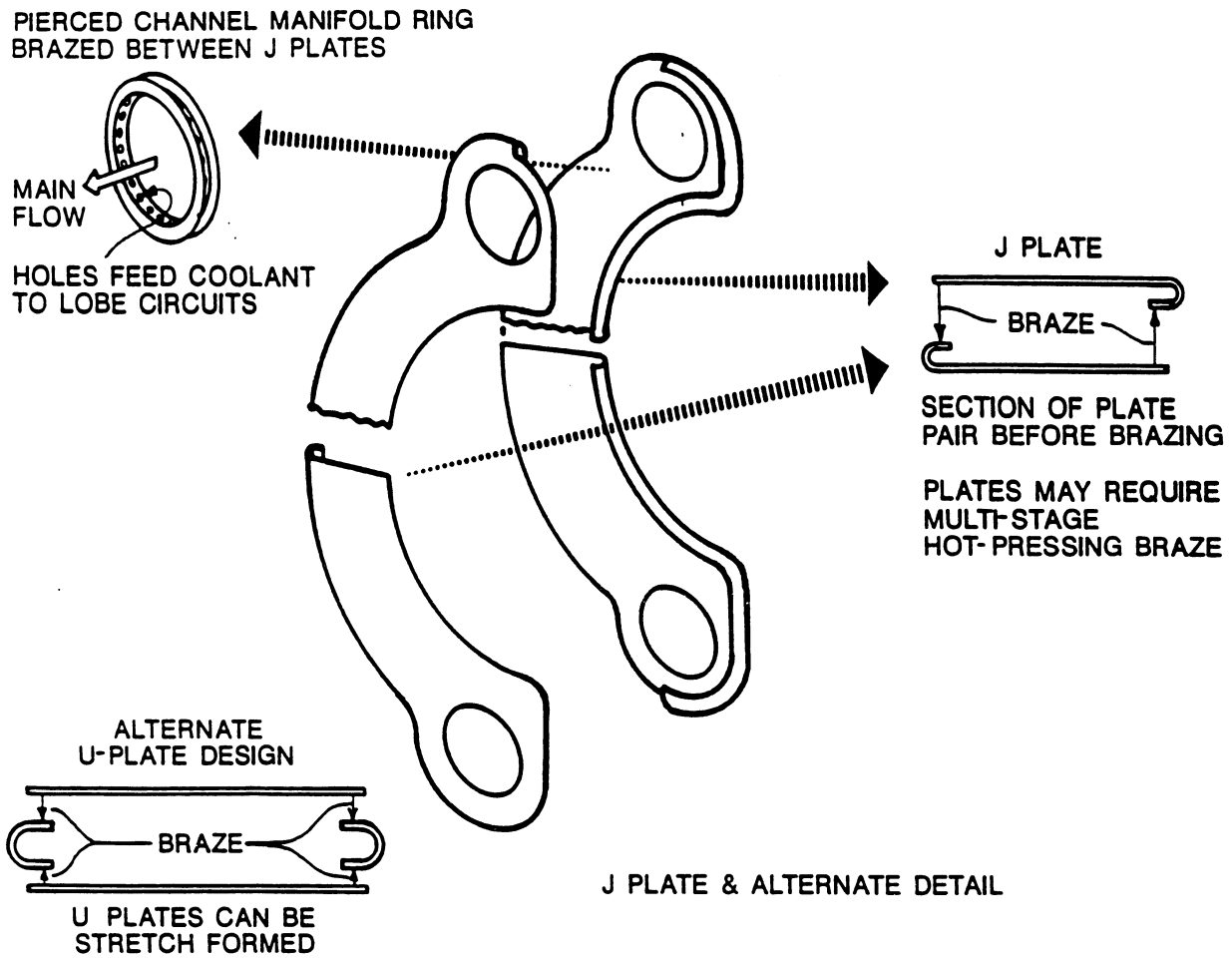


Figure 1.4-3. The TITAN-II blanket lobe, J-plate design.

An alternate design, also shown in Figure 1.4-3, is the U-plate design. The advantages of this design are that the thin material can be used for both sides, and the edge U members are easier to make than the J-plates. However, acceptance of either configuration will depend on detailed investigation of the thick braze or weld area to ensure that there is no focusing of thermal radiation or other heat-transfer problems.

The outer dimensions of the blanket lobes are 3 cm toroidally and 30 cm radially. The lobe wall thickness is 1.4 mm. The cross section of the first wall is a semicircular channel with the convex side facing the plasma. The outer diameter is 3 cm, and the wall thickness of 1.5 mm includes a 0.25-mm allowance for erosion (the first-wall erosion is estimated to be negligible). A neutron multiplier zone is located behind the first wall and contains 7 rows of beryllium rods clad in 9-C alloy, with a diameter of 2.6 cm. The thickness of the clad is 0.25 mm. The multiplier zone is 20-cm long in the radial direction and contains 12% structure, 59% beryllium, and 29% coolant (all by volume). Nuclear heating rate in the blanket decreases away from the first wall, therefore, to ensure proper coolant velocity, poloidal flow separators are placed behind the 2nd, 4th, and 7th rows of beryllium rods to form channels which have individual orifices. The remaining 10 cm of the blanket lobe (the breeder/reflector zone) does not contain beryllium and consists of 9% structure and 91% coolant (by volume).

Seventy blanket lobes are then stacked side-by-side to form a blanket module. The structural details of a blanket module are shown in Figure 1.4-4. This arrangement is structurally a membrane pressure vessel with balancing forces, which are derived from identical neighboring lobes, maintaining its flat sides. This configuration requires an external constraining structure to keep it pressed into oval form which is readily derived from the shield as discussed below. The advantage of this design is that the structural fraction in the important near-first-wall radial zone is nearly as low as ideally possible, giving good tritium-breeding performance. This configuration also has a much lower void fraction when compared to a tubular design, giving a minimum-thickness blanket. The assembly technique for each blanket module is expected to be multistage brazing with intermediate leak checking. Since the lobes only require constraint in the blanket toroidal direction, and they are structurally soft in this direction, high precision is not necessary.

The TITAN-II FPC consists of three sectors, separated by the divertor modules. Four blanket modules are assembled together to form a sector. The shield is made of cast half-ring sectors, welded together at the inside edge (Figure 1.4-4) to form a blanket container. The shield is 10-cm thick in the radial direction and contains two rows of circular coolant channels. The volume percentages of structure and coolant in the shield are 90% and 10%, respectively.

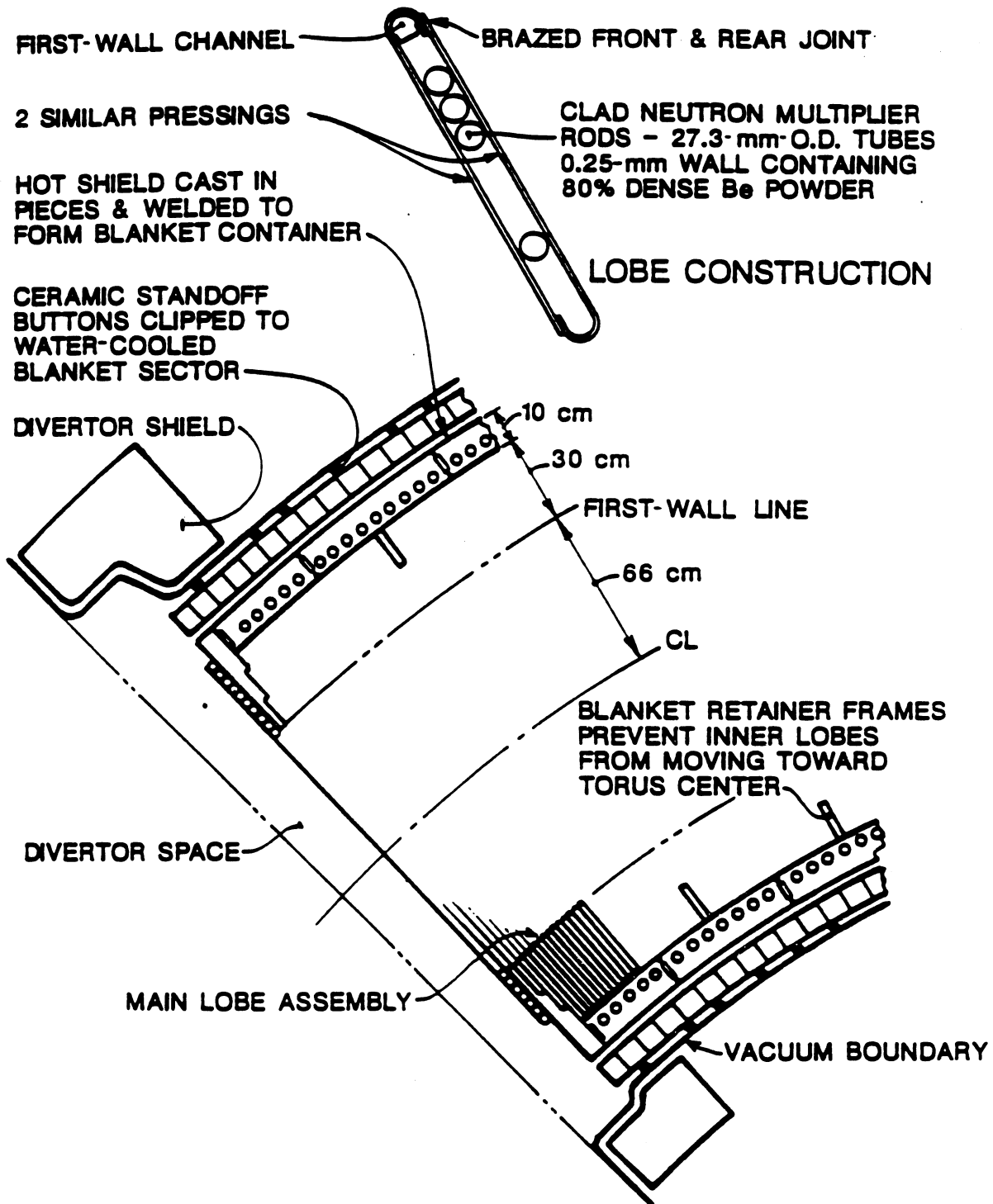


Figure 1.4-4. Equatorial-plane cross section of a TITAN-II blanket module.

The split at the top and bottom of the torus divides the blanket and the shield into inner and outer half shells which are structurally independent. The coolant channels are in the poloidal direction. The coolant enters at the bottom and exits at the top of the torus. One set of coolant channels runs along the out-board side of the torus and the other along the in-board side. The tendency of the flat sides of a sector to blow out has to be resisted by what are, in effect, the divertor walls (Figure 1.4-4). These walls are 12-cm-thick cantilever beam members which also derive some of their strength from their torsional stiffness and will require internal cooling. These walls are anchored to the shield shell by welds at the inside and outside of the shield.

Immediately behind the shield there is a 5-cm-thick zone occupied by the toroidal field (TF) coil which is a multi-turn copper coil held in position by ceramic standoffs from the shield (Figure 1.4-4). The design of the TF-coil support elements is straightforward since the gravitational and magnetic forces on the TF coils are relatively small and are carried externally.

The vacuum boundary is a continuous, 5-mm-thick metal shell immediately outside the TF coil. Because of the large toroidal radius of 5.06 m, such a shell cannot withstand the atmospheric and water-pool pressures totaling about 3 atm without buckling. Accordingly, since the working stress is only about 7 MPa, nonconducting stabilizers similar to those used for the 5-cm-thick TF coil can be used. If necessary, the vacuum boundary can be electrically insulated in the toroidal direction by alternate layers of soft aluminum and hard, anodized 7075 aluminum-alloy sheets. The soft aluminum provides a deformable vacuum seal, and the anodized layer provides the electrical insulation. The two vacuum boundary skins can then be held together by 15-mm-thick stainless-steel, insulator-lined swagged clamps. Details of this method of vacuum-vessel insulation will still need to be demonstrated.

A number of electrically insulated penetrations of the vacuum shell also have to be made for the TF-coil leads. It is envisaged that the technology of automotive spark plugs can be developed to do this job. This consists of the embedment of a precision ceramic insulator in soft metal (usually copper) gaskets. This technique is presently available for diameters an order of magnitude larger than spark plugs, and its extension to sizes relevant to our task appears feasible. This also needs to be developed.

A skirt, welded to the lower header system and extended to the pool bottom, will support the entire removable first wall, blanket, and shield assembly. This skirt will be of open-frame form to allow free circulation of the pool.

The lifetime of the TITAN-II reactor torus (including the first wall, blanket, shield, and divertor modules) is estimated to be in the range of 15 to 18 MWy/m<sup>2</sup>, with the more conservative value of 15 MWy/m<sup>2</sup> requiring the change-out of the reactor torus on a yearly basis for operation at 18 MW/m<sup>2</sup> of neutron wall loading at 76% availability. The TF coils are designed to last the entire plant life (30 full-power years). However, during the maintenance procedure, the TF coils are not separated from the reactor torus and are replaced each year. After the completion of the maintenance procedure, the used TF coils can be separated from the reactor torus and reused at a later time. The impact of discarding (not reusing) the TF-coil set annually is negligible on the COE.

#### 1.4.2. Materials

The TITAN-II FPC is cooled by an aqueous lithium-salt solution which also acts as the breeder material [83]. Issues of corrosion and radiolysis, therefore, greatly impact the choice of the dissolved lithium salt and the structural material.

Two candidate lithium salts, lithium hydroxide (LiOH) and lithium nitrate (LiNO<sub>3</sub>), are considered because they are highly soluble in water. The LiNO<sub>3</sub> salt is selected as the reference salt material for two main reasons. First, LiOH is more corrosive than LiNO<sub>3</sub> (Section 16.2.1). Recently, electrochemical corrosion tests were performed for LiOH and LiNO<sub>3</sub> aqueous solutions in contact with AISI-316L stainless steels [84]. It was found that stainless steels, particularly low-carbon steels, exhibit better corrosion resistance in an LiNO<sub>3</sub> solution than in LiOH. From the point of view of radiolysis, lithium-nitrate solutions are also preferable. Radiolytic decomposition of water results in the formation of free radicals that will ultimately form highly corrosive hydrogen peroxide and OH ions. Nitrate ions (NO<sub>3</sub><sup>-</sup>) in a lithium-nitrate solution, act as scavengers to reduce the probability of survival of highly reactive radicals in the water during exposure to radiation (Section 16.2.2).

Among the candidate low-activation vanadium alloys, V-3Ti-1Si (the structural material for the TITAN-I design) had to be ruled out because of its poor water-corrosion resistance. Other vanadium alloys which contain chromium (*e.g.*, V-15Cr-5Ti) show excellent resistance to corrosion by water coolant but their properties are inferior to those of ferritic steels when helium-embrittlement effects are taken into account [85] (Section 10.2). Therefore, various steels were considered as TITAN-II structural material.

Reported results of the low-activation ferritic-steel (LAFS) development program indicate that a reduced-activation alloy can be developed without compromising mechanical properties, primarily by replacing Mo with W. For the TITAN-II reactor, the

HEDL/UCLA 12Cr-0.3V-1W-6.5Mn alloy (alloy 9-C) has been chosen as the structural material primarily because of its high strength and good elongation behavior after irradiation as compared with other LAFs [17]. The high chromium content of this alloy ensures an excellent corrosion resistance. The low carbon content of this alloy results in good weldability, high sensitization resistance (Section 16.2.1), and reduces hydrogen-embrittlement susceptibility (Section 16.2.5). Furthermore, alloy 9-C has a low tungsten content ( $< 0.9\%$ ) which reduces the waste-disposal concerns of the production of the radionuclide  $^{186m}\text{Re}$  by fusion-neutron reaction with W [86]. The high concentration of manganese in alloy 9-C prevents the formation of delta-ferrite phases, which is responsible for high ductile-to-brittle transition temperature (DBTT) and low hardness. The composition (wt.%) of alloy 9-C was determined by the vendor as: 11.81Cr, 0.097C, 0.28V, 0.89W, 6.47Mn, 0.11Si, 0.003N,  $< 0.005\text{P}$ ,  $0.005\text{S}$  with the balance in iron.

Radiolytic decomposition of aqueous solutions exposed to a radiation environment is always cause for concern. Radiolysis of pure water and of aqueous  $\text{LiNO}_3$  salt solutions by light particles ( $e$ ,  $\gamma$ , X ray) and heavy particles ( $n$ ,  $p$ ,  $T$ ,  $\alpha$ ) was investigated. Gamma-ray radiolysis yields of  $\text{LiNO}_3$  salt solutions are known as a function of salt concentration. At high concentrations, the  $\text{H}_2$  yields are very small and the  $\text{H}_2\text{O}_2$  yield decreases by a factor of about 3 relative to pure water. Oxygen yields of light-particle radiation are fairly independent of the salt concentration.

Energetic alpha particles ( $\sim 2\text{ MeV}$ ) are produced by nuclear reactions with lithium in the aqueous  $\text{LiNO}_3$  salt solution. Reaction yields were estimated as a function of salt concentration based on the power law measurements of  $3.4\text{ MeV}$  alpha particles. The oxygen production by heavy-particle radiation increases while the yields of  $\text{H}_2$ ,  $\text{H}_2\text{O}_2$ ,  $\text{H}$ ,  $\text{OH}$ , and  $\text{HO}_2$  all decrease with increasing salt concentration. The increase in oxygen production due to radiolysis may be balanced by the production of tritium atoms. It has been shown that oxygen added to non-boiling fission-reactor coolants at high power levels rapidly combines with any hydrogen present. The decrease in the yield of free radicals in concentrated  $\text{LiNO}_3$  solutions makes this salt more favored than  $\text{LiOH}$  solutions.

The effect of elevated temperature on radiolysis was investigated. From experience gained in the fission industry with pure water, it can be ascertained that the stability of non-boiling water to radiolysis increases as temperature increases. The apparent stability is actually caused by an increase in recombination-reaction rates of radicals at elevated temperatures.

In summary, although many uncertainties remain and much research is required in the area of radiolysis, the use of a highly concentrated, aqueous  $\text{LiNO}_3$  salt solutions should not lead to the formation of volatile or explosive gas mixtures. The effects of radiolytic

decomposition products on corrosion, however, remain uncertain and experimental data on the behavior of radiolytic decomposition products in a fusion environment are needed.

Stress-corrosion cracking (SCC) is a major concern in the nuclear industry. Most recent experiences with SCC in a nuclear environment clearly show that reducing the oxygen content through the addition of hydrogen to the coolant can reduce SCC in most ferritic and austenitic alloys. The production of tritium in an aqueous lithium-salt solution is seen as an SCC controlling mechanism. The proper choice of structural material can further reduce the probability of SCC. In particular, a high chromium content together with a low carbon content is shown to reduce SCC. The ferritic alloy, 9-C, fulfills this requirement.

Experience with various aqueous nitrate-salt solutions shows that the choice of the cation will affect the degree of corrosion attack. The aggressiveness of nitrates decreases with choice of cation in the following order:  $\text{NH}_4$ , Ca, Li, K, and Na. Thus, for the  $\text{LiNO}_3$  salt, the aggressiveness of  $\text{NO}_3^-$  ions is in the medium range. The effect of the cation choice on SCC has been related to the acidity of the solution. Investigations into buffering the  $\text{LiNO}_3$  salt solutions to an optimum pH value could lead to a marked reduction in the aggressiveness of the solution. Reduction of the oxidizing strength of the salt solution has been found to retard failure of test samples by SCC. On the other hand, an increase in the oxidizing power of the solution decreases radiolytic decomposition rates. An optimum oxidizing strength will have to be established experimentally since the number of factors involved are too large to make analytical predictions.

Recent experiments [87] on the corrosion rates of  $\text{LiNO}_3$  salt solutions with 316-SS and a martensitic alloy at 95 and 250 °C show a lack of a marked transition between the primary and secondary passive regions. This data implies that a relatively stable passive layer is formed in this salt. Microscopic examination of the 316-SS showed that a smooth oxide film was formed on the metal surface in  $\text{LiNO}_3$ , with the roughness independent of solution concentration and temperature. Recently, electrochemical corrosion tests were performed for aqueous  $\text{LiOH}$  and  $\text{LiNO}_3$  solutions in contact with AISI-316L stainless steel [84]. It was found that stainless steels, particularly low-carbon steels, exhibit better corrosion resistance in  $\text{LiNO}_3$  solution than in  $\text{LiOH}$ .

It should be noted that most of the above experimental findings regarding corrosion and SCC of steels in  $\text{LiNO}_3$  salt solutions were obtained without any control of the oxygen content of the solution which plays a significant role in corrosion processes. In a fusion environment, the production of tritium will undoubtedly affect the oxygen content of the aqueous solution through recombination. Thus, breeding of tritium in the aqueous

solution can potentially reduce corrosion and SCC of the structural material used in the FPC.

The investigation of the corrosion of ferritic steels in an aqueous  $\text{LiNO}_3$  salt solution does not show unexpectedly high corrosion rates or high susceptibility to SCC. In addition, the latest experimental findings do not indicate any unforeseen catastrophic corrosion attack. However, an extensive research effort needs to be undertaken to confirm these observations. Furthermore, the effects of high-energy neutron irradiation on corrosion mechanisms and rates should be examined.

Another form of attack on structural material in an aqueous environment is hydrogen embrittlement, caused primarily by the trapping of absorbed hydrogen in metals under applied stresses. The main factor influencing hydrogen embrittlement is the hydrogen content, which depends strongly on the temperature, microstructure, and strength of the alloy. Hydrogen content can be reduced by minimizing the source of nascent hydrogen (mostly due to corrosion) and by operating at high temperatures ( $> 200^\circ\text{C}$ ), provided that a low-carbon steel is used. High concentrations of chromium, nickel, or molybdenum ( $> 10 \text{ wt.}\%$ ) increase the resistance of ferrous alloys to hydrogen damage. Microstructural features (*e.g.*, a fine-grained and annealed alloy with minimum cold work) further reduce susceptibility to hydrogen embrittlement. Because of the lower strength and higher ductility of ferritic steels, these alloys are generally less susceptible to hydrogen embrittlement than austenitic steels.

Atomic hydrogen is produced on metal surfaces during corrosion processes. Thus, minimizing corrosion also reduces hydrogen embrittlement of the structure. The addition of nitrate salts to the aqueous solution reduces the corrosion rate of ferrous alloys (Section 10.2.1), resulting in a reduction in the production of hydrogen atoms on the surfaces, and thus reducing the nascent hydrogen content. The production of tritium in the coolant does not necessarily result in an increased hydrogen attack because of rapid recombination to form molecular hydrogen or water molecules. The production of hydrogen by nuclear reactions and by plasma-driven permeation through the first wall of a fusion device increases the hydrogen content inside the alloy matrix which may lead to unacceptable hydrogen embrittlement of the structure for operation at or near room temperature (the highest susceptibility of high-strength alloys to hydrogen embrittlement is at or near room temperature [88]). But the TITAN-II structural material operates at high temperatures ( $> 400^\circ\text{C}$ ), minimizing the effective trapping of hydrogen inside the matrix. Experiments show that above  $\sim 200^\circ\text{C}$ , hydrogen embrittlement of ferrous alloys is reduced markedly [89]. Furthermore, the Nelson curves [90], used by the petrochemical industry as guidelines, show that chromium steels can operate at  $400^\circ\text{C}$  with a hydrogen

partial pressure of 17 MPa without experiencing internal decarburization and hydrogen embrittlement [88].

Based on the above discussion, the ferritic alloy 9-C is expected to exhibit a high resistance to hydrogen embrittlement. The number of factors influencing hydrogen embrittlement are numerous and their interdependence is a complex function of the specific microstructure and operating conditions of an alloy. Therefore, experimental data are needed in order to perform a complete evaluation of hydrogen embrittlement of the 9-C alloy under TITAN-II operating conditions.

The physical properties of concentrated solutions of  $\text{LiNO}_3$  at high temperatures differ from those of pure water. Therefore, the exact coolant conditions should be considered in designing the blanket. The thermal-hydraulic design of an aqueous-salt blanket can be very different from that of a water-cooled design, and advantage can be taken of the differences in properties by, for example, reducing the coolant pressure or increasing the temperature without incurring an increased risk of burnout.

A fairly detailed investigation of the physical properties of the aqueous solutions was made, including an extensive literature survey, to ensure that reliable data were used in analyzing the performance of the TITAN-II FPC. In many cases, experimental data for some physical properties of interest for  $\text{LiNO}_3$  solutions are not available at high temperatures. Where this is the case, and reasonable extrapolations cannot be made, the corresponding data for  $\text{NaCl}$  solutions have been used. The  $\text{NaCl-H}_2\text{O}$  system has been much more widely studied than any other solution and many solutions of 1-1 electrolytes (*e.g.*,  $\text{NaCl}$ ,  $\text{KBr}$ , and  $\text{LiNO}_3$ ) have similar properties at the same concentrations. It is expected that such estimates should be accurate to about 20% [91], which is adequate for a worthwhile assessment of the thermal performance of the blanket to be made.

The physical properties of  $\text{LiNO}_3$  solutions as a function of temperature and salt concentration are given in Section 10.2.3. The most drastic effect of adding  $\text{LiNO}_3$  to the coolant water lies in the elevation of the boiling point of the solution. This implies that the thermal-hydraulic design of such an aqueous-salt blanket will be different from that of a pure-water-cooled design. Therefore, a lower coolant pressure or a higher operating temperature can be chosen. The estimated boiling temperature of the  $\text{LiNO}_3$  solutions at various pressures are shown in Figure 1.4-5 for a range of lithium-atom concentration in the aqueous coolant.

Many of the estimates of the properties of  $\text{LiNO}_3$  aqueous solution are extrapolations from experimental data or have been obtained from the results for other salt solutions. Although these predictions should give good indications of the expected trends for the

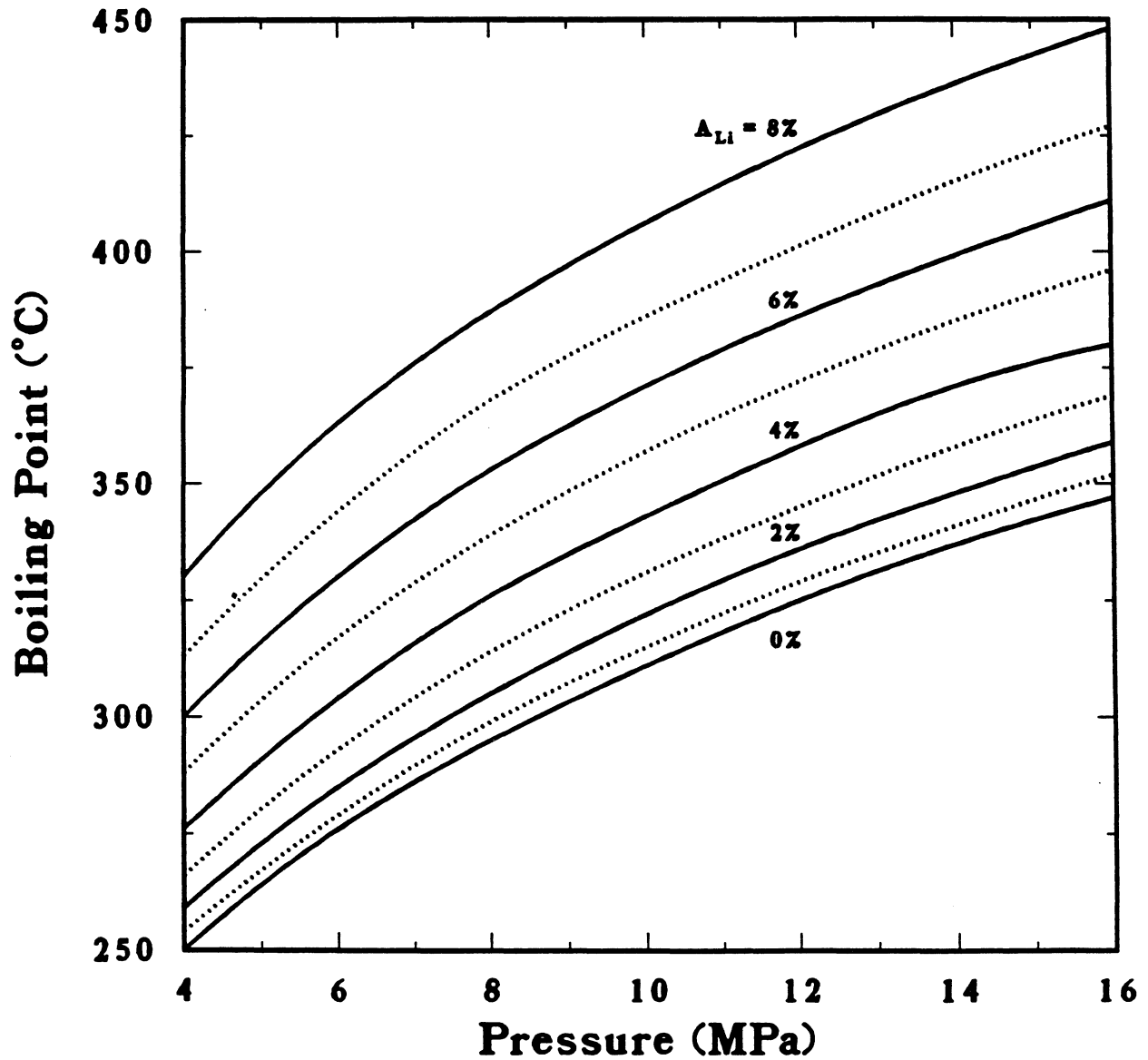


Figure 1.4-5. Boiling temperatures of  $\text{LiNO}_3$  solutions at various pressures and for a range of lithium-atom percentages ( $A_{Li}$ ).

various properties, a much expanded experimental data base is required for the salts and conditions proposed before the thermal performance of an aqueous-salt blanket at high temperature can be confidently predicted.

The TITAN-II design requires a neutron multiplier to achieve an adequate tritium-breeding ratio. Beryllium is the primary neutron multiplier for the TITAN-II design. Corrosion of beryllium in aqueous solutions is a function of the cleanliness of the beryllium surface and of solution impurities. Beryllium surfaces should be free of carbonates and sulfates and the water should have minimum chlorate and sulfate impurities to assure minimum corrosion rates. Coatings to protect beryllium against attack have been developed and their effectiveness has been demonstrated in a neutron-free environment. Research is needed to develop coatings that can withstand harsh radiation environments. For the TITAN-II design, a cladding of 9-C surrounds the beryllium rods.

Swelling levels of above  $\sim 10\%$  will most likely result in a network of interlinking helium bubbles, thus promoting helium release. This means that swelling will stop temporarily until large enough temperature gradients cause sintering of open channels. The sintering temperature for beryllium has been estimated to be around  $660^\circ\text{C}$ . The ongoing process of closing and opening of porosity will ultimately lead to an equilibrium helium-venting rate with an associated maximum swelling value. Realistic prediction of this process is currently not feasible because of the lack of experimental data. A phenomenological swelling equation for beryllium is developed which predicts a maximum swelling value between  $9\%$  and  $15\%$  depending on the amount of retained helium atoms. A swelling value of  $10\%$  is taken as the basis for design calculations. Swelling may be accommodated, to a degree, by employing beryllium with low theoretical density ( $\sim 70\%$ ). This density can easily be achieved by using sphere-packed beryllium. The maximum operating temperature must be kept below  $660^\circ\text{C}$  to prevent sintering of the spheres.

Two methods for accommodating the high rate of swelling in beryllium are available: (1) using a very fine grain beryllium operating at temperatures above  $750^\circ\text{C}$  to ensure interlinkage of bubbles to vent the helium gas into the plenum of the cladding tube and (2) using sphere-packed beryllium with a low theoretical density (about  $70\%$ ) and accumulating the helium inside the porosity. The latter approach, however, results in a lower neutron multiplication and a reduction of thermal conductivity.

Irradiation data on the strength of beryllium are sparse. Irradiation hardening does occur at temperatures above  $300^\circ\text{C}$ . McCarville *et al.* [92], predict that thermal creep may help extend the lifetime by relieving stresses caused by differential swelling, with irradiation-creep effects being negligible.

### 1.4.3. Neutronics

Neutronics calculations for the TITAN-II design were performed with ANISN [70], a 1-D neutron and gamma-ray transport code, using a  $P_3S_8$  approximation in cylindrical geometry. The nuclear data library ENDF/B-V-based MATXS5 was used. The energy group structures in this library are 30 groups for the neutron cross-sections and 12 groups for the gamma-ray cross sections. The library was processed with the NJOY system at Los Alamos National Laboratory [71] for coupled neutron and gamma-ray transport calculations. Neutronics scoping studies are performed with the configurational parameters based on the coupled mechanical and thermal-hydraulic design evaluations of the TITAN-II FPC.

Scoping calculations were performed for several combinations of blanket and shield thicknesses and different levels of  ${}^6\text{Li}$  enrichment in the  $\text{LiNO}_3$  salt dissolved in the water coolant. The option of using heavy water ( $\text{D}_2\text{O}$ ) as the coolant for TITAN-II design was also considered, since  $\text{D}_2\text{O}$  has a lower neutron absorption cross section compared to ordinary water ( $\text{H}_2\text{O}$ ). It is of interest to determine if heavy water can be used alone without any beryllium for the TITAN-II design. The effects of the beryllium density factor on the neutronics performance of the TITAN-II design were also studied. It is found that:

1. The thickness of the Be zone or the level of  ${}^6\text{Li}$  enrichment can be adjusted to obtain the desired tritium-breeding ratio (TBR). A 0.15-m-thick Be zone with 30%  ${}^6\text{Li}$  enrichment level results in a TBR of 1.2.
2. The ordinary-water blanket has a higher TBR than the one cooled by heavy water, within the range of blanket parameters used. The reason is that hydrogen has a better neutron moderation capability than deuterium. As a result, the neutron leakage into the TF coils is also higher for heavy-water blanket.
3. Without beryllium, both  $\text{H}_2\text{O}$  and  $\text{D}_2\text{O}$  aqueous nitrate-salt blankets have insufficient TBR. Marginal TBR can be achieved for a heavy-water blanket if the structural content is reduced to 1% to 2%.
4. For blankets that were considered, the blanket-energy multiplication ranges from 1.25 to 1.4.

Based on the neutronics scoping studies, the reference design of the TITAN-II reactor was determined and is illustrated in Figure 1.4-6. The neutronics performance of the

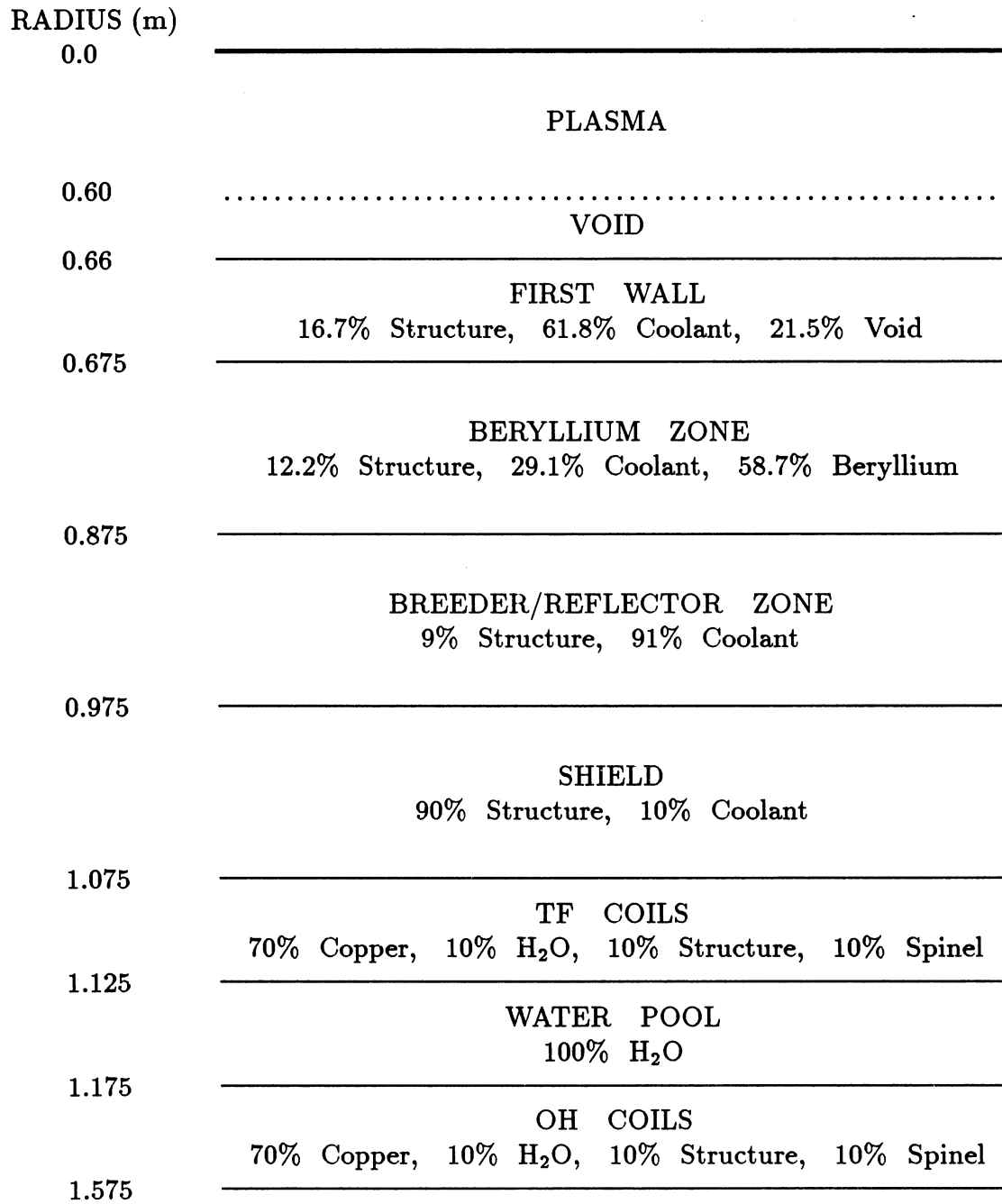


**Figure 1.4-6.** Schematic of the blanket and shield for the TITAN-II reference design. The coolant is an aqueous lithium-nitrate salt solution (6.4 at.% Li) and beryllium is 90% dense.

reference design is given in Table 1.4-I. The  ${}^6\text{Li}$  enrichment level is 12%, beryllium density factor is 0.9, TBR is 1.22, and the blanket-energy multiplication is 1.36. The fast-neutron flux at the TF coils is about  $3 \times 10^{25}$  n/m<sup>2</sup> and the total fast-neutron fluence on the TF coils after 30 full-power years of operation is about  $1 \times 10^{27}$  n/m<sup>2</sup>, about a factor of 2 to 3 below the lifetime estimate for the spinel insulator.

#### 1.4.4. Thermal and Structural Design

The TITAN-II design uses an aqueous salt solution as the coolant. The coolant circulation is essentially loop-type, similar to that of TITAN-I, although the geometry of the blanket-coolant channels is very different. The salt is  $\text{LiNO}_3$  and its lithium atom concentration is 6.4 at.% with a  ${}^6\text{Li}$  enrichment of 12%. The aqueous salt solution has two advantages as coolant. First, the coolant can act as tritium breeder. Second, the salt content elevates the boiling point of the coolant which can be utilized to reduce primary-coolant pressure below the pressure in the steam generator, eliminating the need for intermediate heat exchangers. Pressure reduction in a pure-water system cannot be realized because of the lower saturation temperature and the resulting lower critical heat flux.

The design peak heat flux on the TITAN-II first wall is  $4.6 \text{ MW/m}^2$ , corresponding to a plasma radiation fraction of 0.95. The inlet and exit temperatures of the coolant are, respectively, 298 and 330°C. The resulting exit subcooling is 17°C and, at moderate coolant velocities, nucleate boiling will take place in the first-wall coolant channels because of the high heat flux. Therefore, the mode of heat transfer in the first-wall coolant channels will be subcooled flow boiling (SFB).

In any application of boiling heat transfer, it must be ensured that the maximum possible heat flux is less than the critical heat-flux (CHF) limit by a certain safety margin. A large amount of data for CHF of pure liquids, especially for water, is available and numerous empirical correlations for the CHF exist. Because of the scatter in the data, these correlations are generally accurate to  $\pm 20\%$  over the applicable range of the data [93]. In the absence of any CHF correlations specifically for high-temperature aqueous solutions, a general correlation, derived for water, has been used. This correlation for CHF,  $q''_{CHF}$ , was developed by Jens and Lottes [94] and has the range of parameters for boiling heat transfer which is close to those of the first-wall coolant channel of TITAN-II. Conversion to more convenient units of  $\text{MW/m}^2$  yields

$$q''_{CHF} = C \left( \frac{G}{1356} \right)^m (\Delta T_{sub})^{0.22}, \quad (1.4-1)$$

**Table 1.4-I.**  
**NEUTRONICS PERFORMANCE OF THE TITAN-II REFERENCE  
 DESIGN**

---

Beryllium zone thickness (m)	0.2
Breeder/reflector zone thickness (m)	0.1
Shield thickness (m)	0.1
<sup>6</sup> Li enrichment (%)	12.
Tritium-breeding ratio	1.22
Blanket-energy multiplication, <i>M</i>	1.36
Fraction (% of <i>M</i> ) of nuclear energy in	
First wall	12.4
Beryllium zone	69.2
Breeder/reflector zone	12.7
Shield	5.7
Energy leakage (% of <i>M</i> ) to	
TF coils	1.27
Water pool	0.31
OH coils	1.09
<i>TOTAL:</i>	2.67

---

where  $G$  is the mass velocity of the coolant ( $= \rho v$ ) in  $\text{kg}/\text{m}^2\text{s}$ , the factor 1356 arises from the conversion of units, and  $\Delta T_{sub}$  is the local subcooling in  $^{\circ}\text{C}$ . Constants  $C$  and  $m$  depend on the pressure,  $p$ , through:

$$C = 3.00 - 0.102p, \quad (1.4-2)$$

$$m = \frac{p}{30} + 0.04. \quad (1.4-3)$$

Data used in deriving the above CHF correlation was limited to maximum values of critical heat flux of  $38 \text{ MW}/\text{m}^2$ , water velocity of  $17 \text{ m}/\text{s}$ , pressure of  $13.6 \text{ MPa}$ , and local subcooling of  $90^{\circ}\text{C}$ .

Because of the scatter in the data for critical heat flux, the maximum heat flux on the TITAN-II first wall is kept within 60% of that predicted by the correlation of Jens and Lottes so that an adequate safety margin for CHF is available. References cited in [93] show that the CHF is increased by about 40% in an aqueous solution of ethanol compared with that of pure water. Since CHF correlation for pure water is used for TITAN-II design, any increase in the CHF because of the lithium salt content will add to the safety margin.

The important temperatures in the blanket and shield are those at the center of the beryllium rods, the clad, the channel wall, and the maximum temperature in the shield region which should not exceed the design limits. In the blanket and shield regions, the heat flux removed by the coolant is very low, and the coolant flow is turbulent. Forced-convective heat transfer is adequate to remove the heat without raising the wall temperature to the level which would initiate nucleate boiling. Therefore, the maximum structure temperatures in the blanket and shield are calculated under the condition of non-boiling, forced-convective heat transfer.

The thermal-hydraulic design for TITAN-II FPC is found based on certain constraints such as the maximum allowable structure temperature ( $550^{\circ}\text{C}$ ), maximum allowable pressure and thermal stresses in the structure (respectively,  $200$  and  $400 \text{ MPa}$ ), coolant velocities, and pumping power. The inlet and exit temperatures of the primary coolant are set, respectively, at  $298$  and  $330^{\circ}\text{C}$  in order to use an existing fission pressurized-water-reactor-type (PWR) power cycle. Because the salt content elevates the boiling point of the coolant, the primary-coolant pressure is reduced to  $7 \text{ MPa}$ , below the pressure in the steam generator, thus eliminating the need for intermediate heat exchangers. The thermal-hydraulic reference design of TITAN-II first wall is given in Table 1.4-II.

The thermal-hydraulic design of TITAN-II is expected to have adequate safety margins. The maximum heat flux crossing the coolant film in the first-wall channel is

Table 1.4-II.

## THERMAL-HYDRAULIC DESIGN OF TITAN-II FIRST WALL

---

Channel outer diameter, $b$	30.0	mm
Channel inner diameter, $a$	27.0	mm
Wall thickness, $t$	1.5	mm
Erosion allowance	0.25	mm
Structure volume fraction	0.17	
Coolant volume fraction	0.62	
Void volume fraction	0.21	
Volumetric heating (structure)	202	MW/m <sup>3</sup>
Volumetric heating (coolant)	270	MW/m <sup>3</sup>
Total thermal power	770.2	MW
Coolant inlet temperature, $T_{in}$	298	°C
Coolant exit temperature, $T_{ex}$	330	°C
Maximum wall temperature, $T_{w,max}$	503	°C
Coolant pressure, $p$	7	MPa
Maximum primary stress	98	MPa
Maximum secondary stress	363	MPa
Coolant flow velocity, $U$	22.6	m/s
Mass flow rate	$1.15 \times 10^4$	kg/s
Volumetric flow rate	10	m <sup>3</sup> /s
Pressure drop, $\Delta p$	0.5	MPa
Total pumping power	12.5	MW
Reynolds number, $Re$	$1.49 \times 10^6$	
Nusselt number, $Nu$	2360	
Prandtl number, $Pr$	16.5	
Critical heat flux, $q''_{CHF}$	8.3	Mw/m <sup>2</sup>
Subcooling at exit, $T_{ex,sub}$	17	°C

---

5.1 MW/m<sup>2</sup>, 63% lower than the critical heat flux (8.34 MW/m<sup>2</sup>). The maximum temperature at the mid-plane of the first wall is 503 °C which is less than the allowable limit of 550 °C. The structure temperatures in the blanket and shield coolant channels have even greater safety margins. The maximum pressure stress is less than 50% of the allowable, and the thermal stress is below its limit.

Among other effects of the salt content, the specific heat capacity is reduced by a factor of about two while the density increases only by 15% which results in a significant reduction in the heat capacity of the coolant. The temperature rise of the primary coolant is 32 °C. Therefore, although the coolant pressure drop is only 1 MPa, the large coolant-volume flow rate (39 m<sup>3</sup>/s) results in a pumping power of 49 MW, which is very close to that for TITAN-I. For coolant circulation, pumps supplying a head of 1 MPa are used. Because the coolant flows in parallel through the first wall, multiplier, reflector, and shield zones, orifices are used to reduce the pressure as necessary for each channel. Separate coolant supplies for each of the flow channels (or zones) would alleviate the need for orifices and reduce the pumping power considerably. However, the added complexity of more coolant systems and hydraulic separation of the flow channels does not justify this change.

#### 1.4.5. Magnet Engineering

Two types of magnets are employed in the TITAN-II design (Figure 1.4-2). The ohmic-heating (OH), equilibrium-field (EF) trim, divertor coils, and toroidal-field (TF) coils are normal-conducting with copper alloy as the conductor, spinel as the insulator, and pure water as the coolant. The main EF coils are made of NbTi superconductor and steel structural material. The poloidal-field coils are designed to last the life of the plant. The TF coils are removed with the FPC during the scheduled maintenance but are reused on a new torus afterwards. Because of the simple geometry of the TITAN-II magnets, the robust support structure, and the relatively low field produced by these coils, little or no extrapolation of current technology should be required.

#### 1.4.6. Power Cycle

The selection of the inlet and exit temperatures of the TITAN-II primary coolant (respectively, 298 and 330 °C) is motivated by the possibility of using an existing PWR-type power cycle. The lithium-salt content of the aqueous coolant (6.4 at.%) elevates the boiling point of the coolant from 285 °C for pure water to 347 °C at a pressure of 7 MPa.

Since the primary-coolant pressure is less than the steam pressure in the steam generator (7.2 MPa), any leakage in steam generator tubes will not result in the primary coolant leaking into the steam side. Therefore, the TITAN-II reference design uses a power cycle without an intermediate heat exchanger, which results in an increase in the power cycle efficiency. The parameters of TITAN-II reference power cycle are given in Table 1.4-III. The steam cycle conditions are similar to those of existing PWR-type power cycles [95]. The estimated gross thermal efficiency of the TITAN-II power cycle is 35%.

Table 1.4-III.

## TITAN-II REFERENCE POWER CYCLE

---

<b>Primary Coolant (Water):</b>		
Total thermal power	3027	MW
Inlet temperature	298	°C
Exit temperature	330	°C
Coolant pressure	7	MPa
Saturation temperature	347	°C
Exit subcooling	17	°C
Mass flow rate	$4.5 \times 10^4$	kg/s
Total pumping power	49	MW
<b>Throttle Steam Conditions:</b>		
Temperature	308	°C
Pressure	7.2	MPa
Saturation temperature	289	°C
Degree of superheat	19	°C
Gross thermal efficiency	0.35	

---

### 1.4.7. Divertor Engineering

The design of the impurity-control system poses some of the most severe problems of any component of a DT fusion reactor. The final TITAN-II divertor design represents the result of extensive iterations between edge-plasma analysis, magnetic design, thermal-hydraulic and structural analyses, and neutronics.

The TITAN-II impurity-control system is based on the use of toroidal-field divertors to minimize the perturbation to the global magnetic configuration and to minimize the coil currents and stresses. The TITAN divertor uses an “open” configuration, in which the divertor target is located close to the null point, facing the plasma, rather than in a separate chamber. This positioning takes advantage of the increased separation between the magnetic-field lines (flux expansion) in this region, which tends to reduce the heat loading on the divertor plate because the plasma flowing to the target is “tied” to the field lines. The high plasma density in front of the divertor target ensures that the neutral particles emitted from the surface have a short mean free path; a negligible fraction of these neutral particles enter the core plasma (Section 5.5).

The TF-coil design for TITAN-II, which consists of copper coils as opposed to the integrated-blanket coils (IBC) of TITAN-I, prompted a new divertor magnetic design. The final magnetic design, similar to that of TITAN-I, includes three divertor modules which are located 120° apart in the toroidal direction. An equatorial-plane cross section of the one of the divertor modules is shown in Figure 1.2-11. The magnetic-field lines are diverted onto the divertor plate using one nulling and two flanking coils with the latter localizing the nulling effect (divertor-trim coils are not required as opposed to the TITAN-I design). The TITAN-II divertor coils are made of copper and the joule losses in the TITAN-II divertor coils (9.8 MW) are much smaller than those of the TITAN-I IBC divertor coils (120 MW). Also shown on the outboard view in Figure 1.2-11 is the pumping aperture which leads to the vacuum tank surrounding the torus. This aperture is present for only the outboard 90° in poloidal angle; elsewhere shielding material protects the OH coils.

The results of the magnetics design of TITAN-II divertor (*e.g.*, field-line connection length) were not sufficiently different from those of the TITAN-I to warrant a separate edge-plasma analysis. A summary of the results of the edge-plasma modeling for TITAN-I, which is also used for the TITAN-II design, is given in Table 1.3-IV and is described in detail in Section 5.4. The plasma power balance is controlled by the injection of a trace amount of a high atomic number impurity (xenon) into the plasma, causing strong radiation from the core plasma, the scrape-off layer (SOL) plasma, and

the divertor plasma. About 95% of the steady-state heating power (alpha particle and ohmic heating by the current-drive system) is radiated to the first wall and divertor plate, with about 70% being radiated from the core plasma (*i.e.*, inside the separatrix). This intense radiation reduces the power deposited on the divertor target by the plasma to an acceptably low level. Preliminary experimental results [12,13] suggest that beta-limited RFP plasmas can withstand a high fraction of power radiated without seriously affecting the operating point (Section 5.3). A further result of the radiative cooling is to reduce the electron temperature at the first wall and divertor target (also assisted by recycling) which reduces the sputtering-erosion problem.

To satisfy the requirement for a high- $Z$  material for the plasma-facing surface of the divertor target, a tungsten-rhenium alloy (W-26Re) is used. The high rhenium content provides the high ductility and high strength necessary for the severe loading conditions. A single structural material is used for the divertor target to avoid the problem of bonding dissimilar materials and of stress concentrations which occur at the interface of the two materials. The coolant tubes, therefore, are also made from W-26Re alloy.

The coolant for the divertor system is an aqueous  $\text{LiNO}_3$  solution, as used in the TITAN-II blanket. Advantage is taken of the predicted differences in the physical properties of this solution compared with those of pure water to obtain the high critical heat fluxes ( $\sim 16 \text{ MW/m}^2$ ) necessary to provide an adequate safety margin against burnout. The divertor-plate coolant flows in the toroidal/radial direction to equalize the power deposited on each tube, although this causes gaps between adjacent tubes (if they are of constant cross section) because of the double curvature of the divertor plate. Fabrication of the divertor target is based on brazing of the tungsten-alloy plate (which is produced by powder-metallurgy techniques) to a bank of constant cross-section coolant tubes, although alternative methods which allow tubes of variable cross section to be constructed, have also been considered.

Despite the intense radiation arising from the impurities injected into the plasma, careful shaping of the divertor target, as shown in Figure 1.2-11, is also required to maintain the heat flux at acceptable levels at all points on the plate. Figure 1.4-7 shows the distribution of the various components of the surface heat flux along the divertor target for the inboard and outboard locations. The heat flux on the inboard and outboard targets are respectively, 7.5 and 5.8  $\text{MW/m}^2$  (compared with corresponding levels of 9.5 and 6.0  $\text{MW/m}^2$  for TITAN-I).

The temperature distribution of the divertor-plate coolant and structure is shown in Figure 1.4-8. Given the heat loadings on the divertor-plate cooling tubes, the coolant conditions are determined by the requirements of obtaining an adequate safety factor on

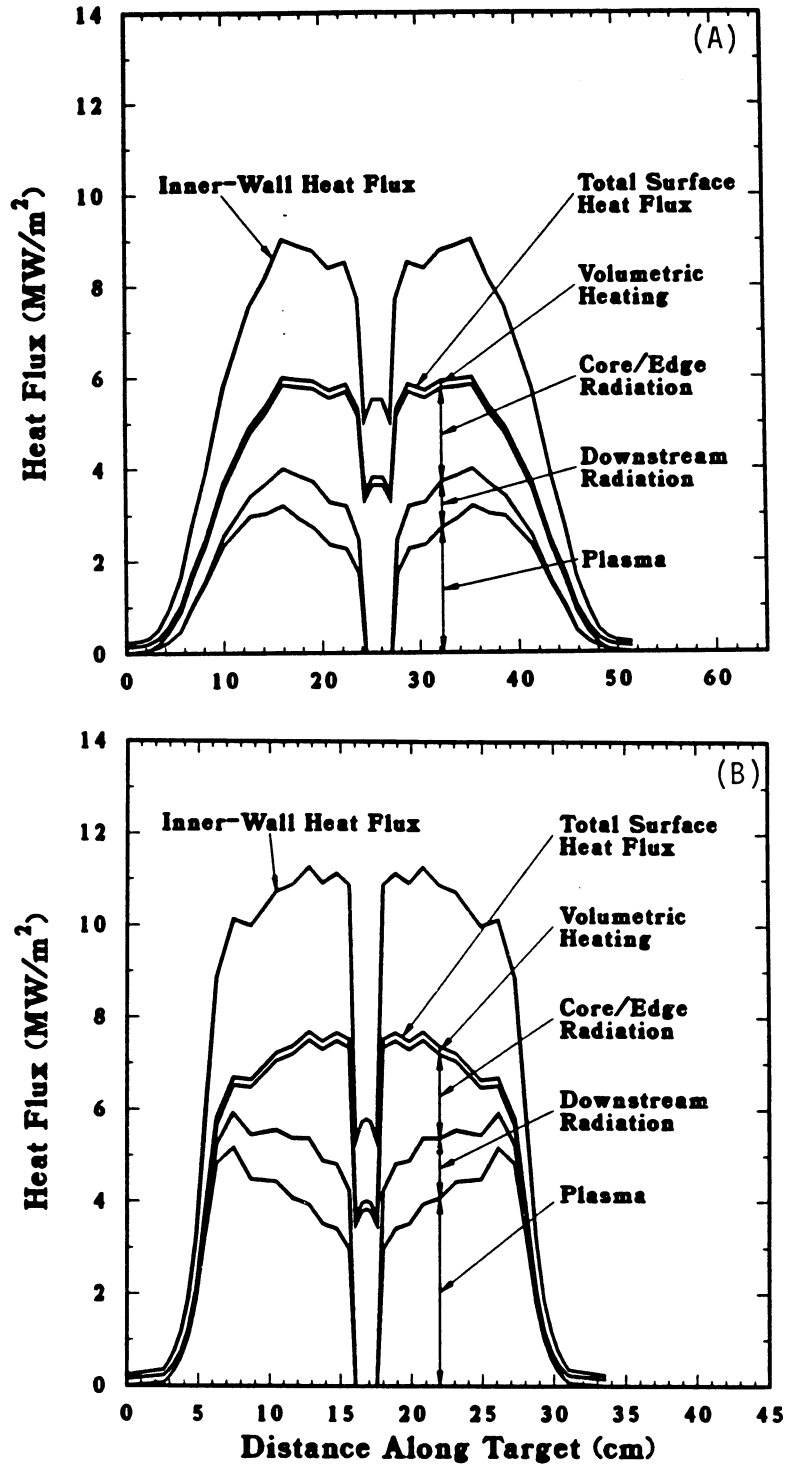


Figure 1.4-7. Heat flux distribution on outboard (A) and inboard (B) sections of divertor target. The critical heat flux for TITAN-II divertor coolant is estimated at  $16.2 \text{ MW/m}^2$ . Distance along target is measured in the direction of coolant flow.

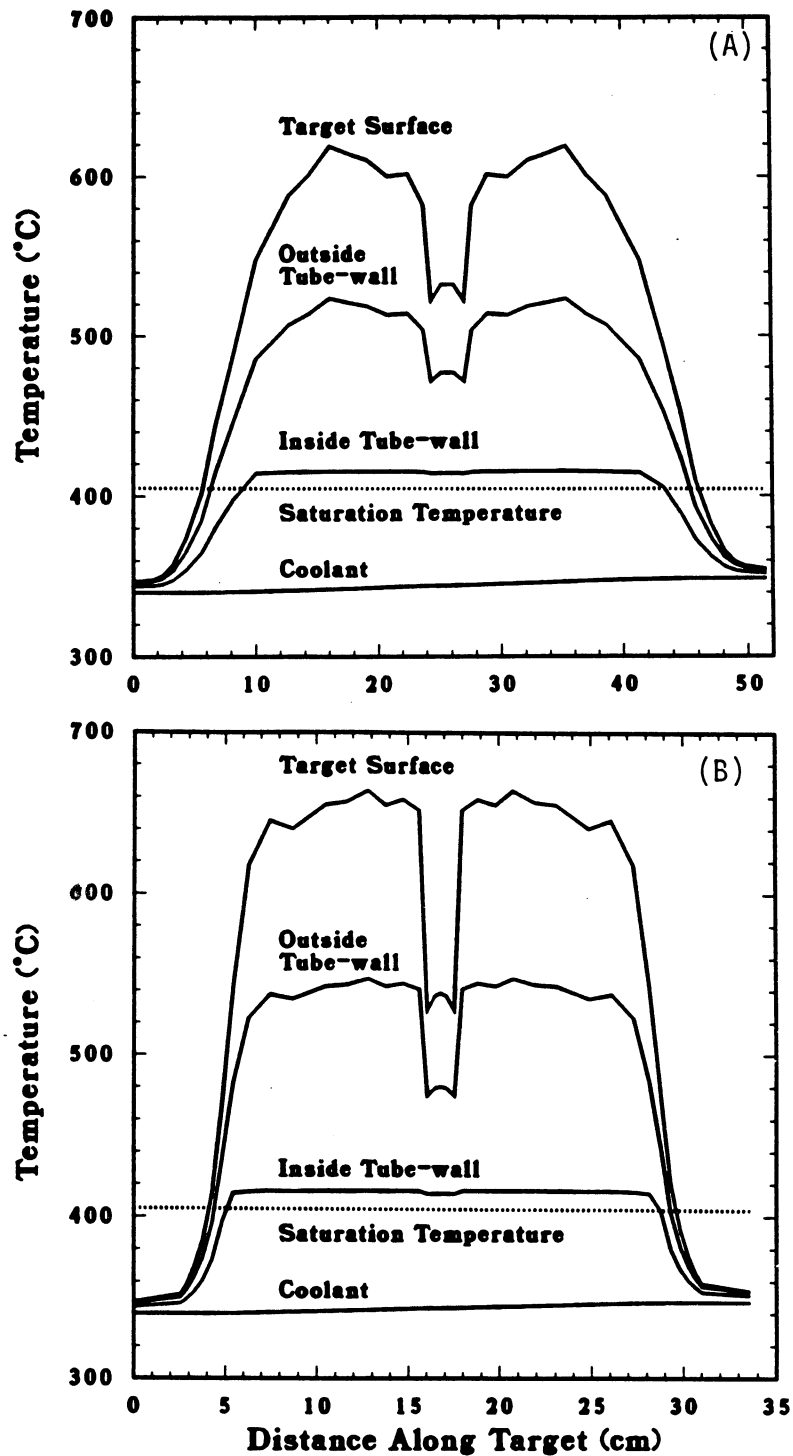


Figure 1.4-8. Coolant and structure temperature distribution on outboard (A) and inboard (B) sections of the divertor target. Distance along target is measured in the direction of coolant flow.

critical heat flux, and allowing the heat deposited into the divertor-target cooling loop to be removed by a heat exchanger with the inlet coolant for the blanket. Additional constraints were that the coolant velocity should not exceed 20 m/s and that its composition should be the same as for the blanket (*i.e.*, a lithium-atom percentage of 6.4%). These considerations led to the selection of the coolant-outlet conditions of 345 °C and 14 MPa. At this pressure, the boiling point of a 6.4% LiNO<sub>3</sub> solution is 405 °C (Section 16.2), yielding a subcooling at the outlet conditions of 60 °C, and a critical heat flux of 16.2 MW/m<sup>2</sup> as predicted by the Jens and Lottes correlation [94] (Equation 1.4-1). A safety factor in excess of 1.4 with respect to critical heat flux is achieved at all points on the target; on the outboard target, where the heat fluxes are lower, the minimum safety factor is about 1.8.

The heat removed from the divertor plate is deposited into the blanket cooling circuit through a heat exchanger. In order to maintain a minimum temperature difference of 20 °C in the heat exchanger between the inlet divertor coolant and the inlet blanket coolant (298 °C), the divertor-coolant inlet temperature must be not less than 318 °C. For a divertor-coolant exit temperature of 345 °C and temperature rise of about 7 °C per pass, the TITAN-II divertor coolant passes four times across the target.

A 2-D finite-element analysis of the steady-state temperatures and stresses in the divertor was made using the finite-element code ANSYS [76]. This analysis indicated that the maximum equivalent thermal stress is about 500 MPa, within the allowable level of 600 MPa for tungsten. The thermal analysis showed that geometric effects concentrate the heat flux from its value on the plate surface to a higher value at the tube-coolant interface, and that the effects of the gaps between adjacent tubes in elevating structural temperatures are acceptable.

The vacuum system is based on the use of a large vacuum tank encompassing the entire torus, and connected to the divertor region by a duct located at each of the three divertor locations. Lubricant-free magnetic-suspension-bearing turbo-molecular pumps are proposed for the high-vacuum pumps to avoid the possibility of tritium contamination of oil lubricants. Pumps of the required size need to be developed.

#### 1.4.8. Tritium Systems

In TITAN-II design, the tritium is bred directly in the aqueous coolant of the primary heat-transport system. Tritium recovery and control of the tritium level in the primary coolant represent critical issues. In particular, tritium recovery from water is required on

a scale larger than existing water-detritionation systems. However, considerable industrial experience with recovery of hydrogen and its isotopes from water is available, and some relevant process equipment is used on a larger scale in non-tritium applications.

The TITAN-II design has a higher tritium level (50 Ci/kg) in the primary-coolant water relative to previous design studies (*e.g.*, 1 Ci/kg in BCSS [66]) in order to minimize the cost of water-processing equipment required for tritium recovery. This tritium level is possible for TITAN-II design because of: (1) a lower pressure in the primary system which is the result of the elevation of the fluid boiling point caused by the addition of the Li salt, (2) possible use of double-walled steam generators, (3) presence of the water pool which captures a large part of the tritiated-water leakage, (4) routine use of welded joints, and (5) removal of tritiated water to safe storage during major maintenance operations. Component leakage rates and air-drier technology are based on CANDU systems performance [18]. The overall tritium-loss rate for the TITAN-II design is estimated at 50 Ci/d.

The tritium inventory in TITAN-II design is shown in Table 1.4-IV. The total tritium inventory is four kilograms, roughly comparable to the inventory in some CANDU reactors at present. The largest inventory is in the primary circuit, which requires a larger blanket processing system.

The blanket tritium-recovery system reference design is summarized in Table 1.4-V. This system recovers 430 g/d of tritium, primarily through a five-stage vapor-phase catalytic-exchange (VPCE) system which transfers the tritium from the water to hydrogen gas, and then by cryogenic distillation for isotope separation. The TITAN-II FPC is submerged in the pool of water to achieve a high level of safety. The water pool contains tritium from primary-coolant system leakage, which is maintained at 0.37 Ci/kg by water distillation, with the enriched tritiated water from the distillation columns mixed with the primary-coolant water for final tritium recovery. The water-feed rate to the VPCE system is about 4000 kg/h at 50 Ci/kg. The estimated installed cost of the TITAN-II tritium recovery system is 130 M\$ (1986), not including building, air cleanup, and indirect costs. Although the water-feed rate is about 10 times larger than the Darlington Tritium-Removal Facility, the cost is only 3 to 4 times larger because of the economy of scale, fewer VPCE stages, and the lower reflux ratio needed in the cryogenic columns by the light-water feed.

The other TITAN-II tritium-related systems and flow rates are also assessed. The fuel-processing systems are similar to those of TITAN-I, which are described in Section 12. Unique features include a redundant impurity-removal loop rather than relying on large tritium storage capacity, and a small feed to the isotope separation system because of

Table 1.4-IV.  
TITAN-II TRITIUM INVENTORIES

System	T Inventory (g)	Form
Primary-heat-transport coolant	1420 <sup>(a)</sup>	HTO
Beryllium	10	T in metal
Piping and structure	< 1	T in metal
Plasma chamber and vacuum system	5	DT
Fuel-processing system	20	DT
Blanket tritium-recovery system	44	HTO
	550	HT
Shield	< 10	HTO
Tritium storage	1000	Metal tritide
Pool	940 <sup>(b)</sup>	HTO
<b>TOTAL</b>	<b>4000</b>	

(a) Based on 274 m<sup>3</sup> at 50 Ci/kg.

(b) Based on 22,640 m<sup>3</sup> at 0.4 Ci/kg.

the use of mixed DT fueling. Plasma-driven permeation is less important in TITAN-II than in TITAN-I because the first wall is at a lower temperature and is made of ferritic steel rather than vanadium. Back diffusion of protium is significant but acceptable. The air-detritionation system has a larger drier (but not recombiner) capacity to recover most of the tritiated water leaking from primary-system components.

The overall cost of the TITAN-II tritium system is 170 M\$ (1986, installed). The cost is dominated by the blanket tritium-recovery system. Since tritium recovery in TITAN-II involves isotope separation of tritium from low concentrations in water, it is expected to be more expensive than for other fusion-blanket concepts. The present design approach is based on proven chemical exchange and distillation concepts. Costs for other tritium

Table 1.4-V.

**TITAN-II BLANKET TRITIUM-RECOVERY SYSTEM  
(BASED ON EXTRACTING 465 g/d of T AT 50 Ci/kg)**

---

Maximum tritium concentration	50 Ci/kg in water
Tritium-extraction rate	465 g/d of T
Tritium inventory as water	44 g T
Tritium inventory as gas	550 g T
Blanket detritiation factor	93% per pass
Hydrogen-refrigeration power	5.7 MWe
Low-pressure steam to water distribution	5.7 MWth at 300 kPa
Low-pressure steam to VPCE	1.2 MWth at 600 kPa
High-pressure steam to VPCE	8.5 MWth at 2.5 MPa
Hydrogen-gas inventory	1500 kg
Building volume	36,000 m <sup>3</sup>

---

systems are similar to those for TITAN-I (except for a larger air-drier capacity). Some costs are estimated from Reference [96].

A major reduction in the costs and tritium levels requires a new water-detritiation approach. At present, laser separation is under investigation, but probably requires improvements in the lasers and optical materials to be attractive. Radiolysis might be helpful if a high yield of HT is obtained (not clear from present experiments), and if the associated O<sub>2</sub> production is acceptable.

Relative to the TITAN-I tritium system (Section 12), the TITAN-II tritium system is more expensive, the total tritium inventory is larger, the overall tritium system is physically larger, and the chronic tritium releases are larger. However, the TITAN-II tritium inventory is much less at risk for major release because of the lack of reactive chemicals, the low temperatures and pressures of most of the tritiated water, and the pool surrounding the FPC hot primary-coolant loop.

### 1.4.9. Safety Design

Strong emphasis has been given to safety engineering in the TITAN study. Instead of an add-on safety design and analysis task, the safety activity was incorporated into the process of design selection and integration at the beginning of the study. The safety-design objectives of the TITAN-II design are: (1) to satisfy all safety-design criteria as specified by the U. S. Nuclear Regulatory Commission on accidental releases, occupational doses, and routine effluents and (2) to aim for the best possible level of passive safety assurance.

The elevation view of TITAN-II reactor is shown in Figures 1.4-1. The TITAN-II FPC is cooled by an aqueous lithium-salt solution and therefore the cooling circuit is a pressurized-water system. Furthermore, the primary coolant contains tritium at a high concentration of 50 Ci/kg. A passive safety system is thus required to handle different accident scenarios, to control the potential release of high-pressure primary coolant which contains tritium, and to prevent the release of induced radioactivities in the reactor structural materials even under the conditions of a loss-of-coolant-accident (LOCA).

The key safety feature of the TITAN-II design is the low-pressure, low-temperature water pool that surrounds the fusion power core and the entire primary-coolant system (Figures 1.4-1). In the case of a major coolant-pipe break, the pressurized coolant in the hot loop will mix with the pool of water since the complete primary loop is in the pool. With this mixing, the temperature of the pool would only rise moderately because of the much larger volume of the water pool. In fact, even if the heat transfer from the pool to the surrounding earth is ignored, it would take more than seven weeks for the temperature of the water pool to reach 100°C. Therefore, the cold pool of water acts as a heat sink to dilute the reactor thermal and radioactive decay afterheat energy and also eliminates the possibility of releasing tritiated water vapor or other radioactive material to the environment.

Based on the "loop-in-pool" concept of the TITAN-II design, different scenarios for handling normal and off-normal situations were evaluated. The size and operating conditions of the TITAN-II water pool are determined by these analyses. In the TITAN-II design, the primary-cooling circuit is not completely insulated from the pool, so the pool can absorb the decay afterheat power in case of a loss-of-flow accident (LOFA) in either the primary circuit or the steam generators. This power is then removed by separate heat exchangers in the pool. The pool temperature should be kept as low as possible to maintain an adequate heat-sink capability in the pool in case of an accident. On the other hand, the pool temperature should be reasonably high so that the size of the

afterheat-removal heat exchangers in the pool, which are capable of removing the steady power of 34 MW, can be minimized. The exact pool temperature should be determined by detailed design. For the TITAN-II reactor, a pool temperature range of 60 to 70 °C is found to be reasonable based on detailed evaluation of the accident scenarios.

A potential accident for pressurized water systems is a double-ended rupture of a main coolant line. The escaping jet of the primary coolant (as steam), which may contain radioactive material, will raise the pressure inside the primary containment building and may result in the release of radioactivity to the environment. Another advantage of the TITAN-II water pool surrounding the FPC is the potential to suppress the consequences of a double-ended rupture of the primary-coolant circuit by containing the escaping jet of the primary coolant inside the water pool. The analysis shows that for a double-ended rupture of a 0.5-m-diameter hot leg, at least 6 to 7 m of cold (60 °C), fully degassed water is needed above the break to prevent a direct discharge of steam into the containment building. This figure has been used to determine the minimum height of TITAN-II pool.

Two of the major accidents postulated for the FPC are the LOFA and LOCA. Thermal responses of the TITAN-II FPC to these accidents are modeled using a finite-element heat-conduction code, TACO2D [79]. Analysis of a LOCA without the pool showed that the peak temperature of the ferritic steel and beryllium would exceed the melting point of these materials. The necessity of the low-pressure pool is evident from these results.

Figure 1.4-9 shows the temperature of the TITAN-II FPC as a function of time after the initiation of a LOFA. For this accident scenario, very little temperature excursion is observed, primarily because of the presence of natural convection within the pool and the primary loop. The first-wall peak temperature of 348 °C is reached after 355 seconds. The TITAN-II reactor appears to be capable of withstanding the loading conditions of this accident scenario.

The thermal response of the TITAN-II FPC to a LOCA in the presence of the pool is also studied. The accident is assumed to be initiated with a "guillotine" break in the primary cold leg, below the level of the torus. At the onset of the accident, a very rapid ( $\sim 1$  s) de-pressurization of the primary loop occurs until the primary-loop pressure reaches the saturation pressure of the primary coolant. Following the initial de-pressurization to saturation conditions, a slower de-pressurization takes place until the primary loop and the pool are at equal pressure. Choked flow at the pipe break determines the rate of de-pressurization. As the pressure in the primary loop drops below the saturation pressure of the primary coolant, flashing of the primary coolant occurs, and the sudden volume change forces the coolant out of the pipe break (blowdown phase). The blowdown phase in typical design-basis accidents for PWRs lasts 10 to 20 seconds,

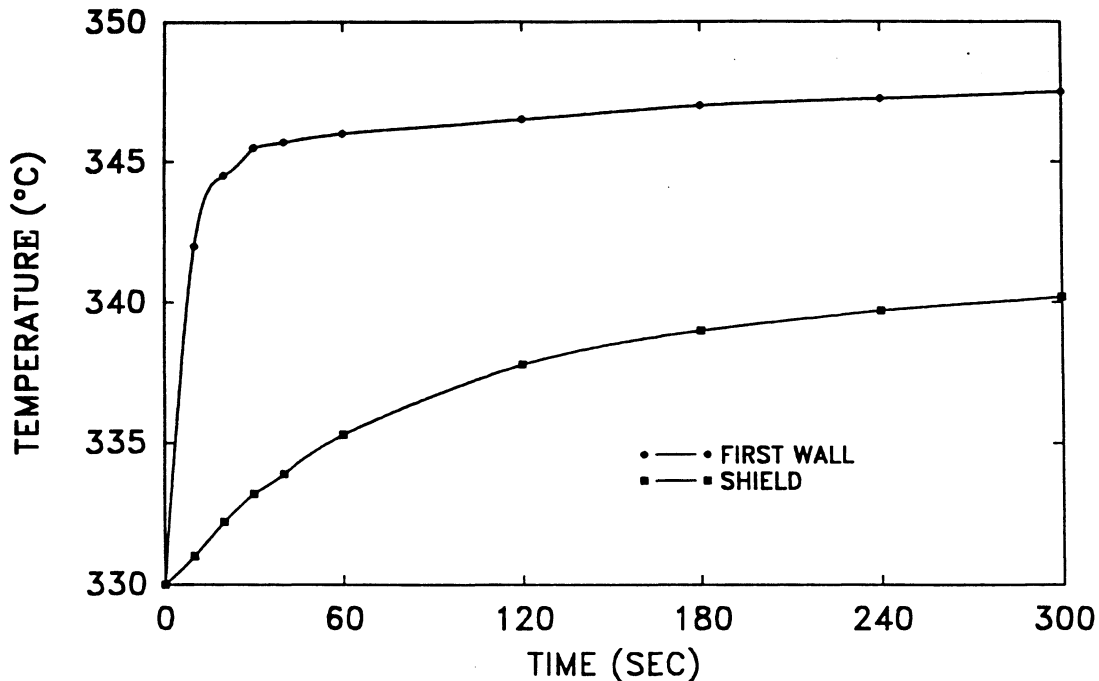


Figure 1.4-9. The thermal response of the TITAN-II FPC to a LOFA with the low-pressure pool as a function of time after the initiation of the accident.

provided that no emergency core-cooling system is engaged. If the pipe break occurs at the lowest point of the primary loop (*i.e.*, the worst case accident) any steam that forms inside the primary piping is trapped because of the buoyancy force. For accident analysis of the TITAN-II FPC, it is conservatively assumed that at the end of blowdown phase, the entire primary loop will be filled with 330 °C steam (operating conditions).

During the re-flood phase, heat is lost from the primary loop (steam) to the surrounding pool and the steam trapped in the primary loop begins to condense. The condensation rate depends on many variables; for this analysis, it is assumed that this phase would last 5 minutes. Virtually any condensation rate can be designed into the system simply by adding insulation to the piping (decreasing the rate of condensation), or by exposing more primary piping to the pool water (increasing the rate of condensation). The final phase of the accident is the onset of natural circulation.

Thermal response of the TITAN-II fusion power core to this accident scenario is shown in Figure 1.4-10. The peak temperature of the FPC is 732 °C which is 688 °C below the melting point of the ferritic steels. The peak beryllium temperature is 481 °C, which is 802 °C below the melting point of beryllium metal.

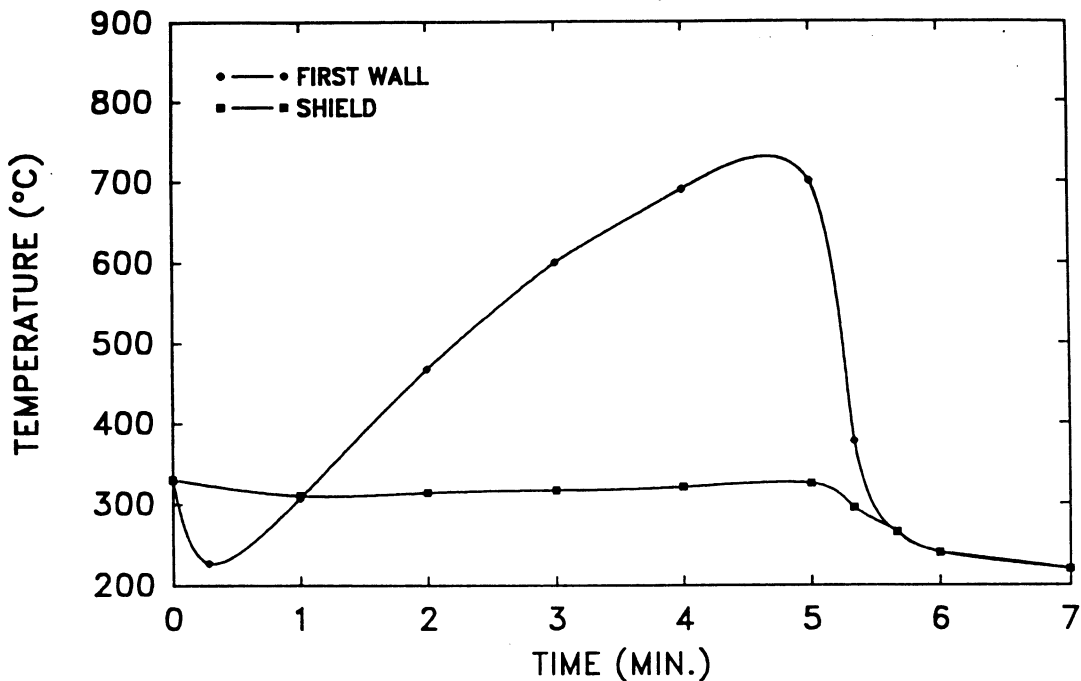


Figure 1.4-10. The thermal response of the TITAN-II FPC to a LOCA with the low-pressure pool as a function of time after the initiation of the accident (with a re-flood time of 300 s).

The key safety feature of the TITAN-II design is the low-pressure, low-temperature water pool that surrounds the FPC. Detailed safety analyses have been performed which show that the TITAN-II pool can contain the thermal and afterheat energy of the FPC and will remain at a low enough temperature so that tritium or other radioactive material in the primary-coolant system will not be released. Therefore, the public safety is assured by maintaining the integrity of the water pool. Since the water-pool structure can be considered a large-scale geometry, the TITAN-II design can be rated as a level-2 of safety assurance design [15,16]. The potential safety concerns are the control of routine tritium releases and the handling of  $^{14}\text{C}$  waste, which is generated from the nitrogen in the  $\text{LiNO}_3$  salt.

Plasma-accident scenarios need to be further evaluated as the physics behavior of RFPs becomes better understood. Preliminary results indicate that passive safety features can be incorporated into the design so that the accidental release of plasma and magnetic energies can be distributed without leading to major releases of radioactivity. Activities in this area need to be continued, especially for high-power-density devices. It should be pointed out that for the TITAN-II design, plasma-related accidents are of con-

cern from the consideration of investment protection and would have minimum impact on public safety. This characteristic is again a result of the presence of the large pool of water that allows the passive protection of the public.

#### 1.4.10. Waste Disposal

The neutron fluxes calculated for the reference TITAN-II reactor were employed as the input to the activation calculation code, REAC [80]. These results were analyzed to obtain the allowable concentrations of alloying and impurity elements in the TITAN-II FPC components. Waste-disposal analysis has shown that the compact, high-power-density TITAN-II reactor can be designed to meet the criteria for Class-C waste disposal [81]. The key features for achieving Class-C waste in the TITAN-II reactor are attributed to: (1) materials selection and (2) control of impurity elements.

The first-wall, blanket, and shield components of the TITAN-II reactor are all integrated in a one-piece lobe design and are all replaced every year. Therefore, one may estimate the allowable concentration levels of the impurity elements by averaging over all components in the lobe. The maximum allowable impurity concentration in the "averaged" TITAN-II FPC are shown in Table 1.4-VI. It appears that the concentration limits for all these impurity elements, except niobium and terbium, are readily achievable when the average limiting concentration levels are imposed. Careful impurity control processes are necessary for Nb and Tb when the structural alloy is fabricated.

The reduced-activation ferritic steel (9-C) used as structural material for the TITAN-II reactor contains tungsten as one of the important alloying elements replacing molybdenum which is an undesirable element for Class-C waste disposal. However, the tungsten content should also be controlled because of the production of a second-step reaction daughter radionuclide,  $^{186m}\text{Re}$  (with a half-life of 200,000 years). The "averaged" allowable concentration level of tungsten is 11.0%, more than two orders of magnitude larger than the present tungsten level in the reduced-activation ferritic steels (0.89%).

Assuming that the structural alloy meets all required levels of impurity and alloying elements as shown in the controlled case in Table 1.4-VI, estimates are made for the TITAN-II reactor materials and related waste quantities for Class-C disposal. The divertor-shield coverage is taken as 13% in the TITAN-II design, identical to the TITAN-I design. The results are presented in Table 1.4-VII. The annual replacement mass of TITAN-II FPC is estimated at about 71 tonnes/FPY ( $9.1 \text{ m}^3$ ), assuming that the entire blanket lobe and the divertor shield are replaced every full-power year (FPY). The data

**Table 1.4-VI.**  
**WASTE-DISPOSAL RATINGS FOR**  
**THE "AVERAGED" TITAN-II BLANKET<sup>(a)</sup>**

Element	Present Case		Controlled Case	
	Nominal Level <sup>(b)</sup> (appm)	Class-C Rating	Controlled Level (appm)	Class-C Rating
Nb	0.1% <sup>(c)</sup>	8.33	1.0 <sup>(d)</sup>	0.42
Mo	1.0% <sup>(c)</sup>	0.27	6.0 <sup>(d)</sup>	0.30
Ag	1.	0.054	0.07	0.054
Tb	5.	1.06	0.1 <sup>(d)</sup>	0.10
Ir	5.	0.0077	0.001	0.0077
W	0.9% <sup>(c,e)</sup>	0.081	0.9% <sup>(c)</sup>	0.081
TOTAL		9.78		0.96

(a) Based on operation at 18 MW/m<sup>2</sup> of neutron wall loading for 1 FPY.

Note that a conservative lifetime fluence value of 15 MWy/m<sup>2</sup> is used for the TITAN-II reference design (0.8 FPY at 18 MW/m<sup>2</sup>).

(b) From Reference [66].

(c) Concentrations in atomic percentage.

(d) Controlled levels lower than impurity levels in ferritic steel.

(e) Present tungsten content in the reduced-activation ferritic steel.

Table 1.4-VII.

**SUMMARY OF TITAN-II REACTOR MATERIALS AND RELATED  
WASTE QUANTITIES FOR CLASS-C WASTE DISPOSAL<sup>(a)</sup>**

Component	Material	Lifetime (FPY) <sup>(a)</sup>	Volume (m <sup>3</sup> )	Weight (tonnes)	Annual
					Replacement Mass (tonnes/FPY)
First wall	Ferritic steel (9-C)	1	0.26	2.0	2.0
Be zone	Ferritic steel (9-C)	1	2.5	19.7	19.7
Breeder zone	Ferritic steel (9-C)	1	2.0	15.3	15.3
Shield	Ferritic steel (9-C)	1	3.9	30.5	30.5
TF coils	Modified steel		0.54	4.8	0.08
	Copper		3.8	34.0	1.13
	Spinel		0.54	2.2	0.08
	TOTAL	30	4.9	41.0	1.39
OH coils	Modified steel		5.4	49.	1.63
	Copper		38.2	342.	11.4
	Spinel		5.4	23.	0.77
	TOTAL	30	49.0	414.	13.8
EF coils shield	Modified steel	30	5.6	50.	1.7
Divertor shield	Ferritic steel	1	0.48	3.78	3.78
TOTAL CLASS-C WASTE (lifetime)			334.	2643.	88.1

(a) Based on operation at 18 MW/m<sup>2</sup> of neutron wall loading for 1 FPY.

Note that a conservative lifetime fluence value of 15 MWy/m<sup>2</sup> is used for the TITAN-II reference design (0.8 FPY at 18 MW/m<sup>2</sup>).

in Table 1.4-VII is for a modified TITAN-II design with a 0.03-m shield and a 0.17-m blanket breeder zone, rather than the 0.1-m shield and 0.1-m blanket breeder zone of the reference design. The reduced shield thickness in this design will decrease the annual replacement mass by about 50 tonnes/FPY and also satisfies the structural-design aspects of the blanket lobe. The penalty for this modified design is a 1.5% reduction in the blanket energy multiplication.

The TITAN-II divertor plates are fabricated with a tungsten armor because of its low sputtering properties. The waste-disposal rating of the divertor plates is estimated to be a factor of 10 higher than for Class-C disposal after one year of operation. The annual disposal mass of this non-Class-C waste is 0.35 tonnes, about 0.4% of the average annual discharge mass.

Because of the use of nitrate salt in the aqueous-solution coolant, the TITAN-II reactor is also producing  $^{14}\text{C}$  from  $^{14}\text{N}$  (n,p) reactions. The annual production rate of  $^{14}\text{C}$  is about  $5.2 \times 10^4$  Ci. Using the present 10CFR61 regulations, where the allowable concentration of  $^{14}\text{C}$  for Class-C disposal is 8 Ci/m<sup>3</sup> and if  $^{14}\text{C}$  remains in the aqueous-solution coolant, the coolant should be replaced at a rate of  $7 \times 10^3$  tonnes/FPY ( $6.5 \times 10^3$  m<sup>3</sup>). The replacement mass of the coolant can be reduced to about 80 tonnes/FPY, if the Reference [82] evaluation is used as the limiting value (700 Ci/m<sup>3</sup>). Because of the large quantities of aqueous solution to be disposed of annually and uncertainties in the transport of the  $^{14}\text{C}$  isotope in the primary loop, extraction of the  $^{14}\text{C}$  activity from the coolant and disposal of the concentrated quantity as non-Class-C waste should be considered.

The safety and environmental conclusions derived from the TITAN reactor study are general, and provide strong indications that Class-C waste disposal can be achieved for other high-power-density approaches to fusion. These conclusions also depend on the acceptance of recent evaluations of specific activity limits carried out under 10CFR61 methodologies [82].

#### 1.4.11. Maintenance

The TITAN reactors are compact, high-power-density designs. The small physical size of these reactors permits each design to be made of only a few pieces, allowing a single-piece maintenance approach [7,8]. Single-piece maintenance refers to a procedure in which all of components that must be changed during the scheduled maintenance are replaced as a single unit, although the actual maintenance procedure may involve the movement, storage, and reinstallation of some other reactor components. The entire reactor torus

in both TITAN designs is replaced as a single unit during scheduled maintenance. Also, because of the small physical size and mass of the TITAN-I FPC, the maintenance procedures can be carried out by vertical lifts, allowing a much smaller reactor vault.

Potential advantages of single-piece maintenance procedures are identified:

1. Shortest period of downtime resulting from scheduled and unscheduled FPC repairs;
2. Improved reliability resulting from integrated FPC pretesting in an on-site, non-nuclear test facility where coolant leaks, coil alignment, thermal-expansion effects, *etc.*, would be corrected by using rapid and inexpensive hands-on repair procedures prior to committing the FPC to nuclear service;
3. No adverse effects resulting from the interaction of new materials operating in parallel with radiation-exposed materials;
4. Ability to modify continually the FPC as may be indicated or desired by reactor performance and technological developments; and
5. Recovery from unscheduled events would be more standard and rapid. The entire reactor torus is replaced and the reactor is brought back on line with the repair work being performed, afterwards, outside the reactor vault.

The lifetime of the TITAN-I reactor torus (including the first wall, blanket, and divertor modules) is estimated to be in the range of 15 to 18 MWy/m<sup>2</sup>, and the more conservative value of 15 MWy/m<sup>2</sup> will require the change-out of the reactor torus on a yearly basis for operation at 18 MW/m<sup>2</sup> of neutron wall loading at 76% availability. The TF coils can last for the entire plant life. However, during the maintenance procedure, the TF coils are not separated from the reactor torus and are replaced each year. After the completion of the maintenance procedure, the TF coils can be separated from the reactor torus and reused at a later time. The impact of discarding (not reusing) the TF coils annually is negligible on the COE. The choice between reusing or discarding the TF coils requires a detailed consideration of: (1) activation intensity of the reused TF coils, (2) remote assembly of activated TF coils to a "clean" FPC, and (3) additional waste generated if TF coils are discarded annually.

Fourteen principal tasks must be accomplished for the annual, scheduled maintenance of the TITAN-II fusion power core. These steps are listed in Table 1.4-VIII. Those tasks that would require a longer time to complete in a modular design are also identified in Table 1.4-VIII (assuming the same configuration for the modular design as that of

Table 1.4-VIII.  
PRINCIPAL TASKS  
DURING THE TITAN-II MAINTENANCE PROCEDURE

---

1. Orderly shutdown of the plasma and discharge of the magnets;
2. Continue cooling the FPC at a reduced level until the decay heat is sufficiently low to allow natural convection cooling in the atmosphere;
3. During the cool-down period:
  - a. Continue vacuum pumping until sufficient tritium is removed from the FPC,
  - b. Valve-off all systems which will be disconnected during maintenance (*i.e.*, vacuum and electrical systems) and, depending on the maintenance method, drain the water pool above the FPC,
  - c. Disconnect electrical and coolant supplies from the upper OH-coil set,
  - d. Break vacuum;
4. Drain primary coolant from FPC;
5. Lift OH-coil set and store in the lay-down area;
6. Disconnect primary-coolant supplies at ring headers;<sup>(a)</sup>
7. Lift the reactor torus and move to the hot cell;<sup>(a)</sup>
8. Inspect FPC area;
9. Install the new, pretested torus assembly;<sup>(a)</sup>
10. Connect primary-coolant supplies, TF-coil electrical supplies, and re-weld all vacuum ducts;<sup>(a)</sup>
11. Replace the upper OH-coil set and connect electrical and coolant supplies;
12. Hot test the FPC;<sup>(b)</sup>
13. Pump-down the system;
14. Initiate plasma operations.

---

(a) The time required to complete these tasks is likely to be longer for a modular system than for a single-piece system, assuming similar configuration.

(b) The new torus assembly is pretested and aligned before commitment to service. Only minimum hot testing would be required.

TITAN-II). Vertical lifts have been chosen for the component movements during maintenance. Lift limits for conventional bridge cranes is around 500 tonnes, with special-order crane capacities in excess of 1000 tonnes. The most massive components lifted during TITAN-II maintenance are the reactor torus (180 tonnes) and the upper OH-coil set (OH coils 2 through 4) and its support structure (120 tonnes), which are easily manageable by the conventional cranes.

An important feature of the TITAN design is the pretest facility. This facility allows the new torus assemblies to be tested fully in a non-nuclear environment prior to committing it to full-power operation in the reactor vault. Any faults discovered during pretesting can be quickly repaired using inexpensive hands-on maintenance. Furthermore, additional testing can be used as a shakedown period to reduce the infant mortality rate of the new assemblies. A comprehensive pretest program could greatly increase the reliability of the FPC, hence increasing the overall plant availability. These benefits of pretesting (higher reliability, higher availability) must be balanced with the additional cost associated with the pretest facility. The more representative the pretests are of the actual operation, the more duplication of the primary-loop components is required.

#### 1.4.12. Summary and Key Technical Issues

The TITAN-II FPC is a self-cooled aqueous "loop-in-pool" design with a dissolved Li salt ( $\text{LiNO}_3$  with 6.4 at.% lithium) as the breeder. The structural material is ferritic steel alloy 9-C [17] (a reduced-activation high-strength alloy, 12Cr-0.3V-1W-6.5Mn-0.08C). The first-wall and blanket lobes are integrated and contain the pressurized coolant at 7 MPa. The structural load from the pressurized lobes is supported by a welded two-piece shield which forms a blanket container packing several lobes into a blanket sector. Three toroidal divertor chambers divide the reactor torus into three sectors. The coolant enters the lobes from the bottom, flows around the torus poloidally, and exits through the top plena. Subcooled-flow-boiling heat transfer is needed to cool the first wall. The blanket contains beryllium rods with ferritic-steel alloy 9-C cladding as the neutron multiplier.

Both lithium-hydroxide ( $\text{LiOH}$ ) and lithium nitrate ( $\text{LiNO}_3$ ) salts were considered because they are highly soluble in water. The  $\text{LiNO}_3$  solution is selected as the reference breeding material because: (1)  $\text{LiOH}$  is more corrosive and (2) radiolytic decomposition of water which results in the formation of highly corrosive substances is minimized when nitrate salts are added to water. Account is taken of the thermo-physical properties of the salt solution, which are significantly different from those of the pure water. The

TITAN-II tritium-control and extraction system would be, in principle, an extension of the technology developed by the Canadian CANDU fission reactor program [18].

A key feature of TITAN-II is that the FPC and the entire primary loop are submerged in a pool of low-temperature, low-pressure water. The basic sources of thermal energy after reactor shutdown are from the hot loop and the induced afterheat from the torus first wall and blanket structures. The first-wall and blanket coolant-channel configurations are designed to allow natural circulation to develop in the case of a loss-of-flow accident (LOFA). In the case of a major break in the primary coolant pipes, the cold pool would absorb the thermal and afterheat energy from the hot loop. Calculations show that the pool remains at a sufficiently low temperature to prevent the release of tritium or other radioactivity in the blanket coolant system. As such, the TITAN-II design appears to achieve complete passive safety (level 2 of safety assurance [15,16]).

The general arrangement of the TITAN-II FPC is illustrated in Figures 1.1-4, 1.1-5, and 1.4-1 to 1.4-4. The operational (maintenance and availability), safety, and environmental issues have been taken into account throughout the design. For example, the size of the expensive containment building is reduced because all maintenance procedures would be performed by vertical lift of the components (heaviest component weighs about 180 tonnes). The compactness of the TITAN designs would reduce the FPC to a few small and relatively low-mass components, making toroidal segmentation unnecessary. A "single-piece" FPC maintenance procedure, in which the first wall and blanket are removed and replaced as a single unit is, therefore, possible. This unique approach permits the complete FPC to be made of a few factory-fabricated pieces, assembled on site into a single torus, and tested to full operational conditions before installation in the reactor vault. The low cost of the FPC means a complete, "ready-for-operation" unit can be kept on site for replacement in case of unscheduled events. All of these features are expected to improve the plant availability.

The results from the TITAN study support the technical feasibility, economic incentive, and operational attractiveness of compact, high mass-power-density RFP reactors. The road towards compact RFP reactors, however, contains major challenges and uncertainties, and many critical issues remain to be resolved. The key engineering issues for TITAN-II FPC have been discussed. In the area of materials, more data on irradiation behavior of the ferritic steel alloy 9-C (especially hydrogen embrittlement) are needed to confirm the materials prediction and accurately estimate the lifetime of TITAN-II first wall. The compatibility of ferritic steels with concentrated  $\text{LiNO}_3$  solution is an important issue. Even though some experimental data do not show high corrosion rates or high susceptibility of stress-corrosion cracking, a research effort is needed to confirm

these results in a fusion environment. The effects of radiolytic decomposition products and high-energy neutron irradiation on corrosion mechanisms and rates should be determined. Ceramic insulators offer the potential of minimum irradiation-induced conductivity, high melting and decomposition temperatures, retention of strength, and minimum irradiation-induced swelling. Further experimental data on irradiation behavior of these insulators are needed.

The physical properties of the concentrated  $\text{LiNO}_3$  salt solution are very different from those of pure water. The exact coolant conditions should be considered in designing the blanket. The thermal-hydraulic design of the FPC can take advantage of the differences in the properties of the concentrated solution, for example, by reducing the coolant pressure or increasing the temperature without incurring an increased risk of burnout. A much expanded experimental data base is required for the salts and conditions proposed before the thermal performance of an aqueous-salt blanket at high temperatures and heat fluxes can be confidently predicted.

The design of the impurity-control system poses some of the most severe problems of any component of a DT fusion reactor; for a compact or high-power-density design, these problems can be particularly challenging. Physics operation of high-recycling toroidal-field divertors in RFPs should be experimentally demonstrated and the impact of OFCD on the divertor performance studied. Cooling of the TITAN-II divertor plate requires experimental data on heat-transfer capabilities of concentrated-salt solutions, as outlined above. Fabrication of the tungsten divertor plate remains to be demonstrated and the degree of precision needed for target shaping and control of the position of the plasma separatrix are particularly difficult tasks.

A key concern for the aqueous blanket design is the area of tritium extraction and control. The overall cost of the TITAN-II tritium-recovery system is 170 M\$. A major reduction in the costs and tritium levels requires a new water-detritionation approach. At present, laser isotope separation is under investigation but probably requires improvements in the laser and optical material to be attractive. Radiolysis might be helpful if a high yield of HT is obtained which is not clear from present experiments, and if the associated production of oxygen is acceptable.

**REFERENCES**

- [1] F. Najmabadi, N. M. Ghoniem, R. W. Conn, *et al.*, "The TITAN Reversed-Field Pinch Reactor Study, Scoping Phase Report," joint report of University of California, Los Angeles, General Atomics, Los Alamos National Laboratory, and Rensselaer Polytechnic Institute, UCLA-PPG-1100 (1987).
- [2] R. W. Conn (chairman and editor), "Magnetic Fusion Advisory Committee Panel X Report on High Power Density Fusion Systems" (May 8, 1985).
- [3] J. Sheffield, R. A. Dory, S. M. Cohn, J. G. Delene, L. F. Parsley, *et al.*, "Cost Assessment of a Generic Magnetic Fusion Reactor," Oak Ridge National Laboratory report ORNL/TM-9311 (1986) 103.
- [4] R. A. Krakowski, R. L. Miller, and R. L. Hagenson, "The Need and Prospect for Improved Fusion Reactors," *J. Fusion Energy* **5** (1986) 213.
- [5] R. A. Krakowski, R. L. Hagenson, N. M. Schnurr, C. Copenhaver, C. G. Bathke, R. L. Miller, and M. J. Embrechts, "Compact Reversed-Field Pinch Reactors (CRFPR)," *Nuclear Eng. Design/Fusion* **4** (1986) 75.
- [6] H. A. Bodin, R. A. Krakowski, and O. Ortolani, "The Reversed-Field Pinch: from Experiment to Reactor," *Fusion Technol.* **10** (1986) 307.
- [7] R. L. Hagenson, R. A. Krakowski, C. G. Bathke, R. L. Miller, M. J. Embrechts, *et al.*, "Compact Reversed-Field Pinch Reactors (CRFPR): Preliminary Engineering Considerations," Los Alamos National Laboratory report LA-10200-MS (1984).
- [8] C. Copenhaver, R. A. Krakowski, N. M. Schnurr, R. L. Miller, C. G. Bathke, *et al.*, "Compact Reversed-Field Pinch Reactors (CRFPR)," Los Alamos National Laboratory report LA-10500-MS (1985).
- [9] M. K. Bevir and J. W. Gray, "Relaxation, Flux Consumption and Quasi Steady State Pinches," *Proc. of RFP Theory Workshop*, Los Alamos, NM, U. S. A. (1980), Los Alamos National Laboratory report LA-8944-C (1982) 176.
- [10] K. F. Schoenberg, J. C. Ingraham, C. P. Munson, *et al.*, "Oscillating-Field Current-Drive Experiments in a Reversed-Field Pinch," *Phys. Fluids* **31** (1988) 2285; also R. A. Scardovelli, R. A. Nebel, and K. A. Werley, "Transport Simulation of the Oscillating Field Current Drive Experiment in the Z-40M," Los Alamos National Laboratory report LA-UR-2802 (1988).

- [11] J. B. Taylor, "Relaxation and Magnetic Reconnection in Plasma," *Rev. Mod. Phys.* **58** (1986) 741; also "Relaxation of Toroidal Plasma and Generation of Reversed Magnetic Fields," *Phys. Rev. Lett.* **33** (1974) 1139; and "Relaxation of Toroidal Discharges," *Proc. 3rd Topical Conf. on Pulsed High-Beta Plasmas*, Abingdon (September 1975), Pergamon Press, London (1976) 59.
- [12] M. M. Pickrell, J. A. Phillips, C. J. Buchenauer, T. Cayton, J. N. Downing, A. Haberstich, *et al.*, "Evidence for a Poloidal Beta Limit on ZT-40M," *Bull. Am. Phys. Soc.* **29** (1984) 1403.
- [13] P. Thullen and K. Schoenberg (Eds.), "ZT-H Reversed-Field Pinch Experiment Technical Proposal," Los Alamos National Laboratory report LA-UR-84-2602 (1984) 26.
- [14] D. Steiner, R. C. Block, and B. K. Malaviya, "The Integrated Blanket-Coil Concept Applied to a Poloidal Field and Blanket Systems of a Tokamak," *Fusion Technol.* **7** (1985) 66.
- [15] J. P. Holdren *et al.*, "Summary of the Report of the Senior Committee on Environmental, Safety and Economic Aspects of Magnetic Fusion Energy," Lawrence Livermore National Laboratory report UCRL-53766-Summary (1987); also J. P. Holdren *et al.*, "Exploring the Competitive Potential of Magnetic Fusion Energy: The Interaction of Economics with Safety and Environmental Characteristics," *Fusion Technol.* **13** (1988) 7.
- [16] S. J. Piet, "Approaches to Achieving Inherently Safe Fusion Power Plants," *Fusion Technol.* **10** (1986); also "Inherent/Passive Safety For Fusion," in *Proc. 7th ANS Topical Meeting on Tech. of Fusion Energy*, Reno, Nevada (1986).
- [17] D. S. Gelles, N. M. Ghoniem, and R. W. Powell, "Low Activation Ferritic Alloys Patent Description," University of California Los Angeles report UCLA/ENG-87-9 PPG-1049 (1987).
- [18] K. Y. Wong, T. A. Khan, F. Guglielmi, *et al.*, "Canadian Tritium Experience," Ontario Hydro report (1984).
- [19] P. G. Weber *et al.*, "Results from the Los Alamos RFP Experiments," *Proc. 12th European Conf. on Cont. Fusion and Plasma Phys.*, Budapest, Hungary (September 1985), *European Phys. Soc.* **1** (1985) 570.

- [20] B. Alper *et al.*, "RFP Confinement Studies in ETA-BETA-II," *Proc. 12th European Conf. on Cont. Fusion and Plasma Phys.*, Budapest, Hungary (September 1985), *European Phys. Soc.* 1 (1985) 578.
- [21] H. A. B. Bodin, "New Results from the HBTX Experiment," *Bull. Am. Phys. Soc.* 32 (1987) 1784.
- [22] G. Malesani and G. Rostagni, "The RFX Experiment," *Proc. 14th Symp. Fusion Technology*, Avignon (1986) 173.
- [23] K. Ogawa, Y. Maejima, T. Shimada, Y. Hirano, P. G. Carolan, C. W. Gowers, A. Nagata, H. Ashida, T. Amano, and Y. Kondoh, "Experimental and Computational Studies of Reversed-Field Pinch on TPE-1R(M)," *Proc. 9th Int. Conf. on Plasma Phys. and Cont. Nucl. Fusion Res.*, Baltimore, U. S. A. (September 1982) IAEA, Vienna, 1 (1983) 575.
- [24] Y. Hirano, T. Shimada, Y. Maejima, and K. Ogawa, "Improved Stability Period in High-Current-Density Operation of Reversed-Field Pinch of ETL-TPE-1R(M)," *Nucl. Fusion* 22 (1982) 1613.
- [25] A. Buffa *et al.*, "First Results from the ETA-BETA-II RFP Experiment," *Proc. 9th European Conf. on Cont. Fusion and Plasma Phys.*, Oxford, U. K. (September 1979), Culham Laboratory (1979) 544.
- [26] V. Antoni *et al.*, "Studies on High-Density RFP Plasmas in the ETA-BETA-II Experiment," *Proc. 9th Int. Conf. on Plasma Phys. and Cont. Nucl. Fusion Res.*, Baltimore, U. S. A. (September 1982), IAEA, Vienna, 1 (1983) 619.
- [27] V. Antoni *et al.*, "Reversed Field Pinch Plasma with Current Flat-Top in ETA-BETA-II," *Proc. 10th Int. Conf. on Plasma Phys. and Cont. Nucl. Fusion Res.*, London, U. K. (September 1984), IAEA, Vienna, 2 (1985) 487.
- [28] H. A. B. Bodin *et al.*, *Proc. 9th Int. Conf. on Plasma Phys. and Cont. Nucl. Fusion Res.*, Baltimore, U. S. A. (September 1982), IAEA, Vienna, 8 (1983) 641.
- [29] P. Carolan *et al.*, "New Results from HBTX1A Reversed Field Pinch," *Proc. 10th Int. Conf. on Plasma Phys. and Cont. Nucl. Fusion Res.* London, U. K. (September 1984), IAEA, Vienna, 2 (1985) 449.
- [30] T. Tamano *et al.*, "Pinch Experiments in OHTE," *Proc. 9th Int. Conf. on Plasma Phys. and Cont. Nucl. Fusion Res.*, Baltimore, U. S. A. (September 1982), IAEA, Vienna, 1 (1983) 609.

- [31] T. Tamano, W. D. Bard, T. N. Carlstrom, C. Chu, B. Curwe, R. K. Fisher, *et al.*, "High Current, High Beta Toroidal Pinch Experiment in OHTE," in *Proc. 10th Int. Conf. on Plasma Phys. and Cont. Nucl. Fusion Res.*, London, U. K. (September 1984) IAEA, Vienna (1985).
- [32] D. A. Baker, M. D. Bausman, C. J. Buchenauer, L. C. Burkhardt, G. Chandler, and J. N. DiMarco, "Performance of the ZT-40M Reversed-Field Pinch with an Inconel Liner," *Proc. 9th Int. Conf. on Plasma Phys. and Cont. Nucl. Fusion Res.*, Baltimore, U. S. A. (September 1982) IAEA, Vienna, 1 (1983) 587.
- [33] D. A. Baker, C. J. Buchenauer, L. C. Burkhardt, E. J. Caramana, J. N. DiMarco, J. N. Downing, *et al.*, "Experimental and Theoretical Studies of the ZT-40M Reversed-Field Pinch," in *Proc. 10th Int. Conf. on Plasma Phys. and Cont. Nucl. Fusion Res.*, London, U. K. (September 1984) IAEA, Vienna (1985).
- [34] D. B. Thomson (Ed.), *Proc. Int. Workshop on Engineering Design of Next Step Reversed Field Pinch Devices*, Los Alamos National Laboratory (July 13-17, 1987).
- [35] C. G. Bathke, R. A. Krakowski, R. A. Krakowski, and R. L. Miller, "A DT Neutron Source Based on the Reversed Field Pinch," *Proc. 12th IEEE Symp. on Fusion Eng.*, Monterey, CA (October 1987) 829.
- [36] C. C. Baker, M. A. Abdou, R. M. Arons, A. E. Bolon, C. D. Boley, J. N. Brooks, *et al.*, "STARFIRE – A Commercial Tokamak Fusion Power Plant Study," Argonne National Laboratory report ANL/FPP-80-1 (September 1980).
- [37] B. G. Logan, C. D. Henning, G. A. Carlson, R. W. Werner, D. E. Baldwin, W. L. Barr, *et al.*, "MARS Mirror Advanced Reactor Study Final Report," Lawrence Livermore National Laboratory report UCRL-53480 (July 1984).
- [38] H. A. B. Bodin and A. A. Newton, "Review Paper: Reversed-Field Pinch Research," *Nucl. Fusion* **20** (1980) 1255.
- [39] D. A. Baker and W. E. Quinn, "The Reversed-Field Pinch," *FUSION I, Part A*, Edward Teller (Ed.), Academic Press, NY (1981) p. 438.
- [40] C. W. Barnes, J. C. Fernandez, I. Henins, H. W. Hoida, T. R. Jarboe, S. O. Knox, G. J. Marklin, and K. F. McKenna, "Experimental Determination of the Conservation of Magnetic Helicity from the Balance Between Source and Spheromak," *Phys. Fluids* **29** (1986) 3415.

- [41] K. F. Schoenberg, C. J. Buchenauer, R. S. Massey, J. G. Melton, R. W. Moses, R. A. Nebel, and J. A. Phillips, " $F - \Theta$  Pumping and Field Modulation Experiments on a Reversed Field Pinch Discharge," *Phys. Fluids* **27** (1984) 548.
- [42] D. C. Robinson and R. E. King, "Factors Influencing the Period of Improved Stability in ZETA," *Proc. 3rd Int. Conf. on Plasma Phys. and Cont. Nucl. Fusion Res.*, Novosibirsk, U. S. S. R. (Aug. 1968), IAEA, Vienna, **1** (1969) 263.
- [43] D. J. Strickler, J. B. Miller, K. E. Rothe, and Y-K. M. Peng, "Equilibrium Modeling of the TFCX Poloidal Field Coil System," Oak Ridge National Laboratory report ORNL/FEDC-83-10 (1984).
- [44] D. Steiner, M. J. Embrechts, R. Mohanti, and W. Kelleher, "The Integrated-Blanket-Coil Concept Applied to the Spherical Torus," *Proc. 11th Symp. on Fusion Eng.*, Austin, TX (November 1985) 530.
- [45] R. L. Spencer, "Magnetic Islands and Stochastic Field Lines in the RFP," *Proc. RFP Theory Workshop*, Los Alamos, NM (April 29 - May 2, 1980), Los Alamos National Laboratory report LA-8944-C (January 1982) 129.
- [46] C. G. Bathke and R. A. Krakowski, "A Comparison Study of Toroidal-Field and Bundle Divertors for a Compact Reversed-Field Pinch Reactor," *Fusion Technol.* **8** (1985) 1616.
- [47] V. D. Shafranov, "Plasma Equilibrium in a Magnetic Field," *Reviews of Plasma Physics*, Vol. 2, Consultant Bureau, New York (1966) p. 103.
- [48] A. K. Prinja and R. W. Conn, "An Axially-Averaged Radial Transport Model of Tokamak Edge Plasmas," *J. Nucl. Mater.* **128-129** (1984) 135.
- [49] A. K. Prinja, R. F. Schafer, R. W. Conn, and H. C. Howe, "Combined Core/Boundary Layer Transport Simulations in Tokamaks," *J. Nucl. Mater.* **145-147** (1987) 868.
- [50] A. K. Prinja, R. F. Schafer, and R. W. Conn, "Modeling of Plasma Boundary Conditions with Pump Limiters and Divertors," *Bull. Am. Phys. Soc.* **31** (1986) 1536.
- [51] M. F. A. Harrison, E. S. Hotston, and A. de Matteis, "Plasma Edge Physics for NET/INTOR," NET report EUR-FU/XII-361/86/50 (1985).

- [52] D. E. Post, R. V. Jensen, C. B. Tarter, W. H. Grasberger, and W. A. Lokke, "Steady-State Radiative Cooling Rates for Low-Density High-Temperature Plasmas," *Atomic and Nucl. Data Tables* **20** (1977) 397.
- [53] M. Petravic, D. Heifetz, and D. E. Post, "Modelling Analyses of Tokamaks with Divertors and Pumped Limiters," *Proc. 10th Int. Conf. Plasma Phys. and Cont. Nucl. Fusion Res.*, London, U. K. (September 1984) IAEA, Vienna **2** (1985) 103.
- [54] D. Heifetz, D. E. Post, M. Petravic, J. Weisheit, and G. Bateman, "A Monte-Carlo Method for Neutral-Particle Transport in Diverted Plasmas," *J. Comp. Phys.* **46** (1982) 309.
- [55] S. L. Milora, "Review of Pellet Fueling," *J. Fusion Energy* **1** (1981) 15.
- [56] S. L. Milora, "Plasma Fueling Program," in *Fusion Energy Division Annual Progress Report*, Oak Ridge National Laboratory report ORNL-6322 (October 1987).
- [57] L. J. Perkins, S. K. Ho, and J. H. Hammer, "Deep Penetration Fueling of Reactor-Grade Plasmas with Accelerated Compact Toroids," Lawrence Livermore National Laboratory preprint UCRL-96894 (June 1987), submitted to *Nucl. Fusion*.
- [58] W. A. Houlberg, S. L. Milora, and S. E. Attenberger, "Neutral and Plasma Shielding Model for Pellet Ablation," Oak Ridge National Laboratory report ORNL/TM-10556 (October 1987).
- [59] G. A. Wurden, P. G. Weber, R. G. Watt, C. P. Munson, J. C. Ingraham, R. B. Howell, T. E. Cayton, K. Buechl, and E. J. Nilles, "Pellet Refueling of the ZT-40M Reversed Field Pinch," *Nucl. Fusion* **27** (1987) 857.
- [60] T. R. Jarboe and B. Alper, "A Model for Loop Voltage of a Reversed-Field Pinch," *Phys. Fluids* **30** (1987) 1177.
- [61] J. A. Phillips, D. A. Baker, R. F. Gribble, and C. Munson, "Start-up of Reversed-Field Pinches and Current Ramping Using Dynamo Action," submitted to *Nucl. Fusion* (1987).
- [62] A. A. Newton and P. G. Noonan, "Controlled Termination of Reversed-Field-Pinch Discharges," *Nucl. Instr. and Methods* **A245** (1986) 167.
- [63] R. Hancox, R. A. Krakowski, and W. R. Spears, "The Reversed-Field Pinch Reactor Concept," *Nucl. Eng. and Res.* **63** (1981) 251.

- [64] K. F. Schoenberg, R. F. Gribble, and D. A. Baker, "Oscillating Field Current Drive for Reversed Field Pinch Discharges," *J. Appl. Phys.* **56** (1984) 2519.
- [65] D. L. Smith, B. A. Loomis, and D. R. Diercks "Vanadium-Base Alloys For Fusion Reactor Applications – A Review," *J. Nucl. Mater.* **135** (1985).
- [66] D. L. Smith, G. D. Morgan, M. A. Abdou, C. C. Baker, J. D. Gordon, *et al.*, "Blanket Comparison and Selection Study – Final Report," Argonne National Laboratory report ANL/FPP-84-1 (1984).
- [67] E. E. Bloom, "Mechanical Properties of Materials in Fusion Reactor First-Wall and Blanket Systems," *J. Nucl. Mater.* **85-86** (1979) 795.
- [68] N. M. Ghoniem and R. W. Conn, "Assessment of Ferritic Steels for Steady State Fusion Reactors," *Proc. of Fusion Reactor Design and Technology*, International Atomic Energy Agency (1983) 389.
- [69] M. E. Sawan and P. L. Walstrom, "Superconducting Magnet Radiation Effects in Fusion Reactors," *Fusion Technol.* **10** (1986) 741.
- [70] W. W. Engle, Jr., "A User's Manual for ANISN, A One-Dimensional Discrete Ordinates Transport Code with Anisotropic Scattering," Oak Ridge Gaseous Diffusion Plant report K-1693 (1967).
- [71] R. MacFarlane, "Nuclear Data Libraries from Los Alamos for Fusion Neutronics Calculations," *Trans. Am. Nucl. Soc.* **36** (1984) 271.
- [72] J. F. Briesmeister (Ed.), "MCNP – A General Monte Carlo Code for Neutron and Photon Transport, Version 3A," Los Alamos National Laboratory report LA-7396-M, Rev. 2 (1986).
- [73] D. S. Kovner, E. Yu. Krasilnikov, and I. C. Panevin, "Experimental Study of the Effects of a Longitudinal Magnetic Field on Convective Heat Transfer in a Turbulent Tube Flow of Conducting Liquid," *Magnitnaya Gidrodinamika* **2** (1966) 101.
- [74] R. A. Gardner and P. S. Lykoudis, "Magento-fluid-mechanics Pipe Flow in a Transverse Magnetic Field, Part 2, Heat Transfer," *J. Fluid Mech.* **48** (1971) 129.
- [75] E. Yu. Krasilnikov, "The Effect of a Transverse Magnetic Field upon Convective Heat Transfer in Magnetohydrodynamic Channel Flow," *Magnitnaya Gidrodinamika* **1** (1965) 37.

- [76] G. J. DeSalvo and J. A. Swanson, "ANSYS User's Manual," Swanson Analysis Systems, Inc. (1979).
- [77] L. C. Fuller and T. K. Stovall, "User's Manual for PRESTO: A Computer Code for the Performance of Regenerative Superheated Steam-Turbine Cycles," Oak Ridge National Laboratory report ORNL-5547, NASA CR-159540 (1975).
- [78] V. A. Maroni, R. D. Wolson, and G. E. Staahl, *Nucl. Technol.* **25** (1975) 83.
- [79] P. J. Burns, "TACO2D - A Finite Element Heat Transfer Code," Lawrence Livermore National Laboratory report UCID-17980, Rev. 2 (1982).
- [80] F. M. Mann, "Transmutation of Alloys in MFE Facilities as Calculated by REAC (A Computer Code for Activation and Transmutation Calculations)," Hanford Engineering and Development Laboratory report HEDL-TME 81-37 (1982).
- [81] "Standards for Protection Against Radiation," U. S. Nuclear Regulatory Commission, Code of Federal Regulations, Title 10, Part 0 to 199 (1986).
- [82] S. Fetter, E. T. Cheng, and F. M. Mann, "Long-term Radioactivity in Fusion Reactors," to be published in *Fusion Engineering and Design*.
- [83] D. Steiner, *et al.*, "A Heavy Water Breeding Blanket," *Proc. 11th Symp. on Fusion Engineering*, Austin, Texas (1985).
- [84] W. F. Bogaerts, M. J. Embrechts, and R. Waeben, "Application of the Aqueous Self-Cooled Blanket Concept to a Tritium Producing Shielding Blanket for NET," University of Leuven (Belgium) report EUR-FU/XII-80/87/75 (1987).
- [85] D. N. Braski, "The Effect of Neutron Irradiation on the Tensile Properties and Microstructure of Several Vanadium Alloys," *Proc. ASTM Conf. on Fusion Reactor Materials*, Seattle, Washington (1986).
- [86] E. T. Cheng and R. W. Conn, "Waste Disposal Ratings in the TITAN RFP Reactor," *Proc. IEEE 12th Symp. on Fusion Engineering*, Monterey, California (October 12-16, 1987) 913.
- [87] R. Waeben, W. Bogaert, and M. Embrecht, "Initial Corrosion Evaluation of Candidate Materials for an ASCB Driver Blanket for NET," *Proc. IEEE 12th Symp. Fusion Engineering*, Monterey, California (Oct. 1987) 1332.

- [88] R. S. Treseder, "Guarding Against Hydrogen Embrittlement," *Chem. Eng.* **29** (1981) 105.
- [89] M. G. Fontana and N. D. Greene, *Corrosion Engineering*, McGraw-Hill International Book Company, Singapore (1978).
- [90] API Publication 941, "Steels for Hydrogen Service at Elevated Temperatures and Pressures in Petroleum Refineries and Petrochemical Plants," Second Edition, 1971.
- [91] R. H. Wood, University of Delaware, Newark, Delaware, personal communication, August 1987.
- [92] T. J. McCarville, D. H. Berwald, W. Wolfer, F. J. Fulton, J. D. Lee, *et al.*, "Technical Issues for Beryllium Use in Fusion Blanket Applications," Lawrence Livermore National Laboratory report UCID-20319 (1985).
- [93] R. D. Boyd, C. P. C. Wong, and Y. S. Cha, "Technical Assessment of Thermal-Hydraulics for High Heat Flux Fusion Components," Sandia National Laboratory report SAND84-0159 (1985).
- [94] W. H. Jens and P. A. Lottes, "Analysis of Heat Transfer, Burnout, Pressure Drop and Density Data for High Pressure Water," U. S. Atomic Energy Commission report ANL-4627 (1951).
- [95] "Steam/Its Generation and Use," Babcock & Wilcox Co. (1978).
- [96] M. Abdou, C. Baker, J. Brooks, *et al.*, "A Demonstration Tokamak Power Plant Study (DEMO)," Argonne National Laboratory report ANL/FPP/82-1 (1982).